GALAXY CLUSTERS AS ASTROPHYSICAL LABORATORIES AND PROBES OF COSMOLOGY

Amandine Marie Camille Le Brun

A thesis submitted in partial fulfilment of the requirements of

Liverpool John Moores University

for the degree of

Doctor of Philosophy.

August 26, 2014

To my grandfather, Georges Le Brun, for teaching me, among others, perseverance, honesty, to pursue my dreams and always strive for perfection.

*Voici mon secret. Il est très simple: on ne voit bien qu'avec le cœur. L'essentiel est invisible pour les yeux.**

Antoine de Saint-Exupéry, Le petit prince.

Declaration

The work presented in this thesis was carried out at the Astrophysics Research Institute, Liverpool John Moores University and at the University of Birmingham for the first fifteen months of the Degree. Unless otherwise stated, it is the original work of the author.

While registered as a candidate for the degree of Doctor of Philosophy, for which submission is now made, the author has not been registered as a candidate for any other award. This thesis has not been submitted in whole, or in part, for any other degree.

Amandine Marie Camille Le Brun

Astrophysics Research Institute

Liverpool John Moores University

IC2, Liverpool Science Park

146 Brownlow Hill

Liverpool

L3 5RF

UK

AUGUST 26, 2014

Abstract

Galaxy clusters are the most recent of cosmological structures to have formed by the present time in the currently favoured hierarchical scenario of structure formation and are widely regarded as powerful probes of cosmology and galaxy formation physics alike. Over the past few years, it became increasingly clear that precision cluster cosmology requires the development of detailed, realistic theoretical models of galaxy clusters and the confrontation of synthetic surveys generated using these models with observations. This motivates a campaign of large cosmological hydrodynamicical simulations, with plausible 'sub-grid' prescriptions for the relevant galaxy formation physics. This thesis presents a new suite of large-volume cosmological hydrodynamical simulations called cosmo-OWLS. They form an extension to the OverWhelmingly Large Simulations (OWLS) project, and have been designed to help improve our understanding of cluster astrophysics and non-linear structure formation, which are now the limiting systematic errors when using clusters as cosmological probes. Starting from identical initial conditions in either the *Planck* or *WMAP*7 cosmologies, the most important 'sub-grid' physics, including feedback from supernovae and active galactic nuclei (AGN), has been systematically varied. Via the production of synthetic surveys of the simulations and comparisons with observations, the realism of these state-of-the-art models was explored. At the same time, the simulations were shown to provide a valuable tool for interpreting the observational data, as well as powerful means for testing commonly-employed methods for estimating, for example, cluster masses and determining survey selection functions, which are crucial for cluster cosmology.

The properties of the simulated galaxy groups and clusters were first compared to

a wide range of observational data, such as X-ray luminosity and temperature, gas mass fractions, entropy and density profiles, Sunyaev–Zel'dovich flux, *I*-band mass-to-light ratio, dominance of the brightest cluster galaxy, and central massive black hole (BH) masses, by producing synthetic observations and mimicking observational analysis techniques. These comparisons demonstrated that some AGN feedback models can produce a realistic population of galaxy groups and clusters, broadly reproducing both the median trend and, for the first time, the scatter in physical properties over approximately two decades in mass (10^{13} M$_\odot \lesssim M_{500} \lesssim 10^{15}$ M$_\odot$) and 1.5 decades in radius ($0.05 \lesssim r/r_{500} \lesssim 1.5$). However, in other models, the AGN feedback is too violent (even though they reproduce the observed BH scaling relations), implying calibration of the models is required. The production of realistic *populations* of simulated groups and clusters, as well as models that bracket the observations, opens the door to the creation of synthetic surveys for assisting the astrophysical and cosmological interpretation of cluster surveys, as well as quantifying the impact of selection effects.

A study of the scatter and evolution of the hot gas properties of the populations of galaxy groups and clusters, such as X-ray luminosity and temperature, gas mass and Sunyaev–Zel'dovich flux, as a function of the important non-gravitational physics of galaxy formation was then conducted. The median relations and the scatter about them are reasonably well-modelled by evolving broken power-laws. The non-radiative model and the model that neglects AGN feedback are consistent with having self-similar mass slopes, whereas the mass slopes of the AGN feedback models deviate significantly from the self-similar expectation. Self-similar evolution, which is widely adopted in current cosmological studies, was also found to break down when efficient feedback is included. The log-normal scatter varies mildly with mass, is relatively insensitive to non-gravitational physics, but shows a moderately strong decreasing trend with increasing redshift. The X-ray luminosity has a significantly larger scatter than all the other hot gas proxies examined. It is thus the poorest one, while the 'best' one is the mean X-ray temperature.

Synthetic Sunyaev–Zel'dovich observations, generated using a 'multi-purpose' light cone software package developed during the thesis, were used to check the veracity of

some of the results reported by the *Planck* collaboration at the end of 2012. Taken at face value, their results seem to favour a close to self-similar scaling relation between the Sunyaev–Zel'dovich flux and total mass all the way down to individual galaxy haloes, which is in contradiction with X-ray and absorption lines observation. The matched filter used by the Planck collaboration recovers fluxes which are biased increasingly high as feedback intensity increases. Two likely causes for the bias, i.e. confusion and deviations from the universal pressure profiles were investigated. Confusion was found to have a negligible effect when the signal is *averaged* over a large number of systems. Instead a shape mismatch (in terms of pressure profiles) was identified as being mostly responsible for the bias.

Finally, synthetic X-ray observations, generated using a combination of the developed light cone software and of the *XMM–Newton* simulator and processed with the detection pipeline of the XXL survey, were used to start quantifying the selection function of the XXL survey. Preliminary results suggest that: (i) XXL is only able to find a very small fraction of the galaxy group population, (ii) the survey is best at finding low-mass clusters ($14.0 \lesssim \log_{10}[M_{500}(\mathrm{M}_\odot)] \lesssim 14.5$) at $z \lesssim 0.75$, and (iii) the detection pipeline misses a few very massive, very extended, nearby systems.

AMANDINE MARIE CAMILLE LE BRUN   AUGUST 26, 2014

Publications

In the course of completing the work presented in this thesis, the following papers have been submitted for publication in a refereed journal:

1. **Amandine M. C. Le Brun**, Ian G. McCarthy, Joop Schaye and Trevor J. Ponman, *Towards a realistic population of simulated galaxy groups and clusters*, 2014, MNRAS, 441, 1270.

2. Ian G. McCarthy, **Amandine M. C. Le Brun**, Joop Schaye and Gilbert P. Holder, *The thermal Sunyaev–Zel'dovich effect power spectrum in light of Planck*, 2014, MNRAS, 440, 3645.

3. Marco Velliscig, Marcel P. van Daalen, Joop Schaye, Ian G. McCarthy, Marcello Cacciato, **Amandine M. C. Le Brun** and Claudio Dalla Vecchia, *The impact of galaxy formation on the total mass, profiles and abundance of haloes*, 2014, MNRAS, 442, 2641.

4. **Amandine M. C. Le Brun** et al., *How well can we recover the Sunyaev-Zel'dovich flux of low-mass haloes? The role of source confusion and deviations from the universal pressure profile*, to be submitted to MNRAS.

5. **Amandine M. C. Le Brun** et al., *Scatter and evolution of the hot gas properties of a realistic population of simulated galaxy clusters*, to be submitted to MNRAS.

AMANDINE MARIE CAMILLE LE BRUN   AUGUST 26, 2014

Acknowledgements

going so well (which happened really often), as well as all the postgraduate students from both the University of Birmingham and the ARI for providing (most of the time) welcome distractions.

I further would like to thank Dan Harman, Lydia Heck, Stuart Macaulay and David Stops for all their assistance with computing, as well as Andre Brabin, Anna Hodgkinson and Luciene Salas Jennings for always being so caring and helpful.

In addition, I am extremely grateful to Yen-Ting Lin, Francesco Shankar (which unfortunately do not feature in this thesis) and Ming Sun for providing their observational data, to Lorenzo Faccioli for running the XMM simulator and the XXL detection pipeline on the X-ray maps for the work presented in Chapter 6 and Jean-Baptiste Melin for running the *Planck* multi-frequency matched filter on the simulated Sunyaev–Zel'dovich maps for the work presented in Chapter 5, and finally to Andrea Merloni for letting me use one of the figures from the *eROSITA* Science Book (Figure 6.1).

Finally, I would like to extend the thanks to my family and friends for always being so understanding, supportive and helping me going through the rough patches.

AMANDINE MARIE CAMILLE LE BRUN   AUGUST 26, 2014

Contents

List of Tables

List of Figures

Chapter 1

General Introduction

The existence of a hierarchy of cosmic structures, spanning a wide range of scales, has been unveiled by the astronomical observations of the past two centuries. Overdensities of 'nebulae' were first noticed by Charles Messier (1784) and William Herschel (1785) in the constellations of Virgo and Coma Berenices, respectively. They are now known as the Virgo and Coma clusters. Once Vesto Melvin Slipher (1914) and Edwin Powell Hubble (1924) had firmly established that the 'nebulae' were other galaxies external to our own, galaxy clusters started to be considered as extragalactic physical systems. A few years later, when Fritz Zwicky first worked out the mass of a galaxy cluster, the Coma cluster, and established simultaneously for the first time the need for dark matter (Zwicky 1933), the concept of galaxy clusters had already been widely accepted.

The modern view of galaxy clusters is that they are gravitationally-bound collections of hundreds to thousands of galaxies in orbit about a common centre of mass within a few Mpc across region of the Universe. They hold a special position within the hierarchy of cosmic structure: they are the most massive objects to have 'collapsed' by the present day according to the currently favoured hierarchical scenario of structure formation. In this scenario, small objects collapse first and later merge to form increasingly larger ones, implying that galaxy clusters are the most recent class of objects to have formed in the Universe. Their individual total masses at the present time are (largely by defini-

tion) roughly 10^{14} to 10^{15} M$_\odot$ and about 80 per cent of this mass is in the form of dark matter (DM); the rest mainly being in form of a hot gaseous plasma, called the intra-cluster medium (ICM; ~ 15 per cent of the total mass), and of stars (principally in the member galaxies; $\lesssim 2 - 3$ per cent of the total mass). It is therefore clear that galaxy formation is globally inefficient. These rather precise estimates of the mass budget of galaxy clusters owe to the fact that they are the *only* systems in the Universe for which all the forms of matter (i.e. gas, stars and dark matter) can be directly observed. This is done using mainly three types of galaxy cluster surveys, which are presented in turn in the three Subsections below.

1.0.1   X-ray surveys

The hot ICM gas, which has been heated by both gravitational compression and non-gravitational processes such as feedback from active galactic nuclei (AGN) and supernovae (SNe), emits thermal bremsstrahlung and line emission from ionised heavy metals (such as iron) that were introduced into the hot plasma by stellar evolution and dynamical process such as tidal stripping from infalling galaxies.

Even though galaxy clusters were first discovered in the optical, X-ray observations are currently the most developed and efficient technique for generating large catalogues of unambiguous galaxy groups and clusters, as they are straightforward to recognise in the X-ray waveband, being the only extragalactic sources with non-variable extended soft X-ray emission (with the exception of circumgalactic X-ray emission from local galaxies; see, for instance, Rasmussen et al. 2009; Mulchaey & Jeltema 2010). In the late 1980s-1990s, using observations from, among others, *Einstein* and *EXOSAT*, the first X-ray cluster cosmological surveys were conducted (e.g. Lahav et al. 1989; Edge et al. 1990; Gioia et al. 1990). In the late 1990s-early 2000s, they were improved upon by surveys constructed using both the all-sky survey (RASS; Voges et al. 1999) and the pointed observations made with *ROSAT* such as the ROSAT Brightest Cluster Survey (Ebeling et al. 1998), ROSAT-ESO Flux Limited X-ray Galaxy Cluster Survey (Böhringer et al. 2001), and the Serendipitous High-Redshift Archival ROSAT Cluster

Survey (Romer et al. 2000). More recently, a number of X-ray cluster cosmological surveys have been and are being conducted using *XMM–Newton* and *Chandra*: for instance, the XXL survey observed two contiguous 25 square degree fields with *XMM–Newton* (Pierre et al. 2011; Pierre et al. in preparation; see also Chapter 6) and the XCS survey (Romer et al. 2001) is being carried out using archival *XMM–Newton* data. In the near-future, the *eRosita* mission (to be launched in 2015; Merloni et al. 2012) will conduct an all-sky survey.

1.0.2   Optical and near-infrared surveys

The optical and near-infrared emission is dominated by the stellar emission from galaxies and intracluster light. At these wavelengths (as well as at radio and sub-millimetre wavelengths though less commonly done), gravitational lensing of background structure provides an unparalleled probe of the total matter distribution in galaxy groups and clusters.

George Abell assembled the first large catalogue of galaxy clusters by visually inspecting observations taken on photographic plates using the telescope on Mount Palomar (Abell 1958) and first defined the concept of optical richness. Another early optical cluster catalogue, which extended to lower richnesses was compiled by Fritz Zwicky and his collaborators (Zwicky et al. 1961). As optical catalogues are plagued with issues due to projection effects (which can be calibrated using, for instance, N-body simulations; see e.g. van Haarlem, Frenk & White 1997), modern optical cluster finding algorithms use colour information to try to reduce their impact as cluster galaxies are usually significantly redder than other galaxies at similar redshifts, due to their negligible current star formation rate.

1.0.3   Sunyav–Zel'dovich surveys

In the millimetre and sub-millimetre, the hot gas trapped in dark matter haloes distorts the Cosmic Microwave Background (CMB) spectrum by inverse Compton scattering

the CMB photons through the thermal Sunyaev–Zel'dovich effect (Sunyaev & Zel-dovich 1970, 1972). It results in a small temperature decrement at radio wavelengths and a small increment at submillimetre wavelengths. There is a second component to the Sunyaev–Zel'dovich effect, known as the kinetic Sunyaev–Zel'dovich effect, which is due to the overall motion of the galaxy cluster with respect to the CMB rest-frame. Sunyaev–Zel'dovich surveys have a great advantage over X-ray and optical cluster surveys: they do not suffer from surface brightness dimming as the Sunyaev–Zel'dovich signal is redshift independent. Yet, this is also a potential curse as it means that they are likely strongly affected by source confusion (see Chapter 5). Sunyaev–Zel'dovich surveys lagged behind X-ray and optical cluster surveys, with only a few reliable detections (e.g. Birkinshaw, Hughes & Arnaud 1991) until recently, but have now started yielding large samples through three main experiments: the South Pole Telescope (e.g. Vanderlinde et al. 2010) which reported the first three galaxy clusters discovered using the Sunyaev–Zel'dovich effect (Staniszewski et al. 2009), the Atacama Cosmology Telescope (e.g. Marriage et al. 2011) and the *Planck* all-sky survey (e.g. Planck Early Results VIII). The kinetic effect was detected for the first time only very recently (Hand et al. 2012).

1.1 A short introduction to the currently favoured cosmological model

Modern cosmology began in 1915 with Einstein's theory of General Relativity. In 1922, Friedmann derived from this theory the homogeneous and isotropic class of models which form the foundation of the currently favoured cosmological standard model (see, for instance, Lachièze-Rey 1995, Peacock 1999, Bartelmann 2010). The first evidence of the existence of the dark matter was found by Fritz Zwicky in galaxy clusters in 1933 (Zwicky 1933): the galaxies were orbiting too fast – in terms of the peculiar velocity, that is the velocity in excess of the velocity due to the expansion of the Universe given by the Hubble's law $v = Hd$ where H is the Hubble parameter and

d the distance of the galaxy from the Earth – around the centre of the cluster compared to what was predicted using the stellar mass inferred from their optical luminosity. It was then concluded that galaxy clusters are about ten times more massive than would be inferred from their luminosities. The same applies to individual (spiral) galaxies. This additional matter was christened dark matter and is still raising questions such as what is its nature. It seems that most of this matter is non-baryonic. The visible matter accounts for four per cent of the energy density of the Universe; if dark matter is added, 25 per cent of this density is reached, the rest corresponding to dark energy. In 1965, the accidental discovery by Penzias and Wilson (Penzias & Wilson 1965) of the Cosmic Microwave Background (hereafter CMB) and its interpretation (Dicke et al. 1965) firmly confirmed a hot big bang origin of the Universe. In 1998, two teams which were studying supernovae proved independently the acceleration of the expansion of the Universe (Riess et al. 1998; Perlmutter et al. 1999). Since Hubble, cosmologists have tried to measure the slowing down of the expansion of the Universe due to gravity. The discovery of its acceleration is then probably one of the most important discoveries of modern science. The origin of its acceleration remains nevertheless a deep mystery. In fact, General Relativity states: if the Universe contains only matter and/or radiation, gravity should lead to a slowing down of its expansion. One possible explanation is to assume that 75 per cent of the energy content of the Universe is made of an unknown form of energy, characterised by its huge negative pressure, christened dark energy. The observational proof of the acceleration of the expansion was quickly accepted by the cosmologists since it was the missing piece of the current cosmological standard model, referred to as ΛCDM. In this model, the Universe is spatially flat and accelerating; made of baryons, dark matter and dark energy; went through an early phase of dense and hot expansion that produced the light elements through primordial nucleosynthesis, and the cosmic microwave background; and has known an even earlier phase of accelerated expansion, known under the name of inflation, that produced density perturbations which were imprinted in the anisotropies of the cosmic microwave background and led by gravitational instability to the formation of the large-scale structures. The present cosmological model is also raising profound questions: from the origins of the expansion itself and the nature of the dark matter to

the baryogenesis and the cause of the accelerating expansion.

The observational fact that the Universe is expanding calls for a change of our conceptions of space and time. The expanding Universe can be described within the framework of General Relativity using the FLRW (Friedmann, Lemaître, Robertson, Walker) metric. It can be written as follows (according to Kolb & Turner 1990):

$$ds^2 = c^2 dt^2 - a^2(t) \left(\frac{dr^2}{1 - kr^2} + r^2 d\theta^2 + r^2 sin^2\theta d\phi^2 \right) = g_{\mu\nu} dx^\mu dx^\nu \qquad (1.1)$$

where (r, θ, ϕ) are the comoving coordinates[1], $a(t)$ is the growth or scale factor, k is the curvature ($k = +1$ corresponding to a positive curvature (spatially finite Universe), $k = 0$ to no curvature (spatially flat Universe) and $k = -1$ to a negative curvature) and $g_{\mu\nu}$ is the metric tensor.

The redshift z is defined as the fractional Doppler shift due to an object's radial motion: $1 + z \equiv \frac{\lambda_0}{\lambda_1} = \frac{a(t_0)}{a(t_1)}$ where λ_0 is the wavelength of the received radiation and λ_1 the one of the emitted radiation. The second equality corresponds to the cosmological definition of redshift.

When the FLRW metric is inserted into Einstein's field equations:

$$R_{\mu\nu} - \frac{1}{2} g_{\mu\nu} R \equiv G_{\mu\nu} = 8\pi G T_{\mu\nu} + \Lambda g_{\mu\nu}, \qquad (1.2)$$

the Friedmann equations are obtained:

$$\left(\frac{\dot{a}}{a} \right)^2 + \frac{kc^2}{a^2} = \frac{8\pi G}{3} \rho + \frac{\Lambda}{3} \qquad (1.3)$$

and

$$2\frac{\ddot{a}}{a} + \left(\frac{\dot{a}}{a} \right)^2 + \frac{kc^2}{a^2} = -8\pi G p \qquad (1.4)$$

where Λ is the cosmological constant that can be written as a pressure or a density of the vacuum $\Lambda \equiv 8\pi G \rho_\Lambda c^2 = -8\pi G p_\Lambda$, $T_{\mu\nu}$ is the energy-impulsion tensor, which is

---

[1]The physical coordinates are the product of the comoving coordinates and of the scale factor $a(t)$ which describes the size-evolution of the background Universe. The comoving coordinates can be said to be carried along with the expansion.

given by $T_{\mu\nu} = diag(\rho c^2, p, p, p)$ for an ideal fluid where ρ is the density and p is the pressure of the fluid. If the Hubble parameter is defined as $H \equiv \frac{\dot{a}}{a}$, the Friedmann equations can be rewritten as follows:

$$H^2 = \frac{8\pi G}{3}\rho - \frac{kc^2}{a^2} + \frac{\Lambda}{3} \tag{1.5}$$

and

$$\frac{\ddot{a}}{a} = -\frac{4\pi G}{3}\left(\rho + \frac{3p}{c^2}\right) + \frac{\Lambda}{3} \tag{1.6}$$

The present density of a spatially flat Universe is called the critical density and its value is: $\rho_{crit} \equiv \frac{3H_0^2}{8\pi G}$. Then the cosmic densities can be normalised by defining: $\Omega_i(z) \equiv \frac{\rho_i(z)}{\rho_{crit}(z)}$. The present-time Hubble constant is often expressed in its dimensionless form h by: $H_0 \equiv 100\, h$ km s^{-1} Mpc^{-1}.

The standard flat ΛCDM model is well-described by six cosmological parameters: the reduced Hubble constant h, the Universe's total matter content Ω_m, its total baryonic content Ω_b, the contribution of dark energy to the critical density Ω_Λ, the normalisation of the power spectrum of the density fluctuations at a scale of $8\, h^{-1}$ Mpc σ_8 and the spectral index of the power spectrum of the density fluctuations n_s. The final two parameters are defined as follows (see, for instance, Peacock 1999):

$$\sigma_8^2 = \frac{1}{2\pi}\int T(k)P(k)W(kR)k^2 dk \tag{1.7}$$

where $P(k) \propto k^{n_s}$ is the primordial matter power spectrum as a function of comoving wavenumber k, $T(k)$ is the transfer function, and W is the Fourier transform of the real-space top-hat window function of radius $R = 8\, h^{-1}$ Mpc.

1.2 Galaxy clusters as astrophysical laboratories and cosmological probes

It is widely recognised that galaxy clusters are potentially powerful tools for probing cosmology, as well as of the physics of galaxy formation (for recent reviews, see Voit 2005; Borgani & Kravtsov 2011; Allen, Evrard & Mantz 2011; Kravtsov & Borgani 2012; Weinberg et al. 2013). Their cosmological sensitivity is related to their previously mentioned special position in the hierarchy of cosmic structures: being the largest bound objects to have reached virial equilibrium, their abundance as a function of mass and redshift (i.e. the evolution of the cluster halo mass function dn/dM) is sensitive to the cosmological parameters that control the growth rate of structures (e.g. σ_8, Ω_m), including the evolution rate of dark energy. In addition, owing to their extremely deep potential wells within which the baryons are trapped, they can potentially be considered as 'closed boxes' whose baryonic matter content is thus expected to reflect the overall baryonic content of the Universe[2] (given by Ω_b/Ω_m; White et al. 1993), and they should contain a wealth of information about the processes of galaxy formation. They are an important probe of the physics of galaxy formation because, as noted before, they are the only systems in the Universe for which all the baryonic components, including the diffuse gaseous component, can be directly observed. (The diffuse gaseous component is too low surface brightness to observe around normal galaxies like the Milky Way but is sufficiently hot and dense in galaxy clusters to be observed with X-ray and radio telescopes.)

The last two decades in particular have witnessed exciting developments in cluster cosmology. The *ROSAT* satellite conducted the first all-sky survey of galaxy clusters in X-rays in the early 1990s (RASS; Voges et al. 1999) and discovered thousands of new clusters, both in the nearby and distant Universe. The higher spectral and spatial resolution of *Chandra* and *XMM–Newton* later led to radical changes in our picture of X-ray clusters (e.g. no evidence for large amounts of cold gas in the central

---

[2]Although, as shown later, the aptness of the 'closed box' designation is a strong function of cluster mass.

regions, non-isothermal temperature profiles; see for instance Peterson et al. 2001 and Peterson et al. 2003). Simultaneously, large optical cluster catalogues became available from the Sloan Digital Sky Survey (SDSS; York et al. 2000) and Sunyaev–Zel'dovich observations progressed from the first reliable detections of individual objects (e.g. Birkinshaw, Hughes & Arnaud 1991; Jones et al. 1993; Pointecouteau et al. 1999) to large cosmological surveys with the Atacama Cosmology Telescope (Menanteau et al. 2010) and the South Pole Telescope (Vanderlinde et al. 2010), culminating in the first all-sky cluster survey since the RASS, the *Planck* survey, whose first results were released in 2011 (Planck Early Results VIII). The increased size and depth of the surveys allowed for the transition of on-going and upcoming cluster cosmological surveys, such as *eRosita* (Merloni et al. 2012), *Euclid* (Laureijs et al. 2011) and the dark energy Survey (The Dark Energy Survey Collaboration 2005), into the 'era of precision cosmology', where the systematic errors involved are now starting to dominate over the statistical uncertainties.

The use of galaxy clusters as probes of cosmology means minimising the systematic uncertainties and has a few key requirements (e.g. Allen, Evrard & Mantz 2011; Pierre et al. 2011): (i) the cluster masses must be reliably inferred from the observed cluster physical properties, such as X-ray luminosity or temperature, Sunyaev–Zel'dovich effect intensity or weak lensing shear, (ii) the scatter and covariance of the employed mass–observable and observable–observable relations must be suitably taken into account in the cosmological modelling, (iii) a detailed knowledge of the selection function of the survey is key, for instance, to comparisons to predictions of the time evolution of the cluster mass function: one needs to be sure that all the clusters above a given mass have been accounted for; and (iv) there needs to be a robust theoretical prediction for the halo mass function (or whatever cosmological test is being undertaken) for comparison.

The calibration of mass-observable relations (and complementing observational self-calibration of these relations), estimation of their scatter and biases, the correction of the observations for the undetected clusters, and the theoretical prediction (e.g. the halo mass function) all rely heavily on physical models of clusters (e.g. Kravtsov, Vikhlinin

& Nagai 2006; Nagai, Vikhlinin & Kravtsov 2007; Mantz et al. 2010b,a; Clerc et al. 2012) . *Hence, our ability to do precision cosmology with clusters is inextricably linked with our astrophysical understanding of these systems.*

1.3 Towards a better understanding of the formation of galaxy clusters

1.3.1 The self-similar model

The simplest model for cluster formation assumes that cluster properties and their correlations are determined by gravity alone and that clusters are virialised. As gravity is scale free, clusters are thus expected to be self-similar, i.e. all cluster properties should depend only upon the cluster mass, and more massive clusters are scaled versions of less massive ones[3] (White & Rees 1978; Kaiser 1986; Voit 2005; Borgani & Kravtsov 2011; Kravtsov & Borgani 2012). If one defines the cluster masses (denoted as M_Δ) as being the mass contained within a region that encloses a mean internal overdensity $\Delta\rho_{crit}$, then, under the assumption of self-similarity, one can predict the redshift evolution of a given cluster mass-observable relation. The redshift evolution arises through the evolution of the critical density: $\rho_{crit}(z) = E(z)^2 \rho_{crit0}$. For instance, since $M_\Delta \propto \rho_{crit}(z) r_\Delta^3$ by definition, the cluster size will scale as $r_\Delta \propto M_\Delta^{1/3} E(z)^{-2/3}$. This means that, if one scales the radius r_Δ by $M_\Delta^{1/3} E(z)^{-2/3}$, the mass density profiles $\rho(r)$ will be similar/identical for all the systems, no matter how massive they are and at which redshift they are observed. A more detailed introduction to the self-similar model will be presented in Chapter 3.

With the first X-ray observations of large number of galaxy clusters with the *Einstein Observatory*, *EXOSAT* and *ROSAT*, in the 1980s-1990s, it was quickly realised that the results of the self-similar model were incompatible with the observations of, among others, the X-ray luminosity evolution (e.g. Evrard & Henry 1991; Kaiser 1991). It led

---

[3]with a scaling factor that depends only upon the mass ratio

to the obvious conclusion that some non-gravitational processes, most likely connected to galaxy formation, must be breaking the self-similarity by introducing some physical scales. In particular, the mass density profiles in fact depend upon the system total mass: groups and low-mass clusters have lower densities than more massive clusters. Kaiser (1991) and Evrard & Henry (1991) both proposed a similar solution to this puzzle: the pre-heating model. In short, some unspecified process is assumed to have heated up the gas before it fell into the collapsing DM haloes and this imposed a minimum gas entropy. Another way to break self-similarity is via radiative cooling (e.g. Bryan 2000; Davé, Katz & Weinberg 2002; Voit & Ponman 2003). In a way, one should not be surprised by the fact that cooling could be a solution to this problem, as galaxies are observed in clusters. Besides, it had been realised that the gas can cool quickly in the centre of groups and clusters through thermal bremsstrahlung and line emission (e.g. White & Rees 1978; White & Frenk 1991).

1.3.2 On the importance of efficient feedback processes

Yet, it was recognised in the late 1990s that the simulations and analytical models, that include only radiative cooling and star formation (SF), result into 'overcooled' galaxies (galaxies/clusters with stellar fractions which are too high given the observational constraints from e.g. X-ray emission of clusters) and unrealistic ICM properties (e.g. Balogh et al. 2001; McCarthy et al. 2004). Cooling alone is thus not the solution to the self-similarity breaking enigma as only a very small fraction of the ICM gas cools and then turns into stars. This new problem, which was christened the 'overcooling' problem, calls for the inclusion of some kind of feedback process in the models. An obvious form of feedback is coming from star formation itself: some of the stars finish their lives as supernovae (SNe) and drive galactic winds which can heat the interstellar medium (ISM) (Larson 1974; White & Frenk 1991; Ponman, Cannon & Navarro 1999; Voit 2005). However, this form of feedback fails to solve the overcooling problem at the groups and cluster scales (Borgani et al. 2004; Kay et al. 2004; Borgani et al. 2005; Borgani et al. 2006; Davé, Oppenheimer & Sivanandam 2008).

Finally, over the past two decades, there has been mounting observational evidence that the growth of the supermassive black holes (SMBHs), that are thought to live in the active galactic nuclei (AGN) at the centre of (massive) galaxies, is closely connected to the growth of their host galaxy. It has also been realised, both theoretically and observationally, that AGN feedback is one of the main drivers of the properties of massive galaxies, groups and clusters (Benson et al. 2003; Bower et al. 2006; De Lucia & Blaizot 2007; McNamara & Nulsen 2007; McCarthy et al. 2010; McCarthy et al. 2011; Fabian 2012). For instance, McCarthy et al. (2011) found that AGN feedback is most important at high redshift, when it ejects low-entropy/high-density gas from the progenitors of groups, rather than heating it as in the pre-heating model.

1.3.3 A first (successful) solution?

Simulations are necessary for self-consistently modelling the *highly non-linear* galaxy formation processes. They can accurately solve at the same time for the gravitational and hydrodynamical aspects of structure formation. Nevertheless, owing to their finite spatial and mass resolutions, some prescriptions are needed for modelling the fundamentally important processes, such as radiative cooling, SF, SNe and AGN feedback, which occur on scales which cannot be resolved by the simulation. These non-resolved physical processes are collectively called 'sub-grid' physics.

A suite of large, cosmological, hydrodynamical simulations, the OverWhelmingly Large Simulations project (hereafter OWLS; Schaye et al. 2010), which aimed to study the various aspects of the physics of galaxy formation, was an important step forward in its modelling: (i) this was the first attempt at a systematic study of the 'sub-grid' physics models and their parameters and (ii) they were the first simulations (and still are the only ones) to simultaneously match the present time properties of the stellar populations and of the hot plasma of galaxy groups. The inclusion of AGN feedback proved key in the latter. Hence, OWLS is a useful tool for making reliable comparisons to observations, which will hopefully lead to parallel improvements of our understanding of the astrophysics of the formation of groups and clusters, and of the constraints

placed on cosmology by galaxy cluster surveys (by providing such surveys with reliable and unbiased mass estimates and with their selection function).

However, the original OWLS simulations are not suited for studying massive and thus rare clusters and generating synthetic cluster cosmological surveys, since the volumes they probe are too small: they are at most $100 \ h^{-1}$ Mpc on a side. Therefore, in order to enable such studies, a set of $400 \ h^{-1}$ Mpc on a side cosmological, hydrodynamical simulations with ~ 2.15 billion particles have been carried out during this PhD programme. This extension to OWLS, dubbed cosmo-OWLS, contains the largest self-consistent cosmological hydrodynamical simulations including AGN feedback run to date. In addition to the much larger volumes, the cosmo-OWLS suite more thoroughly explores the parameter space associated with AGN feedback modelling than previous simulations, which is crucial for assessing the impact of modelling uncertainties in cluster cosmology efforts.

1.4 Thesis outline

This thesis makes use of a new suite of large-volume cosmological hydrodynamical simulations, which were designed with cluster cosmology and large-scale structure surveys in mind, to study the astrophysical and cosmological aspects of galaxy clusters, and is structured as follows:

- Chapter 2 introduces the new suite of large-volume cosmological hydrodynamical simulations with varying 'sub-grid' physics, christened cosmo-OWLS, and compares them to a wide range of observational data, such as X-ray luminosity and temperature, gas mass fractions, entropy and density profiles, Sunyaev–Zel'dovich flux, I-band mass-to-light ratio, dominance of the brightest cluster galaxy and central black hole masses, by producing synthetic observations and mimicking observational analysis techniques.

- Chapter 3 takes advantage of the large volume of the cosmo-OWLS suite of simulations to conduct a study of the scatter and evolution of the hot gas properties

(X-ray luminosity and temperature, gas mass, Sunyaev–Zel'dovich signal and its X-ray analogue) of the simulated populations of groups and clusters.

- Chapter 4 presents the development and testing of a 'multi-purpose' light cone software package, which can be used to create realistic synthetic surveys from various simulations.

- Chapter 5 employs synthetic Sunyaev–Zel'dovich observations, generated for the cosmo-OWLS suite of simulations using the light cone software package developed in Chapter 4, to check the veracity of some of the results reported by the *Planck* collaboration in late 2012: they came to the rather surprising conclusion that the scaling relation of the Sunyaev–Zel'dovich signal with total mass is self-similar down to the scales of individual galaxies, which is in contradiction with X-ray and absorption line observations.

- Chapter 6 presents a first attempt at using synthetic X-ray observations, which had been generated for the cosmo-OWLS suite of simulations using a combination of the light cone software package developed in Chapter 4 and the *XMM–Newton* simulator and processed with the detection pipeline of the XXL survey, to quantify the selection function of the XXL survey.

- Chapter 7 summarises the main results and briefly discusses possible avenues for future work.

Chapter 2

Towards a realistic population of simulated galaxy groups and clusters

The majority of the content of this Chapter and Appendices A and B was published in a peer-reviewed journal: Le Brun, McCarthy, Schaye & Ponman, 2014, MNRAS, 441, 1270.

Ian McCarthy ran the simulations, SUBFIND, generated the APEC tables, wrote the cluster analysis code (which performs the synthetic X-ray observations and the hydrostatic analysis) and ran it on the majority of the simulations. Amandine Le Brun gathered the observational data, computed the conversion factors between X-ray bands (e.g. between 0.1–2.4 keV and 0.5–2.0 keV, between bolometric and 0.5–2.0 keV and in between observer frame and rest-frame) using XSPEC and WebPIMMS, made all the plots and wrote the code that examined the maximum past temperature of the star-forming gas and recently-formed stars for the star-forming fraction Section.

2.1 Introduction

The theoretical modelling of the formation and evolution of galaxy groups and clusters has progressed considerably in recent years. For instance, the 'cooling catastrophe'

(i.e. the general tendency of simulated galaxies, and groups and clusters of galaxies to form far too many stars; e.g. Balogh et al. 2001), which has generally plagued cosmological hydrodynamical simulations since their advent, has largely been overcome in simulations which include feedback from supermassive black holes (e.g. Springel, Di Matteo & Hernquist 2005; Sijacki et al. 2007; Dubois et al. 2010; Fabjan et al. 2010; McCarthy et al. 2010, 2011; Short, Thomas & Young 2013), while feedback from star formation and supernovae (SNe) is insufficient to halt the development of cooling flows and overly massive central galaxies (e.g. Borgani et al. 2004; Nagai, Kravtsov & Vikhlinin 2007). The observation of X-ray cavities in the intracluster medium (ICM) in the centres of galaxy groups and clusters (for reviews, see McNamara & Nulsen 2007; Fabian 2012) provides strong empirical motivation for the inclusion of active galactic nuclei (AGN) in simulations. Recent simulation studies that have implemented AGN feedback have concluded that it also helps to reproduce a number of other important properties of groups and clusters, such as the mean baryon fraction trend with mass (e.g. Bhattacharya, Di Matteo & Kosowsky 2008; Puchwein, Sijacki & Springel 2008; Fabjan et al. 2010; McCarthy et al. 2010; Planelles et al. 2013), the mean luminosity–temperature relation (e.g. Puchwein, Sijacki & Springel 2008; Fabjan et al. 2010; McCarthy et al. 2010; Planelles et al. 2014), and the metallicity and temperature profiles of groups outside of the central regions (e.g. Fabjan et al. 2010; McCarthy et al. 2010; Planelles et al. 2014).

In spite of this progress, no model has yet been able to reproduce the scatter in the global scaling relations over the full range of system total masses from low-mass groups to high-mass clusters, nor the thermodynamic state of the hot gas in the central regions and its scatter. (The latter is another way of saying that models do not reproduce the observed cool-core–non-cool-core dichotomy.) This may be signalling that there is still important physics missing from the simulations. In addition, most previous theoretical studies have focused on relatively small samples of clusters using 'zoomed' resimulations, rather than trying to simulate large representative populations, and have neglected to factor in important biases (e.g. the effects of gas clumping, deviations from hydrostatic equilibrium, and selection effects) when comparing to the

observations, which can affect the qualitative conclusions that are drawn from these comparisons.

The OverWhelmingly Large Simulations project (hereafter OWLS; Schaye et al. 2010), which was a suite of over 50 large cosmological hydrodynamical simulations of periodic boxes with varying 'sub-grid' physics, addressed our ignorance of important sub-grid physics and its impact on large representative populations of systems. The main aim of the project was to use simulations to gain insight into the physics of galaxy formation by conducting a systematic study of 'sub-grid' physics models and their parameters on representative populations. Using OWLS, McCarthy et al. (2010) showed for the first time that the inclusion of AGN feedback allows the simulations to match simultaneously the properties of the hot plasma and of the stellar populations of local galaxy groups (see also Stott et al. 2012). However, due to the finite box size of the OWLS runs (at most $100\ h^{-1}$ Mpc on a side), they were not well suited for studying massive clusters, or undertaking a study of the scatter in the observable and physical properties of groups and clusters as a function of mass and redshift. In addition, the original OWLS runs adopted a now out-of-date cosmology (based on the analysis of *WMAP* 3-year data).

This Chapter presents an extension to the OWLS project (called cosmo-OWLS), consisting of a suite of large-volume cosmological hydrodynamical simulations designed with on-going and upcoming cluster cosmology surveys in mind. The large volumes (simulations in $400\ h^{-1}$ Mpc on a side boxes are presented here) allow for the extension of comparisons to higher masses and redshifts and to examine the scatter in the physical properties of groups and clusters. The main aims of cosmo-OWLS are: (i) to provide a tool for the astrophysical interpretation of cluster survey data, (ii) to help quantify the group/cluster selection functions that are crucial for cluster cosmology, (iii) to quantify the biases in reconstructed (rather than directly observable) quantities, such as system mass, and the resulting bias in the inferred cosmological parameters, and (iv) to make predictions for future observations. Lastly, the study of McCarthy et al. (2010) has not only been extended to higher masses (and with an updated cosmology), but the effects of baryonic physics upon a larger number of observed properties,

such as Sunyaev–Zel'dovich flux, central supermassive black hole scaling relations, and properties of the brightest cluster galaxy of local galaxy groups and clusters, have also been investigated.

The remainder of this Chapter is organised as follows. The cosmo-OWLS runs, as well as how they were post-processed to produce synthetic observations are briefly described in Section 2.2. Like-with-like comparisons with global X-ray scaling relations are then conducted in Section 2.3.1, and the radial distributions of X-ray properties are examined in Section 2.3.2, followed by an investigation of the Sunyaev–Zel'dovich scalings in Section 2.4, and of the optical and black hole properties in Section 2.5. Finally, the main findings are discussed and summarised in Section 2.6.

Masses are quoted in physical $M_\odot$ throughout.

2.2 cosmo-OWLS

2.2.1 Simulation characteristics

The original OWLS runs were limited in size to $100 \ h^{-1}$ Mpc, with initial conditions based on the 3-year *Wilkinson Microwave Anisotropy Probe* (*WMAP*) maximum-likelihood cosmological parameters (Spergel et al. 2007). The corresponding volume is too small to contain more than a handful of massive clusters of galaxies with $M_{500} \gtrsim 10^{14} \ M_\odot$, which have a comoving space density of $\sim 10^{-5} \ \mathrm{Mpc}^{-3}$ at $z = 0$ (e.g. Jenkins et al. 2001). With cosmo-OWLS, much larger volume simulations have been carried out and $400 \ h^{-1}$ (comoving) Mpc on a side periodic box simulations with updated initial conditions based either on the maximum-likelihood cosmological parameters derived from the 7-year *WMAP* data (Komatsu et al. 2011) $\{\Omega_m, \Omega_b, \Omega_\Lambda, \sigma_8, n_s, h\} = \{0.272, 0.0455, 0.728, 0.81, 0.967, 0.704\}$ or the *Planck* data (Planck 2013 Results XVI) = $\{0.3175, 0.0490, 0.6825, 0.834, 0.9624, 0.6711\}$ are presented here. The prescription of Eisenstein & Hu (1999) is used to compute the transfer function and

the software package N-GENIC[1] (developed by V. Springel) based on the Zel'dovich approximation is used to generate the initial conditions. For each of the models presented below, simulations have been run with both cosmologies. The results of the *Planck* cosmology runs only are presented here, but any significant differences in the corresponding *WMAP*7 runs are commented upon.

The simulations presented here all have 2×1024^3 particles (as opposed to 2×512^3 for the original $100~h^{-1}$ Mpc OWLS volumes), yielding dark matter and (initial) baryon particle masses of $\approx 4.44 \times 10^9~h^{-1}~\mathrm{M}_\odot$ ($\approx 3.75 \times 10^9~h^{-1}~\mathrm{M}_\odot$) and $\approx 8.12 \times 10^8~h^{-1}~\mathrm{M}_\odot$ ($\approx 7.54 \times 10^8~h^{-1}~\mathrm{M}_\odot$), respectively for the *Planck* (*WMAP*7) cosmology. As the volume has been increased by a factor of 64 but the number of particles has 'only' been increased by a factor of 8 with respect to OWLS, the runs presented here are approximately a factor of 8 lower in mass resolution compared to OWLS[2]. However, as demonstrated in Appendix A (see also McCarthy et al. 2010), good convergence is achieved in global properties down to halo masses of a few $10^{13}~\mathrm{M}_\odot$ at cosmo-OWLS resolution. Note that the gravitational softening of the runs presented here is fixed to $4~h^{-1}$ kpc (in physical coordinates below $z = 3$ and in comoving coordinates at higher redshifts).

As the hydrodynamic code and its sub-grid physics prescriptions used for cosmo-OWLS have not been modified from that used for OWLS, and have been described in detail elsewhere (e.g. McCarthy et al. 2010; Schaye et al. 2010), only a brief description is presented below.

The simulations were carried out with a version of the Lagrangian TreePM-SPH code GADGET3 (Springel 2005), which has been significantly modified to include new 'sub-grid' physics. Radiative cooling rates are computed element by element, using the method of Wiersma, Schaye & Smith (2009), by interpolating as a function of density, temperature and redshift from pre-computed tables, that were generated with the publicly available photoionisation package CLOUDY (Ferland et al. 1998) and calcu-

---

[1]http://www.mpa-garching.mpg.de/gadget/

[2]Running higher resolution simulations in such large volumes is rendered unfeasible by currently available hardware. A single cosmo-OWLS run has a peak memory consumption of approximately 2.5 TB of RAM, while 6 TB of storage is required for the snapshot data.

lated in the presence of the cosmic microwave background (CMB) and of the Haardt & Madau (2001) ultraviolet (UV) and X-ray photoionising backgrounds. Reionisation is modelled by switching on the UV background at $z = 9$. Star formation (SF) is implemented stochastically following the prescription of Schaye & Dalla Vecchia (2008). Since the simulations lack both the physics and the resolution to model the cold interstellar medium (ISM), an effective equation of state (EOS) is imposed with $P \propto \rho^{4/3}$ for gas with $n_H > n_H^*$ where $n_H^* = 0.1$ cm^{-3}, and only gas on the effective EOS is allowed to form stars, at a pressure-dependent rate which reproduces the observed Kennicutt–Schmidt SF law without requiring any tuning (see Schaye & Dalla Vecchia 2008). Stellar evolution and chemical enrichment are implemented using the model of Wiersma et al. (2009), which computes the timed-release of 11 elements (H, He, C, N, O, Ne, Mg, Si, S, Ca and Fe, which represent all of the important ones for radiative cooling) due to both Type Ia and Type II supernovae (SNe) and Asymptotic Giant Branch stars.

Feedback from SNe is implemented using the local kinetic wind model of Dalla Vecchia & Schaye (2008) with the initial mass-loading factor and the initial wind velocity chosen to be respectively $\eta = 2$ and $v_w = 600$ km s^{-1}. These parameter values correspond to a total wind energy which is approximately 40 per cent of the total energy available for the Chabrier (2003) initial mass function (IMF) used by the simulations. Note that the hot gas properties of galaxy groups and clusters are generally insensitive to these parameters, since SN feedback is ineffective at these high masses (i.e. the entropy SNe inject is small compared to that generated by gravitational shock heating or removed by radiative losses).

Three of the runs presented here include AGN feedback due to accretion of matter on to supermassive black holes (BHs). This is incorporated using the sub-grid prescription of Booth & Schaye (2009), which is a modified version of the model of Springel, Di Matteo & Hernquist (2005). The main features of this model are summarised below.

During the simulation, an on-the-fly friends-of-friends (FoF) algorithm is run on the dark matter distribution. New haloes with more than 100 particles (corresponding to a mass of $\log_{10}[M_{FoF}(\mathrm{M}_\odot/h)] \approx 11.6$) are seeded with black hole sink particles

with an initial mass that is 0.001 times the gas particle mass. Note that this is the same prescription as used for the OWLS AGN model (see Booth & Schaye 2009). The fixed dark matter particle number for seeding implies that BHs are injected into more massive haloes (by approximately a factor of 8) in cosmo-OWLS compared to OWLS. In Appendix A, the growth histories of black hole particles using the OWLS and cosmo-OWLS BH seeding schemes are compared.

BHs can grow via (Eddington-limited) Bondi–Hoyle–Lyttleton accretion and through mergers with other BHs. Since the simulations lack the physics and resolution to model the cold ISM, they will generally underestimate the true Bondi accretion rate on to the BH by a large factor. Recognising this issue, Springel, Di Matteo & Hernquist (2005)– and most studies which have adopted this model since then–scaled the Bondi rate up by a constant factor $\alpha \sim 100$. The Booth & Schaye (2009) model which is adopted here, however, has α vary as a power law of the local density for gas above the SF threshold n_H^*. The power-law exponent β is set to 2 and the power law is normalised so that $\alpha = 1$ for densities equal to the SF threshold. Thus, at low densities, which *can* be resolved and where no cold interstellar phase is expected, the accretion rate asymptotes to the true Bondi rate.

A fraction of the rest-mass energy of the gas accreted on to the BH is used to heat neighbouring gas particles, by increasing their temperature. As discussed in detail by Dalla Vecchia & Schaye (2008, 2012), thermal feedback in cosmological simulations, be it from SNe or BHs, has traditionally been inefficient: as the feedback energy is being injected into a large amount of mass, it can only raise the temperature of the gas by a small amount. The feedback energy is then radiated away quickly because of the short post-heating cooling time. In nature, the energy is injected into a much smaller mass of gas and thus the post-heating cooling time is typically very long. While much algorithmic progress has been made recently to overcome this problem in the context of SN feedback (see Dalla Vecchia & Schaye 2012 for discussion), less attention has been devoted to this artificial overcooling problem in the context of AGN feedback. The Booth & Schaye (2009) model overcomes this problem by increasing the temperature of the gas by a pre-defined level ΔT_{heat}. More specifically, a fraction ϵ of the accreted

energy heats up a certain number n_{heat} of randomly chosen surrounding gas particles (within the SPH kernel which contains 48 particles) by increasing their temperature by ΔT_{heat}, with the BHs *storing* the feedback energy until it is large enough to heat the n_{heat} particles by ΔT_{heat}. These two parameters are chosen such that the heated gas has a sufficiently long cooling time and so that the time needed to have a feedback event is shorter than the Salpeter time for Eddington-limited accretion. Booth & Schaye (2009) found that $\Delta T_{heat} = 10^8$ K and $n_{heat} = 1$ correspond to a good balance between these two constraints. These values were hence used for the OWLS 'AGN' model. This model is hereafter referred to as AGN 8.0.

The efficiency ϵ is set to 0.015, which results in a good match to the normalisation of the $z = 0$ relations between BH mass and stellar mass and velocity dispersion (the slopes of the relations are largely independent of ϵ), as well as to the observed cosmic BH density, as demonstrated by Booth & Schaye (2009, 2010) (see also Appendix A). McCarthy et al. (2011) found that galaxy groups simulated using this model for AGN feedback are fairly insensitive to the choice of β and n_{heat}, whilst they are sensitive to ΔT_{heat}, particularly if it is similar to, or smaller than the group's virial temperature. In the latter cases, the feedback will be inefficient. It is worth noting that the most massive systems expected in the much larger simulated volumes presented here will have $\Delta T_{heat} \sim T_{vir}$. AGN feedback is therefore anticipated to become less efficient for these systems. For this reason, two additional runs with increased heating temperatures (leaving n_{heat} and ϵ fixed) were carried out: $\Delta T_{heat} = 3 \times 10^8$ K (hereafter AGN 8.5) and $\Delta T_{heat} = 5 \times 10^8$ K (hereafter AGN 8.7). Note that since the same amount of gas is being heated in these models as in the AGN 8.0 model, more time is required for the BHs to accrete enough mass to be able to heat neighbouring gas to a higher temperature. Thus, increasing the heating temperature leads to more bursty and more energetic feedback events.

Table 2.1 provides a list of the new runs presented here and the sub-grid physics that they include.

Simulation	UV/X-ray background	Cooling	Star formation	SN feedback	AGN feedback	ΔT_{heat}
NOCOOL	Yes	No	No	No	No	...
REF	Yes	Yes	Yes	Yes	No	...
AGN 8.0	Yes	Yes	Yes	Yes	Yes	$10^{8.0}$ K
AGN 8.5	Yes	Yes	Yes	Yes	Yes	$10^{8.5}$ K
AGN 8.7	Yes	Yes	Yes	Yes	Yes	$10^{8.7}$ K

Table 2.1: cosmo-OWLS runs presented here and their included sub-grid physics. Each model has been run in both the *WMAP7* and *Planck* cosmologies.

2.2.2 Post-processing

Halo properties

Haloes are identified by using a standard friends-of-friends percolation algorithm on the dark matter particles with a typical value of the linking length in units of the mean interparticle separation (b=0.2). The baryonic content of the haloes is identified by locating the nearest DM particle to each baryonic (i.e. gas or star) particle and associating it with the FoF group of the DM particle. Artificial haloes are removed by performing an unbinding calculation with the SUBFIND algorithm (Springel et al. 2001; Dolag et al. 2009): any FoF halo that does not have at least one self-bound substructure (called subhalo) is removed from the FoF groups list. Subhaloes are defined to be locally overdense, self-bound particle groups within a larger parent group (the FoF halo) and are found by SUBFIND by looking for regions (which correspond to the subhaloes) that are encompassed by an isodensity contour that goes through a saddle point of the density field (see Springel et al. 2001 for details). A 'galaxy' is a collection of star and gas particles bound to a subhalo. A halo can thus host several galaxies.

Spherical overdensity masses M_Δ (where M_Δ is the total mass within a radius r_Δ that encloses a mean internal overdensity of Δ times the critical density of the Universe) with $\Delta = 200$, 500 and 2500 have been computed (total, gas and stars) for all the FoF haloes. The spheres are centred on the position of the most bound particle of the main subhalo (the most massive subhalo of the FoF halo). Then, all galaxy groups and clusters with $M_{500} \geq 10^{13}$ M$_\odot$ are extracted from each snapshot for analysis. There are roughly $14,000$ such systems at $z = 0$ in the NOCOOL run with the *Planck* cosmology, for example.

X-ray observables and analysis

It has been demonstrated in a number of previous studies that there can be non-negligible biases in the derived hot gas properties (e.g. due to multi-temperature structure and clumping) and system mass (e.g. M_{500}) inferred from X-ray analyses (e.g. Mathiesen

& Evrard 2001; Mazzotta et al. 2004; Rasia et al. 2006; Nagai, Vikhlinin & Kravtsov 2007; Khedekar et al. 2013). Thus, to make like-with-like comparisons with X-ray observations, synthetic X-ray data are produced and then analysed in a way that is faithful to what is done for the real data. The procedure used for producing and analysing synthetic X-ray observations is described below.

For each hot gas particle within r_{500}, the X-ray spectrum in the 0.5–10.0 keV band is computed using the Astrophysical Plasma Emission Code (APEC; Smith et al. 2001) with updated atomic data and calculations from the AtomDB v2.0.2 (Foster et al. 2012). The spectrum of each gas particle is computed using the particle's density, temperature, and full abundance information. More specifically, for each particle, a spectrum for each of the 11 elements tracked by the simulations is computed, scaled appropriately using the particle's elemental abundance (the fiducial APEC spectrum assumes the Solar abundances of Anders & Grevesse 1989), and the individual element spectra are summed to create a total spectrum for the particle. Note that cold gas below 10^5 K which contributes negligibly to the total X-ray emission is excluded. Any (hot or cold) gas which is bound to self-gravitating substructures ('subhaloes') is also excluded, as observers also typically excise substructures from their X-ray data. Note that the smallest subhaloes that can be resolved in the present simulations have masses $\sim 10^{11}$ M$_\odot$.

Gas density, temperature, and metallicity profiles are 'measured' for each simulated system by fitting single-temperature APEC models with a metallicity that is a fixed fraction of Solar (as commonly assumed in observational studies) to spatially-resolved X-ray spectra in (three-dimensional) radial bins. (Note that the observed radial profiles that the simulations are compared to in Section 3.2 are all derived under the assumption of spherical symmetry.) The radial bins are spaced logarithmically and between 10-20 bins are used within r_{500} (similar to what is possible for relatively deep *Chandra* observations of nearby systems). To more closely mimic the actual data quality and analysis, the cluster spectra (and the single-temperature APEC model spectra to be fitted to the cluster spectra) are multiplied by the effective area energy curve of *Chandra*, subjected to Galactic absorption due to HI with a typical column density of 2×10^{20} cm^2, and

re-binned to an energy resolution of 150 eV (i.e. similar to the *Chandra* energy resolution). The single-temperature model spectra are fitted to the cluster spectra using the MPFIT least-squares package in IDL (Markwardt 2009). In general, including a Galactic absorption column and multiplying by the effective energy curve of *Chandra* have only very small effects (a few per cent) on the recovered density, temperature and metallicity profiles, by affecting which parts of the spectra are most heavily weighted in the fit.

In addition to profiles, 'mean' system X-ray temperatures and metallicities are also derived by following the above procedure but using only a single radial bin: either $[0–1]r_{500}$ ('uncorrected') or $[0.15–1]r_{500}$ ('cooling flow-corrected'). System X-ray luminosities within r_{500} are computed in the soft 0.5–2.0 keV band by summing the luminosities of the individual particles within this three-dimensional radius (the luminosity of an individual particle is computed by integrating the particle's spectrum over this band).

When making comparisons to X-ray-derived mass measurements (e.g. M_{500}), a hydrostatic mass analysis of the simulated systems is employed using the measured gas density and temperature profiles inferred from the synthetic X-ray analysis described above. In particular, the density and temperature profiles are fitted using the functional forms proposed by Vikhlinin et al. (2006) and hydrostatic equilibrium (HSE; as explained in e.g. Kravtsov & Borgani 2012) is assumed to derive the mass profile. The subscript 'hse' will be used to denote quantities inferred from (virtual) observations under the assumption of hydrostatic equilibrium.

The sensitivities of the HSE and spectroscopic temperature biases (and scatter about the bias) to sub-grid physics are explored in Appendix B.

'Optical' observables

Optical and near-infrared luminosities and colours are computed using the GALAXEV model of Bruzual & Charlot (2003) to derive a spectral energy distribution for each star particle, which is then convolved with the transmission function of the chosen band fil-

ter. When doing so, each star particle is treated as a simple stellar population with a Chabrier (2003) IMF and the star particle's age and metallicity. The effects of dust attenuation are ignored but the simulations are compared to dust-corrected observations where possible.

2.3 X-ray properties

The X-ray properties of the simulated groups and clusters are first compared to observations of local ($z \sim 0$) systems. In Section 2.3.1, the global hot gas properties are examined as a function of system mass and, in Section 2.3.2, the observed radial distributions of entropy and density are compared to their observational counterparts.

For clarity, the observational error bars have been omitted from the global hot gas property plots below. For reference, the typical *statistical* errors are of the order of 10 per cent in gas mass and temperature, 5 per cent in X-ray luminosity, and 10–20 per cent in halo mass for the observational samples compared to below. For the same reason, the scatter has only been plotted (using shaded regions) for the AGN 8.0 model as the intrinsic scatter does not vary much between the different physical models.

2.3.1 Global scaling relations

Luminosity–mass relation

In figure 2.1, the soft (0.5–2.0 keV band) X-ray luminosity–M_{500} relation is plotted for the various simulations (coloured solid curves and shaded region) and compared to observations of individual X-ray-selected systems (data points in left panel) and stacking measurements of the mass–luminosity relation for the optically-selected maxBCG sample (Rozo et al. 2009; black lines in right panel) and the X-ray-selected COSMOS sample (Leauthaud et al. 2010; data points in right panel). As the observational mass measurements of the data in the left panel of figure 2.1 are based on a hydrostatic analysis of the X-ray observations, the synthetic X-ray observation methodology described

in Section 2.2.2 is used to measure $M_{500,hse}$ for the simulated systems. The maxBCG and COSMOS data in the right panel, on the other hand, use stacked weak lensing masses (in bins of richness and X-ray luminosity, respectively). The true M_{500} is used for the simulated systems in this comparison, as weak lensing masses are thought to be biased on average by only a few per cent (e.g. Becker & Kravtsov 2011; Bahé, McCarthy & King 2012, but see Rasia et al. 2012 who find somewhat larger biases).

For the Leauthaud et al. (2010) data, their 0.1–2.4 keV luminosities have been converted into 0.5–2.0 keV luminosities using the online WebPIMMS[3] tool (the conversion factor is ≈ 0.6 and is insensitive to the temperature adopted for the range considered here). Their M_{200} masses have been converted into M_{500} assuming a Navarro–Frenk–White (NFW; Navarro, Frenk & White 1997) profile with a concentration of 4 (e.g. Duffy et al. 2008), which yields $M_{500} \approx 0.69 M_{200}$. Finally, their luminosities and masses have been scaled to $z = 0.25$ assuming self-similar evolution (many of the COSMOS groups are close to this redshift in any case), to be directly comparable to the Rozo et al. (2009) relation and the simulations presented in the right panel of figure 2.1.

The AGN feedback model with the 'standard' OWLS heating temperature of $\Delta T_{heat} = 10^8$ K (i.e. AGN 8.0, or just 'AGN' in McCarthy et al. 2010) broadly reproduces the observed luminosity-mass relation over nearly two orders of magnitude in mass. There is a slight difference in slope with respect to the individual X-ray-selected systems in the left panel of figure 2.1, such that the lowest mass observed systems are a factor of a few more luminous than their simulated counterparts. However, no such offset is evident in the comparison to the stacking results in the right panel, which suggests that observational selection may be important (see discussion below). Interestingly, when the same model is examined in the *WMAP*7 cosmology, the discrepancy in the left panel largely goes away (the simulated clusters are brighter, presumably due to the increased baryon fraction in the *WMAP*7 cosmology), although one is introduced in the right panel, in the sense that the simulated clusters become slightly brighter on average than the maxBCG/COSMOS stacking results indicate.

---

[3]http://heasarc.gsfc.nasa.gov/Tools/w3pimms_pro.html
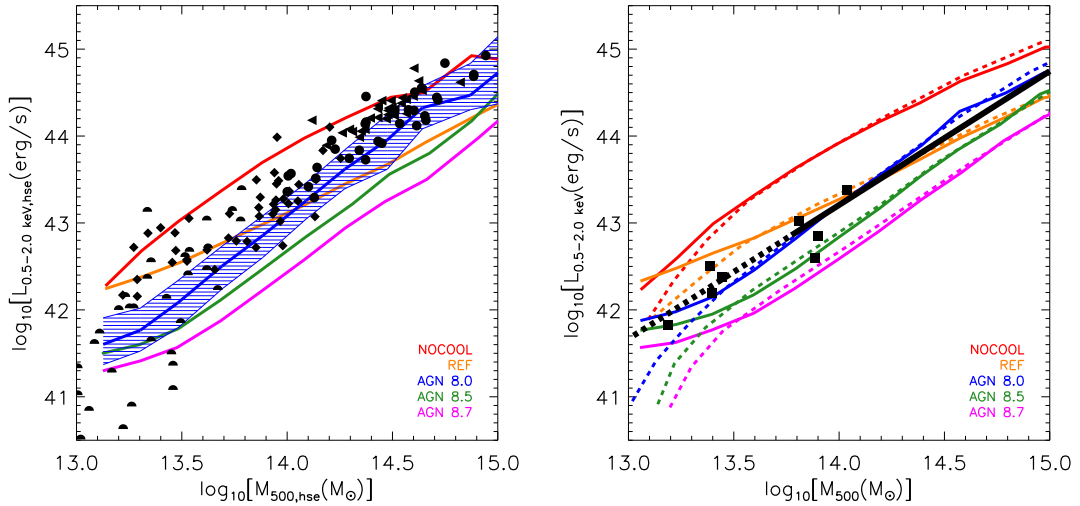
Figure 2.1: The soft X-ray luminosity–M_{500} relation at $z = 0$. The X-ray luminosity refers to the 0.5–2.0 keV band (rest-frame) and is computed respectively within $r_{500,hse}$ for the left panel and within r_{500} for the right one. *Left:* The filled black circles (clusters), left-facing triangles (clusters), diamonds (groups), and semi-circles (groups) represent the observational data (at $z \approx 0$) of Pratt et al. (2009), Vikhlinin et al. (2009a), Sun et al. (2009) and Osmond & Ponman (2004), respectively. The solid curves (red, orange, blue, green and magenta) represent the median $L_X - M_{500,hse}$ relations in bins of $M_{500,hse}$ for the different simulations at $z = 0$ and the blue shaded region encloses 68 per cent of the simulated systems for the AGN 8.0 model. *Right:* The solid and dashed black lines represent the stacked relation and its extrapolation down to lower masses of Rozo et al. (2009) at $z \approx 0.25$, derived by stacking X-ray (RASS) and weak lensing (SDSS) data in bins of richness for the optically-selected maxBCG sample. The filled black squares represent the stacked relation of Leauthaud et al. (2010) scaled to $z = 0.25$, which uses stacked weak lensing masses for COSMOS groups in bins of X-ray luminosity for a sample of X-ray-selected groups. The solid and dashed curves (red, orange, blue, green and magenta) represent the simulated mean X-ray-luminosity–M_{500} relations at $z = 0.25$ in bins of M_{500} and L_X, respectively. The AGN model with a heating temperature of $\Delta T_{heat} = 10^8$ K (i.e. AGN 8.0) reproduces the observed relations relatively well. Higher heating temperatures (i.e. more bursty feedback) lead to under-luminous systems, while lack of AGN feedback altogether (REF) results in over-luminous groups and under-luminous clusters.

Increasing the AGN heating temperature significantly (e.g. AGN 8.7, magenta solid line), which makes the AGN feedback more violent and bursty in nature, tends to result in under-luminous systems at all mass scales, irrespective of the used cosmology. As shown in Section 2.3.2, this lower luminosity is due to a strong reduction in the central gas density. Neglect of AGN feedback altogether (REF) results in a flatter than observed luminosity–mass relation, such that groups (clusters) are over-luminous (under-luminous) with respect to the observations.

Previous simulation studies, such as those of Puchwein, Sijacki & Springel (2008), Fabjan et al. (2010), Short, Thomas & Young (2013) and Planelles et al. (2014) have also concluded that the inclusion of AGN feedback helps to reproduce the mean luminosity–temperature relation.

Interestingly, the observed scatter in the luminosity-mass relation is also broadly reproduced by the models from $\log_{10}[M_{500}(\mathrm{M}_\odot)] \gtrsim 14$ or so. This suggests that the simulations have produced reasonably realistic *populations* of clusters. At lower masses ($\log_{10}[M_{500}(\mathrm{M}_\odot)] \lesssim 13.5$), the observed scatter appears to be considerably larger than in the AGN 8.0 model. This could indicate either the impact of selection effects (see discussion below) in observed surveys, or that the history of AGN activity is more variable in low-mass systems than is allowed by the models.

Note that while every attempt has been made to 'measure' the X-ray properties of the simulated systems in an observational manner, an important caveat to bear in mind is that no attempt was made to *select* them in the same way as in the observational samples (which generally have poorly understood selection functions). This may affect the quantitative conclusions that can be drawn from comparisons of X-ray luminosities, particularly for galaxy groups where observations of individual groups (left panel) are typically limited to the very brightest and nearest systems (Rasmussen et al. 2006).

Indeed, there appears to be a noticeable difference in the mean X-ray luminosity of groups (with masses $M_{500} \sim 10^{13-13.5}\,\mathrm{M}_\odot$) for the different observational studies. In particular, the Sun et al. (2009) X-ray-selected sample (black diamonds in the left panel of figure 2.1) has a significantly higher mean luminosity than the Osmond & Ponman (2004) X-ray-selected sample (black semi-circles in the left panel), the Rozo et al. (2009) optically-selected sample (black lines in the right panel), and the Leauthaud et al. (2010) X-ray-selected sample (black squares in the right panel). The Sun et al. (2009) sample is based on archival data with the requirement that there be a sufficiently large number of photons to measure spatially-resolved spectra (and therefore temperature and density profiles) out to a significant fraction of r_{500}. The Osmond & Ponman (2004) study, on the other hand, required only enough photons to measure a single mean temperature, which has been converted to M_{500} using the mass–temperature re-

lation of Sun et al. (2009). For the Leauthaud et al. (2010) sample, galaxy groups only need be detected and have a robust X-ray luminosity (i.e. they do not require a temperature measurement) to be considered in their stacking analyses. Finally, the Rozo et al. (2009) sample is optically-selected and mean X-ray luminosities are derived by stacking shallow RASS X-ray data of many groups and clusters (contamination due to point sources and to false groups may be an issue at such low richnesses, however).

In the future, large samples of homogeneously analysed and selected X-ray groups will be available through the XXL (Pierre et al. 2011) and *eRosita* (Merloni et al. 2012) surveys. Particular attention is being devoted in these surveys to the selection function using synthetic observations of cosmological simulations. For the present, the importance of selection remains an open question for the observed mass–luminosity and luminosity–temperature relations.

Mass–temperature relation

In the left panel of figure 2.2, the $M_{500,hse}-$X-ray temperature relation at $z = 0$ is plotted for the various simulations and compared to observations of individual X-ray-selected systems. For both the observations and simulations, the X-ray temperature is measured by fitting a single-temperature plasma model to the integrated X-ray spectrum within the annulus $[0.15–1]r_{500,hse}$ (i.e. a mean 'cooling flow-corrected' temperature). In the right panel of figure 2.2, the temperature has been normalised by the virial temperature $k_B T_{500,hse} \equiv \mu m_p G M_{500,hse}/2r_{500,hse}$ to take out the explicit gravitational halo mass dependence, in order to more closely examine the effects of baryonic physics on the mass–temperature relation. Note that the virial temperature is computed using the hydrostatically-derived mass for both the observed and simulated systems.

The mass–temperature relation is similar for all the runs examined and independent of the choice of cosmology. This insensitivity owes to the fact that, to first order, the temperature is set by the depth of the potential well, which is dominated by dark matter. As a result, the X-ray temperature is always close to the virial temperature (as

demonstrated in the right panel), particularly for the core-excised temperatures[4] used in figure 2.2, which probe gas with long cooling times. This is consistent with the findings of previous simulation studies (e.g. McCarthy et al. 2010; Short et al. 2010).
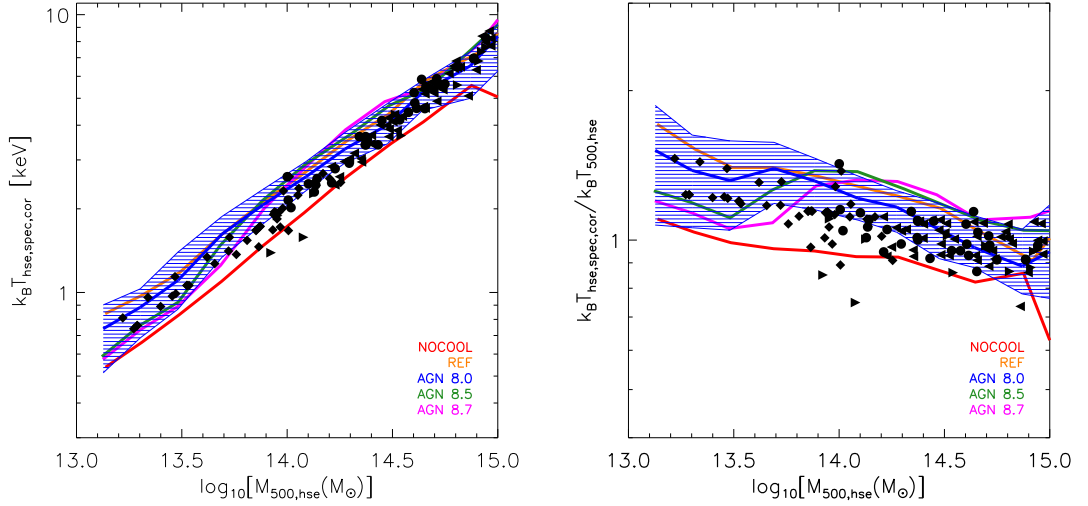
Figure 2.2: The X-ray temperature–$M_{500,hse}$ relation at $z = 0$. The X-ray temperature is measured by fitting a single-temperature plasma model to the X-ray spectrum within the annulus $[0.15–1]r_{500,hse}$ (i.e. a mean 'cooling flow-corrected' temperature). The filled black circles (clusters), right-facing triangles (clusters), left-facing triangles (clusters), and diamonds (groups) represent the observational data of Pratt et al. (2009), Vikhlinin et al. (2009a), Vikhlinin et al. (2006) and Sun et al. (2009), respectively. The coloured solid curves represent the median mass–temperature relations in bins of $M_{500,hse}$ for the different simulations and the blue shaded region encloses 68 per cent of the simulated systems for the AGN 8.0 model. In the left panel, the observed temperature (in keV) is plotted, while in the right panel the temperature is normalised by the virial temperature $k_B T_{500,hse} \equiv \mu m_p G M_{500,hse}/2r_{500,hse}$ to take out the gravitational halo mass dependence. The AGN 8.0 and REF models broadly reproduce the observed relations, while the non-radiative (NOCOOL) and AGN models with higher heating temperatures (AGN 8.7 in particular) under- and overshoot (respectively) the observed relation by about 10 per cent.

The NOCOOL model lies below the observed relation by roughly 10 per cent (i.e. it has too low temperatures at fixed masses compared to the observations). As will be shown below (see Section 2.3.2), this is because the ICM has a lower entropy in this run compared to the other runs, due both to its inability to cool (which would remove the lowest-entropy gas from the ICM) and to the lack of feedback (which heats and ejects low-entropy gas). On the other hand, AGN models with high heating temperatures

---

[4]Coalescence of baryons can potentially become gravitationally important in the very central regions of simulations that suffer from overcooling (e.g. Nagai, Kravtsov & Vikhlinin 2007 and the REF model here), which can lead to strong gravitational compression and 'heating'.

(AGN 8.5 and, in particular, AGN 8.7) lie above the observed relation at $z = 0$ because they eject too much low-entropy gas. Finally, there is a slight difference in the shape of the relations predicted by all the radiative simulations compared to the observations, with a 'bump' in the median trends of the simulations at $\log_{10}[M_{500}(\mathbf{M}_\odot)] \sim 14$. This is due to the differences in detailed entropy structure of the gas between the simulations and observations (see figures 2.5 and 2.6).

Gas mass fraction–mass relation

In figure 2.3, the gas mass fraction–$M_{500,hse}$ relation at $z = 0$ is plotted for the various simulations and compared to observations of individual X-ray-selected systems. The gas mass fraction is measured within $r_{500,hse}$. For the simulated systems, the synthetic X-ray observations/analysis methodology of Section 2.2.2 is used to 'measure' the halo mass and gas mass fraction of the simulated systems.

As is well known, the observed relation shows a strong trend in gas mass fraction with total system mass, such that galaxy groups have significantly lower fractions compared to massive clusters and the universal baryon fraction $f_b \equiv \Omega_b/\Omega_m$. Some previous observational studies argued that this was due to a much higher star formation efficiency in groups relative to clusters (e.g. Gonzalez, Zaritsky & Zabludoff 2007; Giodini et al. 2009), but some recent observational results suggest that the star formation efficiency of groups is similar to that of clusters (e.g. Leauthaud et al. 2012; Budzynski et al. 2014) and is therefore far below what is needed to 'baryonically close' groups (e.g. Sanderson et al. 2013), even when intracluster light (ICL) is explicitly accounted for (Budzynski et al. 2014).

The observed trend, as well as its scatter, are reproduced extremely well by the AGN 8.0 model from groups up to massive clusters in the *Planck* cosmology. In the *WMAP*7 cosmology (not shown), which has a universal baryon fraction of $\Omega_b/\Omega_m = 0.167$ (compared to the *Planck* value of 0.154 – dotted horizontal line), the observed trend is approximately bracketed by the AGN 8.0 and AGN 8.5 models (more gas must be ejected in the *WMAP*7 cosmology to recover the observed gas mass fraction). As
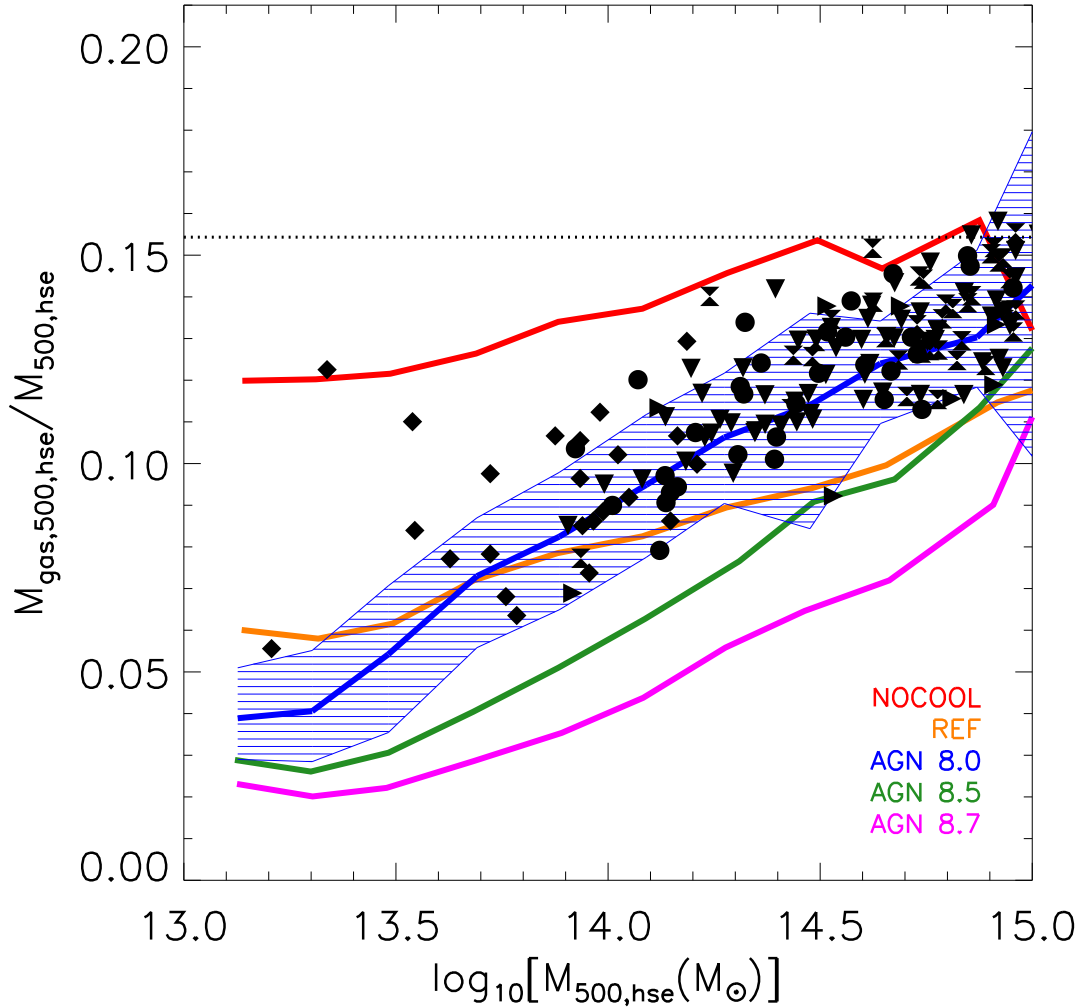
Figure 2.3: The gas mass fraction within $r_{500,hse}$ as a function of $M_{500,hse}$ at $z = 0$. The filled black circles (clusters), right-facing triangles (clusters), downward triangles (clusters), hourglass (clusters) and diamonds (groups) represent the observational data of Pratt et al. (2009), Vikhlinin et al. (2006), Lin et al. (2012), Maughan et al. (2008) and Sun et al. (2009), respectively. The coloured solid curves represent the median gas mass fraction–$M_{500,hse}$ relations in bins of $M_{500,hse}$ for the different simulations and the blue shaded region encloses 68 per cent of the simulated systems for the AGN 8.0 model. The observed trend is reproduced very well by the standard AGN model (AGN 8.0) in the *Planck* cosmology (in the *WMAP*7 cosmology, not shown, it is approximately bracketed by the AGN 8.0 and AGN 8.5 models). Raising the AGN heating temperature further results in too much gas being ejected from (the progenitors of) groups and clusters. The REF model (which lacks AGN feedback) also approximately reproduces the observed trend for low-intermediate masses (though not for $M_{500,hse} \gtrsim 10^{14.5}$ M$_\odot$), but at the expense of significant overcooling (see figure 2.10).

demonstrated by McCarthy et al. (2011), the reduced gas mass fraction with respect to the universal mean in the AGN models is achieved primarily by the ejection of

gas from the high redshift progenitors of today's groups and clusters. (Star formation accounts for only ~ 10 per cent of the removal of hot gas in these models.) The lower binding energies of groups compared to clusters result in more efficient gas ejection from groups, which naturally leads to the trend in decreasing gas fraction at lower halo masses. This is consistent with the findings of previous simulation studies, such as those of Bhattacharya, Di Matteo & Kosowsky (2008), Puchwein, Sijacki & Springel (2008), Short & Thomas (2009), Fabjan et al. (2010), Stanek et al. (2010) and Planelles et al. (2013).

Note that increasing the heating temperature of the AGN further results in too much gas being ejected from all systems. The REF model, which lacks AGN feedback altogether, also yields reasonable gas mass fractions, but the relation with mass is flatter than observed, because the star formation efficiency does not depend strongly on halo mass. The low gas fractions in this model are achieved by overly efficient star formation (see figure 2.10).

Note that the non-radiative run, NOCOOL, has a slight trend with mass and that some massive clusters apparently have gas mass fractions well in excess of the universal baryon fraction (the scatter, not shown, is somewhat larger in magnitude compared to that of the AGN 8.0 model). Naively, this would appear to contradict previous studies which also examined non-radiative simulations and found that the baryon fraction does not depend on halo mass and is very nearly the universal fraction within r_{500} with little scatter (e.g. Crain et al. 2007). There is, in fact, no contradiction – the non-radiative results presented here agree very well with previous studies when considering the *true* baryon fraction versus halo mass trend. The slight trend indicated in figure 2.3 and the large scatter (not shown) are due to biases in the recovered gas density and total mass profiles introduced during the synthetic X-ray observation analysis. In particular, because it is unable to cool, there is a lot more gas at short cooling times (low temperature and high density) in this run, which biases the recovered ICM density and temperature due to its high X-ray emissivity. These biases are significantly reduced in radiative simulations, where cooling and feedback tend to remove low-entropy gas from the systems.

Y_X-**mass relation**

In the left panel of figure 2.4, the $Y_X - M_{500,hse}$ relation at $z = 0$ is plotted for the various simulations and compared to observations of individual X-ray-selected systems. Y_X is the X-ray analogue of the SZ flux and is hence defined as the product of the hot gas mass within $r_{500,hse}$ and the core-excised mean X-ray spectral temperature (as in figure 2.2) and is thus closely related to the total thermal energy of the ICM. Kravtsov, Vikhlinin & Nagai (2006) first proposed Y_X as a cluster mass proxy, arguing that it should be relatively insensitive to the details of ICM physics and merging.
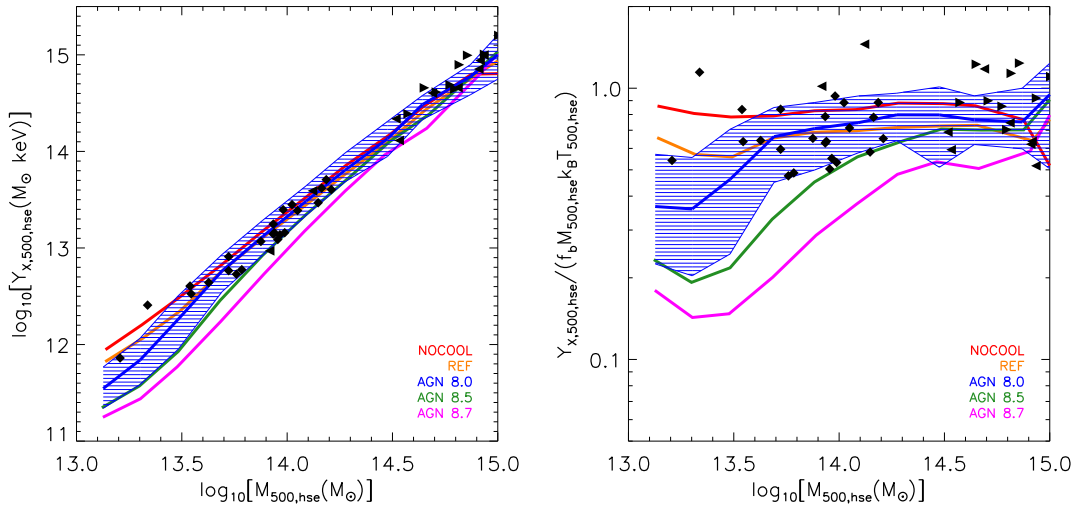
Figure 2.4: The $Y_X - M_{500,hse}$ relation at $z = 0$. The filled black left-facing triangles (clusters), right-facing triangles (clusters) and diamonds (groups) represent the observational data of Vikhlinin et al. (2006), Planck Intermediate Results IV and Sun et al. (2009), respectively. The coloured solid curves represent the median $Y_X-M_{500,hse}$ relations in bins of $M_{500,hse}$ for the different simulations and the blue shaded region encloses 68 per cent of the simulated systems for the AGN 8.0 model. In the left panel, the observed Y_X (in $M_\odot$ keV) is plotted, while in the right panel, Y_X is normalised by $f_b M_{500,hse} k_B T_{500,hse}$ to take out the explicit gravitational halo mass dependence. The AGN 8.0 model reproduces the observed trend over approximately two orders of magnitude in mass. Higher heating temperatures result in too low Y_X for low-mass groups relative to the observations (due to overefficient gas ejection).

In the left panel of figure 2.4, one can see that the various simulations indeed yield similar $Y_X - M_{500,hse}$ relations (the REF, NOCOOL, and AGN 8.0 models reproduce the data best) and Y_X is clearly strongly correlated with system mass. However, due to the large dynamic range in Y_X plotted in the left panel of figure 2.4, one perhaps gets a mislead-

ing impression of the sensitivity of Y_X to ICM physics. To address this, the dimensionless quantity $Y_X/(f_b M_{500,hse} k_B T_{500,hse})$, where $k_B T_{500,hse} \equiv \mu m_p G M_{500,hse}/2 r_{500,hse}$ is plotted in the right panel of figure 2.4. The denominator takes out the explicit halo mass dependence of Y_X and greatly reduces the dynamic range on the y-axis, allowing for a better examination of the sensitivity of Y_X to the important non-gravitational physics. Note that $f_b M_{500,hse} k_B T_{500,hse}$ is the Y_X a cluster of mass $M_{500,hse}$ would possess if the hot gas were isothermal with the virial temperature and the gas mass fraction had the universal value (i.e. the self-similar prediction).

From the right hand panel of figure 2.4, one immediately concludes that Y_X *is* in fact sensitive to ICM physics, contrary to the claims of Kravtsov, Vikhlinin & Nagai (2006). More specifically, energetic AGN, which were not examined by Kravtsov et al., can eject large quantities of gas that can significantly lower Y_X. This reduction in gas mass can be compensated to a degree by the slight increase in temperature due to the fact that much of the ejected gas had low entropy (and also additional high entropy gas is able to accrete within r_{500}; McCarthy et al. 2011). However, hydrostatic equilibrium forces the temperature of the ICM to remain near the virial temperature, and thus arbitrarily large amounts of gas ejection cannot be compensated for.

At $z = 0$, observed groups and clusters have sufficiently high gas mass fractions that Y_X is not significantly depressed compared to the self-similar prediction. However, figure 2.4 should serve as a warning against blindly applying Y_X to, e.g. lower halo masses and/or higher redshifts, where independent direct halo mass estimates are increasingly scarce. This caution should also obviously be heeded (perhaps even more so) by studies which use gas mass (fractions) as total mass proxies as opposed to Y_X.

2.3.2 Profiles

Entropy

In figure 2.5, the three-dimensional radial entropy profiles of groups (left panel) and clusters (right panel) are plotted for the various simulations and compared to observa-
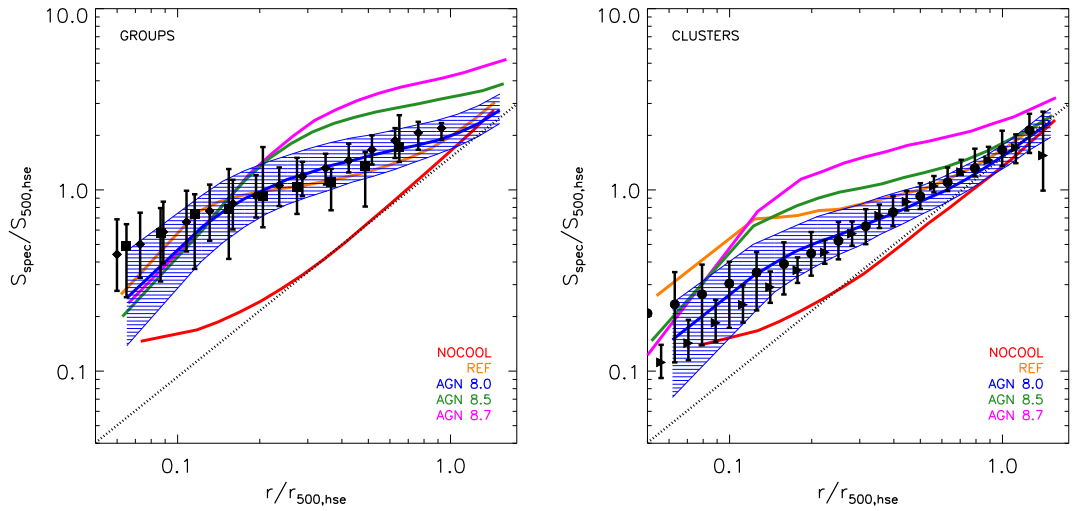
Figure 2.5: The radial entropy profiles of groups (*left*) and clusters (*right*) at $z = 0$. The simulated systems have been selected to match the median mass of the observational data. The filled black diamonds (groups), squares (groups), circles (clusters) and right-facing triangles (clusters) with error bars correspond to the observational data of Sun et al. (2009), Johnson, Ponman & Finoguenov (2009), Pratt et al. (2010) and Vikhlinin et al. (2006) (in the latter case, the entropy profiles were obtained by combining their best-fitting density and temperature profiles), respectively. The error bars enclose 90 per cent and 68 per cent of the observed systems for groups and clusters, respectively. The dotted line represents the power-law fit of Voit, Kay & Bryan (2005) to the entropy profiles of a sample of simulated non-radiative SPH groups and clusters. The coloured solid curves represent the median entropy profiles for the different simulations and the blue shaded region encloses 68 per cent of the simulated systems for the AGN 8.0 model. The standard AGN 8.0 model reproduces the observed radial profiles of groups and clusters over 1.5 decades in radius, and the observed scatter is also broadly reproduced.

tions of X-ray-selected systems. As the shape and amplitude of the entropy profiles are fairly strong functions of halo mass (as shown in figure 2.6), the mass distributions of the observational and simulated samples have been slightly re-sampled so that they have approximately the same median mass for both, which is $M_{500} \approx 8.6 \times 10^{13}$ M$_\odot$ for groups and $M_{500} \approx 3.5 \times 10^{14}$ M$_\odot$ for clusters. (This was achieved by keeping only the simulated groups with 5.75×10^{13} M$_\odot \leq M_{500} \leq 1.54 \times 10^{14}$ M$_\odot$, the simulated clusters with 2.5×10^{14} M$_\odot \leq M_{500} \leq 10^{15}$ M$_\odot$, the REXCESS clusters with $M_{500} \geq 1.5 \times 10^{14}$ M$_\odot$ and the Vikhlinin et al. (2006) clusters with 1.2×10^{14} M$_\odot \leq M_{500} \leq 1.1 \times 10^{15}$ M$_\odot$.) The definition of entropy commonly used in X-ray astronomy, i.e. $S \equiv k_B T / n_e^{2/3}$, which here has units of keV cm^2 is used and is related to the thermodynamic entropy by a logarithm and an additive constant. The radii are nor-

malised by $r_{500,hse}$ and the entropies by the characteristic entropy scale $S_{500,hse}$, which is defined as

$$S_{500,hse} \equiv \frac{k_B T_{500,hse}}{n_{e,500,hse}^{2/3}} = \frac{GM_{500,hse}\mu m_p}{2r_{500,hse}(500f_b\rho_{crit}/(\mu_e m_p))^{2/3}}, \quad (2.1)$$

where μ_e is the mean molecular weight per free electron, in order to take out the explicit halo mass dependence. The baseline entropy profile of Voit, Kay & Bryan (2005) is also shown as a dotted line on both panels. This represents the self-similar answer, which was obtained by fitting a power-law to the entropy profiles of a sample of non-radiative SPH groups and clusters. Finally, as the observed entropy profiles were obtained through spectral fitting of X-ray observations, the synthetic X-ray observations methodology of Section 2.2.2 was used to compute spectral entropy profiles for the simulated systems.

As is well known, observed groups and clusters exhibit a significant level of 'excess entropy' compared to the self-similar expectation (e.g. Ponman, Cannon & Navarro 1999; Ponman, Sanderson & Finoguenov 2003), which is a clear signature of the non-gravitational physics of structure formation. This effect is stronger in groups compared to clusters. Figure 2.5 shows that all the radiative models (REF and the AGN models) yield profiles that are similar to the observed ones in the central regions ($r \lesssim 0.2r_{500,hse}$) of groups. In more massive clusters, however, only the AGN 8.0 model provides an adequate match to the observations. At intermediate/large radii, the AGN models with the two highest heating temperatures (AGN 8.5 and AGN 8.7) have too high entropy at intermediate and large radii compared to the observed levels (particularly in groups), due to the ejection of too much (preferentially low-entropy) gas from the progenitors of the present-day systems. Short, Thomas & Young (2013) also find that the inclusion of AGN feedback leads to better agreement at intermediate radii for clusters.

Note that the consequences of observational selection are also apparent in figure 2.5. In particular, the filled black circles in the right panel represent the median entropy profile from Pratt et al. (2010), derived from REXCESS – a representative sample of

33 clusters derived from a flux-limited parent sample (Böhringer et al. 2007), whereas the black right-facing triangles represent the sample of Vikhlinin et al. (2006), who targeted relaxed, cool core clusters. It is apparent that the clusters from the Pratt et al. (2010) sample have a higher mean central entropy and larger central scatter, as one might expect, since there is no requirement for their clusters to have a central temperature dip (which necessitates a low central entropy). The comparison to the Pratt et al. (2010) sample is therefore perhaps more appropriate. However, there still remains the question of how 'representative' flux-limited samples really are relative to a halo mass-selected sample, as typically derived from models/simulations such as those presented here. While it is doubtful that X-ray surveys are missing many massive nearby clusters, it is nevertheless possible that the mix of clusters in a given bin may be skewed. Furthermore, our confidence in the completeness of X-ray surveys (even above a given luminosity, let alone mass) weakens considerably as we move into the group regime.

To better explore the relatively strong dependence on halo mass apparent in figure 2.5, the entropy at three reference radii ($0.15r_{500,hse} \approx r_{13000,hse}$, $r_{2500,hse} \approx 0.45r_{500,hse}$ and $r_{500,hse}$ from top to bottom) is plotted in figure 2.6 as a function of $M_{500,hse}$ for the various simulations and compared to observations of individual X-ray-selected groups and clusters. The baseline entropy profile of Voit, Kay & Bryan (2005) is also shown as a dotted line in all three panels. Deviations from the baseline self-similar results are strongest at the lowest halo masses and smallest radii. Only the standard AGN model (AGN 8.0) is able to reproduce the observed trends with radius and halo mass. Similar results were obtained by Fabjan et al. (2010) and Planelles et al. (2014), but they only looked at the relation for the largest two of the characteristic radii.
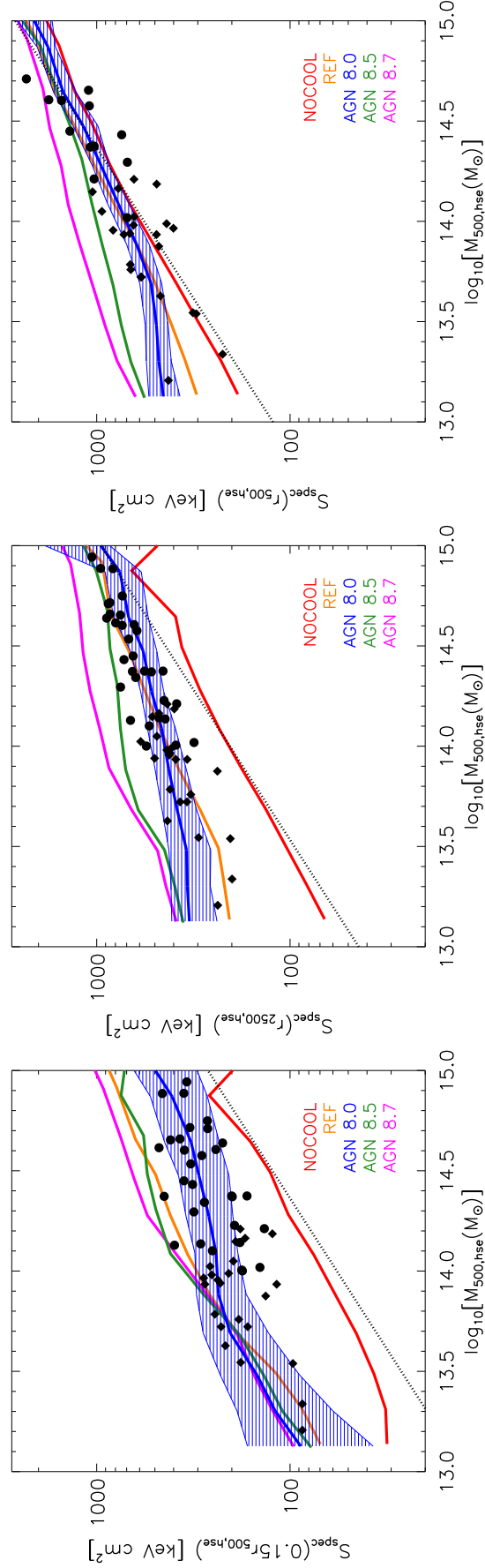
Figure 2.6: The $z = 0$ entropy measured at various characteristic radii ($0.15r_{500,hse}$ (*top*), $r_{2500,hse}$ (*middle*) and $r_{500,hse}$ (*bottom*)) as a function of $M_{500,hse}$. The filled black circles (clusters) and diamonds (groups) correspond to the observations of Pratt et al. (2010) and Sun et al. (2009), respectively, while the dotted line represents the power-law fit of Voit, Kay & Bryan (2005) to the entropy profiles of a sample of simulated non-radiative SPH groups and clusters. The coloured solid curves represent the median reference entropy–mass relations in bins of $M_{500,hse}$ for the different simulations and the blue shaded region encloses 68 per cent of the simulated systems for the AGN 8.0 model. Deviations from the self-similar prediction are largest at small radii and low halo masses. Only the AGN 8.0 model reproduces the observational data over the full range of radii and halo masses.

Density

In figure 2.7, the three-dimensional radial density profiles of groups (left panel) and clusters (right panel) are plotted for the various simulations and compared to observations of X-ray-selected systems (symbols with error bars). As was done for the entropy profile comparison above, the median masses of the observed and simulated samples have been approximately matched by excising some systems from each. The resulting samples are identical to those used for the entropy profiles in the previous subsection. The radii are normalised by $r_{500,hse}$ and the densities by the critical density of the Universe for the adopted cosmological parameters. Finally, as the observed density profiles were obtained through spectral fitting of X-ray observations, the synthetic X-ray observations methodology of Section 2.2.2 was used to compute spectral density profiles for the simulated systems.
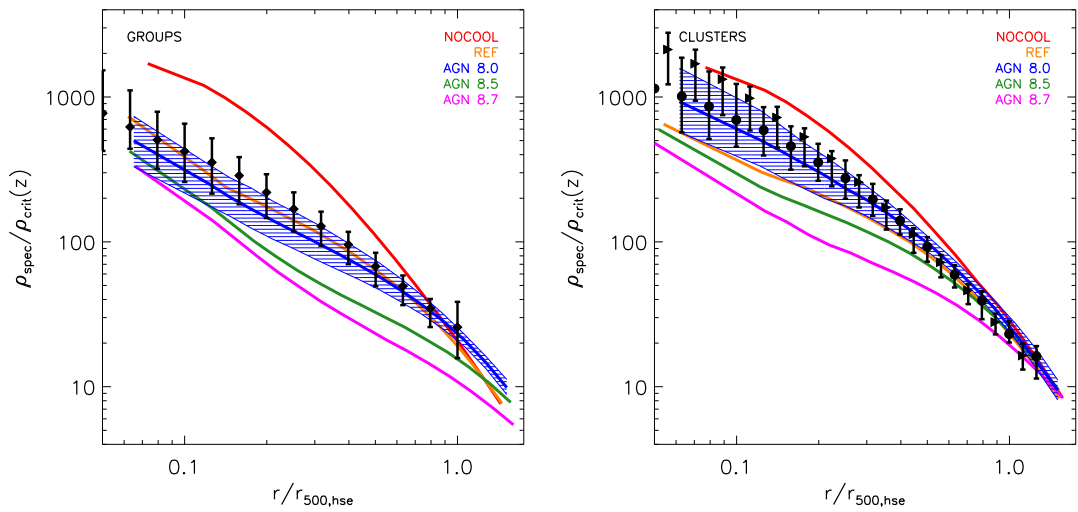
Figure 2.7: The radial density profiles of groups (*left*) and clusters (*right*) at $z = 0$. The simulated systems have been selected to match the median mass of the observational data. The filled black diamonds (groups), circles (clusters) and right-facing triangles (clusters) with error bars correspond to the observational data of Sun et al. (2009), Croston et al. (2008) and Vikhlinin et al. (2006), respectively. The error bars enclose 68 per cent of the observed systems. The coloured solid curves represent the median density profiles for the different simulations and the blue shaded region encloses 68 per cent of the simulated systems for the AGN 8.0 model. The observed trends are reproduced well in the *Planck* cosmology by the standard AGN model (AGN 8.0). In the *WMAP*7 cosmology (not shown), the simulated density profiles are shifted up by approximately 10 per cent.

The AGN 8.0 model reproduces the observed profiles (including the scatter) quite well over the whole radial range for both groups and clusters in the *Planck* cosmology. (In the *WMAP*7 cosmology, the simulation gas density profiles are shifted up by approximately the ratio of universal baryons in *WMAP*7 and *Planck* cosmologies.) Increased heating temperatures, which lead to more violent and bursty AGN feedback (e.g. AGN 8.7), result in a strongly reduced density, especially in the central regions and in low-mass systems. Conversely, when both feedback and radiative cooling are omitted (NOCOOL), the gas is too dense and too centrally concentrated. It is worth noting that the non-gravitational physics of galaxy formation has a noticeable effect on the group gas density profiles as far out as $\sim r_{500,hse}$, whereas in the case of clusters, the profiles have all approximately converged to the self-similar answer at these radii.

As discussed above, the role of observational selection is an important caveat to bear in mind, particularly for groups. Note that the median central density of the observed sample of groups in Sun et al. (2009) is slightly higher than that of the fiducial AGN model, consistent with the offset in the mass–luminosity relation at low masses (see figure 2.1). As was discussed in Section 2.3.1, however, the Sun et al. (2009) sample has a higher mean X-ray luminosity compared to other observational group samples, most likely due to selection.

Demographics of cluster cores

The observed large scatter in the properties of the hot gas in the cores of galaxy clusters is a subject that has attracted much interest in recent years. It was previously noted that the scatter in the observed global scaling relations, such as the luminosity–temperature relation, is driven primarily by the scatter in the thermodynamic properties of the gas within the central ~ 200 kpc (e.g. Fabian 1994; McCarthy et al. 2004, 2008). The origin of this scatter is still being debated. It may be due to merger activity and/or differences in the feedback histories of clusters. It is of interest to see whether the simulations presented here reproduce the detailed scatter at small radii.

Detailed studies of the radial structure of the gas with *Chandra* and *XMM-Newton* have
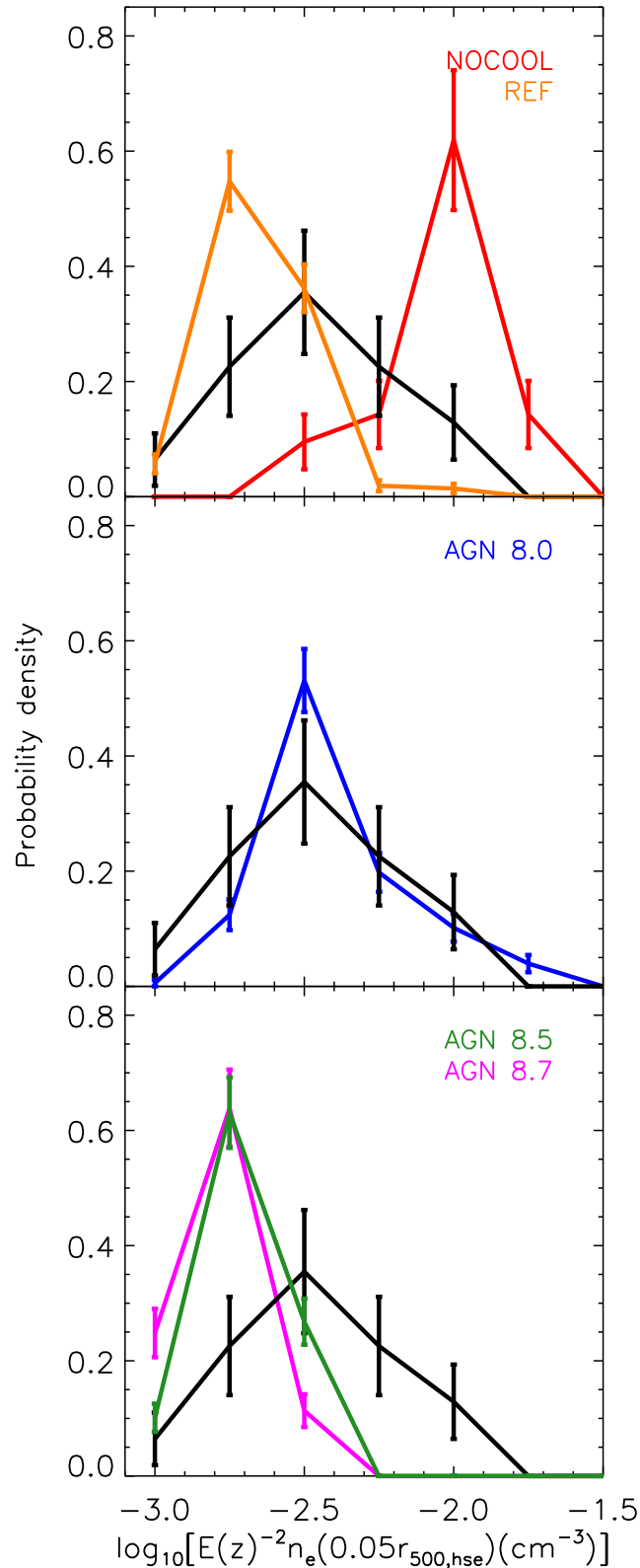
Figure 2.8: Distribution of central (at $0.05r_{500,hse}$) electron densities at $z = 0$. The thick solid histograms (red, orange, blue, green and magenta) are for the different simulations while the black one corresponds to the observational data of Croston et al. (2008) with $z \leq 0.25$ scaled to $z = 0$ assuming self-similar evolution. The error bars represent Poisson noise. The AGN 8.0 model reproduces the observed large spread in the central density distribution of the hot gas, which shows no strong evidence for bimodality.

suggested that there may be a bimodality in the central entropy (Cavagnolo et al. 2009; Pratt et al. 2010), although this has been called into question recently (Panagoulia, Fabian & Sanders 2014). As pointed out by Panagoulia, Fabian & Sanders (2014), the derived central entropy is sensitive to what is assumed about the temperature distribution at small radii, which cannot be measured in as finely spaced radial bins as the gas density and is somewhat sensitive to the uncertain metallicity of the gas. Furthermore, by experimentation, the results have been found to be sensitive to the way in which the data is binned in radius when fitting power-law + constant models to the entropy distribution (as done in the Cavagnolo et al. and Pratt et al. studies).

To overcome these issues, a non-parametric approach is adopted and applied to the central gas density distribution, which can be robustly determined from observations. In particular, the gas density measured at $0.05r_{500,hse}$ is plotted in figure 2.8 for the simulations and compared to the observational estimates of Croston et al. (2008) for the representative REXCESS cluster sample. As in previous plots, the mass distributions have been re-sampled to achieve the same median mass for the observed and simulated samples.

Encouragingly, the fiducial AGN model has a central density distribution that is quite similar to the observed one. The central density varies by over an order of magnitude in both. Furthermore, there is no strong evidence for a bimodal distribution in either the observed or simulated density distributions. This does not imply that the entropy cannot be bimodal, as the entropy depends on the temperature as well. Note that to have a bimodal distribution in the entropy but not in the density requires there to be a bimodal distribution in the shape of the potential well at small radii (or else the system is not convectively stable), with high-entropy systems having *deeper* potential wells. In the models, however, the entropy measured at $0.05r_{500,hse}$ is *not* bimodal, in qualitative agreement with the recent observational findings of Panagoulia, Fabian & Sanders (2014).

Based on the above, the dividing line between 'cool-core' and 'non-cool-core' is therefore somewhat arbitrary. The fact that the fiducial AGN model has a similar central density distribution to that of the REXCESS sample implies that, regardless of how

they are exactly defined, both types of clusters are present in this model and in approximately the correct proportion.

2.4 Sunyaev–Zel'dovich scalings

The Sunyaev–Zel'dovich (hereafter SZ) effect provides an alternative, complementary way to probe the thermodynamic state of the hot gas in groups and clusters (see e.g. Birkinshaw 1999; Carlstrom, Holder & Reese 2002 for reviews). Below the simulated and observed integrated SZ fluxes are compared as a function of halo mass. Integrated over the volume of a system, the SZ effect is proportional to the total thermal energy content of the hot gas.

In figure 2.9, the SZ flux–$M_{500,hse}$ relation for the various simulations is plotted and compared to observations of individual SZ selected systems (re-)discovered by the *Planck* satellite, mostly during the first ten months of its mission (The Early Sunyaev–Zel'dovich catalogue; Planck Early Results VIII) and, either followed up in X-ray with *XMM–Newton* (Planck Early Results IX; Planck Intermediate Results I; Planck Intermediate Results V) using Director's Discretionary Time, or with high-quality archival *XMM–Newton* data (Planck Early Results XI; Planck Intermediate Results IV). As the observational data are compared to the $z = 0$ simulation results, only the *Planck* systems with $z \leq 0.25$ were kept. Since the observational mass measurements (and apertures within which the SZ fluxes are measured) are based on either a hydrostatic analysis of the X-ray observations, or on the Arnaud et al. (2010) $Y_X - M_{500,hse}$ relation which was calibrated using a sample of 20 nearby relaxed clusters with high quality *XMM–Newton* X-ray data[5], the hydrostatic masses obtained using the synthetic X-ray analysis outlined in Section 2.2.2 and their corresponding $r_{500,hse}$ are used to compute the SZ signal.

The SZ signal is characterised by the value of its spherically integrated Compton parameter $d_A^2 Y_{500} = (\sigma_T/m_e c^2) \int P dV$ where d_A is the angular diameter distance, σ_T the

---

[5]Eight clusters come from the sample of Arnaud, Pointecouteau & Pratt (2007) and the remaining 12 are relaxed REXCESS clusters with mass profiles measured at least out to R_{550}.

Thomson cross-section, c the speed of light, m_e the electron rest mass, $P = n_e k_B T_e$ the electron pressure and the integration is done over the sphere of radius r_{500}.
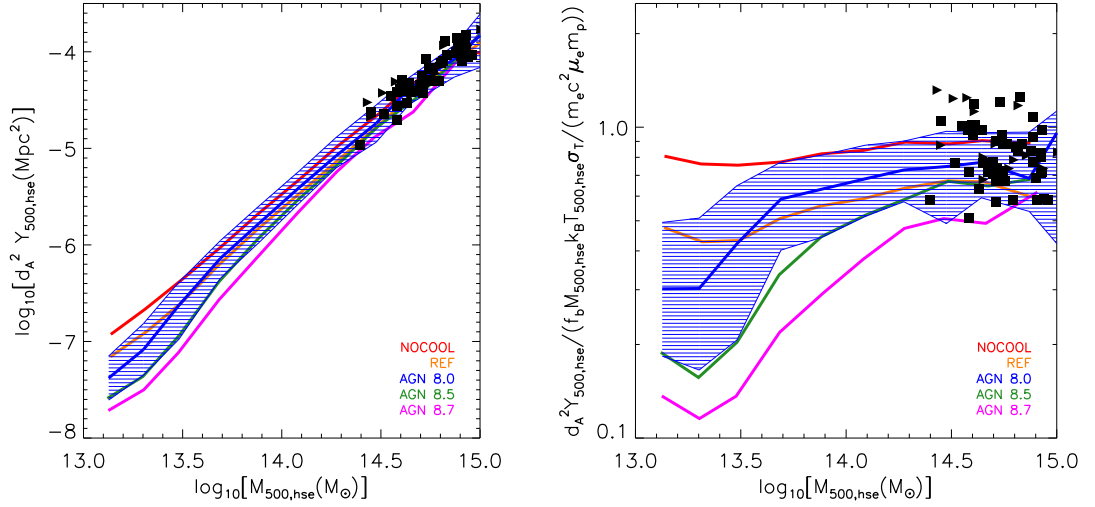
Figure 2.9: The $Y_{500,hse} - M_{500,hse}$ relation at $z = 0$. The filled black squares and right-facing triangles represent the observational data of Planck Early Results and Planck Intermediate Results with $z \leq 0.25$, respectively. The solid curves (red, orange, blue, green and magenta) represent the median SZ flux–$M_{500,hse}$ relations in bins of $M_{500,hse}$ for the different simulations and the blue shaded region encloses 68 per cent of the simulated systems for the AGN 8.0 model. In the left panel, the observed SZ signal (in Mpc^2) is plotted, whereas in the right panel, the SZ flux is normalized by $\sigma_T/(m_e c^2 \mu_e m_p) f_b M_{500,hse} k_B T_{500,hse}$ in order to take out the explicit gravitational mass dependence. Consistent with the conclusions derived from the X-ray comparisons in Section 2.3, the fiducial AGN model (AGN 8.0) reproduces the observed trend well in the *Planck* cosmology. In the *WMAP*7 cosmology (not shown), the simulated curves are shifted up by approximately 10 per cent, so that more gas ejection (a slightly higher heating temperature) is required to reproduce the normalisation.

All the simulations produce fairly similar $Y_{500,hse} - M_{500,hse}$ relations, which are in reasonable agreement with the observations by *Planck* of low-redshift massive clusters, in agreement with the results of Battaglia et al. (2012) and Kay et al. (2012). Yet, as was the case for Y_X in Section 2.3.1, the large dynamic range in total SZ flux in the left panel of figure 2.9 gives a somewhat misleading impression of the sensitivity of the SZ signal to galaxy formation physics. Therefore, in the right panel of figure 2.9, the total SZ signal is normalised by the self-similar expectation $\sigma_T/(m_e c^2 \mu_e m_p) f_b M_{500,hse} k_B T_{500,hse}$ (where $k_B T_{500,hse} \equiv \mu m_p G M_{500,hse}/2 r_{500,hse}$) in order to remove the explicit gravitational halo mass dependence and to make more apparent any potential effects of baryonic physics upon the SZ signal–mass relation. The right panel of figure 2.9 clearly

shows that the integrated SZ signal is sensitive to ICM physics.

In the *Planck* cosmology, the standard AGN model reproduces the observed relation best of any of the radiative models (the unphysical NOCOOL model performs similarly well, due to a conspiracy of having too high density and too low temperature). The scatter in the relation (which for clarity is only shown for the AGN 8.0 model) is also roughly reproduced. Thus, there is excellent consistency between the X-ray and SZ observables in terms of the physical story they tell.

It is worth noting that the sensitivity to baryonic physics increases with decreasing mass. A detailed comparison to the stacked SZ signal–halo mass relation obtained by the Planck collaboration using $\sim 260,000$ Locally Brightest Galaxies taken from SDSS (Planck Intermediate Results XI) has also been conducted. As such a comparison requires synthetic SZ observations, its results will be presented elsewhere (see Chapter 5).

2.5 Optical and black hole scalings

Finally, the optical and black hole properties of the simulated systems are compared to observations of local ($z \sim 0$) groups and clusters. In Section 2.5.1, the global stellar properties are looked at, then in Section 2.5.2, the optical properties of the brightest cluster galaxy (BCG) are investigated and, lastly, in Section 2.5.3, the properties of the central supermassive black hole are examined.

2.5.1 Total mass-to-light ratio

In figure 2.10, the *I*-band total mass-to-light ratio (within $r_{500,hse}$)–$M_{500,hse}$ relation at $z = 0$ is plotted for the various simulations and compared to recent observations that explicitly include an intracluster light (ICL) component (thus avoiding the difficulty of having to define what is the ICL in the simulations). To make like-with-like comparisons to the observations, the Cousins *I*-band luminosities have been computed using

the GALAXEV model of Bruzual & Charlot (2003) (as described in Section 2.2.2). As the observational total mass measurements of figure 2.10 are based on a hydrostatic analysis of X-ray data, the halo masses derived from the synthetic X-ray analysis of Section 2.2.2 were used. For the Gonzalez et al. (2013) and Sanderson et al. (2013) data (note that the Sanderson et al. sample is a subset of the Gonzalez et al. sample and uses their optical data, but the X-ray masses are computed somewhat differently), the stellar masses have been converted back into *I*-band luminosities using their adopted stellar mass-to-light ratios. For the best-fitting trend of Budzynski et al. (2014) (from their image stacking analysis), their derived *I*-band stellar mass-to-light ratios (see their table 2) were used to convert their mean stellar masses into mean *I*-band luminosities. Note that comparing luminosities should be more robust than comparing stellar masses, since stellar mass estimates rely on either dynamical mass-to-light ratios or stellar population synthesis modelling, which must assume a particular star formation history and metallicity (both must assume something about the stellar IMF as well). Both methods have significant ($\gtrsim 0.1$ dex) systematic uncertainties. While going from stellar masses to luminosities in the simulations also requires a stellar population model, at least in this case the precise star formation history and metallicity of the star particles that make up the simulated galaxies are known, whereas these must be *assumed* for real galaxies.

Observed galaxy clusters have high total mass-to-light ratios of ~ 100. Only the simulations that include feedback from supermassive black holes yield such high values. The REF model, which neglects AGN feedback, produces mass-to-light ratios that are approximately a factor of three to five too low due to overly efficient star formation. These conclusions are insensitive to the choice of cosmology.

As discussed in detail in Budzynski et al. (2014), there is a difference in the slope of the trend of the stellar mass/light with halo mass that they measure and that measured by Gonzalez, Zaritsky & Zabludoff (2007) (and now Gonzalez et al. 2013). The origin of this difference is unclear. As noted by Budzynski et al. (2014) (see also Leauthaud et al. 2012), it is *not* driven by differences in the derived contributions of the ICL. Indeed, the largest differences are at the highest masses, where Gonzalez et al. estimate that
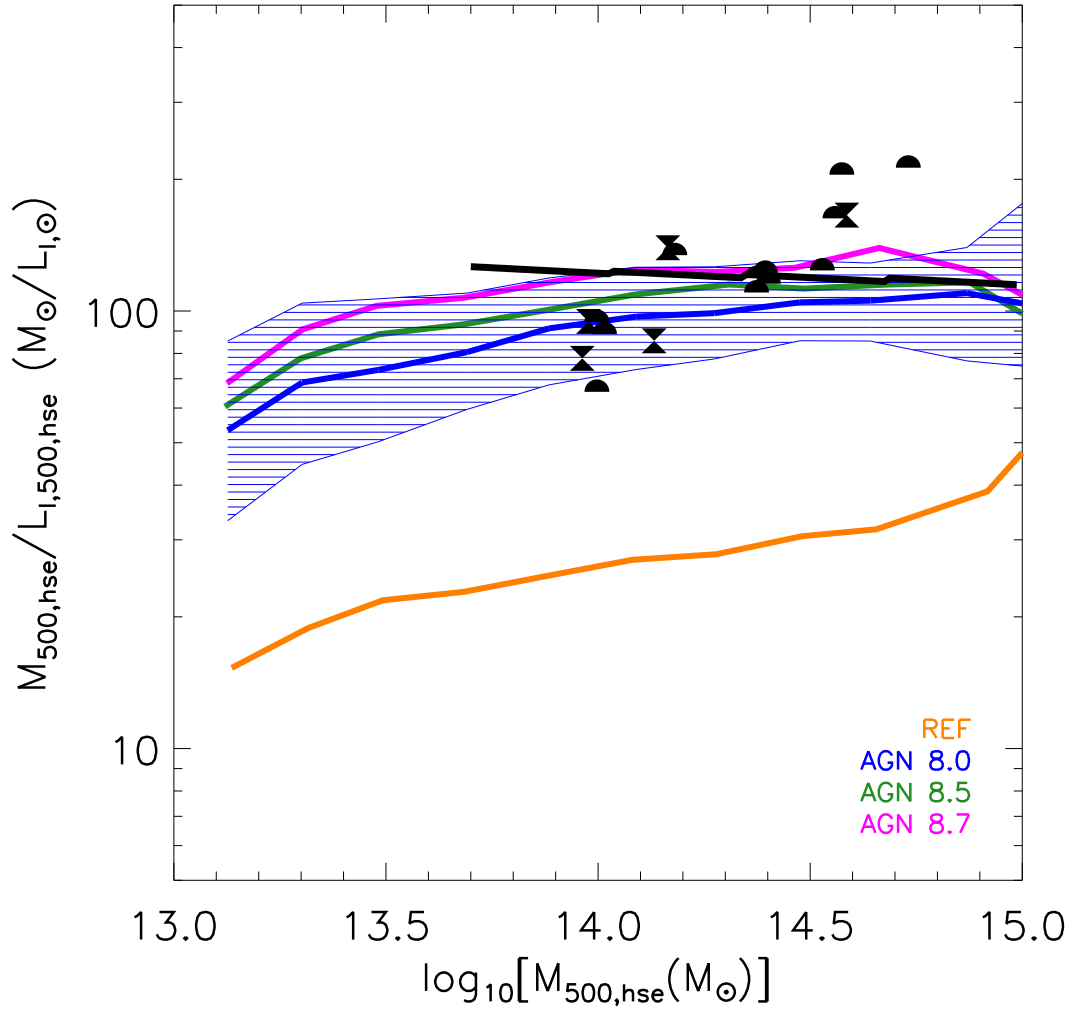
Figure 2.10: *I*-band total mass-to-light ratio as a function of $M_{500,hse}$ at $z = 0$. The filled black hourglass and semi-circles represent the observational data of Sanderson et al. (2013) and Gonzalez et al. (2013), respectively. The solid black line represents the SDSS image stacking results of Budzynski et al. (2014). The three observational studies and the simulations include the contribution from intracluster light. The coloured solid curves represent the median *I*-band total mass-to-light ratio–$M_{500,hse}$ relations in bins of $M_{500,hse}$ for the different simulations and the blue shaded region encloses 68 per cent of the simulated systems for the AGN 8.0 model. The observational studies differ in their findings of the *steepness* of the trend with halo mass, but consistently find high mass-to-light ratios for massive clusters. The inclusion of AGN feedback is essential for reproducing the observed high normalisation.

the ICL contributes a relatively small fraction of the total light. Budzynski et al. (2014) conclude that Gonzalez et al. consistently measure *lower* luminosities (and therefore higher total mass-to-light ratios) for the highest-mass systems compared to all the other observational studies they compared to (including Lin & Mohr 2004 and Leauthaud

et al. 2012). Irrespective of this discrepancy, the observations strongly point to a high total mass-to-light ratio that cannot be achieved by means of stellar feedback alone.

2.5.2 Properties of the BCGs

Dominance of the BCG

In figure 2.11, the ratio of the *K*-band light in the BCG to that in the BCG and satellite galaxies (i.e. no ICL) as a function of halo mass at $z = 0$ is plotted for the various simulations and compared to observations of individual X-ray-selected systems of Lin & Mohr (2004) and Lin, Mohr & Stanford (2004) (hereafter collectively referred to as Lin et al. 2004) and Rasmussen & Ponman (2009). In both cases, the observed mean X-ray temperatures have been converted into a halo mass using the mass–temperature relation of Vikhlinin et al. (2009a). For the simulations, the *K*-band light of the BCG is computed in a simple way by summing the luminosities of all the star particles within an aperture of 30 kpc. This is similar to the average effective radius of observed BCGs (e.g. Stott et al. 2011). Adjusting the aperture changes the normalisation of the relation somewhat but does not significantly affect the shape of the relation.

Note that in both the observations and simulations plotted in figure 2.11, the BCG is defined to be the most (stellar) massive/luminous galaxy, and that there is no requirement that the BCG be, for instance, coincident with the X-ray emission peak or the 'central' galaxy. Indeed, recent observational studies (e.g. Balogh et al. 2011; Skibba et al. 2011) have shown that there can sometimes be relatively large offsets between the BCG and these other choices of centre .

As can clearly be seen, the stellar fraction in the BCG is a strongly decreasing function of total mass. All the models reproduce that trend, but the REF model produces BCGs which are too dominant compared to the observed ones, whereas all the AGN models yield similar stellar fractions in the BCGs which are consistent with the observed ones. This is due both to suppression of star formation in massive satellite galaxies which eventually merge with the BCG, as well as to the suppression of the central cooling
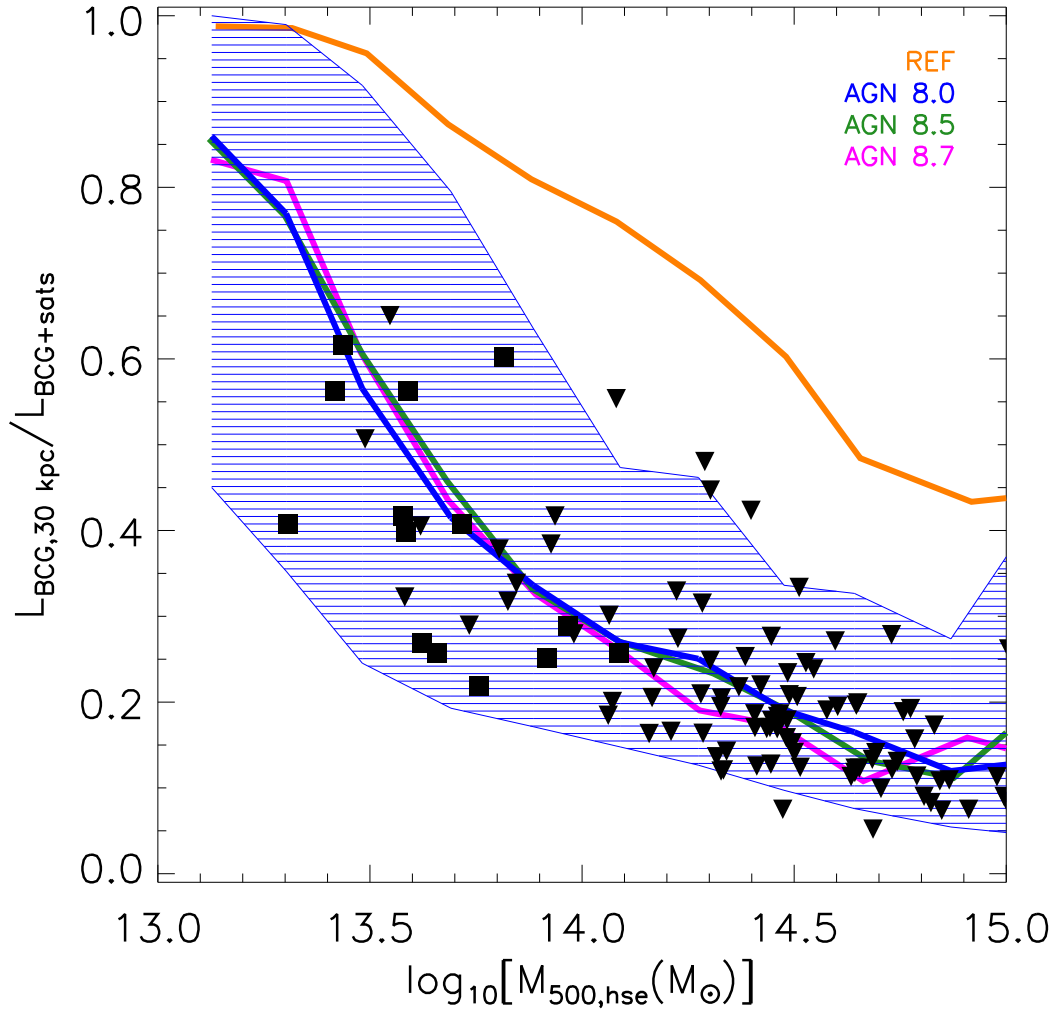
Figure 2.11: *K*-band luminosity fraction in the BCG at $z = 0$. The filled black squares (groups) and downward triangles (clusters) represent the observational data of Rasmussen & Ponman (2009) and Lin et al. (2004), respectively. The coloured solid curves represent the median *K*-band light fraction in the BCG–$M_{500,hse}$ relations in bins of $M_{500,hse}$ for the different simulations and the blue shaded region encloses 68 per cent of the simulated systems for the AGN 8.0 model. Lack of AGN feedback leads to BCGs which are too dominant compared to the satellite galaxy population.

flows by the AGN feedback. As will be shown in the next subsection, central cooling flows and the star formation they induce in BCGs are indeed strongly suppressed by AGN feedback. No reasonable choice of aperture can reconcile the observed trend with the REF model.

Star-forming fraction

In figure 2.12, the fraction of the BCGs that are currently forming stars at an appreciable rate ($SFR > 3$ M$_\odot$ yr^{-1}) as a function of system mass is plotted for the various simulations. They are compared to the observations of the BCGs of both X-ray-selected groups and clusters (from the National Optical Astronomy Observatory Fundamental Plane Survey (NFPS); Smith et al. 2004) and optically-selected groups and clusters from the SDSS Data Release 3 (DR3) C4 cluster catalogue (Miller et al., 2005) by Edwards et al. (2007) (black dashed lines). The thick solid, thin dotted and dot-dashed curves represent the median relations for the simulations when respectively a 10, 20 and 30 kpc aperture is used to define the BCG.

Edwards et al. (2007) find that the star-forming fraction of BCGs (i.e. those with detectable optical line emission, corresponding to an SFR threshold of a few solar masses per year) is approximately independent of system mass. The spectroscopic measurements are made within 2 or 3 arcsecond fibres, which at the typical redshifts of the NFPS and C4 samples corresponds to an aperture of a few kpc across. When the star-forming fraction is computed in a similar aperture (solid thick curve in figure 2.12), a similar trend and normalisation to the observed one are found for the models that include AGN feedback. The REF model, which only includes stellar feedback, fails to suppress the central cooling flows and their induced star formation in BCGs. However, as demonstrated by the dotted and dot-dashed curves, when the aperture is expanded, the star-forming fraction begins to rise with halo mass. Although unaware of any observations that show that such large-scale star formation does not exist in general in real BCGs, this trend is suspected to be at least partly numerical in origin. Specifically, the maximum past temperature (the simulation code tracks this quantity for each particle over all time steps) of star-forming gas and recently-formed star particles (those formed within the past Gyr) within the annulus 10 kpc $< r \leq 30$ kpc centred on the BCG have been examined. The vast majority of the particles have a maximum past temperature of just below $10^{5.0}$ K, corresponding to the temperature floor imposed by UV/X-ray photoheating in the simulations, with a further contribution from gas with a maximum past temperature between $10^{5.5}$ K and $10^{6.0}$ K and a negligible contribution
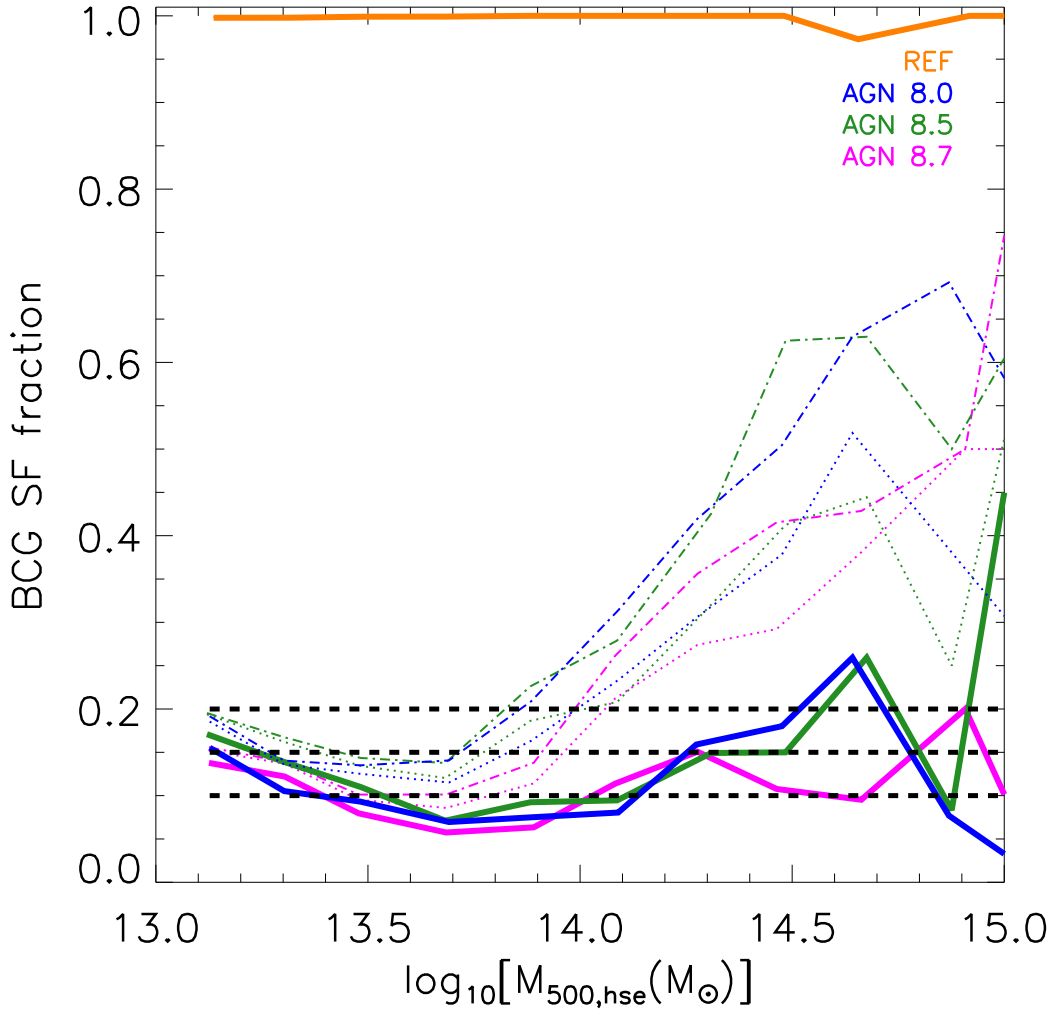
Figure 2.12: Fraction of the BCGs that are currently forming stars at an appreciable rate ($SFR > 3\,\mathrm{M}_\odot\,\mathrm{yr}^{-1}$) as a function of $M_{500,hse}$. The black dashed lines correspond to the observational results of Edwards et al. (2007). The thick solid, thin dotted and dot-dashed curves (orange, blue, green and magenta) represent the median relations for the different simulations in 10, 20 and 30 kpc apertures, respectively. The observed star-forming fraction is roughly reproduced in the AGN models when measured approximately within an observed aperture. However, the star-forming fraction increases with halo mass when the aperture is enlarged.

from gas with a maximum past temperature between $10^{6.5}$ K and $10^{7.5}$ K. In short, the recent extended star formation is being driven by gas that was *never* part of the hot ICM. Instead, the gas was stripped by orbiting satellites (e.g. Puchwein et al. 2010) and the reason why more massive clusters are more likely to have extended star formation is simply because there are more satellites to deposit cold gas in this fashion. However, this extended star formation may be numerical in origin, as it is known that standard

SPH inherently suppresses mixing through, for instance, the Kelvin–Helmholtz instability (e.g. Agertz et al. 2007; Mitchell et al. 2009), which might otherwise dissolve the cold gas clumps.

Colour

In figure 2.13, the $z = 0$ distribution of the $J - K$ BCG colours is plotted for the various simulations and compared to the observations from the X-ray-selected rich galaxy clusters of Stott et al. (2008). The $J - K$ colours of Stott et al. (2008) are observer-frame colours. In order to reliably compare with the simulation rest-frame colours at $z = 0$, the observed colours have been K-corrected to the $z = 0$ rest-frame using the CALC_KCOR IDL routine, which is based upon the analytical approximation of Chilingarian, Melchior & Zolotukhin (2010) and Chilingarian & Zolotukhin (2012). In addition, as Stott et al. (2008) have selected BCGs whose host clusters have $L_X > 10^{44}$ erg s^{-1}, only the BCGs with $M_{500,hse} \geq 10^{14}$ M$_\odot$ (which roughly corresponds to $L_X = 10^{44}$ erg s^{-1} according to figure 2.1) were used. The benefit of using $J - K$ is that it is relatively insensitive to dust attenuation as well as to 'frosting' due to recent low levels of star formation (since it is probing mainly old main sequence stars).

Surprisingly, all the models produce BCGs with $J - K$ colours that are too blue compared to the observations of Stott et al. (2008), by about 0.15 dex on average in the case of the AGN models. One possible reason for this discrepancy is that the simulated BCGs may have unrealistically low metallicities. Indeed, McCarthy et al. (2010) found that the central galaxies of simulated groups in OWLS had too low metallicity by about 0.5 dex (this holds true here as well). As discussed by McCarthy et al., this could plausibly be explained by the adoption of nucleosynthetic yields and/or SNIa rates in the simulations that are too low. Both were chosen based on empirical constraints but have uncertainties at the factor of 2 level each (Wiersma et al. 2009). Boosting the metallicity of the star particles by factors of two and three (in post-processing) has therefore been tried for the AGN 8.0 model when computing the $J - K$ colours. (Note that it is
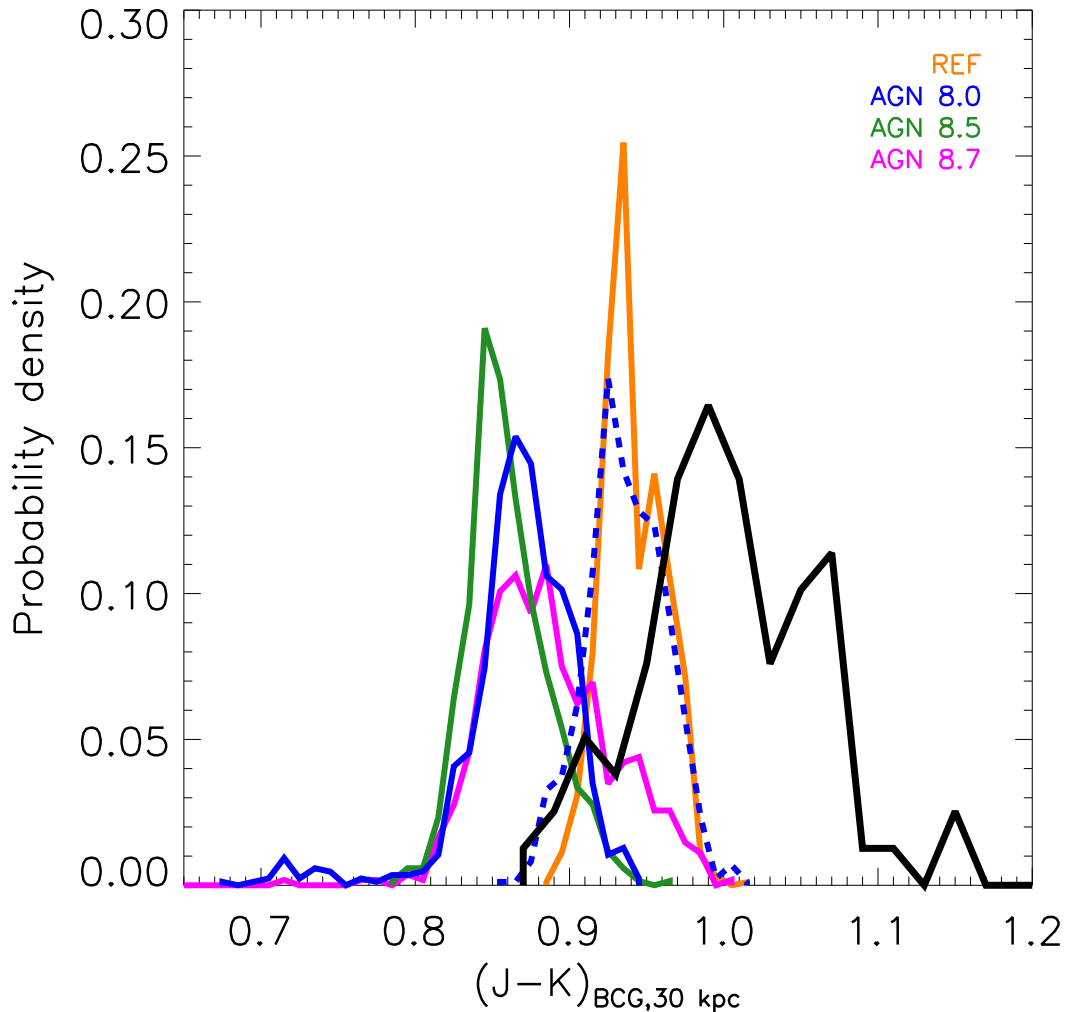
Figure 2.13: Distribution of BCG rest-frame $J - K$ colour at $z = 0$. The thick solid histograms (orange, blue, green and magenta) are for the different simulations while the black one corresponds to the observational data of Stott et al. (2008) with $z \leq 0.25$. The blue dashed histogram corresponds to the AGN 8.0 model when the metallicity of each of the star particles is doubled. All models produce BCGs with $J - K$ colours that are too blue, signalling that the empirical nucleosynthetic yields and/or the SNIa rates adopted in the simulations may be somewhat too low.

the high metallicity of the BCGs in the REF model which makes them somewhat redder than the BCGs in the AGN models, in spite of their higher star formation rates – but as shown by McCarthy et al. 2010, the REF model BCGs have too *high* metallicities compared to observations.) This indeed reduces the level of disagreement: when the stellar metallicities are doubled (blue dashed line), the colours are too blue by ≈ 0.075 dex on average (i.e. the level of disagreement is halved); while when they are tripled,

the peaks of the observed and simulated distributions are roughly in the same position (i.e. the average discrepancy has nearly disappeared), but the observed distribution has a larger tail towards red colours.

It is unclear what the origin of the remaining discrepancy (the tail towards redder colours) is. A variety of stellar population synthesis models have been experimented using the online tool EzGal[6]. Conservatively adopting simple stellar populations, one is unable to produce rest-frame $J - K$ colours $\gtrsim 1.0$ for even fairly extreme choices of the formation redshift (e.g. $z_f = 5$) and super-solar metallicities ($Z = 1.5 \, \mathrm{Z_\odot}$). This suggests that either there is a systematic error inherent to current stellar population synthesis models and/or there is an issue with the observed colours. One possible cause of redder colours could be relatively large amounts of dust either in the BCG itself or along the line of sight, which have not been accounted for.

It is worth noting that the colours have been computed using 30 kpc apertures, which contain extended star formation (see figure 2.12) but reducing the aperture size (to both 10 and 20 kpc) cannot explain the discrepancy. It only shifts the maximum of the distribution by no more than ~ 0.03 dex and does not seem to affect the position of its peak (note that $J - K$ is generally insensitive to recent star formation).

2.5.3 Black hole scalings

In the left panel of figure 2.14, the relation between the mass of the BCG central supermassive BH and M_{500} is plotted for the various simulations which include AGN feedback and compared to the observations of individual strong gravitational lenses of Bandara, Crampton & Simard (2009). As their mass measurements (their M_{200} masses have been converted into M_{500} assuming an NFW profile with a concentration of 4, which yields $M_{500} \approx 0.69 M_{200}$) come from strong lensing, the true M_{500} are used for the simulated systems for this comparison. In the right panel of figure 2.14, the mass of the BCG's central supermassive black hole as a function of the one-dimensional BCG velocity dispersion in a 30 kpc aperture is plotted for the various simulations and

---

[6]http://www.baryons.org/ezgal/
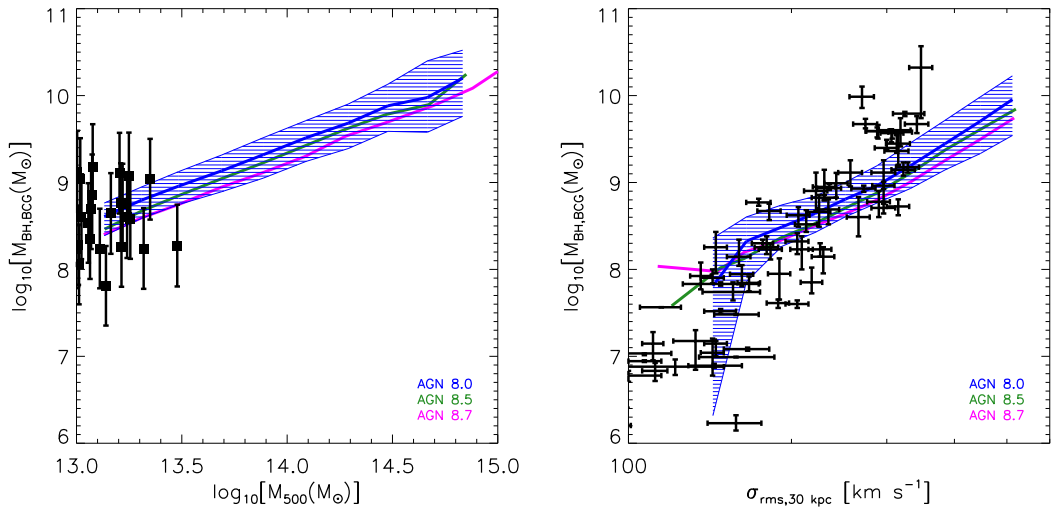
Figure 2.14: Mass of the central supermassive black hole as a function of M_{500} (*left*) and of the root mean square one-dimensional stellar velocity dispersion of the BCG in a 30 kpc aperture (*right*). The filled black circles and squares with error bars correspond to the observational data of McConnell & Ma (2013) and Bandara, Crampton & Simard (2009), respectively. The coloured solid curves represent the median central supermassive black hole mass in bins of M_{500} or stellar velocity dispersion for the different simulations and the blue shaded region encloses 68 per cent of the simulated systems for the AGN 8.0 model. The AGN models broadly reproduce the normalisation of the observed black hole scaling relations.

compared to the recent compilation of the properties of 72 central black holes and their host galaxies of McConnell & Ma (2013).

Both relations are reasonably reproduced by the three AGN feedback models considered here. The fact that the normalisations of the BH scaling relations are well reproduced is not too surprising, as the efficiency of the feedback ϵ was tuned by Booth & Schaye (2009) roughly to match the normalization of $m_{BH} - m_{halo}$ relation at $z = 0$ as well as the present-time cosmic BH density (see also Appendix A). They also showed that the simulations roughly reproduce the normalisation of the $z = 0$ relations between BH mass, stellar mass and velocity dispersion. It was nevertheless worth checking that the calibration which was done using smaller simulations (up to $100 \, h^{-1} \, \mathrm{Mpc}$) with higher mass resolution (up to 8 times higher) remains valid for simulations with larger volume and lower mass resolution. This shows that supermassive BHs are still able to regulate their growth even though the simulation volume has been increased and the mass resolution decreased. Finally, the fact that the three AGN models yield

similar scaling relations means that the heating temperature has not been increased beyond the value at which the supermassive BHs are no longer able to regulate their growth, because the time between heating events exceeds the Salpeter time-scale for Eddington-limited accretion (see Booth & Schaye 2009).

Note that there is an hint of a difference in the slopes of the observed and simulated trends in the right panel of figure 2.14. It is unclear whether this difference is real or not, as a full observational selection and analysis of the simulated systems have not been mimicked. Furthermore, the observed velocity dispersion is generally measured on smaller scales (e.g. inside the galaxy's half-light radius) than can be reliably done with the current simulations, due to their limited resolution.

2.6 Summary and Discussion

A new suite of large volume ($400\ h^{-1}$ Mpc on a side) cosmological hydrodynamical simulations (called cosmo-OWLS, an extension to the OverWhelmingly Large Simulations project; Schaye et al. 2010) which has been specifically designed to aid our understanding of galaxy cluster astrophysics and thereby attempt to minimise the main systematic error in using clusters as probes of cosmology was presented. Five different physical models have been investigated: a non-radiative model (NOCOOL), a model which includes metal-dependent radiative cooling, star formation and stellar feedback (REF) and three models which further include AGN feedback with increasing heating temperatures (from AGN 8.0 with $\Delta T_{heat} = 10^8$ K to AGN 8.7 with $\Delta T_{heat} = 10^{8.7}$ K through AGN 8.5 with $\Delta T_{heat} = 10^{8.5}$ K).

In this first Chapter, detailed comparisons to the observed X-ray, Sunyaev–Zel'dovich effect, optical, and central supermassive black hole properties of local groups and clusters have been made. In order to make like-with-like comparisons, synthetic observations have been produced and observational analysis techniques mimicked. For instance, not only X-ray spectra have been computed for each of the simulated systems and single-temperature plasma models have been fitted to them in order to obtain

metallicity, temperature and density profiles, but also a hydrostatic mass analysis was conducted using the best-fitting temperature and density profiles and the functional forms of Vikhlinin et al. (2006). From these comparisons, one can conclude the following:

1. AGN feedback is essential for reproducing the strong trend in the observed gas fractions with halo mass (figure 2.3) and the high total mass-to-light ratios (i.e. low star formation efficiencies) of groups and clusters (figure 2.10). All the models consistently predict a weak dependence of the star formation efficiency on halo mass, in accordance with the trends observed by Budzynski et al. (2014) (see also Leauthaud et al. 2012) but significantly shallower than the trend derived by Gonzalez et al. (2013).

2. In the *Planck* cosmology, the fiducial AGN model (AGN 8.0) reproduces the global hot gas properties over approximately two orders of magnitude in halo mass (10^{13} M$_\odot \lesssim M_{500} \lesssim 10^{15}$ M$_\odot$), including the observed luminosity–mass, mass–temperature, f_{gas}–mass, Y_X–mass, and SZ flux–mass trends (figures 2.1 to 2.4 and 2.9, respectively). For the first time, the simulations also broadly reproduce the observed scatter. Higher AGN heating temperatures (leading to more violent, bursty feedback when using the OWLS implementation of AGN feedback) lead to under-luminous (and slightly overheated) and under-dense clusters with lower-than-observed SZ fluxes, although this can be mitigated to an extent by appealing to a higher universal baryon fraction (e.g. as in the *WMAP*7 cosmology).

3. Contrary to previous claims, the SZ flux (figure 2.9) and its X-ray analogue Y_X (figure 2.4) *are* found to be sensitive to baryonic physics. In particular, gas ejection by AGN can significantly reduce both quantities (the corresponding increase in temperature resulting from the ejection of low-entropy gas is not sufficient to compensate for the lower gas density if large quantities of gas are ejected). This serves as a warning against blindly applying Y_X, SZ flux, and gas mass (fraction) scalings to low halo masses ($M_{500} \lesssim 10^{14}$ M$_\odot$) and/or high redshifts without an

independent mass check.

4. The fiducial AGN model reproduces not only the global hot gas properties over two decades in mass, but also the observed density and entropy (and therefore also temperature and pressure) radial distributions of the ICM over 1.5 decades in radius, from $0.05 \lesssim r/r_{500} \lesssim 1.5$, over this mass range (figures 2.5 to 2.7). To our knowledge, this is the first time a cosmological hydrodynamical simulation has reproduced the detailed radial distribution of the hot gas, including the central regions.

5. The fiducial AGN model also reproduces the observed large scatter in the central density distribution of the hot gas. Interestingly, the central gas density shows no evidence for significant bimodality (figure 2.8).

6. AGN feedback is essential not only to lower the overall star formation efficiencies of groups and clusters, but also to reduce the dominance of the brightest cluster galaxy (BCG) with respect to the satellite population, and to prevent significant present-day star formation (figures 2.10 to 2.12).

7. While successfully shutting off cooling in the very central regions of the BCG in accordance with observations, the simulated BCGs have low levels of spatially-extended star formation (figure 2.12), which is being driven by recently deposited cold gas (ISM) from ram pressure-stripped satellite galaxies. This trend may be at least partly numerical in origin, due to suppression of mixing (e.g. via the Kelvin–Helmholtz instability) in standard SPH.

8. The simulated BCGs, while having approximately the correct stellar mass and central star-forming fraction, are too blue in $J - K$ (by about 0.15 dex on average; figure 2.13) compared to observed local BCGs (Stott et al. 2008). This discrepancy may be due to adopting incorrect yields and/or SNIa rates in the simulations (which are based on empirical constraints that have uncertainties at the factor of ≈ 2 level). Tripling the stellar metallicities for the AGN 8.0 model brings the position of the peak of the distribution into agreement with the peak of the observed distribution.

9. The simulations broadly reproduce the observed black hole mass – halo mass – velocity dispersion relations (figure 2.14). The feedback efficiency was calibrated by Booth & Schaye (2009) to approximately match the normalisation of these relations in higher resolution simulations and at lower halo masses. The agreement is shown here to continue to hold at much larger masses and somewhat lower resolution. Neither the black hole feedback efficiency nor the accretion model were tuned in any way to reproduce the properties of galaxy groups and clusters.

The success of the fiducial AGN model in reproducing the detailed hot gas properties over 1.5 decades in radius and the global hot gas and global optical properties over two decades in halo mass, as well as the system-to-system scatter in the X-ray/SZ properties, is an important step forward. The production of reasonably realistic simulated *populations*, as well as models that bracket the observations, opens the door to producing synthetic cluster surveys to aid the astrophysical and cosmological interpretation of up-coming/on-going cluster surveys and to help quantify the important effects of observational selection. cosmo-OWLS is being used for precisely this purpose (see Chapters 4, 5 and 6).

The predicted hot gas and stellar properties are highly model dependent. Indeed, even for a fixed sub-grid AGN feedback efficiency, i.e. for models that inject a fixed amount of energy per unit of accreted gas mass, the effective efficiency of the AGN feedback is sensitive to the way in which the energy is injected. A higher heating temperature, which corresponds to less frequent but more energetic outbursts, results in more efficient feedback. As discussed in Section 2.2.1, it was anticipated that using increased heating temperatures may be necessary to avoid overcooling in the most massive clusters, where $T_{\mathrm{vir}} \sim 10^8$ K. However, increasing the heating temperature had a large effect on the *progenitors* of these (massive galaxies and low-mass groups at $z \sim 2$) which in turn had important knock-on effects for the $z = 0$ population of massive clusters (most importantly significantly reduced gas fractions). The complicated merger history of clusters makes it difficult to anticipate these results. In any case, the demonstrated sensitivity to model parameters means that the models must continue to be

challenged with new observables (e.g. detailed properties of the satellite galaxy pop-
ulation, which have not been explored here) and over a wider range of masses and
redshifts than has been considered here. In addition, quantitative comparisons of the
simulations to the observations (rather than the rough 'by eye' evaluations presented
here) require careful consideration of observational selection effects, particularly in the
group regime.

From the comparisons made thus far (both here and in McCarthy et al. 2010, 2011),
the total mass-to-light ratio (star formation efficiency) appears to be the best discrim-
inator for distinguishing between the impact of different sources of feedback (stellar
feedback versus AGN). However, the detailed hot gas properties are more sensitive to
the nature of the AGN feedback than are the stellar properties or BH scaling relations.
In particular, given that the fiducial model reproduces the observations significantly
better than models with higher heating temperatures, this suggests that the AGN feed-
back mechanism in real clusters is/was similarly violent and bursty as in this model.
An independent test of the models will therefore be to compare to the demographics
of the observed AGN population (e.g. 'radio' versus 'quasar' mode duty cycles and
luminosity functions and their dependencies on redshift and environment).

Chapter 3

Scatter and evolution of the hot gas properties of a realistic population of simulated galaxy clusters

This Chapter uses the results of the cluster analysis code developed by Ian McCarthy for Chapter 2. Ian McCarthy also provided the best-fitting temperature dependence of the cooling function Λ for the soft X-ray band. Amandine Le Brun fitted the scaling relations, computed the self-similar expectations and gathered the observational constraints on scatter.

3.1 Introduction

Galaxy clusters have long been proposed as tools for measuring fundamental cosmological parameters, such as the overall matter density of the universe, the amplitude of the matter power spectrum, as well as the evolution of dark energy (for recent reviews, see Voit 2005; Allen, Evrard & Mantz 2011; Kravtsov & Borgani 2012; Weinberg et al. 2013). However, they can only be used as probes of cosmology (and galaxy formation physics alike), if the observations and their processing meet a few key requirements

(e.g. Allen, Evrard & Mantz 2011; Pierre et al. 2011): (i) the cluster masses must be accurately deduced from the observed cluster physical properties, (ii) the scatter and covariance of the adopted mass–observable relation must be properly included in the cosmological modelling, and (iii) a detailed knowledge of the selection function of the survey is necessary. Over the past two decades, it has become commonplace to use models and/or simulations to calibrate mass–observable relations and assess their scatter and biases (e.g. Kravtsov, Vikhlinin & Nagai 2006; Nagai, Vikhlinin & Kravtsov 2007). (Little attention has been devoted to the important issue of selection so far, however.)

The ongoing and upcoming galaxy cluster surveys, such as *eRosita* (Merloni et al. 2012), *Euclid* (Laureijs et al. 2011), XXL (Pierre et al. 2011), XCS (Romer et al. 2001) and the Dark Energy Survey (The Dark Energy Survey Collaboration 2005) have now transitioned into the 'era of precision cosmology' due to their increased size and depth. The limiting systematics are now due to our partial knowledge of galaxy formation physics and the impact of selection effects. Additional progress will come from the confrontation of increasingly realistic synthetic surveys with the observations.

Since Chapter 2 has demonstrated that the simulations that include AGN feedback have produced a realistic population of galaxy groups and clusters, which roughly reproduce the median trend and scatter of a wide range of observed low-redshift physical properties, this Chapter will conduct a study of the scatter and evolution of the hot gas properties of galaxy groups and clusters as a function of the important non-gravitational physics of galaxy formation using a state-of-the-art large-volume cosmological hydrodynamical simulation. This Chapter is organised as follows. The cosmo-OWLS simulation suite used here is briefly introduced in Section 3.2 and the self-similar theory is summarised in Section 3.3. The fitting procedures used for the mass–observable scaling relations and the scatter about them are then presented in Section 3.4, followed by the evolution of the mass slopes of the mass–observables in Section 3.5 and of the normalisation in Section 3.6, as well as by an investigation of the scatter about the median scaling relations in Section 3.7. Finally, the main findings are discussed and summarised in Section 3.8.

Throughout the Chapter, masses, luminosities, temperatures, integrated Sunyaev–Zel'dovich signal and X-ray analogues of the integrated Sunyaev–Zel'dovich signal are quoted in physical $M_\odot$, erg s^{-1}, keV, Mpc^2 and $M_\odot$ keV, respectively; ln denotes natural logarithm, while $\log_{10}$ corresponds to decimal logarithm.

3.2   Simulations

Four of the physical models from the cosmo-OWLS suite of cosmological simulations described in detail in Chapter 2 (see also McCarthy et al. 2014; van Daalen et al. 2014; Velliscig et al. 2014) are employed. The reasons for keeping only four of the models (NOCOOL, REF, AGN 8.0 and 8.5) are mainly the following: (i) REF, AGN 8.0 and 8.5 were shown in Chapter 2 to be the most compatible with the gas properties of low-redshift groups and clusters, whereas (ii) AGN 8.7 and NOCOOL are incompatible with these observational constraints, but (iii) the latter is included as a baseline model for the comparisons since its behaviour is expected to be close to self-similar. The cosmo-OWLS simulations constitute an extension to the OverWhelmingly Large Simulation project (OWLS; Schaye et al. 2010) which were conceived with cluster cosmology in mind and consist of large volume ($400\ h^{-1}$ Mpc on a side) periodic box simulations with 2×1024^3 particles with updated initial conditions derived from the *Planck* data[1] (Planck 2013 Results XVI) $\{\Omega_m, \Omega_b, \Omega_\Lambda, \sigma_8, n_s, h\}$ = {0.3175, 0.0490, 0.6825, 0.834, 0.9624, 0.6711}. This yields dark matter and (initial) baryon particle masses of $\approx 4.44 \times 10^9\ h^{-1}\ M_\odot$ and $\approx 8.12 \times 10^8\ h^{-1}\ M_\odot$, respectively. The gravitational softening of the runs presented here is fixed to $4\ h^{-1}$ kpc (in physical coordinates below $z = 3$ and in comoving coordinates at higher redshifts). Note that $N_{ngb} = 48$ neighbouring particles are used for computing the physical quantities using smoothed particle hydrodynamics (SPH) interpolation and the minimum SPH smoothing length is set to one tenth of the gravitational softening. The extension to larger volumes is fun-

---

[1]Simulations using initial conditions derived from the 7-year *Wilkinson Microwave Anisotropy Probe* (*WMAP*) data were also run. Only results from some of the *Planck* cosmology ones will be presented here, but any notable differences with the equivalent runs in the *WMAP*7 cosmology will be commented upon.

damental for the present study as the original runs (which were $100\ h^{-1}$ Mpc on a side at most) were too small for being suited to a study of the (scatter and evolution of) the physical properties of massive groups and clusters as they have very low space densities (systems with $M_{500} \gtrsim 10^{14}\ M_\odot$ have a comoving space density of $\sim 10^{-5}$ Mpc^{-3}; e.g. Jenkins et al. 2001).

The simulations were carried out with a version of the Lagrangian TreePM-SPH code GADGET3 (Springel 2005) and four of the five physical models presented in Chapter 2 were used:

- **NOCOOL :** A standard non-radiative model. It also includes net heating from the Haardt & Madau (2001) X-ray and ultra-violet photoionising background, whose effects on the intracluster medium (ICM) are negligible.

- **REF :** This model also includes prescriptions for metal-dependent radiative cooling (Wiersma, Schaye & Smith 2009), star formation (Schaye & Dalla Vecchia 2008), stellar evolution, mass loss and chemical enrichment (Wiersma et al. 2009) and kinetic stellar feedback (Dalla Vecchia & Schaye 2008) from both Type II and Ia supernovae and Asymptotic Giant Branch stars.

- **AGN 8.0 and 8.5:** They further include a prescription for supermassive black hole growth (through both Eddington-limited Bondi–Hoyle–Lyttleton accretion and mergers with other black holes) and AGN feedback (Booth & Schaye 2009, which is a modified version of the model originally developed by Springel, Di Matteo & Hernquist 2005). The black holes accumulate the feedback energy until they can heat neighbouring gas particles by a pre-determined amount ΔT_{heat}. As in Booth & Schaye (2009), 1.5 per cent of the rest-mass energy of the gas which is accreted on to the supermassive black holes is used for the feedback. This results in a satisfactory match to the normalisation of the black hole scaling relations (Booth & Schaye 2009; see also Section 2.5.3) which is independent of the exact value of ΔT_{heat}. The two AGN models used here only differ by their value of ΔT_{heat}, which is the most important parameter of the AGN feedback model in terms of the gas-phase properties of the resulting simulated population

of groups and clusters (McCarthy et al. 2011; see also Sections 2.3 and 2.4). It is set to $\Delta T_{heat} = 10^8$ K for AGN 8.0 and $\Delta T_{heat} = 3 \times 10^8$ K for AGN 8.5. Note that since the same quantity of gas is being heated in these models, more time is required for the black holes to accrete a sufficient amount of gas for heating the adjacent gas to a higher temperature. Hence, increased heating temperatures result into more episodic and more violent feedback episodes.

Table 3.1 provides a list of the runs used here and the sub-grid physics that they include.

Haloes are identified and their spherical overdensity masses are computed as described in Subsection 2.2.2. The Sunyaev–Zel'dovich signal is characterised by the value of its spherically integrated Compton parameter $d_A^2 Y_{500} = (\sigma_T/m_e c^2) \int P dV$ where d_A is the angular diameter distance, σ_T the Thomson cross-section, c the speed of light, m_e the electron rest mass, $P = n_e k_B T_e$ the electron pressure and the integration is done over the sphere of radius r_{500}.

Note that contrary to what was done in the previous Chapter, in this Chapter, true halo masses (as opposed to halo masses computed under the assumption of hydrostatic equilibrium) are used and that the X-ray luminosities, spectral temperatures, gas masses and integrated Sunyaev–Zel'dovich signals were computed within the true r_{500} aperture (as opposed to within $r_{500,hse}$). Yet, the spectral temperatures and X-ray luminosities were computed using the synthetic X-ray methodology presented in Section 2.2.2. The rationale behind these choices is that the aim is to elucidate the relations between the hot gas observables and true halo mass, since those are useful for: (i) calibrating the mass–observable relations whose use is of paramount importance when doing (precision) cosmology with galaxy clusters, and (ii) making large synthetic surveys by applying template methods to large dark matter-only simulations (e.g. Bode et al. 2007; Sehgal et al. 2007, 2010).

These models have been compared to a wide range of observational data in both Chapter 2 and McCarthy et al. (2014). In Chapter 2, the focus was on the comparison to low-redshift properties such as X-ray luminosities and temperatures, gas mass fractions, entropy and density profiles, integrated Sunyaev–Zel'dovich signal, I-band mass-to-light

ratio, dominance of the brightest cluster galaxy and central black hole masses; reaching the conclusion that the fiducial AGN model (AGN 8.0) can produce a realistic population of galaxy groups and clusters, broadly reproducing both the median trend and, for the first time, the scatter in physical properties over approximately two decades in mass (10^{13} M$_\odot \lesssim M_{500} \lesssim 10^{15}$ M$_\odot$) and 1.5 decades in radius ($0.05 \lesssim r/r_{500} \lesssim 1.5$); whereas in McCarthy et al. (2014), the sensitivity of the thermal Sunyaev–Zel'dovich power spectrum to important non-gravitational physics was explored and it was found that while the signal on small and intermediate scales is highly sensitive to the included galaxy formation physics, the signal on large scales is only mildly affected.

Simulation	UV/X-ray background	Cooling	Star formation	SN feedback	AGN feedback	ΔT_{heat}
NOCOOL	Yes	No	No	No	No	...
REF	Yes	Yes	Yes	Yes	No	...
AGN 8.0	Yes	Yes	Yes	Yes	Yes	$10^{8.0}$ K
AGN 8.5	Yes	Yes	Yes	Yes	Yes	$10^{8.5}$ K

Table 3.1: cosmo-OWLS runs presented here and their included sub-grid physics. Each model has been run in both the *WMAP7* and *Planck* cosmologies.

3.3 Self-similar scalings

Although far too simple to capture all the complexities of galaxy cluster formation, the self-similar model for cluster formation is useful as a baseline for the interpretation of simulations and observations alike. It assumes that galaxy cluster properties and their correlations are determined by gravity alone and that clusters are virialised. As gravity is scale free, galaxy clusters are thus expected to be self-similar in the absence of important non-gravitational physical processes, that is, that all galaxy cluster properties only depend upon the cluster mass, and more massive galaxy clusters are scaled versions of less massive ones with a scaling factor that depends only upon the mass ratios[2] (e.g. White & Rees 1978; Kaiser 1986; Voit 2005; Borgani & Kravtsov 2011; Kravtsov & Borgani 2012). If one defines the cluster masses (denoted as M_Δ) as being the mass contained within a region that encloses a mean overdensity $\Delta \rho_{crit}$, then, under the assumption of self-similarity, one can predict the redshift evolution (which is in this case only due to the increasing mean density of the Universe) and the slope of a given mass-observable relation. The redshift evolution comes from the evolution of the critical density for closure:

$$\rho_{crit}(z) \equiv \frac{3H(z)^2}{8\pi G} = E(z)^2 \frac{3H_0^2}{8\pi G} = E(z)^2 \rho_{crit}(z=0) \tag{3.1}$$

where

$$E(z) \equiv \frac{H(z)}{H_0} = \sqrt{\Omega_m(1+z)^3 + \Omega_\Lambda} \tag{3.2}$$

gives the redshift evolution of the Hubble parameter $H(z)$ in a flat ΛCDM Universe. For instance, since

$$M_\Delta \propto \Delta \rho_{crit}(z) r_\Delta^3 \tag{3.3}$$

by definition, the cluster size will scale as

$$r_\Delta \propto M_\Delta^{1/3} E(z)^{-2/3}. \tag{3.4}$$

---

[2]Yet, even in the dark matter only case, haloes are already not strictly self-similar as lower mass haloes, which collapsed at earlier times, are more concentrated.

Gas is heated by gravitational infall into the cluster potential well, eventually settling and achieving virial equilibrium within that potential (as explained in e.g. Voit 2005 and Borgani & Kravtsov 2011). The gas is then expected to have a temperature close to the virial temperature:

$$k_B T_\Delta \equiv \frac{1}{2}\Phi = \frac{GM_\Delta \mu m_p}{2r_\Delta} \tag{3.5}$$

where k_B is the Boltzmann constant and μ is the mean molecular weight. Thus, the self-similar temperature–total mass relation can be obtained by combining equations (3.4) and (3.5) and is as follows

$$T_\Delta \propto M_\Delta^{2/3} E(z)^{2/3}. \tag{3.6}$$

Similarly, the bolometric X-ray emission of massive clusters is dominated by thermal bremsstrahlung, implying that their bolometric X-ray luminosity scales as $L_X^{bol} \propto \rho^2 \Lambda(T) r_\Delta^3 \propto \rho^2 T^{1/2} r_\Delta^3$ as the cooling function $\Lambda(T) \propto T^{1/2}$ in the bolometric case (e.g. Sarazin 1986; Peterson & Fabian 2006), which combined with equations (3.4) and (3.6) gives the self-similar bolometric X-ray luminosity–total mass and bolometric X-ray luminosity–temperature relations:

$$L_{X,\Delta}^{bol} \propto M_\Delta^{4/3} E(z)^{7/3} \tag{3.7}$$

and

$$L_{X,\Delta}^{bol} \propto T_\Delta^2 E(z). \tag{3.8}$$

However, what is measured by X-ray observations is the X-ray luminosity in a relatively narrow observer frame band (usually the soft X-ray 0.5–2.0 keV band) which is then converted into the X-ray luminosity in the same band for the rest-frame of the source. Hence, the soft X-ray luminosity has been computed in the 0.5–2.0 keV rest-frame band for the simulated groups and clusters. As the temperature dependence of the cooling function depends on the energy band considered (but not metallicity dependent for X-ray emitting hot gas), $\Lambda(T, Z)$ has been computed for the rest-frame

0.5–2.0 keV band and metallicity equal to one third of solar[3] using the Astrophysical Plasma Emission Code (APEC; Smith et al. 2001) with updated atomic data and calculations from the AtomDB v2.0.2 (Foster et al. 2012), a temperature power-law was fitted to it and $\Lambda \propto T^{\sim -1/4}$ was obtained. The soft X-ray luminosity thus scales as $L_X^{soft} \propto \rho^2 \Lambda(T, Z) r_\Delta^3 \propto \rho^2 T^{\sim -1/4} r_\Delta^3$, which combined with equations (3.4) and (3.6) gives the self-similar soft X-ray luminosity–total mass and soft X-ray luminosity–temperature relations:

$$L_{X,\Delta}^{soft} \propto M_\Delta^{5/6} E(z)^{11/6} \tag{3.9}$$

and

$$L_{X,\Delta}^{soft} \propto T_\Delta^{5/4} E(z). \tag{3.10}$$

Hereafter, the soft X-ray luminosity L_X^{soft} will be simply denoted as L_X.

Finally, $Y_{SZ,\Delta} \propto Y_{X,\Delta} \equiv M_{gas,\Delta} T_\Delta \propto M_\Delta T_\Delta$ assuming a constant gas fraction. Thus, the self-similar integrated Sunyaev–Zel'dovich signal–total mass and X-ray analogue of the integrated Sunyaev–Zel'dovich signal–total mass relations follow from equation (3.6):

$$Y_{X/SZ,\Delta} \propto M_\Delta^{5/3} E(z)^{2/3}. \tag{3.11}$$

With the launch of the first X-ray telescopes, such as the Einstein Observatory, EXOSAT and ROSAT, in the 1980s-1990s, it was quickly realised that the results of the self-similar model were incompatible with the observations of, among others, the X-ray luminosity–temperature relation (e.g. Mushotzky 1984; Edge & Stewart 1991; Markevitch 1998; Arnaud & Evrard 1999; Lumb et al. 2004; Osmond & Ponman 2004; Pratt et al. 2009; Hilton et al. 2012), which was found to be significantly steeper than the self-similar expectation ($L_X \propto T^\alpha$ with $\alpha \simeq 2.5 - 3$ for clusters and likely even steeper for groups). It led to the obvious conclusion that some non-gravitational processes, most likely connected to galaxy formation, must be breaking the self-similarity by introducing some physical scales (see for instance Evrard & Henry 1991; Kaiser 1991 for the first solutions proposed to this puzzle). What is still less clear is how strongly the evolution of the properties of 'real' clusters deviate from the self-similar

---

[3] The same result was obtained for $Z = 0\, Z_\odot$ and $Z = Z_\odot$.

prediction, as well as whether or not the self-similarity in mass still holds at higher redshift. Furthermore, how selection effects impact the evolution and slope of the inferred scaling relations is still mostly unknown (see e.g. Stanek et al. 2006; Pacaud et al. 2007; Nord et al. 2008 for first attempts at quantifying the repercussions of selection effects on scaling relations). For these reasons, self-similar evolution is still commonly adopted in cosmological analyses (e.g. Allen et al. 2008; Vikhlinin et al. 2009b; Planck 2013 Results XX; Mantz et al. 2014).

3.4 Fitting of relations

In order to obtain a value for the median observable and the scatter at fixed total mass about the median relation as a function of total mass and redshift as well as simple functional forms for their total mass and redshift dependencies (which are extremely useful for both calibrating observable–mass relation and for using them as templates for making large synthetic surveys from dark matter only simulations), log-normal distributions were fitted in a few mass bins at several redshifts. Specifically, for each of the scaling relations studied here (i.e. $T - M$, $L_X - M$, $M_{gas} - M$, $Y_X - M$ and $Y_{SZ} - M$) and each of the physical models presented in Section 3.2, the median scaling relations at nine different redshifts ($z = 0, 0.125, 0.25, 0.375, 0.5, 0.75, 1.0, 1.25$ and 1.5) were obtained by fitting a spline to the median observable–total mass relation computed in ten equally logarithmically spaced mass bins in the range $13.0 \leq \log_{10} M_{500} \leq 15.5$. The best-fitting spline is used to factor out the median relation when fitting a log-normal distribution to the distribution of Y (hereafter Y denotes one of T, L_X, M_{gas}, Y_X and Y_{SZ}) in four bins of M_{500} (chosen to be $13.0 \leq \log_{10}[M_{500}(\mathbf{M}_\odot)] < 13.5$, $13.5 \leq \log_{10}[M_{500}(\mathbf{M}_\odot)] < 14.0$, $14.0 \leq \log_{10}[M_{500}(\mathbf{M}_\odot)] < 14.5$ and $14.5 \leq \log_{10}[M_{500}(\mathbf{M}_\odot)] < 15.5$; hereafter denoted as mass bin j with j going from 1 to 4). More specifically, in each of the four mass bins j, a log-normal distribution is fitted to the histogram of Y/Y_{spline} where Y_{spline} is the value of Y obtained for M_{500} using

the best-fitting spline, which is of the following form:

$$P(X) = \frac{binsize}{X\sqrt{2\pi\sigma^2}} \exp\left(-\frac{(\ln X - \mu)^2}{2\sigma^2}\right), \qquad (3.12)$$

with μ kept fixed to 0 (i.e. the central value of the histogram of $\ln Y$ is imposed to be equal to the value of Y_{spline} corresponding to the median value of M_{500} in mass bin j) using the MPFIT least-square minimisation package in IDL (Markwardt 2009). The $binsize$ prefactor is needed for turning the log-normal probability distribution function into an histogram whose bin width is equal to $binsize$. In order to limit the impact of potential outliers when setting the $binsize$ parameter for each pair of scaling relation and mass bin, it is taken to be equal to the range of Y/Y_{spline} values that includes 90 per cent of the simulated systems contained in the mass bin divided by ten. The root mean square dispersion about the median scaling relation in mass bin j was also computed as a function of mass and redshift, and was defined as follows:

$$\sigma_{j,rms}(z) = \sqrt{\frac{\sum_{i=1}^{N_j}\left(\ln Y_i(z) - \ln Y_{spline,i}(z)\right)^2}{N_j(z)}} \qquad (3.13)$$

where $N_j(z)$ is the number of systems in mass bin j at redshift z and $Y_{spline,i}(z)$ is the value of $Y(z)$ obtained for $M_{500,i}(z)$ using the best-fitting spline. Since the trends obtained using the root mean square dispersion are nearly identical to the ones obtained with the log-normal scatter (the only noticeable difference is that the root mean square dispersion tends to be slightly bigger than the log-normal scatter at fixed physical model, scaling relation, mass and redshift), in the remainder of the Chapter, only the results obtained for the log-normal scatter are presented.

From the above procedure, a median scaling relation and the log-normal scatter about it (in the observable at fixed mass) are obtained for each pair of scaling relations and physical models as a function of mass and redshift. An evolving power-law of the form:

$$Y = 10^A E(z)^\alpha \left(\frac{M_{500}}{10^{14}\,\mathbf{M}_\odot}\right)^\beta, \qquad (3.14)$$

an evolving broken power-law of the form:

$$Y = 10^{A'} E(z)^{\alpha'} \left(\frac{M_{500}}{10^{14} \, \mathbf{M}_\odot} \right)^{\epsilon'} \tag{3.15}$$

where

$$\epsilon' = \begin{cases} \beta' & \text{if } M_{500} \leq 10^{14} \, \mathbf{M}_\odot \\ \gamma' & \text{if } M_{500} > 10^{14} \, \mathbf{M}_\odot, \end{cases} \tag{3.16}$$

and finally an evolving broken power-law with a redshift dependent low-mass power-law index of the form:

$$Y = 10^{A''} E(z)^{\alpha''} \left(\frac{M_{500}}{10^{14} \, \mathbf{M}_\odot} \right)^{\epsilon''} \tag{3.17}$$

where

$$\epsilon'' = \begin{cases} \beta'' + \delta'' E(z) & \text{if } M_{500} \leq 10^{14} \, \mathbf{M}_\odot \\ \gamma'' & \text{if } M_{500} > 10^{14} \, \mathbf{M}_\odot \end{cases} \tag{3.18}$$

can then be fitted to the median relation and the log-normal scatter about it as a function of both mass and redshift. The fitting is done using an ordinary least-square minimisation procedure. Note that here χ^2 is defined as

$$\chi^2 \equiv \sum_{i=1}^{N_{bin}} (Y_i - Y_{bf,i})^2 \tag{3.19}$$

where $Y_{bf,i}$ is given by one of the following equations: (3.14), or (3.15) or (3.17); as no errors can straightforwardly be assigned to the variables[4]. For the same reason, no errors are quoted for the best-fitting parameters. The results of the evolving power-law and broken power-law with an evolving low-mass power-law index fitting for the AGN 8.0 simulation are presented in Tables 3.2 and 3.3, respectively[5]. Hereafter, β, ϵ' and ϵ'' are called mass slope.

---

[4]Therefore, the values of χ^2 should *only* be used to compare the respective quality of the fits for the evolving power law and broken power-law models at fixed scaling relation and physical model, as their differences and/or ratios are otherwise meaningless.

[5]The results for the other simulations are given in Appendix C.

Scaling relation	Median or scatter	A	α	β	χ^2	Number of degrees of freedom
$T_{spec} - M_{500}$	Median	0.250	0.385	0.574	0.069	21
$T_{spec} - M_{500}$	Scatter	−0.882	−0.342	−0.152	0.403	21
$L_{0.5-2.0keV} - M_{500}$	Median	43.004	2.988	1.686	0.345	21
$L_{0.5-2.0keV} - M_{500}$	Scatter	−0.442	−0.721	0.031	0.549	21
$M_{gas,500} - M_{500}$	Median	12.890	0.373	1.263	0.061	21
$M_{gas,500} - M_{500}$	Scatter	−1.001	−0.369	−0.326	0.286	21
$Y_{X,500} - M_{500}$	Median	13.180	0.683	1.825	0.127	21
$Y_{X,500} - M_{500}$	Scatter	−0.799	−0.304	−0.106	1.082	21
$d_A^2 Y_{500} - M_{500}$	Median	−5.712	0.732	1.846	0.072	21
$d_A^2 Y_{500} - M_{500}$	Scatter	−0.904	0.149	−0.167	0.709	21

Table 3.2: Results of the evolving power-law fitting (given by equation 3.14) to both the median relation and the log-normal scatter about it for the AGN 8.0 simulation. The scatter is the log-normal scatter in the natural logarithm of the Y variable. The results for the other simulations are given in Appendix C.

Scaling relation	Median or scatter	A''	α''	β''	γ''	δ''	χ^2	Number of degrees of freedom
$T_{spec} - M_{500}$	Median	0.300	0.315	0.851	0.471	−0.082	0.016	19
$T_{spec} - M_{500}$	Scatter	−0.999	−0.080	−1.026	0.059	0.381	0.152	19
$L_{0.5-2.0keV} - M_{500}$	Median	43.062	2.725	2.423	1.619	−0.443	0.216	19
$L_{0.5-2.0keV} - M_{500}$	Scatter	−0.515	−0.804	0.050	0.230	−0.231	0.230	19
$M_{gas,500} - M_{500}$	Median	12.940	0.234	1.700	1.179	−0.214	0.012	19
$M_{gas,500} - M_{500}$	Scatter	−1.014	−0.262	−0.600	−0.324	0.190	0.260	19
$Y_{X,500} - M_{500}$	Median	13.260	0.492	2.449	1.685	−0.283	0.010	19
$Y_{X,500} - M_{500}$	Scatter	−0.987	0.106	−1.487	0.235	0.594	0.435	19
$d_A^2 Y_{500} - M_{500}$	Median	−5.658	0.653	2.153	1.737	−0.097	0.013	19
$d_A^2 Y_{500} - M_{500}$	Scatter	−1.045	0.514	−1.334	0.074	0.555	0.334	19

Table 3.3: Results of the evolving broken power-law fitting (given by equation 3.17) to both the median relation and the log-normal scatter about it for the AGN 8.0 simulation. The scatter is the log-normal scatter in the natural logarithm of the Y variable. The results for the other simulations are given in Appendix C.

Self-similar theory predicts that all the scaling relations should be described by evolving power-laws of the form given by equation (3.14). However, it is well-known that most of the observed scaling relations in the local Universe show deviations from a single power-law and are ill-described by evolving power-laws. In fact, even evolving broken power-laws (as in equation 3.15) do not fully encapsulate the evolution of our simulated clusters as figure 3.1 shows. The fact that only the low-mass power-law index depends upon redshift, as well as the functional form for its redshift dependence, were inferred empirically by looking at the redshift dependencies of β' and γ' (see figure 3.3 and corresponding text). Note that in all three cases (evolving power-law given by equation 3.14, evolving broken power-law given by equation 3.15 and evolving broken power-law with redshift dependent low-mass power-law index given by equation 3.17), the total mass pivot point was not fitted for, but rather held fixed to 10^{14} M$_\odot$. There were two main reasons for this: all the scaling relations seem to break at $M_{500} \sim 10^{14}$ M$_\odot$ for all the radiative models, and having a fixed pivot point renders comparisons between physical models and fitting formulae straightforward.

It is worth mentioning that the redshift dependencies of the median relations, of the scatter about them and of the low-mass power-law index were also modelled using powers of $1 + z$ instead of $E(z)$ in equations (3.14), (3.15) and (3.17) as is sometimes done in the literature for simulations and observations alike (e.g. Ettori et al. 2004; Maughan et al. 2006; Kay et al. 2007; Sehgal et al. 2011; Lin et al. 2012) but this generally leads to poorer fits (especially in the evolving power-law case) and is less straightforwardly compared to self-similar expectations. For these reasons, the results obtained using powers of $1 + z$ will not be discussed any further.

Figure 3.1 shows the reconstruction of the scaling relations at various redshifts for two of the variables studied here: namely, the gas mass (left panel) and the soft X-ray luminosity (right panel), which are two representative variables. On each subpanel, the black dots correspond to the individual simulated groups and clusters with $\log_{10}[M_{500}(\text{M}_\odot)] \geq 13.0$ taken from the AGN 8.0 model, the solid blue, green and red lines respectively correspond to the best-fitting evolving power-law (given by equation 3.14), broken power-law (given by equation 3.15) and broken power-law with a

redshift dependent low-mass power-law index (given by equation 3.17) to the median gas mass (left panel) or soft X-ray luminosity (right panel) in bins of mass and redshift and the dashed red lines correspond to the best-fitting evolving broken power-law with a redshift dependent low-mass power-law index to the log-normal scatter in bins of mass and redshift. For both observables and for $z \leq 1.5$, the median relations and the scatter about them are reasonably well modelled by evolving broken power-laws with redshift dependent low-mass power-law indices of the form given by equation (3.17), whereas power-laws and broken power-laws of the form given by equations (3.14) and (3.15) fail to reproduce the median relations especially at the low-mass end.
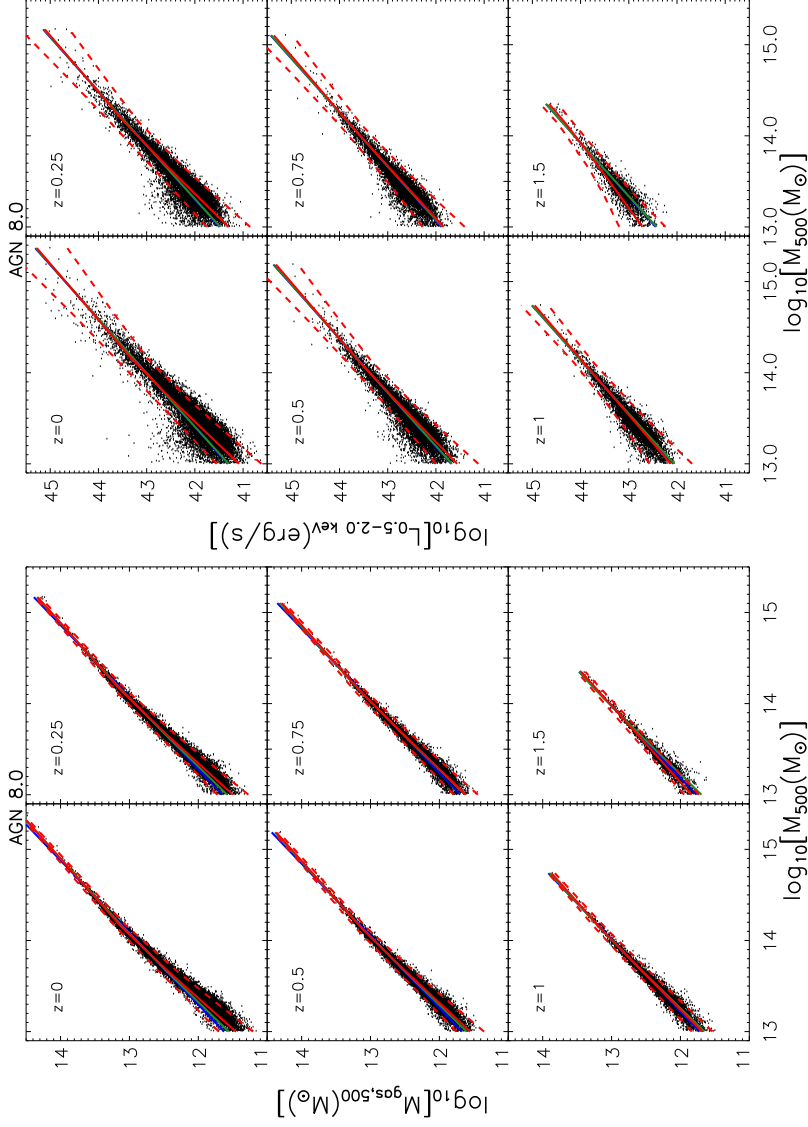
Figure 3.1: Reconstructed gas mass–M_{500} (*left*) and soft X-ray luminosity–M_{500} (*right*) relations at six redshifts ($z = 0$, $z = 0.25$, $z = 0.5$, $z = 0.75$, $z = 1.0$ and $z = 1.5$ from *top left* to *bottom right*). The soft X-ray luminosity refers to the 0.5–2.0 keV band (rest-frame) and is computed within r_{500}. On each subpanel, the black dots correspond to the individual simulated groups and clusters with $\log_{10}[M_{500}(\mathrm{M}_\odot)] \geq 13.0$ taken from the AGN 8.0 model, the solid blue, green and red lines respectively correspond to the best-fitting evolving power-law, broken power-law and broken power-law with a redshift dependent low-mass power-law index to the median gas mass (*left*) or soft X-ray luminosity (*right*) in bins of mass and redshift and the dashed red lines correspond to the best-fitting evolving broken power-law with a redshift dependent low-mass power-law index to the log-normal scatter in bins of mass and redshift. The median relations and the scatter about them are reasonably well modelled by evolving broken power-laws with redshift dependent low-mass power-law indices of the form given by equation (3.17), whereas power-laws and broken power-laws of the form given by equations (3.14) and (3.15) fail to reproduce the median relations especially at the low-mass end.

3.5 Evolution of mass slope

In the context of the self-similar evolution theory, no evolution of the mass slope is expected. It is supposed to be a constant number which can be predicted using only Newtonian gravity and the assumption that the gas is in virial equilibrium (see Section 3.3). Any evolution or deviation at any redshift from the predicted mass slope signals that either some non-gravitational physics is at play, or that the gas is not virialised (or both).

Figures 3.2 and 3.3 show the evolution of the mass slopes from $z = 0$ to $z = 1.5$ for the total mass–temperature (for both mass-weighted and X-ray temperature), X-ray luminosity–total mass, gas mass–total mass, X-ray analogue of the integrated Sunyaev–Zel'dovich signal–total mass and the integrated Sunyaev–Zel'dovich signal–total mass scaling relations (from top left to bottom right) for each of the four physical models. In figure 3.2, the redshift evolution of the best-fitting power-law indices obtained by fitting the power-law given by equation (3.14) with the $E(z)$ factor removed to the median relations at fixed redshift are plotted with the solid curves (red, orange, blue and green) corresponding to the different simulations and the horizontal dashed lines to the self-similar expectation. In figure 3.3, the redshift evolutions of the low-mass (left panel) and high-mass (right panel) best-fitting power-law indices obtained by fitting the broken power-law given by equation (3.15) with the $E(z)$ factor removed to the median relations at fixed redshift are plotted with the solid curves (red, orange, blue and green) corresponding to the different simulations and the horizontal dashed lines to the self-similar expectation.

The mass–X-ray temperature relation is slightly shallower than the self-similar expectation for the mass slope of 2/3 (see equation 3.6) for all the models. This result is mostly independent of redshift and mass, but depends upon the ICM physics: as the AGN feedback intensity is increased, the slope gets progressively steeper, particularly at the low-mass end. This is probably due to the spectral fitting procedure used for computing the X-ray temperature as the values of the mass slope are closer to the self-similar expectation for the non-core-excised mass-weighted temperature as can be
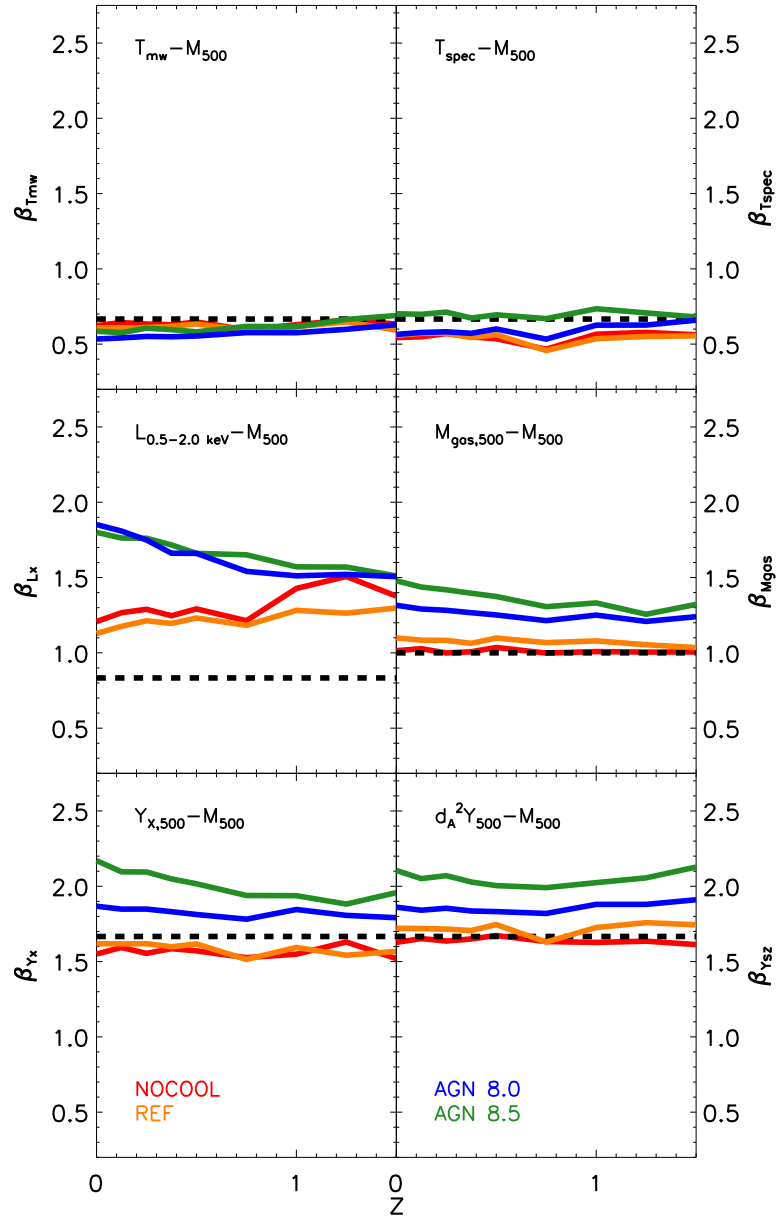
Figure 3.2: Evolution of the mass slope from $z = 0$ to $z = 1.5$ for the the mass–temperature (for both mass-weighted and X-ray temperature), soft X-ray luminosity–total mass, gas mass–total mass, X-ray analogue of the integrated Sunyaev–Zel'dovich signal–total mass and the integrated Sunyaev–Zel'dovich signal–total mass scaling relations (from *top left* to *bottom right*). In each panel, the redshift evolution of the best-fitting power-law indices obtained by fitting the power-law given by equation (3.14) with the $E(z)$ factor removed to the median relations at fixed redshift is plotted. The solid curves (red, orange, blue and green) correspond to the different simulations and the horizontal dashed lines to the self-similar expectation, respectively. With the exception of the X-ray temperature and the soft X-ray luminosity, the non-radiative (NOCOOL) model and the model that neglects AGN feedback altogether (REF) are consistent with being self-similar, whereas the models that include AGN feedback significantly deviate from self-similarity and the amplitude of the deviation increases with increasing intensity of the AGN feedback.
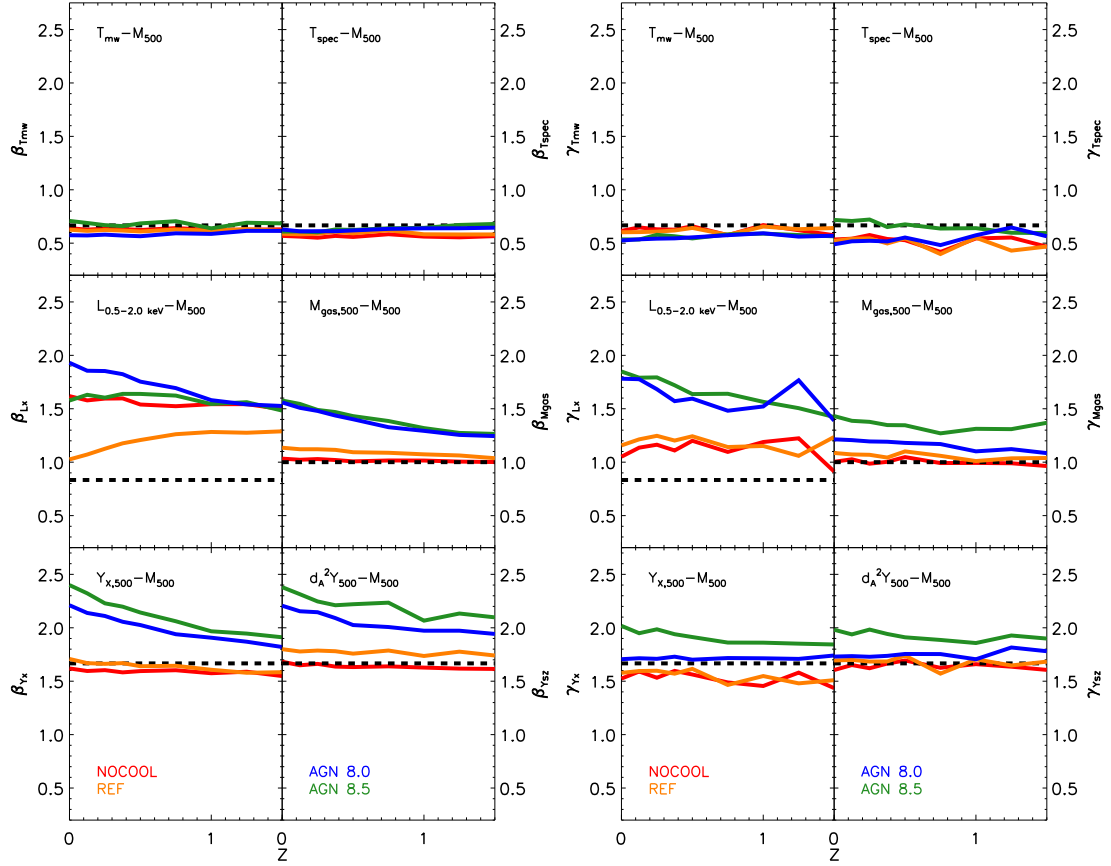
Figure 3.3: Evolution of the mass slope from $z = 0$ to $z = 1.5$ for the total the mass–temperature (for both mass-weighted and X-ray temperature), soft X-ray luminosity–total mass, gas mass–total mass, X-ray analogue of the integrated Sunyaev–Zel'dovich signal–total mass and the integrated Sunyaev–Zel'dovich signal–total mass scaling relations (from *top left* to *bottom right*). In each subpanel, the redshift evolutions of the low-mass (*left* panel) and high-mass (*right* panel) best-fitting power-law indices obtained by fitting the broken power-law given by equation (3.15) with the $E(z)$ factor removed to the median relations at fixed redshift are plotted. The solid curves (red, orange, blue and green) correspond to the different simulations and the horizontal dashed lines to the self-similar expectation, respectively. With the exception of the X-ray temperature and the soft X-ray luminosity, for both the low-mass and the high-mass slopes, the non-radiative (NOCOOL) model and the model that neglects AGN feedback altogether (REF) are consistent with being self-similar, whereas the models that include AGN feedback significantly deviate from self-similarity and the amplitude of the deviation increases with increasing intensity of the AGN feedback. The main difference between the two power-law indices at fixed scaling relation and physical model is that the low-mass one displays a stronger redshift dependence. All these results are cosmology independent.

seen on the top left panel of figure 3.2. Some of the deviation could also be due to departures from virial equilibrium, including non-thermal pressure support.

The picture is not as clear-cut in the case of the soft X-ray luminosity–total mass relation, for which the mass slope displays strong simultaneous redshift and non-gravitational physics dependencies. When the self-similar prediction of 5/6 for soft X-ray luminosity (see equation 3.9) is considered (which is the correct thing to do as what is plotted here is the rest-frame soft X-ray luminosity), the non-radiative simulation (NOCOOL) and the simulation which neglects AGN feedback altogether (REF) have soft X-ray luminosity–mass scaling relations that are significantly steeper than self-similar, and this independently of mass and redshift. The deviations from self-similarity are probably due to the fact that the gas does not trace the dark matter (it has e.g. a different mass–concentration relation compared to the dark matter) which affects both the density and the temperature, and hence the X-ray luminosity. The temperature and density are also potentially affected by non-thermal pressure support. The impact of AGN heating which is larger for groups than for clusters is likely to be responsible for the steepening of the mass slope at the low-mass end (especially for the AGN 8.0 model).

The gas mass–total mass relation is steeper than the self-similar expectation for the mass slope of 1 (which assumes a constant gas fraction) for all the radiative models, whereas it is consistent with it for the non-radiative (NOCOOL) one. This result is mostly independent of mass and redshift with the only clear exceptions being the AGN feedback models, for which the slope steepens with decreasing redshift and mass. The redshift dependence of the low-mass power-law index becomes stronger as the intensity of the AGN feedback is increased. In addition, the mass slope steepens with increasing feedback (be it from SNe or AGN) intensity. According to figure 3.3, this steepening is mostly driven by a steepening at the low-mass end and the difference between the two AGN feedback models is mostly induced by different behaviours at the high-mass end. The deviations from self-similarity and the steepening of the mass slope at the low-mass end are due to the fact that AGN feedback is more efficient at ejecting gas from the high-redshift progenitors of groups than those of clusters (see

McCarthy et al. 2011; see also Chapter 2).

The integrated Sunyaev–Zel'dovich signal and its X-ray analogue reveal similar trends. Their mass slopes are slightly shallower than, if not consistent with, the self-similar expectation of 5/3 (see equation 3.11) for NOCOOL, but become steeper than the expectation when feedback is included (SN feedback is sufficient in the integrated Sunyaev–Zel'dovich signal case, while efficient AGN feedback is required for its X-ray analogue) and steepens as its intensity is increased. They display a relatively strong mass dependence, especially when AGN feedback is added: both scaling relations steepen at the low-mass end, including in the non-radiative case for the X-ray analogue. They both exhibit redshift evolutions which get stronger as the feedback intensity is increased and both relations steepen as redshift decreases. These similar behaviours were to be expected as they both probe the total thermal energy of the ICM, even though the ratio of the integrated Sunyaev–Zel'dovich signal to its X-ray analogue is proportional to the ratio of the mass-weighted temperature to the X-ray temperature divided by the mean density, and is therefore sensitive to the biases introduced by the X-ray spectral fitting and to the gas distribution. Here, the departures from self-similarity are most likely due to a combination of gas ejection, which steepens the gas mass–total mass relation as already alluded to and heating which both increases the gas temperature and lowers its density and impacts more groups than clusters due to their lower binding energies. All these effects lead to a steepening of the scaling relations overall (with respect to the self-similar expectation) but also to a steepening of the mass slope at the low-mass end compared to the high-mass end.

Finally, it is worth pointing out that all the above results are independent of the choice of cosmology (there is virtually no difference between the results for the *Planck* cosmology presented here and those for the *WMAP*7 one (not shown)).

In short, with the exception of the X-ray temperature and the soft X-ray luminosity, the non-radiative (NOCOOL) model and the model that neglects AGN feedback altogether (REF) are consistent with being self-similar, whereas the models that include AGN feedback significantly deviate from self-similarity and the amplitude of the deviation increases with decreasing mass and increasing intensity of the AGN feedback. The

main difference between the low-mass and high-mass power-law indices of the evolving broken power-law at fixed scaling relation and physical model is that the low-mass one displays a stronger redshift dependence.

3.6 Evolution of normalisation

Figure 3.4 shows the evolution of the normalisation from $z = 0$ to $z = 1.5$ for the mass–temperature (for both mass-weighted and X-ray temperature), X-ray luminosity–total mass, gas mass–total mass, X-ray analogue of the integrated Sunyaev–Zel'dovich signal–total mass and the integrated Sunyaev–Zel'dovich signal–total mass scaling relations (from top left to bottom right) for the four physical models considered here. The normalisations of each scaling relation in the four $\log_{10}[M_{500}(\mathrm{M_\odot})]$ bins (denoted by solid lines of different colours) have been normalised by the self-similar expectation for the redshift evolution at fixed mass (shown as an horizontal dashed line). In the remainder of the Chapter, a scaling relation whose $E(z)$ exponent is smaller (bigger) than the self-similar expectations listed in Section 3.3 will be referred to as having negative (positive) evolution.

Surprisingly, given that temperature was found in Chapter 2 to be robust to changes in the included non-gravitational physics of galaxy formation, as, to first order, it is only determined by the depth of the dark matter dominated gravitational potential well, the normalisation of the mass–temperature relation does not evolve self-similarly (it evolves negatively compared to the self-similar expectation). This could be due to a combination of the evolution of the mass–concentration relation and of the non-thermal pressure support. The amplitude of the deviation from the self-similar expectation becomes slightly more pronounced with increasing mass and feedback intensity (i.e. it becomes more negative).

The amplitude of the soft X-ray luminosity–total mass relation evolves positively for all the the physical models (including the non-radiative one). The amplitude of the evolution is strongly mass dependent, slightly redshift dependent (it flattens out as
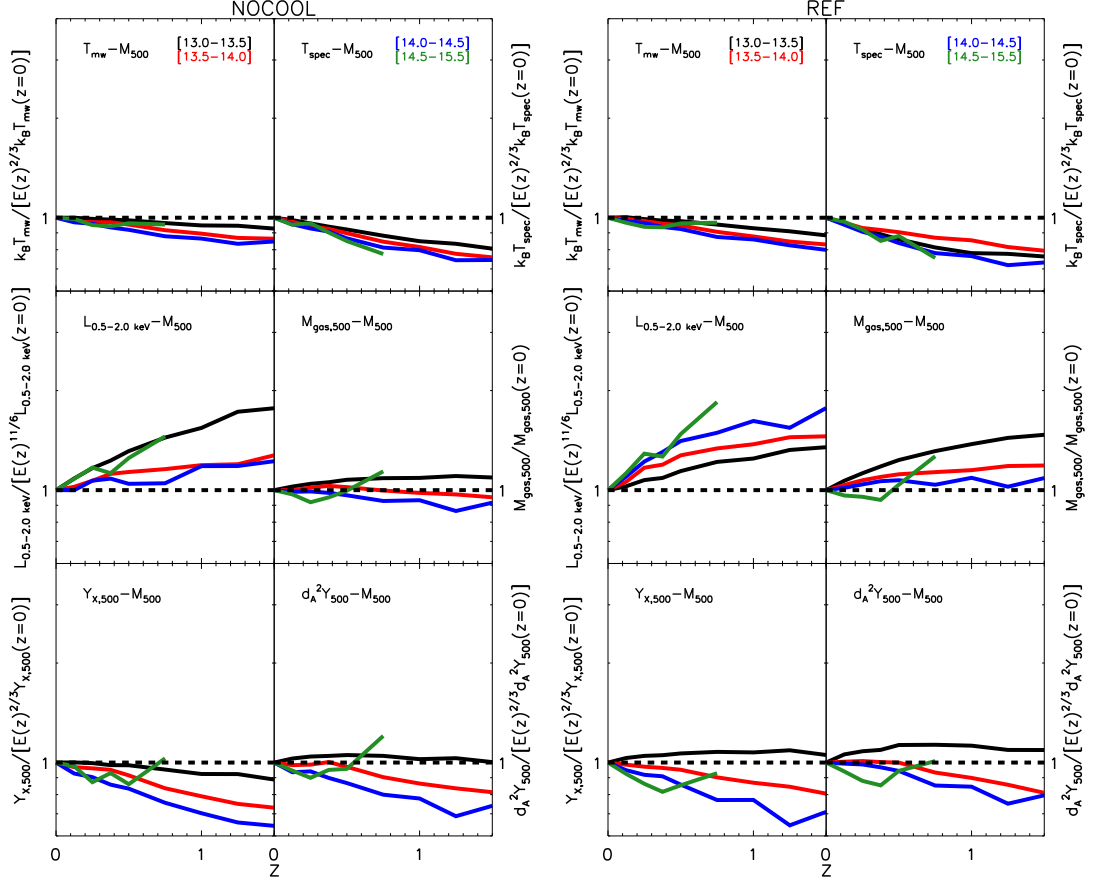
Figure 3.4: Evolution of the normalisation from $z = 0$ to $z = 1.5$ for the mass–temperature (for both mass-weighted and X-ray temperature), X-ray luminosity–total mass, gas mass–total mass, X-ray analogue of the integrated Sunyaev–Zel'dovich signal–total mass and the integrated Sunyaev–Zel'dovich signal–total mass scaling relations (from *top left* to *bottom right*). The two leftmost sets of subpanels correspond to the non-radiative simulation (NOCOOL) and the two rightmost ones to the REF simulation. The normalisations of each scaling relation in the four $\log_{10}[M_{500}(\mathrm{M}_\odot)]$ bins (denoted by solid lines of different colours) have been normalised by the self-similar expectation for the redshift evolution at fixed mass (shown as an horizontal dashed line). All the scaling relations are nearly self-similar for both the non-radiative (NOCOOL) simulation and the radiative simulation which includes SN feedback (REF) and for very massive haloes in the simulations which further include AGN feedback. This conclusion is cosmology independent.

redshift increases) and is strongly sensitive to the non-gravitational physics of galaxy formation (it becomes more positive as the feedback intensity is increased).

As far as the amplitude of the gas mass–total mass relation is concerned, it is more or less consistent with self-similar evolution for the non-radiative model but starts exhibiting positive evolution when non-gravitational physics is included, whose amplitude
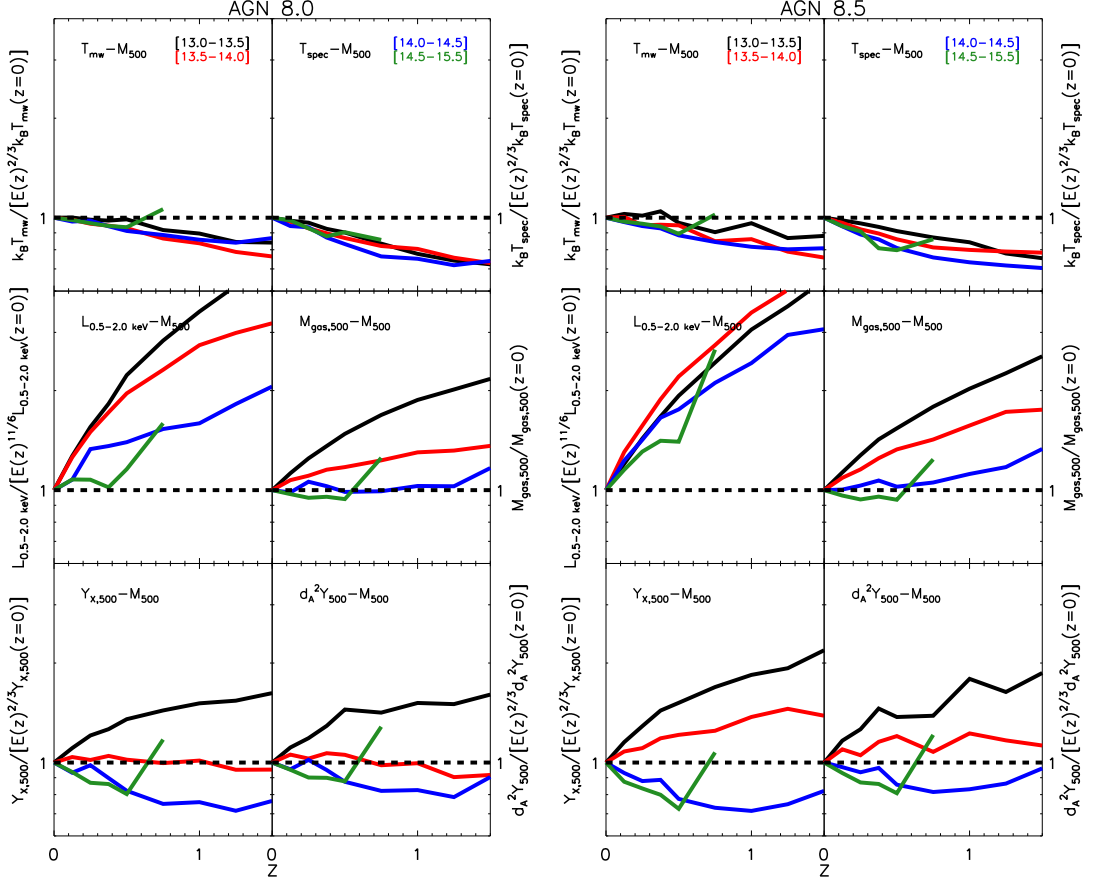
Figure 3.5: Same as figure 3.4 but for the AGN 8.0 and AGN 8.5 simulations.

increases with increasing feedback intensity. Similarly to the soft X-ray luminosity–mass relation, it is strongly mass dependent (the highest mass bins are the closest to behaving self-similarly as expected) and mildly redshift dependent (it sometimes flattens out at high-redshift). One possible explanation for the positive evolution of the amplitudes of the gas mass–total mass and soft X-ray luminosity–total mass relations is that, since haloes of fixed mass are denser at higher redshift, more energy is required to eject gas from these higher redshift haloes. More precisely, the binding energy can be approximated by

$$E_{bind} \propto \frac{GM_\Delta^2}{r_\Delta}, \tag{3.20}$$

which combined with equation (3.4) gives

$$E_{bind}(z) \propto M_\Delta^{5/3} E(z)^{2/3}. \tag{3.21}$$

Hence, as the binding energy increases with redshift, more energy is indeed required to eject gas from haloes at higher redshift.

Finally, as was the case for the mass slope, the normalisations of the integrated Sunyaev–Zel'dovich signal and its X-ray analogue exhibit similar behaviours, with evolutions whose amplitude and even direction depend strongly simultaneously upon redshift (mildly), and a combination of physical model and total mass (rather strongly). In the latter case, the direction of the evolution is different at the low-mass end (negative) compared to the high-mass end (positive) with a total mass scale at which the reversal occurs being a function of feedback intensity. As mentioned at the end of Section 3.5, these comparable behaviours are barely surprising as both quantities reflect the total thermal energy of the hot gas. These trends are probably the results of the combination of the fact that gas ejection is more difficult at higher redshift as already mentioned in the previous paragraph, that the mass–concentration relation evolves with redshift likely leading to non self-similar evolution of the mass–temperature relation and that deviations from hydrostatic equilibrium are presumably more frequent and possibly larger at higher redshift.

Lastly, the results described in this section are mostly independent of the choice of cosmology in the sense that the general trends are preserved but the exact values of e.g. the $E(z)$ exponents will be slightly different.

To summarise, all the scaling relations studied here are nearly self-similar for both the non-radiative (NOCOOL) simulation and the radiative simulation which includes SN feedback (REF) and for very massive haloes in the simulations which further include AGN feedback. Put another way, self-similarity breaks down when efficient feedback is included and this especially at the low-mass end.

3.7 Scatter about the median relations

Figure 3.6 shows the evolution of the log-normal scatter (at fixed total mass) from $z = 0$ to $z = 1.5$ for the total mass–X-ray temperature, X-ray luminosity–total mass, gas mass–total mass, X-ray analogue of the integrated Sunyaev–Zel'dovich signal–total mass and the integrated Sunyaev–Zel'dovich signal–total mass scaling relations (from top to bottom) for the four physical models considered here. For each simulation and each scaling relation, the log-normal scatter is plotted as a function of M_{500} and the redshift is denoted using lines of different colours. For most scaling relations, the log-normal scatter varies only mildly with mass, is relatively insensitive to non-gravitational physics (especially if one excludes the non-physical non-radiative model (NOCOOL)), but displays a moderately strong redshift dependence (it tends to decrease with increasing redshift). The only striking exceptions are: (i) the scatter in gas mass increases with the increased complexity of the included galaxy formation physics and with increasing AGN feedback intensity, which is not surprising as these processes strongly affect the gas fractions (e.g. McCarthy et al. 2010; Stanek et al. 2010; Planelles et al. 2013; see also Chapter 2) and (ii) the scatter in the X-ray temperature increases when AGN feedback is introduced and starts displaying a stronger redshift dependence. These results are robust to changes in cosmology from *Planck* to *WMAP*7.

Table 3.4 presents the scatter about the median scaling relations. $\sigma_{\ln Y|M}$ was computed using the best-fitting A'' values for the log-normal scatter of the AGN 8.0 model listed in Table 3.3. It was turned into $\sigma_{\ln M|Y}$ by dividing it by the values of the mass power-law exponents (β) obtained for the median relation of the AGN 8.0 model listed in Table 3.2. This conversion is justified when the halo mass function can be well-approximated by a power-law at the relevant mass scale (see for instance the appendix of Leauthaud et al. 2010). The zero-point uncertainty of Y was computed by computing the root mean square dispersion of the normalisation A of the best-fitting evolving power-law obtained for the median relations of the three radiative models (REF, AGN 8.0 and 8.5) and by multiplying it by $\ln 10$. The unphysical non-radiative simulation (NOCOOL)

was excluded from the computation of the latter. All but one of the hot gas proxies examined here (i.e. X-ray temperature, gas mass, Sunyaev–Zel'dovich signal and its X-ray analogue) have a similar scatter at fixed total mass of about 10 per cent. The X-ray luminosity has a significantly larger scatter at fixed total mass (it is about three times higher). They thus all exhibit values of $\sigma_{\ln Y|M}$ which are slightly smaller than the observational constraints summarised in the rightmost column of Table 3.4 (see e.g. Pratt et al. 2009; Vikhlinin et al. 2009a; Mantz et al. 2010a; Andersson et al. 2011; Planck Early Results XI; Lin et al. 2012; Planck Intermediate Results III; Planck 2013 Results XX and Allen, Evrard & Mantz 2011 for a review). This is at least partly owing to the fact that here the results of the full synthetic X-ray analysis conducted in Section 2.2.2 are not being used. For instance, the scatter in gas mass at fixed total mass increases from ~ 10 per cent to ~ 15 for the AGN 8.0 simulation when the full synthetic X-ray analysis is used. As discussed in Chapter 2, the increase in scatter is due to the biases in the gas and total mass density profiles induced by the spectral fitting and hydrostatic analysis. Besides, even if the full synthetic analysis had been used, it still corresponds to 'perfect' X-ray observations: in the sense that these do not include any noise be it astrophysical (e.g. AGN contamination), or instrumental (e.g. Poisson noise, PSF smearing).
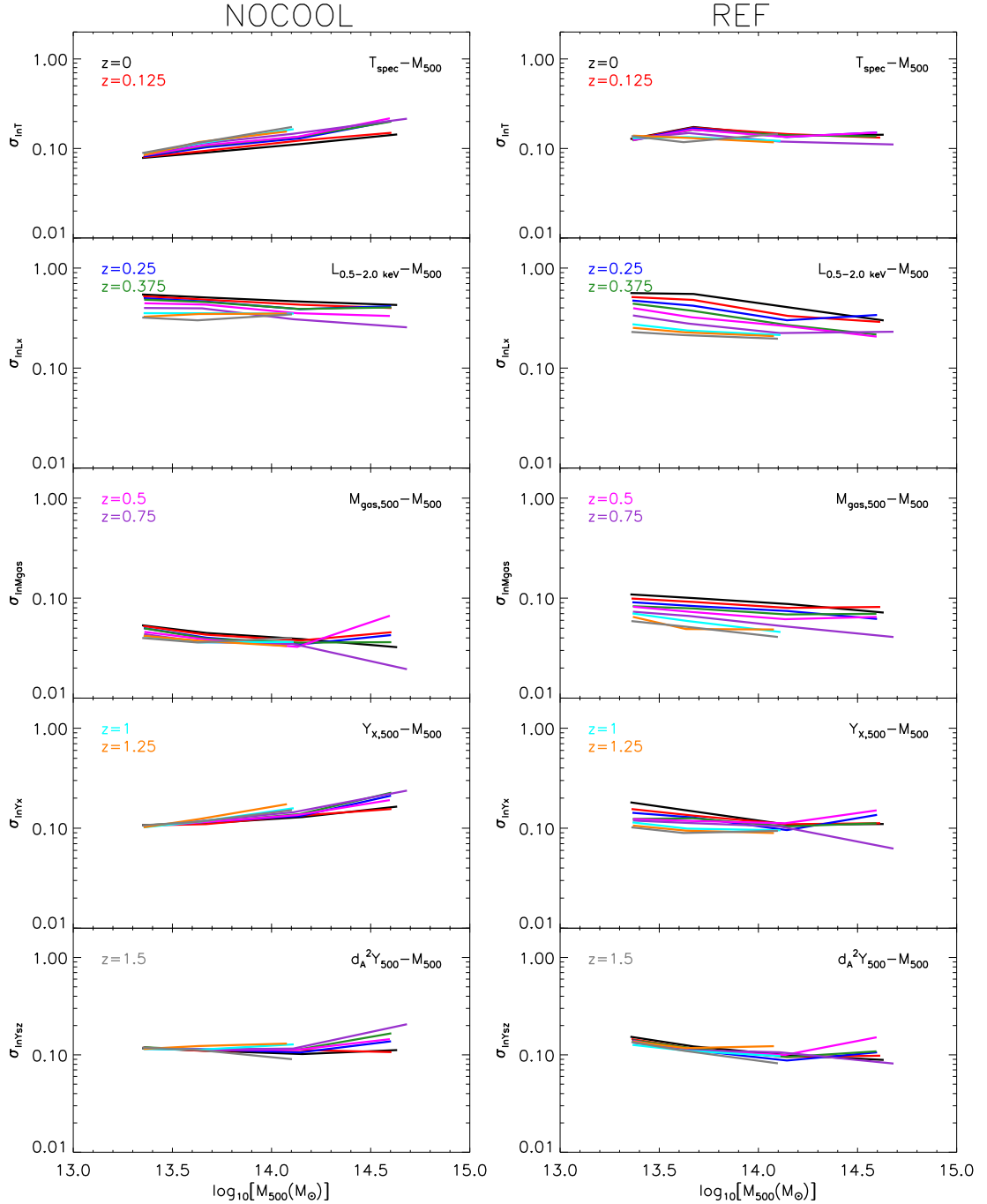
Figure 3.6: Evolution of the log-normal scatter from $z = 0$ to $z = 1.5$ for the total mass–temperature, X-ray luminosity–total mass, gas mass–total mass, X-ray analogue of the integrated Sunyaev–Zel'dovich signal–total mass and the integrated Sunyaev–Zel'dovich signal–total mass scaling relations (from *top* to *bottom*). The left set of subpanels corresponds to the non-radiative simulation (NOCOOL) and the right one to the REF simulation. For each simulation and each scaling relation, the log-normal scatter is plotted as a function of M_{500} and the redshift is denoted using lines of different colours. For most scaling relations, the log-normal scatter varies only mildly with mass, is relatively insensitive to non-gravitational physics, but displays a moderately strong redshift dependence. The only striking exceptions are: (i) the scatter in gas mass increases with the increased complexity of the included galaxy formation physics and with increasing AGN feedback intensity and (ii) the scatter in the X-ray temperature increases when AGN feedback is introduced and starts displaying a stronger redshift dependence. These results are robust to changes in cosmology from *Planck* to *WMAP*7.
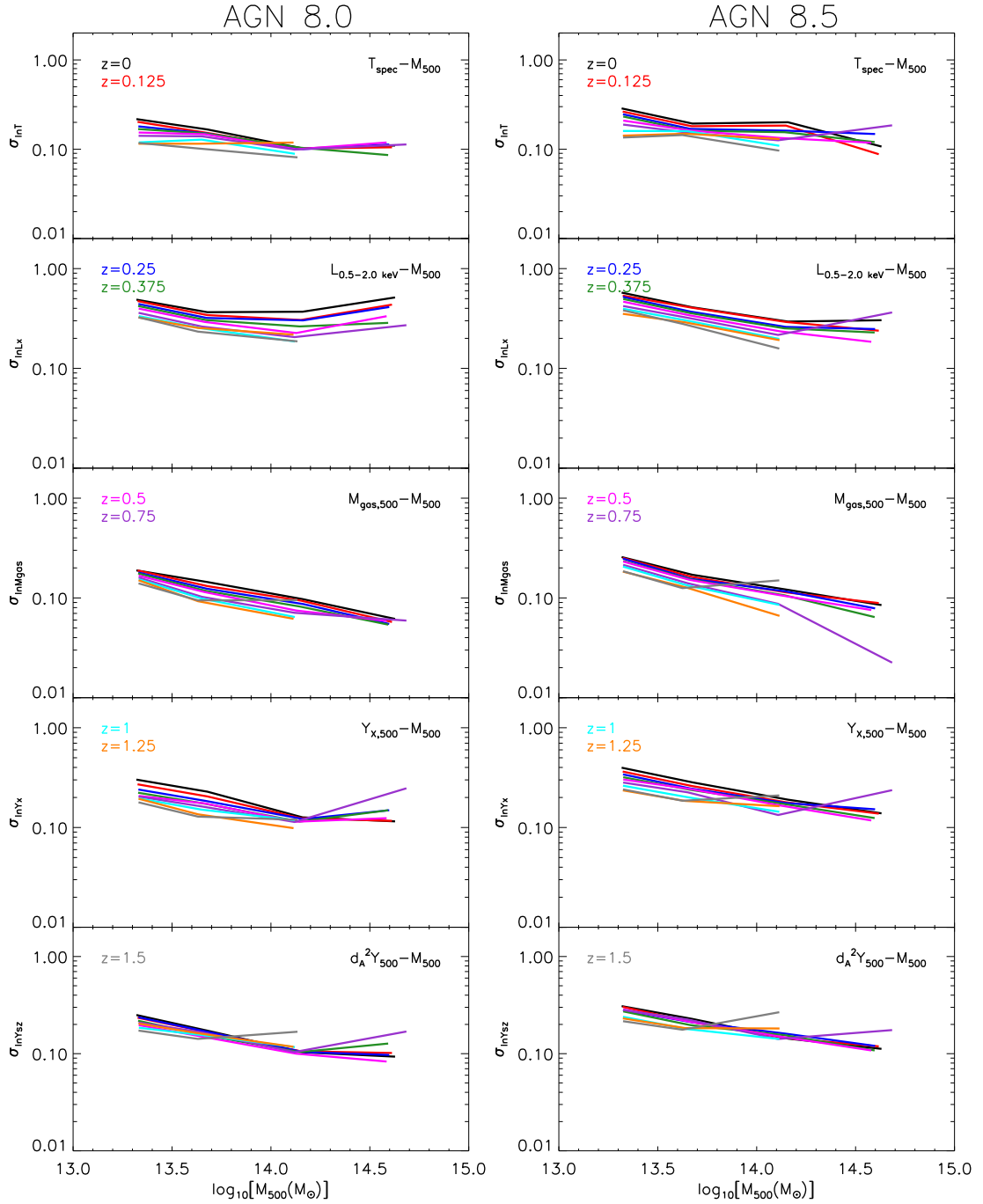
Figure 3.7: Same as figure 3.6 but for the AGN 8.0 and AGN 8.5 simulations.

Scaling relation	$\sigma_{\ln Y\|M}$	$\sigma_{\ln M\|Y}$	Zero-point uncertainty in Y	Observational constraints on $\sigma_{\ln Y\|M}$
$T_{spec} - M_{500}$	$\sim 10\,\%$	$\sim 20\,\%$	$\sim 10\,\%$	$\sim 15\,\%$
$L_{0.5-2.0keV} - M_{500}$	$\sim 30\,\%$	$\sim 20\,\%$	$\sim 45\,\%$	$\sim 40\,\%$
$M_{gas,500} - M_{500}$	$\sim 10\,\%$	$\sim 10\,\%$	$\sim 20\,\%$	$\sim 15\,\%$
$Y_{X,500} - M_{500}$	$\sim 10\,\%$	$\sim 5\,\%$	$\sim 30\,\%$	$\sim 20\,\%$
$d_A^2 Y_{500} - M_{500}$	$\sim 10\,\%$	$\sim 5\,\%$	$\sim 20\,\%$	$\sim 20\,\%$

Table 3.4: Scatter about the median scaling relations. $\sigma_{\ln Y\|M}$ was computed using the best-fitting A'' values for the log-normal scatter of the AGN 8.0 model listed in Table 3.3. It was turned into $\sigma_{\ln M\|Y}$ by dividing it by the values of the mass power-law exponents (β) obtained for the median relation of the AGN 8.0 model listed in Table 3.2. The zero-point uncertainty of Y was computed by computing the root mean square dispersion of the normalisation A of the best-fitting evolving power-law obtained for the median relations of the three radiative models (REF, AGN 8.0 and 8.5) and by multiplying it by $\ln 10$.

3.8   Summary and Discussion

The cosmo-OWLS suite of large-volume hydrodynamical simulations described in detail in Chapter 2 was employed to investigate the scatter and evolution of the hot gas properties of a realistic population of simulated galaxy groups and clusters. cosmo-OWLS forms an extension of the OWLS project (Schaye et al. 2010) and has been specially designed with ongoing and upcoming cluster cosmology and large-scale structure surveys in mind.

From the study presented here, the following conclusions are reached:

1. The median relations and the scatter about them are reasonably well modelled by evolving broken power-laws with redshift dependent low-mass power-law indices of the form given by equation (3.17), whereas power-laws and broken power-laws of the form given by equations (3.14) and (3.15) fail to reproduce the median relations especially at the low-mass end (figure 3.1).

2. With the exception of the X-ray temperature and the soft X-ray luminosity, the non-radiative (NOCOOL) model and the model that neglects AGN feedback altogether (REF) are consistent with having self-similar mass slopes at all redshifts $z \leq 1.5$, whereas the mass slopes of the models that include AGN feedback significantly deviate from the self-similar expectation and the amplitude of the deviation increases with decreasing mass and increasing intensity of the AGN feedback. The main difference between the low-mass and high-mass mass slopes of the evolving broken power-law at fixed scaling relation and physical model is that the low-mass one displays a stronger redshift dependence (figures 3.2 to 3.3).

3. All the scaling relations studied here evolve nearly self-similarly for both the non-radiative (NOCOOL) simulation and the radiative simulation which includes SN feedback (REF) and for very massive haloes in the simulations which further include AGN feedback. Put another way, self-similar evolution breaks down when efficient feedback is included and this especially at the low-mass end (fig-

ure 3.4).

4. For most scaling relations, the log-normal scatter varies only mildly with mass, is relatively insensitive to non-gravitational physics (especially if one excludes the non-physical non-radiative model (NOCOOL)), but displays a moderately strong redshift dependence (it tends to decrease with increasing redshift). The only striking exceptions are: (i) the scatter in gas mass increases with the increased complexity of the included galaxy formation physics and with increasing AGN feedback intensity and (ii) the scatter in the X-ray temperature increases when AGN feedback is introduced and starts displaying a stronger redshift dependence (figure 3.6).

5. All but one of the hot gas mass proxies examined here (i.e. X-ray temperature, gas mass, Sunyaev–Zel'dovich signal and its X-ray analogue) have a similar scatter at fixed total of about 10 per cent. The X-ray luminosity has a significantly larger scatter at fixed total mass (it is about three times higher). They thus all exhibit values of $\sigma_{\ln Y|M}$ which are slightly smaller than the observational constraints. This is at least to some extent due to using true physical quantities instead of the ones that would be inferred from a synthetic X-ray analysis (table 3.4).

6. All these results are robust to changes in cosmology from *Planck* to *WMAP*7.

As total mass is the only independent variable in structure formation theory, the cluster masses have to be reliably determined in order to enable the use of galaxy clusters as cosmological probes. Unfortunately, the cluster total masses are not directly observable. Therefore, in order to constrain cosmology with galaxy clusters, one has to, for instance, rely on well-calibrated/understood total mass–observable relations being used as mass proxies. A good mass proxy should ideally be: (i) easy to measure (including with relatively shallow data), (ii) tightly correlated with mass, (iii) have a small intrinsic scatter, (iv) be insensitive to the choice of cosmology, (v) be insensitive to the cluster dynamical state and to the uncertain non-gravitational physics of galaxy formation (i.e. the zero point is well-known) and (vi) have a redshift evolution which is

easy to characterise. Judging by these criteria, the mean X-ray temperature is the 'best' mass proxy among all the cluster global hot gas properties considered as it has: (i) the smallest zero-point uncertainty, (ii) has a relatively small intrinsic scatter in mass at fixed proxy (even in the absence of core excision) and (iii) its evolution and mass slope are the least affected by baryonic physics, mass and redshift. The mass–temperature relation is also the closest to being a single power-law (i.e. it is close to not being broken). The integrated Sunyaev–Zel'dovich signal, its X-ray analogue and gas mass have smaller intrinsic scatter in mass at fixed proxy but have a larger zero-point uncertainty and, in general, are much more affected by the effects of the physics of galaxy formation (e.g. their mass slopes and evolution are much more mass and physics dependent). The X-ray luminosity is the poorest one with the highest intrinsic scatter, and the strongest dependence upon the ICM physics.

Chapter 4

Synthetic observations of cosmological simulations

Ian McCarthy wrote the code that takes the outputs of the light cone software for gas particles, computes the X-ray and Sunyaev–Zel'dovich fluxes for each of the gas particles and produces maps by SPH smoothing the fluxes onto $2.5''$ on a side pixels.

4.1 Introduction

One of the factors that contributed to the recent rapid progress of cosmology is the confrontation of increasingly large observational datasets with more and more sophisticated theoretical models. In particular, both theory and observations stand to benefit from the use of as realistic as possible synthetic observations generated from cosmological simulations. This was first recognised in the late 1980s and several approaches have been used since then. The use of progressively more refined methods is mainly driven by the progress of (i) cosmological simulations and (ii) galaxy formation models.

The first galaxy (clusters) catalogues where generated using biasing schemes, i.e. by 'painting' galaxies/clusters on DM-only cosmological simulations (see e.g. van Haar-

lem, Frenk & White 1997; Cole et al. 1998; Coil, Davis & Szapudi 2001; Evrard et al. 2002). Even though this method is extremely quick and efficient for large and low-resolution cosmological simulations, it does not take explicitly into account the (non-gravitational) physics of galaxy formation.

A second approach uses 'halo' models. It is probably the most widely used and comes in several flavours. In the simplest case, haloes that have been identified in DM-only simulations are populated according to a model for halo occupation distribution (for instance Yang et al. 2004). A slightly more sophisticated procedure uses semi-analytic models (SAM) to follow galaxy formation in the simulation identified haloes and a Monte-Carlo scheme is used to build merger trees for these haloes (Benson et al. 2000). Finally, SAM are used but this time on merger trees that have extracted directly from the simulation (see among others Diaferio et al. 1999; Coil, Davis & Szapudi 2001; Blaizot et al. 2005; Kitzbichler & White 2007).

A final approach uses hydrodynamic cosmological simulations, which include (some of) the galaxy formation physics to generate synthetic observations, usually for X-ray (see for instance Croft et al. 2001 and Roncarelli et al. 2006 which studied the diffuse X-ray background) and Sunyaev–Zel'dovich effect (Thomas & Carlberg 1989; Scaramella, Cen & Ostriker 1993; da Silva et al. 2000) surveys.

Synthetic observations are constructed by putting a virtual observer somewhere in the $z = 0$ simulation box and by finding the objects which are located within his past light cone. The past light cone is defined as in Special Relativity: it is the set of all the light-like world lines which intersect the spacetime position of the observer[1]. Hence, it is a three-dimensional (3D) sphere in 4D spacetime. Hereafter, the term light cone will denote a wedge cut out from this sphere according to the survey geometry.

As Chapter 2 demonstrated the ability of some of the cosmo-OWLS models to produce realistic galaxy group and cluster populations, the remainder of this Chapter will describe the methods used for generating synthetic observations (in Section 4.2), as well as the way they were tested against publicly available[2] synthetic surveys of the

---

[1]i.e. its spatial position within the $z = 0$ box at $z = 0$

[2]through the MILLENNIUM online database at http://www.virgo.dur.ac.uk

MILLENNIUM simulation (in Section 4.3). It will then summarise the comparison of different versions of the developed light cone software and justify the use of the simplest possible method (in Section 4.4) and finally present a first application to synthetic Sunyaev–Zel'dovich surveys such as the ones used for Chapter 5 and McCarthy et al. (2014) (in Section 4.5).

4.2 Methodology

The developed light cone software uses methods that are similar in spirit to the ones developed by Blaizot et al. (2005) and slightly modified by Kitzbichler & White (2007). As they both pointed out, the main issues one faces when trying to generate synthetic surveys from cosmological simulations stem from the finite size of the box and from the discrete character of the simulation data storage: galaxy/particle properties are only saved for a given number of redshifts between the start of the simulation and the present time ($z = 0$) whereas redshift increases continuously within the past light cone. The first problem is that depending on the depth and width of the survey beam, one might need to replicate the box, both along the central line of sight (l.o.s.) (hereafter radial replications) and perpendicular to it (i.e. at the same redshift). For instance, the cosmo-OWLS $400\ h^{-1}$ Mpc box corresponds to the comoving distance to $z \sim 0.15$ and $z \sim 0.14$ in the *WMAP*7 and *Planck* cosmologies, respectively. It is thus necessary to try to both minimise the effects of these two simulation characteristics and to assess the sensitivity of the synthetic observations to these presently[3] unavoidable effects. The new method is general and has been used to generate light cones for gas, star and black hole particles as well as for FoF haloes and galaxies (hereafter called collectively objects).

---

[3] given the currently available computational resources

4.2.1 Required inputs from the cosmological simulation

The method relies upon the construction of a 3D pavement of simulation boxes. Hence, the simulations need to be of constant comoving volume cubic boxes with periodic boundary conditions. Furthermore, their snapshots need to contain at least the following information: (i) the redshift of the snapshot, (ii) the position of each object within the simulation box and (iii) the relevant indices (particle indices for particles, FoF indices for FoF haloes, and FoF and subhalo indices for galaxies). The indices of the objects which fall within the light cone will be saved, together with the index of the snapshot they were taken from; this allows for the computation of their observable properties in post-processing. This has several advantages: (i) it means that the light cones are not limited to producing synthetic observations for one type of survey, (ii) it makes the file sizes more reasonable and (iii) it saves computing time since the properties do not have to be computed for the whole simulation volume and for all the snapshots before running the light cone software.

4.2.2 Tiling and dealing with replications

A 3D pavement of boxes is first constructed. It goes until the comoving distance $d_{c,end}$ that corresponds to the depth redshift of the survey z_{end}. Then, depending upon the geometry of the survey beam, the direction of the l.o.s. is chosen so that it minimises the number of radial replications. Here, replications mean not only replicating the box along the l.o.s. since $d_{c,end} > L_{box}$ where L_{box} is the comoving box size, but also that the light cone passes through parts of the simulation volume for at least the second time. As structures move slowly, it means including the same structures more than once, as illustrated on the top panel of figure 4.1, and this leads to spurious perspective effects. In order to minimise the number of radial replications, the software uses the method described in detail in Kitzbichler & White (2007).

In brief, for a rectangular survey of size $\sim 1/m^2 n \times 1/n^2 m$ steradians, with a central l.o.s. going into the 'slanted' direction going through the point $(L_{box}/m, L_{box}/n, L_{box})$,
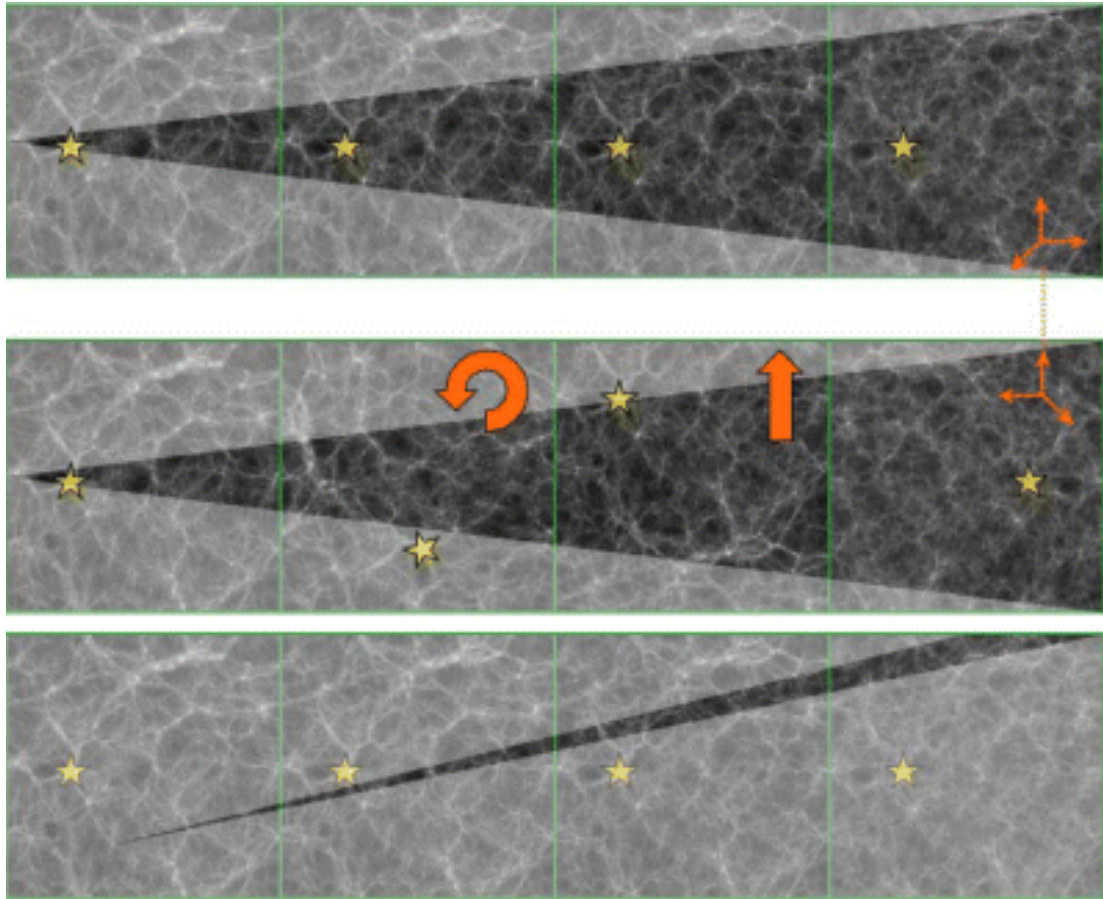
Figure 4.1: *Top*: Basic pavement of snapshots. *Middle*: Effects of the three sorts of transformations (from left to right: rotation, translation, and inversion of one axis) applied to the snapshots. *Bottom*: Pencil beam generated without transformations, thanks to the 'slanted' direction. Figure taken from Blaizot et al. (2005).

the first replication of the origin will be hit by the central l.o.s. after going through nm replications of the simulations box, i.e. at the point $(L_{box}, L_{box}, nmL_{box})$. This corresponds to a comoving distance from the origin of the cone given by:

$$d_{c,rep} = \sqrt{n^2 + m^2 + n^2m^2}L_{box} \qquad (4.1)$$

This method is shown on the bottom panel of figure 4.1.

It is worth noting that this approach assumes that n and m are integers with no common factor. This means that this formula for d_{rep} is only valid for rectangular beam surveys. Nevertheless, it is possible to extend the reasoning to square beams, which have $n = m$. In this case, the first replication of the origin hit by the central l.o.s. is

$(L_{box}, L_{box}, nL_{box})$ and thus the comoving distance to this first replication is given by:

$$d_{c,rep} = \sqrt{n^2 + 2}L_{box} \tag{4.2}$$

In both cases, for $d_{c,end} > d_{c,rep}$, one will either have to live with the artefacts due to the replications or to apply random transformations to the snapshots in order to reshuffle the structures within the simulation box. The effects of random transformations such as rotations and translations are shown on the middle panel of figure 4.1. The developed software applies random transformations, contrarily to Kitzbichler & White (2007), as for the currently simulated beam sizes (e.g. 7×7 deg^2 which corresponds to the angular size of the box at $z_{end} = 1.5$ and is close to the total size of the XXL survey fields[4] (described in Section 6.1)), $d_{c,rep}$ corresponds to a redshift $z_{rep} \sim 0.3$ in the *WMAP*7 cosmology, which means that there will be a significant number of replications. It uses the same type of random transformations as in Blaizot et al. (2005) that is, a combination of:

1. translations of random amplitude (between 0 and L_{box}) along each of the three box axes,

2. rotations of 0, $\pi/2$, π or $3\pi/2$ (randomly chosen) about each of the axes,

3. and inversion of up to one randomly chosen axis (e.g. $z \to -z$).

A different set of these transformations is applied to each of the boxes encountered after $d_{c,rep}$. Obviously, applying such transformations means that some of the spatial information of the original simulation is lost (especially on the largest scales) as it decorrelates the boxes used to make the cones from one another. Nevertheless, it might be possible to limit this information loss by slightly modifying the method employed by Blaizot et al. (2005), and taking advantage of the 'slanted' direction of the light cone which means that replications occur at every multiple of $d_{c,rep}$: hence, one only needs to apply one identical set of random transformations to all the boxes within the cone

---

[4]two 25 square degrees fields

slice which is in between two consecutive replications of the origin. A new version of the light cone software was written in order to test that idea. The different versions of the light cone software and their comparison will be presented in Section 4.4.

4.2.3 Choosing the right snapshot and inclusion within the cone

In principle, any object at a comoving distance d_c from the observer should have the physical properties it had at a redshift z such that:

$$d_c(z) = \frac{c}{H_0} \int_0^z \frac{dz'}{\sqrt{\Omega_m(1+z)^3 + \Omega_\Lambda}}$$

(4.3)

but the physical properties of particles/galaxies were only stored for a discrete number of snapshots at redshifts z_i (with $z_0 = d_{c,0} = 0$), which correspond to comoving distances $d_{c,i}$. The developed software deals with this problem in a way that is similar to the one used by Kitzbichler & White (2007). In short, they use the properties at redshift z_i for all the objects with a comoving distance d from the observer such that $\frac{d_{c,i-1}+d_{c,i}}{2} < d_c < \frac{d_{c,i}+d_{c,i+1}}{2}$ and interpolate the positions between z_i and z_{i+1} for the objects which are close to the upper bound in order to decide on which side of it they sit. However, the developed software does not interpolate, as it would have been too CPU intensive to do so for FoF haloes/galaxies (no merger trees for cosmo-OWLS), and there is no equivalent to a merger tree for particles. Therefore, it just uses the properties at redshift z_i for all the objects with :

$$\frac{d_{c,i-1} + d_{c,i}}{2} < d_c \leq \frac{d_{c,i} + d_{c,i+1}}{2}.$$

(4.4)

Finally, objects are included within the light cone if they fulfil the distance condition given by equation 4.4 as well as the following conditions on their Right Ascensions

(RA) α and their Declinations (Dec) δ[5]:

$$|\tan \alpha| \leq \tan \Delta\alpha/2 \tag{4.5}$$

$$|\tan \delta| \leq \tan \Delta\delta/2 \tag{4.6}$$

where $\Delta\alpha$ and $\Delta\delta$ are the angular extent of the survey in the two orthogonal RA and Dec directions.

4.3 Testing the software

4.3.1 Comparison to the results of Kitzbichler & White (2007)

Kitzbichler & White (2007) used the large N-body DM-only simulation called MIL-LENNIUM, which was carried out by the Virgo consortium. A full description of this simulation is given in Springel et al. (2005) and only its main properties are described here. It follows the hierarchical growth of structures from redshift $z = 127$ to the present, using the TreePM code GADGET2 (Springel, Yoshida & White 2001; Springel 2005), in a box $500 \; h^{-1}$ comoving Mpc on a side and using 2160^3, which is slightly over 10 billion, DM particles. The particle mass is then $8.6 \times 10^8 \; h^{-1} \; \mathrm{M}_\odot$.

The formation and evolution of galaxies and quasars is followed, in post-processing, by using semi-analytic models (SAM), which were first introduced by White & Frenk (1991) more than two decades ago. They start from merger trees that describe the growth history of structures over cosmic time, and are a simplified way to simulate galaxy formation where star formation and its regulation by various feedback processes are described by simple analytical physical models. An extensive description of the physical principles behind semi-analytic modelling can be found, for instance, in Baugh (2006). Kitzbichler & White (2007) used a modified version of the Croton et al. (2006) semi-analytic model as updated by De Lucia & Blaizot (2007) and further

---

[5]They are obtained by projecting the objects' 3D cartesian coordinates in the box frame onto a 3D right-handed cartesian system of axes. One of the axis of the new system of coordinates is the central l.o.s.

improved the treatment of dust.

Six of their 1.4×1.4 square degrees light cones which go until $z = 7$ are publicly available through the MILLENNIUM database. As the data of the De Lucia & Blaizot (2007) SAM applied to MILLENNIUM are also available from that database, one of the easiest ways to test the developed software was to generate a cone with similar characteristics (1.4×1.4 square degrees going until $z = 4.5$).

One of the conducted comparisons is illustrated in figure 4.2: the stellar mass function ($dN/dlogM_*/arcmin^2$) is computed for various values of the depth redshift, for the retrieved Kitzbichler & White (2007) cone, as well as for the cone generated using the developed software. The agreement is extremely good, except at the high mass end of the cone with the smallest depth. Redshift number counts ($dN/dz/arcmin^2$) with various stellar masses and magnitude cuts, as well as magnitude number counts ($dN/dm/arcmin^2$) in the K band, were also compared and likewise show reasonable agreement.
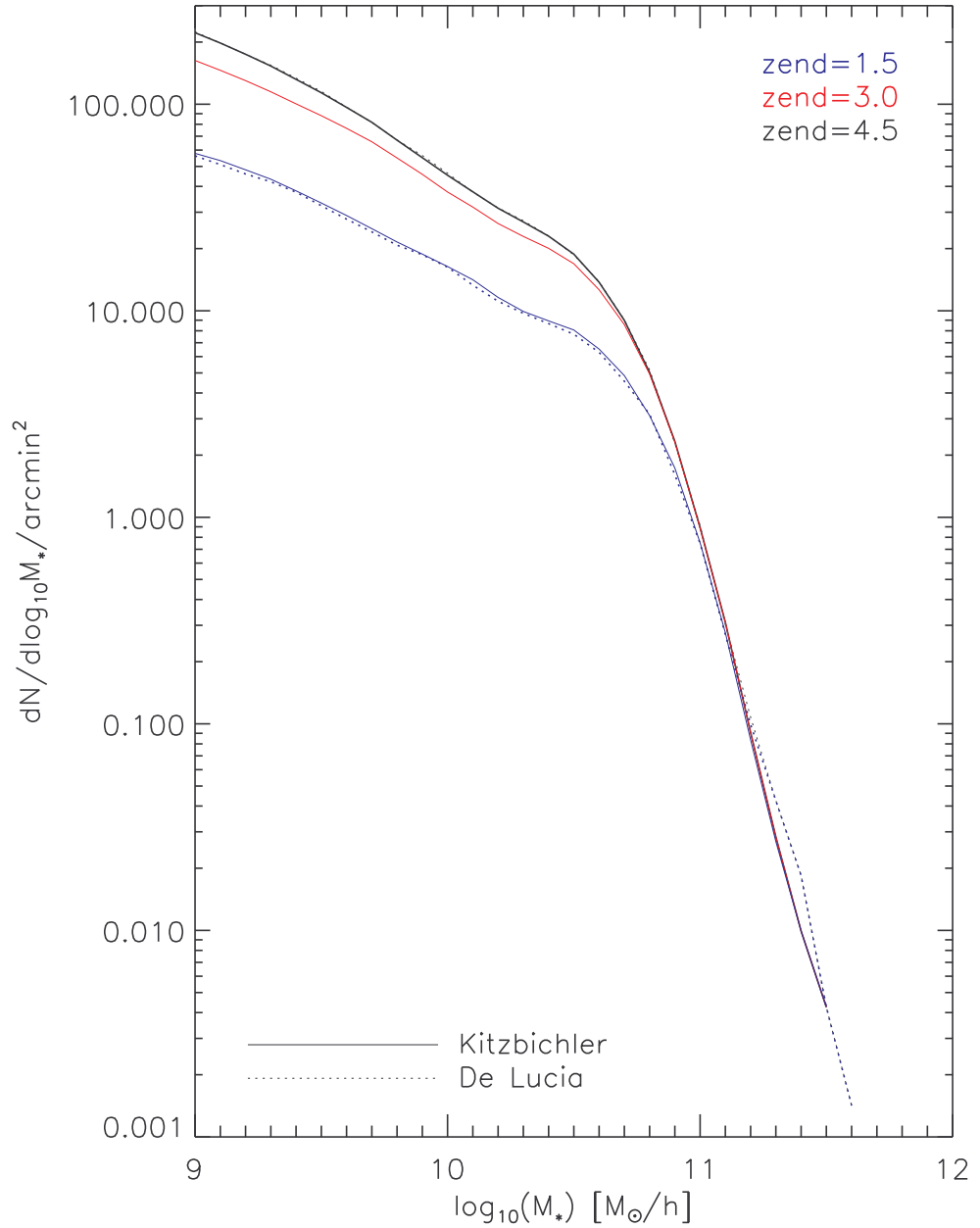
Figure 4.2: Stellar mass function ($dN/dlogM_*/arcmin^2$) for a cone with similar characteristics to the publicly available Kitzbichler & White (2007) cones (1.4×1.4 square degrees, depth redshift of 4.5) generated using the De Lucia & Blaizot (2007) SAM applied on the MIL-LENNIUM simulation. The solid lines correspond to one of the retrieved cones and the dotted lines correspond to the cones generated with the developed software. Blue, red and black lines correspond respectively to a synthetic survey redshift depth of 1.5, 3.0 and 4.5. The agreement is extremely good, except at the high mass end of the cone with the smallest depth.

4.3.2 Comparison to 2dFGRS

The two-degree field galaxy redshift survey (2dFGRS; Colless et al. 2001) covers a total of 2000 square degrees (split into one 75×10 square degrees field in the Northern hemisphere and one 80×15 square degrees field in the Southern one) with a median depth of $z = 0.11$. Survey plots of their two fields are presented on figure 4.3.

A survey with similar size (32×23 square degrees) and depth ($z = 0.25$) has been generated using the $400 \ h^{-1}$ Mpc *WMAP*7 AGN simulation of the cosmo-OWLS suite described in Section 2.2.1. A similar survey plot for this synthetic survey is shown on figure 4.4, on which some level of clustering is visible.
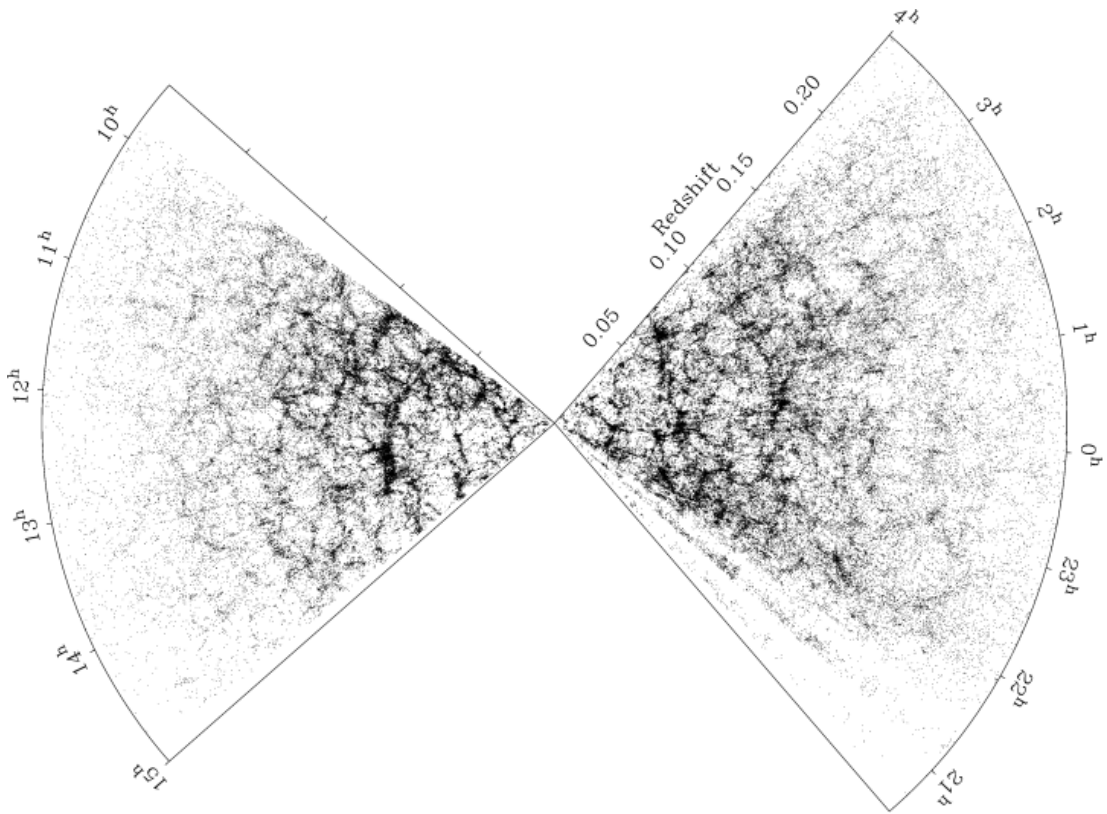
Figure 4.3: Projected galaxy distribution in the two 2dFGRS fields as a function of RA and redshift. Figure taken from Colless et al. (2001).
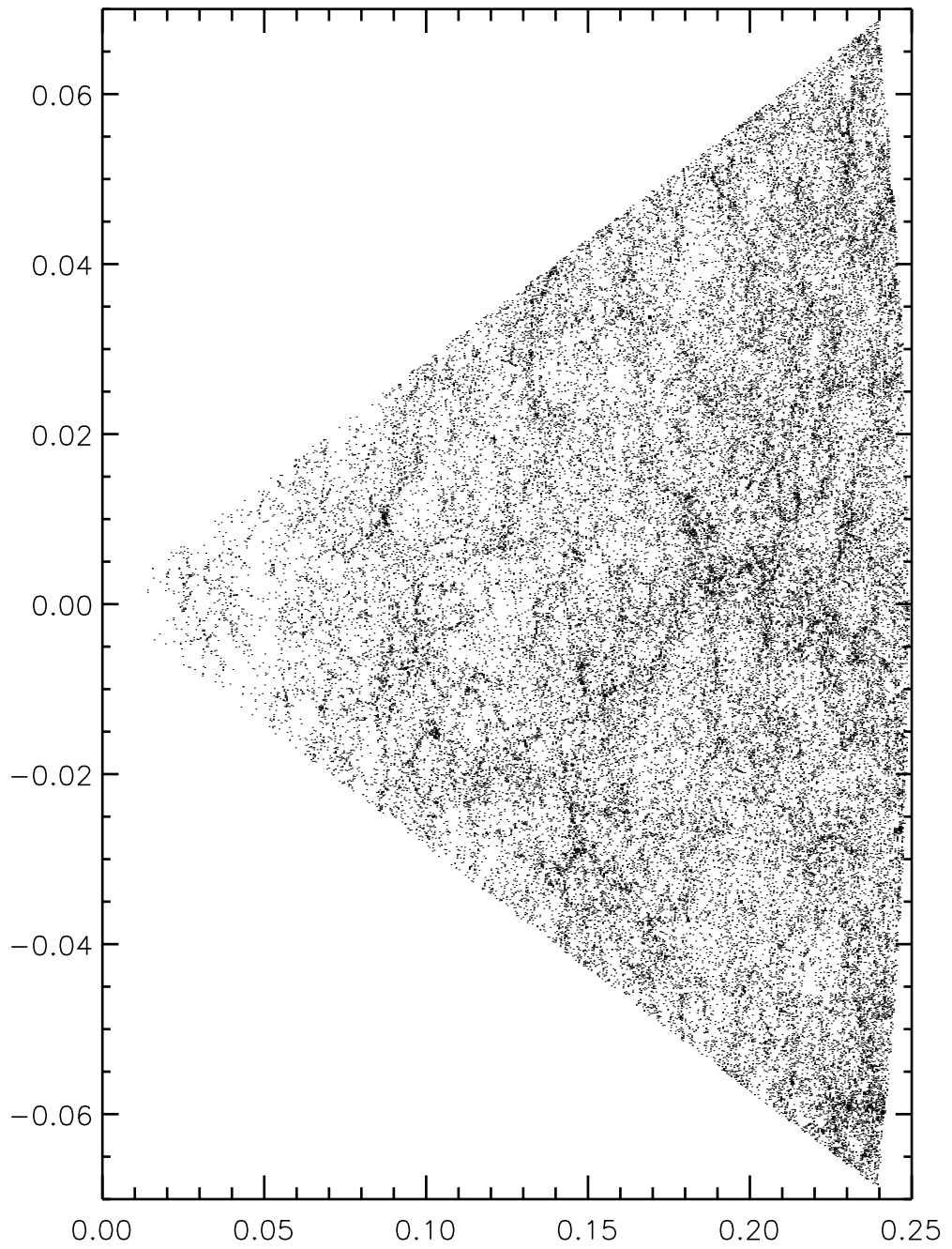
Figure 4.4: Projected galaxy distribution in the 2dFGRS synthetic field as a function of RA and redshift.

4.4 Comparison of several of the versions of the light cone software.

4.4.1 Description of the three main versions

First version: the modified Kitzbichler & White (2007).

This version is described in detail in Section 4.2 above.

Second version: the modified Kitzbichler & White (2007) with an improved random transformation scheme.

As already alluded to in the last paragraph of Section 4.2.2, the different random transformations applied to each of the boxes encountered after $d_{c,rep}$ lead to a loss of some of the large scale correlations of the original simulation. A second version of the software was thus written which applied the same random transformations to all the boxes with $nd_{c,rep} \leq d_{int} < (n+1)d_{c,rep}$ where d_{int} is the distance to the point where the beam centreline intersects the front of the box and $n \geq 0$ in order to try to mitigate the effects of the random transformations.

Third version: the simplest method.

This third method is as simple as possible and similar to the one commonly employed in the literature (e.g. Scaramella, Cen & Ostriker 1993; da Silva et al. 2000; Croft et al. 2001; Blaizot et al. 2005; Roncarelli et al. 2006, 2007; Kay et al. 2012 to cite but a few). It resembles the method showed in the middle panel of figure 4.1. In brief, in this version, the observer is placed at the centre of one of the faces of the box and the end redshift z_{end} is chosen so that the desired field does not subtend more than the comoving size of the box L_{box} at redshift z_{end} (or vice versa) in order to avoid perpendicular replications. The central line of sight in this case no longer goes through the box in a 'slanted' direction but in a straight line. A set of random transformations

of the type described in the final paragraph of Section 4.2.2 is applied to each of the simulation boxes which have been stacked in order to reach $d_{c,end}$. The choice of the right snapshot and the inclusion within the cone are done using criteria analogous to the ones described in Section 4.2.3, the only difference being that the definition of a new 3D right-handed cartesian system of axes with one axis being the central l.o.s. to compute α and δ is no longer needed as the central l.o.s is now parallel to one of the axes of the simulation box (i.e. one can now directly turn the 3D cartesian coordinates in the box frame into α and δ).

4.4.2 Comparison of the FoF halo power spectra

The accuracy with which the various methods reproduce the FoF halo power spectrum of the original simulation traces their ability to conserve the large-scale clustering. The best method will be the one that offers the best compromise between computing time and preservation of the clustering at large scales.

The FoF halo power spectrum was computed for both the FoF light cones generated using the three methods described in the previous Section and for the original simulation using the method pioneered by Szalay et al. (1991) for galaxies as follows (see also Yoshida et al. 2001; van Daalen et al. 2011):

1. The FoF halo density field was computed by representing each FoF halo by a Dirac δ function at its position $r_n = (\alpha, \delta, z)$: $\rho_{halo}(r) = \sum \delta(r - r_n)$. In practice, this was computed by interpolating using a nearest grid point IDL routine the RA (α) and Dec (δ) of the FoF haloes found in a narrow range of redshift around one of the simulation snapshots. Hereafter, the number of FoF haloes in this narrow redshift range will be denoted by N_h.

2. The power in each of the Fourier components of ρ_{halo} is then given by $P_k = |f_k|^2$ where:

$$f_k = \frac{1}{N_h} \sum_{n=1}^{N_h} e^{2i\pi k r_n} = \frac{\tilde{\rho}_{halo}}{N_h} \tag{4.7}$$

where $\tilde{\rho}_{halo}$ is the Fourier transform of ρ_{halo}, which was computed using an IDL fast Fourier transform routine.

3. For each of the three methods, the reference FoF halo power spectrum (represented by dashed lines on figure 4.5) was computed using only the SUBFIND outputs for the haloes contained in the light cone. The same random transformations as the ones used for the light cones were applied to the outputs of SUBFIND before computing the reference power spectra.

Figure 4.5 presents the light cones (solid lines) and reference (dashed lines) FoF halo power spectra at $z = 2$ for the three methods presented in the previous Section: the magenta lines correspond to the first method, the black lines to the second method (which is supposed to improve the large-scale correlations of the first by applying the same random transformations to all the connected boxes) and the red lines to the third method, which is the simplest one. Note that for this figure, P_k has been turned into $P(l)$ and plotted as a function of multipole $l = 2\pi k$ as is nearly always done in the literature. All three methods lead to similar power spectra at small scales (large l) and are close to their reference spectra at those scales (the small difference at large l is likely due to the need to assign a distance from the observer to the FoF haloes when computing the reference power spectrum for each method: $d_c(z = 2)$ was used here). The first and second methods which are much more complicated and CPU intensive (it takes about 30 days to generate a single 5 degrees on a side gas cone going up to $z = 3$ using the first two methods, whereas it takes about 30 hours when using the third method) than the simplest one (the third one) do not do significantly better at large scales (low-multipole) in terms of conservation of the large scale clustering. The increased complexity of the first and second methods and the resulting order of magnitude increase in the required computing time are thus not leading to a significant enough improvement at large scales for justifying their use. Hence, only light cones generated using the simplest method will be used in the remainder of the thesis. The order of magnitude decrease in computing times furthermore allows for the generation of more realisations (by varying the seeds for the generation of the random transformations) of a given synthetic survey, which are extremely useful for assessing the cosmic
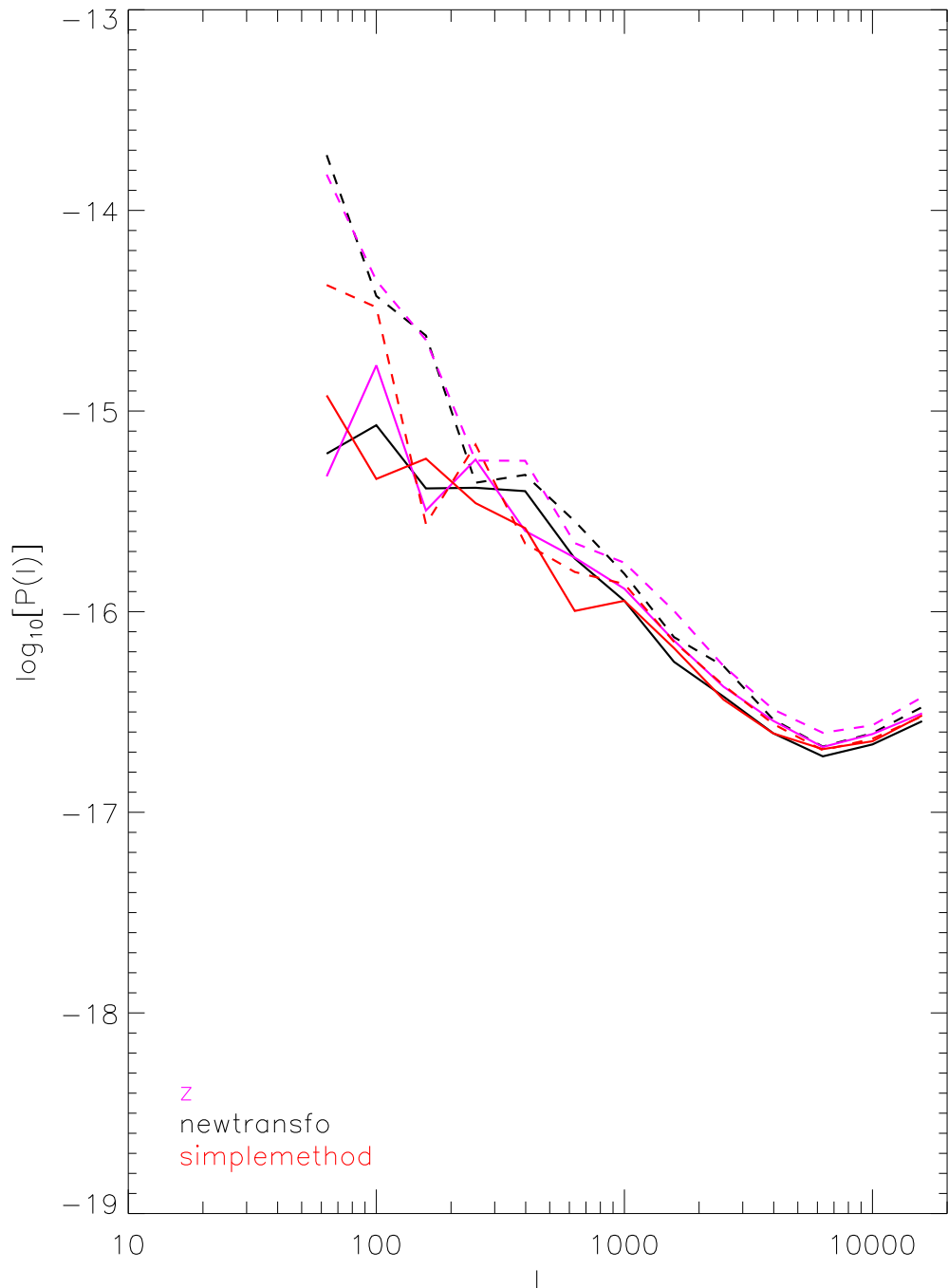
Figure 4.5: FoF halo power spectra at $z = 2$ for the three light cone generation methods presented in Section 4.4.1. The reference power spectra computed using the simulation SUBFIND outputs and the power spectra computed using the light cones are depicted by dashed and solid lines, respectively. The three methods are represented by lines of different colours: the magenta lines correspond to the first method, the black lines to the second method (which is supposed to improve the large-scale correlations of the first by applying the same random transformations to all the connected boxes) and the red lines to the third method, which is the simplest one.

variance (see for instance Chapter 5).

4.5 An example application: synthetic Sunyaev–Zel'dovich observations

The thermal Sunyaev–Zel'dovich signal is characterised by the dimensionless Compton y parameter, defined as:

$$y \equiv \frac{\sigma_T}{m_e c^2} \int P_e dl \tag{4.8}$$

where σ_T is the Thomson cross-Section, c the speed of light, m_e the electron rest-mass and $P_e = n_e k_B T_e$ is the electron pressure with k_B being the Boltzmann constant. The integration is done along the observer's line of sight.

Figure 4.6 shows an example set of synthetic Compton y maps for the five physical models in the *Planck* cosmology, in addition to one in the *WMAP*7 cosmology (bottom right panel). Each map is 5 degrees on a side and was generated using the same random transformations with the simplest method for light cone making described in Section 4.4.1.

The method of Roncarelli et al. (2006, 2007) was followed and

$$\Upsilon_i \equiv \frac{\sigma_T}{m_e c^2} \frac{k_B T_i m_i}{\mu_{e,i} m_H} \tag{4.9}$$

was computed for the ith gas particle, where T_i, m_i and $\mu_{e,i}$ are respectively the temperature, mass and mean molecular weight per free electron of the gas particle and m_H is the atomic mass of hydrogen. The contribution to the Compton y parameter by the ith particle is given by

$$y_i \equiv \Upsilon_i / L_{pix,i}^2 \tag{4.10}$$

where $L_{pix,i}^2$ is the physical area of the pixel in which the ith particle falls at the angular diameter distance from the observer to the particle. Finally, y_i is SPH-smoothed onto the map using the SPH smoothing kernel which was used by GADGET3 for the com-
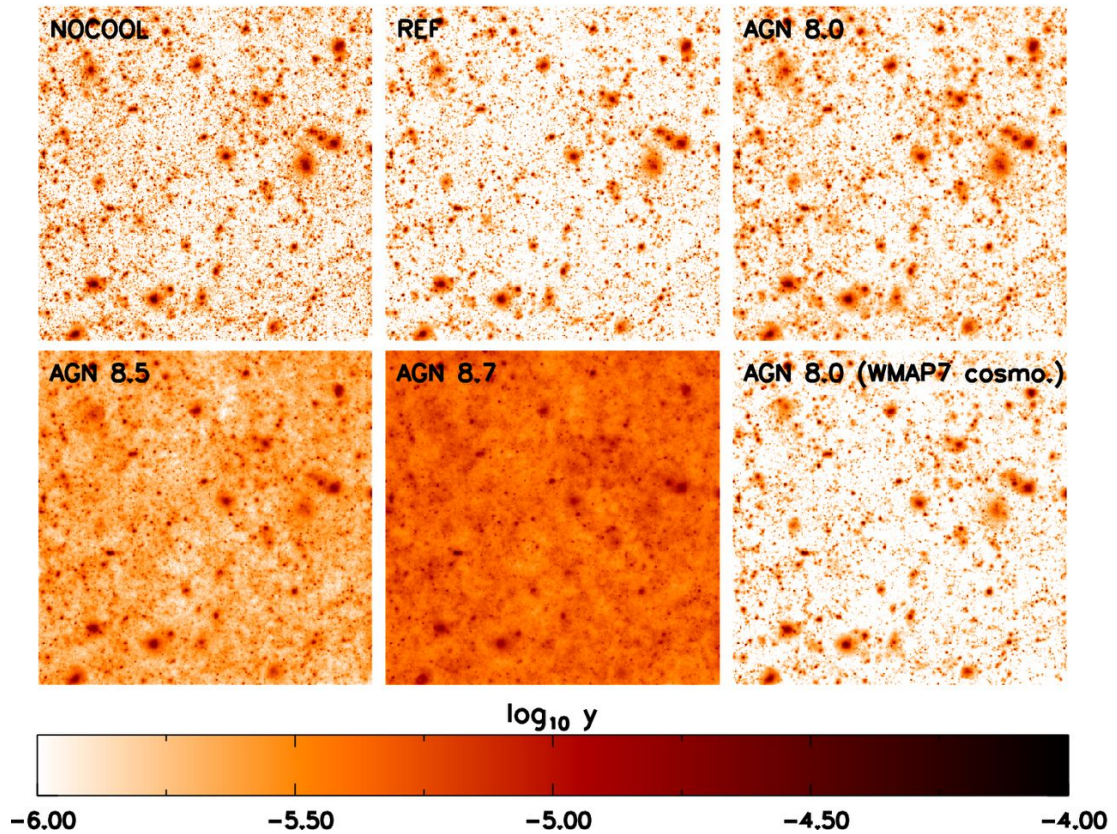
Figure 4.6: Example synthetic Compton y maps for the five physical models in the *Planck* cosmology, in addition to one in the *WMAP*7 cosmology (*bottom right* panel). Each map is 5 degrees on a side and was generated using the same random transformations with the simplest method for light cone making described in Section 4.4.1. Figure taken from McCarthy et al. (2014).

putation of the hydrodynamical forces and the three-dimensional smoothing length of the particle (as computed by GADGET3).

Figure 4.6 illustrates the fact that the Sunyaev–Zel'dovich signal is extremely sensitive to the effects of 'sub-grid' physics (which are readily visible by eye) and to slight changes in cosmology. The latter sensitivity is the main reason for the recent widespread enthusiasm for the use of Sunyaev–Zel'dovich observations for cosmological studies.

Chapter 5

How well can we recover the Sunyaev–Zel'dovich flux of low-mass haloes? The role of source confusion and deviations from the universal pressure profile.

Ian McCarthy generated the majority of the Sunyaev–Zel'dovich maps (the rest was generated by Amandine Le Brun using the same code) and ran a new version of SUB-FIND that stores the particles within $5r_{200}$ for each of the FoF haloes (whose outputs were used to compute the pressure profiles within $5r_{500}$). Jean-Baptiste Melin ran the *Planck* matched filter on the maps, generated maps that contain only GNFW haloes, and wrote and ran a modified version of the *Planck* matched filter (modified to use the best-fitting pressure profiles from the AGN 8.0 simulations as a spatial template) on the maps. Amandine Le Brun generated the gas light cones that were used as input to the map-making software, the halo light cones and extracted the LBG-like samples from the above, made the predictions for confusion and all the plots, computed the pressure profiles within $5r_{500}$ and found the best-fitting functional form for the pressure profiles.

117

5.1 Introduction

In late 2012, the *Planck* collaboration reported a significant detection of the thermal Sunyaev–Zel'dovich signal emitted by the hot gas trapped in the potential wells of individual galaxies (Planck Intermediate Results XI; hereafter PIntXI). Their result implies, rather surprisingly, that the $Y_{500} - M_{500}$ scaling relation is nearly self-similar from galaxy clusters down to galaxies not much bigger than the Milky Way (in terms of their total mass). The naive interpretation of their results is that the gas mass fraction is constant and nearly universal, which is in contradiction with X-ray observations of mostly groups and clusters (e.g. David et al. 2006; Gastaldello et al. 2007; Pratt et al. 2009; Sun et al. 2009) and absorption line studies of local galaxies (e.g. Miller & Bregman 2013). Yet, stacking and assumptions about the pressure profiles were required in order to extract a significant signal. In addition, the contribution of both correlated and uncorrelated line-of-sight hot gas is not well known. The impact of all these effects on the recovered signal can be tested using synthetic observations from a suite of reasonably realistic hydrodynamical simulations. If it holds, the PIntXI result has fundamental consequences for theories of galaxy formation, as the fraction of hot gas which is trapped within the virial radius of individual galaxies, groups and clusters is a sensitive probe of the feedback mechanisms (e.g. Bhattacharya, Di Matteo & Kosowsky 2008; Puchwein, Sijacki & Springel 2008; Short & Thomas 2009; Fabjan et al. 2010; McCarthy et al. 2010; Stanek et al. 2010; Planelles et al. 2013; see also Chapter 2).

This motivated the present Chapter, which employs synthetic observations generated for a state-of-the-art suite of large-volume hydrodynamical cosmological simulations to assess and attempt to explain the potential biases in the analysis conducted in PIntXI. The remainder of this Chapter is organised as follows. The cosmo-OWLS suite used here and the generation of a synthetic sample as similar as possible to the one used for the PIntXI analysis are briefly introduced in Section 5.2. The need for synthetic Sunyaev–Zel'dovich observations is then justified in Section 5.3, the potential impact of confusion is tested in Section 5.4.1 and lastly the role of deviations from the

universal pressure profile is determined in Section 5.4.2. Finally, the main results are discussed and summarised in Section 5.5.

5.2 Simulations

5.2.1 cosmo-OWLS

Some of the physical models from the cosmo-OWLS suite of cosmological hydrodynamical simulations described in detail in Chapter 2 (see also McCarthy et al. 2014; van Daalen et al. 2014; Velliscig et al. 2014) were used. They form an extension to the OverWhelmingly Large Simulations project (OWLS; Schaye et al. 2010) which has been specifically designed to help improve our understanding of galaxy cluster astrophysics and with on-going and up-coming cluster cosmology surveys in mind.

Some of the simulations have been run at eight times higher mass resolution and two times higher spatial resolution, but in a smaller volume (the boxes are $100 \ h^{-1}$ comoving Mpc on a side) as currently available hardware precludes the running of higher resolution simulations in $400 \ h^{-1}$ Mpc on a side boxes. Thus only the *WMAP*7 runs which have an associated higher resolution simulation will be used. The hierarchy of boxes is fundamental for conducting the study presented here as haloes need to be adequately resolved over the wide range of mass scale which was probed by the *Planck* observations presented in PIntXI – from individual galaxies with $M_{500} \sim 2 - 3 \times 10^{12} \ \mathrm{M}_\odot$ up to massive clusters with $M_{500} \sim 2 - 3 \times 10^{15} \ \mathrm{M}_\odot$ – as the high resolution needed to reasonably resolve the former systems is unfortunately unreachable in the large volumes needed to have the latter systems which have very low space densities ($\lesssim 10^{-5.4} \ \mathrm{Mpc}^{-3}$; e.g. Jenkins et al. 2001).

Four of the five physical models described in Chapter 2 were used: a non-radiative model (NOCOOL); a model (REF which corresponds to the OWLS reference model) which includes prescriptions for metal-dependent radiative cooling (Wiersma, Schaye & Smith 2009), stellar evolution, mass loss and chemical enrichment (Wiersma et al.

2009), star formation (Schaye & Dalla Vecchia 2008) and kinetic stellar feedback (Dalla Vecchia & Schaye 2008) and two models (AGN 8.0, which was simply called AGN in the original OWLS papers, and AGN 8.5) which further include a prescription for supermassive black hole growth and AGN feedback (Booth & Schaye 2009), which is a modified version of the model developed by Springel, Di Matteo & Hernquist (2005).

Table 3.1 provides a list of the runs used here and the sub-grid physics that they include.

These models have been compared to a wide range of observational data in both Chapter 2 and McCarthy et al. (2014). In Chapter 2, the focus was on the comparison to the resolved hot gas (e.g. X-ray luminosities and temperatures, gas fraction, entropy and density profiles, integrated Sunyaev–Zel'dovich signal) and stellar properties (e.g. I-band total-mass-to-light ratio, dominance of the brightest cluster galaxies) of local galaxy groups and clusters, as well as the properties of the central black hole, concluding that the fiducial AGN model (AGN 8.0) produces a realistic population of galaxy groups and clusters, broadly reproducing both the median trend and, for the first time, the scatter in physical properties over approximately two decades in mass (10^{13} M$_\odot \lesssim M_{500} \lesssim 10^{15}$ M$_\odot$) and 1.5 decades in radius ($0.05 \lesssim r/r_{500} \lesssim 1.5$); whereas in McCarthy et al. (2014), the sensitivity of the thermal Sunyaev–Zel'dovich power spectrum to important non-gravitational physics was explored and it was found that while the signal on small and intermediate scales is highly sensitive to the included galaxy formation physics, the signal on large scales is only mildly affected and also shown that the fiducial AGN model adequately matches the observed pressure profiles of local groups (outside $\gtrsim 0.3r_{500}$) and clusters (see their figure 2).

5.2.2 Synthetic Sunyaev–Zel'dovich observations

The thermal Sunyaev–Zel'dovich maps

The thermal Sunyaev–Zel'dovich signal is characterised by the dimensionless Compton y parameter as defined by equation (4.8).

Compton y maps were generated by stacking randomly transformed (by a combination of translations, rotations and axis inversions) snapshots along the observer's line of sight using a light cone software, which uses methods that are similar in spirit to the 'random tiling' method developed by Blaizot et al. (2005) and slightly modified by Kitzbichler & White (2007). The light cones extend back to $z = 3$. McCarthy et al. (2014) showed that this redshift is high enough for the thermal Sunyaev–Zel'dovich power spectrum to approximately converge. Therefore, the maps should provide a sufficiently good approximation of the unresolved Sunyaev–Zel'dovich background for the purposes of the study presented here. Ten (sixteen) quasi-independent realisations were obtained by varying the initial random seeds for the large lower resolution (smaller higher resolution) simulations. As the methods used for the production of the Compton y maps are described in some detail in McCarthy et al. (2014), only a brief summary will be presented below.

The method described in Section 4.5 was used to generate the Compton y maps using an angular pixel size of 2.5 arcseconds. This corresponds to a finer resolution than that currently reached by Sunyaev–Zel'dovich experiments. This high angular resolution was adopted because it is similar to that achieved by contemporary X-ray telescopes (e.g. *XMM–Newton* and *Chandra*) and X-ray maps are generated simultaneously with the thermal Sunyaev–Zel'dovich maps. Note that McCarthy et al. (2014) have shown that the specific choices of smoothing kernel (here the SPH smoothing kernel used by GADGET3 for the evaluation of the hydrodynamical forces) and smoothing length (the three-dimensional smoothing length of the particle as computed by GADGET3) have no impact upon the thermal Sunyaev–Zel'dovich power spectrum.

The maps are five degrees (1.25 degrees) on a side for the large lower resolution

(smaller higher resolution) simulations. This roughly corresponds to the angular size of the $400 \, h^{-1}$ comoving Mpc ($100 \, h^{-1}$ comoving Mpc) at $z = 3.0$. The ten (sixteen) realisations are therefore only quasi-independent as they were produced using the same simulation: at high redshift, they then use most of the volume of that simulation and thus contain many of the same structures. But, at lower redshift, the maps correspond to a rather small fraction of the simulated volume and the different realisations are hence really independent. The rationale behind using several quasi-independent realisations is to mitigate the impact of cosmic variance upon the results presented here.

Table 5.1 provides a list of the maps used here and their main properties.

Simulation	Box size	Number of particles	Map angular size	Pixel size	Number of pixels	Number of realisations
Large lower resolution	400 h^{-1} Mpc	2×1024^3	$5°$	$2.5''$	7200	10
Small higher resolution	100 h^{-1} Mpc	2×512^3	$1.25°$	$2.5''$	1800	16

Table 5.1: Characteristics of the maps used here.

Mimicking the Planck locally brightest galaxy sample

PIntXI stacked $\sim 260\,000$ locally brightest galaxies taken from the Sloan Digital Sky Survey in order to extend the relation between the Sunyaev–Zel'dovich signal and the halo mass down to $M_{500} \sim 4 \times 10^{12}$ M$_\odot$. They defined their locally brightest galaxy (hereafter LBG) sample as all the galaxies with $z > 0.03$ that are brighter in the r-band than any other of the galaxies with $r < 17.7$[1] projected within 1.0 Mpc and with a redshift difference smaller than $1,000$ km s^{-1} taken from the spectroscopic New York University Value Added Galaxy Catalogue (NYU-VAGC)[2], which is based on the seventh data release of the Sloan Digital Sky Survey (SDSS/DR7; Abazajian et al., 2009) and was put together by Blanton et al. (2005). It covers 7966 square degrees. As the SDSS spectroscopic coverage is incomplete, SDSS galaxies without spectroscopic data could violate the selection criteria chosen by the Planck collaboration. In order to alleviate this potential problem, the Planck collaboration used one of the SDSS photometric redshift catalogues (Cunha et al. 2009) to eliminate any candidate galaxy with a companion in the photometric catalogue which is at least as bright in the r-band, projected within 1.0 Mpc and with a photometric redshift distribution consistent with the spectroscopic redshift of the candidate galaxy. This results in a final cleaned sample of 259 579 locally brightest galaxies. The NYU-VAGC also provides, among other properties, stellar masses which were computed by Blanton & Roweis (2007) by fitting stellar populations to the five-band SDSS photometry assuming a Chabrier (2003) initial mass function.

In order to relate the observed stellar mass of the LBGs to their unobservable halo mass, they use the publicly available[3] semi-analytic galaxy formation model of Guo et al. (2011) which was tuned to very closely match the observed luminosity and stellar mass functions of SDSS galaxies in a *WMAP*7 cosmology (Guo et al. 2013) to get the median stellar mass–halo mass relation for a sample of simulated galaxies selected in the same way as the SDSS LBG sample. The median stellar mass–halo mass relation

---

[1] where r is the r-band, extinction-corrected Petrosian magnitude
[2] http://sdss.physics.nyu.edu/vagc/
[3] http://mpa-garching.mpg.de/millennium

was used by the Planck collaboration to set the angular size of the matched filter when they stacked the Sunyaev–Zel'dovich signal in bins of stellar mass and to turn the integrated Sunyaev–Zel'dovich signal–stellar mass relation that resulted into an integrated Sunyaev–Zel'dovich signal–halo mass scaling relation.

The Sunyaev–Zel'dovich signal is characterised by the value of its spherically integrated Compton parameter

$$d_A(z)^2 Y_{500} = \frac{\sigma_T}{m_e c^2} \int P_e dV, \qquad (5.1)$$

where $d_A(z)$ is the angular diameter distance and the integration is done over a sphere of radius r_{500}. Throughout the Chapter, unless otherwise stated, the following quantity is used:

$$\tilde{Y}_{500} \equiv Y_{500} E^{-2/3}(z) \left(\frac{d_A(z)}{500 \text{ Mpc}} \right)^2, \qquad (5.2)$$

where $E(z) \equiv H(z)/H_0 = \sqrt{\Omega_m(1+z)^3 + \Omega_\Lambda}$ gives the redshift evolution of the Hubble parameter $H(z)$ in a flat ΛCDM Universe. $\tilde{Y}_{500}$ corresponds to the intrinsic Sunyaev–Zel'dovich signal self-similarly scaled to $z = 0$ and scaled to a fixed angular diameter distance. The thermal Sunyaev–Zel'dovich signal is extracted using a multi-frequency matched filter (MMF; Herranz et al. 2002; Melin, Bartlett & Delabrouille 2006), which is optimised in both frequency and angular space[4] by assuming the known frequency dependence of the thermal Sunyaev–Zel'dovich effect and the 'universal pressure profile' (Arnaud et al. 2010; hereafter A10), derived from a combination of X-ray observations of the *XMM–Newton* REXCESS cluster sample (Böhringer et al., 2007). In order to mitigate the impact of dust on their results, the Planck collaboration decided to use only the three lowest frequencies of the *Planck* HFI instrument (see PIntXI for discussion). The matched filter is run in non-blind mode: it uses the known position and size of the target LBG. Specifically, the stellar mass–halo mass relation is used to get the median M_{200} as a function of LBG stellar mass, which is then converted into a M_{500} assuming an NFW profile (Navarro, Frenk & White 1997) and the Neto et al. (2007) mass–concentration relation. The resulting R_{500} is finally

---

[4]It maximises the signal-to-noise ratio of objects which follow the assumed spectral and spatial templates.

turned into a θ_{500} which is used to set the angular scale of the matched filter (see Planck Early Results VIII, Planck Early Results IX, Planck Early Results XI and PIntXI for details and discussion). The MMF then gives a measure of the strength of the Sunyaev–Zel'dovich signal $\tilde{Y}_{500}(i)$ and its associated measurement uncertainty $\tilde{\sigma}_{\theta_{500}}(i)$ for the halo surrounding the ith galaxy. The measurement uncertainty takes into account the statistical uncertainties due to astrophysical (e.g. primary CMB, dust) and instrumental (e.g. beam smearing) noise, but not the uncertainties due to halo modelling (e.g. shape of the pressure profile, size).

In order to make comparisons that are as like-with-like as possible, the Planck LBG sample and its analysis have been mimicked. In brief, halo catalogues corresponding to the maps described in Section 5.2.2 were constructed using a standard friends-of-friends (FoF) algorithm run on the snapshot data. They contain the positions on the map of the centre of mass, the angular size θ_{500} and the halo mass M_{500} of all the haloes with $z < 0.4$ and $M_{500} > 2 \times 10^{13}$ $M_{\odot}$ ($M_{500} > 10^{12}$ $M_{\odot}$) for the large lower resolution (smaller higher resolution) simulations. The redshift and mass thresholds have been chosen such that the combination of the two sizes of simulations for the same physical model results in a synthetic LBG catalogue. The simulated maps were downgraded from their original 2.5 arcseconds resolution to a 0.83 arcminute resolution[5]. The effects of primary CMB, of the Planck beams and their associated noise were then added to obtain six synthetic observations at the frequencies of the Planck HFI instrument (100, 143, 217, 353, 545 and 857 GHz). The multi-frequency matched filter which was used by the Planck collaboration for the analysis of the LBG sample was then used on the synthetic observations. It was run by Jean-Baptiste Melin in a non-blind mode using the positions and the size of the synthetic LBG halo catalogue. The maps for the small higher resolution simulation, which are 1.25 degree on a side, turned out to be too small for the MMF to work properly[6]. In order to circumvent that problem, the sixteen realisations of the small higher resolution simulations were stitched together to form a 5 degrees on a side map, i.e. it has the same size as an individual map of the large lower resolution simulations. Finally, as cosmic variance

---

[5]which corresponds to 20 pixels at the original resolution

[6]The Planck collaboration is running the MMF on maps that are 10 degrees on a side.

could potentially affect the results for the simulations[7] as the simulated maps are only 5 degrees on a side, 25 different realisations of the primary CMB and of the instrumental effects were added to the ten quasi-independent maps used for the large lower resolution simulation and to the combined map used for the small higher resolution simulation before processing with the MMF in order to limit its impact. As many of these realisations as was needed for having error bars that are comparable to the observed ones have been used: this meant only two of the 25 realisations were required for each of the ten maps for the large lower resolution simulation and twenty-five realisations of the combined map for the small higher resolution simulation.

Finally, for both simulations and observations, the Sunyaev–Zel'dovich signal is binned by (stellar) mass with the bin-average signal and the corresponding uncertainty given by (Planck Early Results VIII; Planck Early Results XI; PIntXI)

$$\langle \tilde{Y}_{500} \rangle_b = \frac{\sum_{i=1}^{N_b} \tilde{Y}_{500}(i)/\tilde{\sigma}_{\theta_{500}}^2(i)}{\sum_{i=1}^{N_b} 1/\tilde{\sigma}_{\theta_{500}}^2(i)} \tag{5.3}$$

and

$$\sigma_b^{-2} = \sum_{i=1}^{N_b} 1/\tilde{\sigma}_{\theta_{500}}^2(i), \tag{5.4}$$

where N_b is the number of galaxies in bin b. The integrated Sunyaev–Zel'dovich signal is often normalized by the self-similar integrated Sunyaev–Zel'dovich signal–mass relation, as given in appendix B of A10:

$$\tilde{Y}_{500,A10} = 9.07 \times 10^{-4} \left[\frac{M_{500}}{3 \times 10^{14} h_{70}^{-1} \mathrm{M}_\odot} \right]^{5/3} h_{70}^{-1} \ \mathrm{arcmin}^2 \tag{5.5}$$

---

[7]It should not be an issue for the Planck LBG sample as the NYU-VAGC covers 7966 square degrees.

5.3 The need for synthetic Sunyaev–Zel'dovich observations

The Planck LBG results are first compared to the intrinsic spherically integrated Sunyaev–Zel'dovich signal–mass relation of the simulated galaxy, group and cluster populations for the four physical models used here. In figure 5.1, the intrinsic spherically integrated Sunyaev–Zel'dovich signal–M_{500} relation is plotted for the various simulations and compared to the Planck LBG result (PIntXI). The solid and dashed curves respectively represent the mean and median relations in bins of M_{500} for the different simulations. The $z = 0$ snapshots (i.e. no synthetic observations were used) of the high resolution simulations were used below $M_{500} = 2 \times 10^{13}$ M$_{\odot}$ and the production runs above that threshold. The filled red circles with error bars represent the observational data of PIntXI. From this figure, it is readily apparent that, taken at face value, the Planck LBG result seems to favour a close to self-similar Y_{500}–M_{500} relation, as obtained in non-radiative simulations (such as NOCOOL; red lines). This implies that the haloes of galaxies, groups and clusters have gas fractions within r_{500} that are nearly equal to the universal baryon fraction f_b, which is in contradiction with X-ray observations (e.g. David et al. 2006; Vikhlinin et al. 2006; Pratt et al. 2009; Sun et al. 2009; Lin et al. 2012).

But, Planck is not directly measuring the intrinsic three-dimensional spherically integrated Sunyaev–Zel'dovich signal within r_{500}: it makes use of a MMF (Melin, Bartlett & Delabrouille 2006) which measures the two-dimensional flux within $5\theta_{500}$ assuming the known spectral shape of the thermal Sunyaev–Zel'dovich effect and that the haloes follow the universal pressure profile of A10 (see Section 5.2.2 for details). The two-dimensional flux within $5\theta_{500}$ is then turned into a three-dimensional flux within a sphere of radius r_{500} assuming both spherical symmetry and that the universal pressure profile holds[8].

---

[8]Using the universal pressure profile given in Section 5 of A10 and assuming spherical symmetry, one gets: $Y_{500} = Y_{5r_{500}}/1.796$.
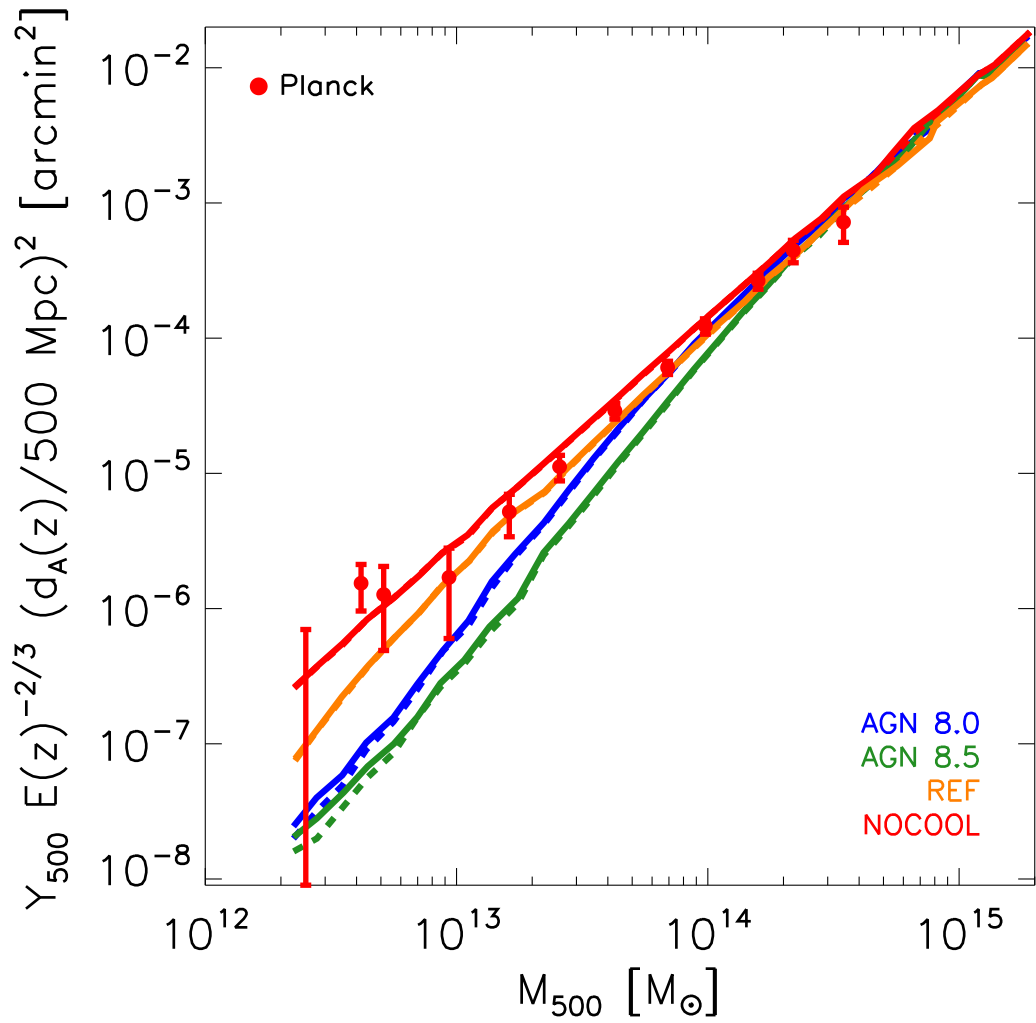
Figure 5.1: The $Y_{500} - M_{500}$ relation at $z = 0$. The filled red circles with error bars represent the observational data of PIntXI. The solid and dashed curves (red, orange, blue and green) represent the mean and median integrated Sunyaev–Zel'dovich signal–M_{500} relations in bins of M_{500} for the different simulations, respectively. The high resolution simulations are used below $M_{500} = 2 \times 10^{13}$ $M_\odot$ and the production runs above that threshold. Taken at face value, the Planck LBG result seems to favour a close to self-similar Y_{500}–M_{500} relation, which is in contradiction with X-ray observations.

In figure 5.2, the mean intrinsic spherically integrated Sunyaev–Zel'dovich signal–M_{500} relation in bins of M_{500} is shown, both unweighted (solid lines) and weighted (dotted lines; as given by equation 5.3), as well as the observational data (filled red circles with error bars) and the results of the synthetic observations of the simulated maps for $z \leq 0.4$ (empty black diamonds). The integrated Sunyaev–Zel'dovich signals have been normalised using the best-fitting scaling relation of A10 (see equation 5.5).
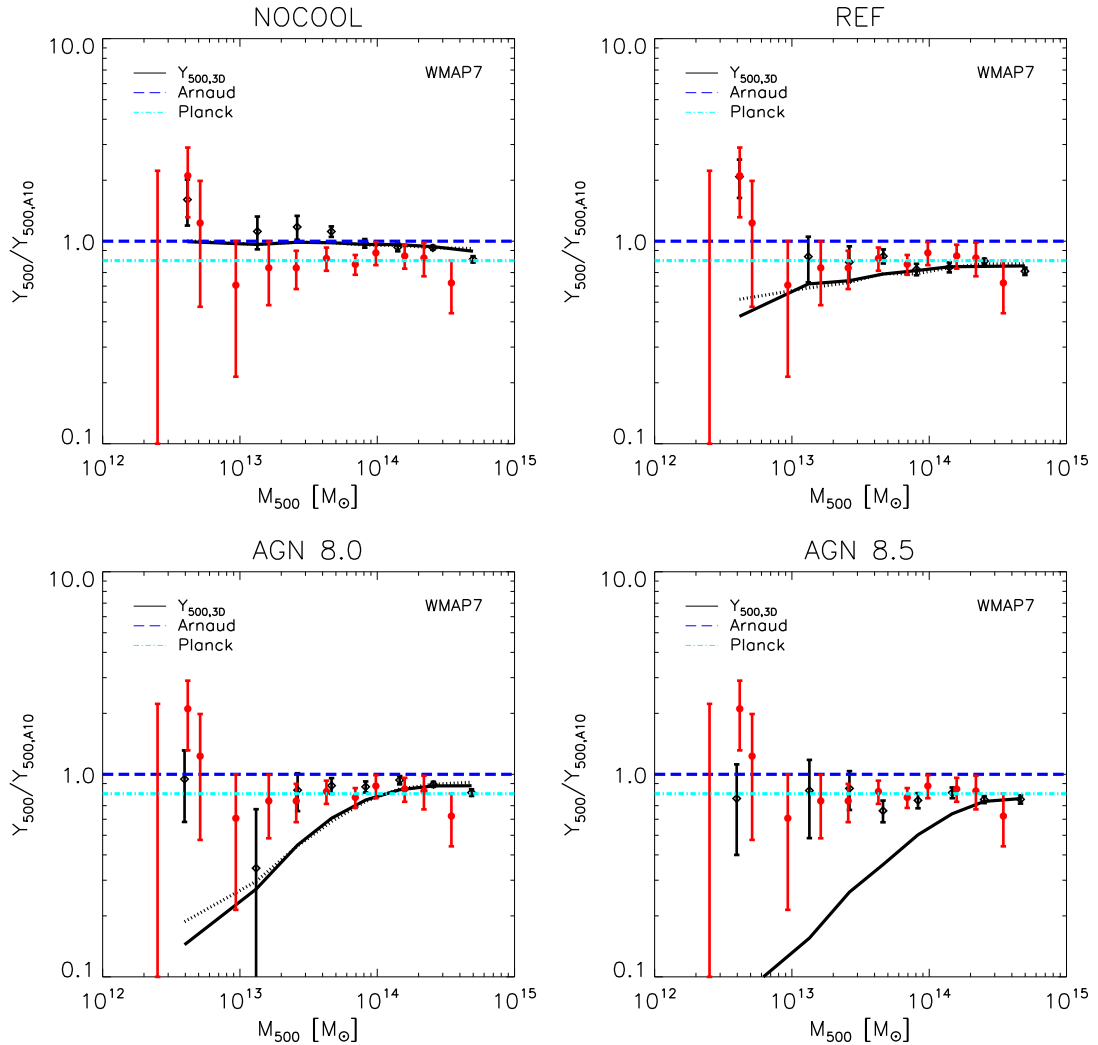
Figure 5.2: The $Y_{500} - M_{500}$ relation for $z \leq 0.4$. The blue dashed and cyan dot-dashed lines correspond to the best-fitting scaling relations of A10 and PIntXI, respectively. The solid and dotted black curves correspond to the unweighted and weighted mean spherically integrated Sunyaev–Zel'dovich signal–M_{500} relations in bins of M_{500} for the different simulations, respectively. The filled red circles with error bars and empty black diamonds correspond to the observational data of PIntXI and the results of the synthetic observations of the simulated maps, respectively. The integrated Sunyaev–Zel'dovich signals have been normalised using the best-fitting scaling relation of A10. The different panels correspond to the different physical models: from NOCOOL (*top left*) to AGN 8.5 (*bottom right*) through REF (*top right*) and AGN 8.0 (*bottom left*). The four panels use the high resolution simulations below $M_{500} = 2 \times 10^{13}$ M$_\odot$ and the production runs above that threshold. The MMF recovers the intrinsic Y_{500}–M_{500} well, with the exception of the lowest mass bin where it is biased high and the amplitude of the bias between the Y_{500}–M_{500} relation recovered by the MMF and the intrinsic one increases and the bias starts at increasingly high masses when AGN feedback is included (and its intensity increased).

The different panels correspond to the different physical models: from NOCOOL (top left) to AGN 8.5 (bottom right) through REF (top right) and AGN 8.0 (bottom left). The four panels use the high resolution simulations below $M_{500} = 2 \times 10^{13}$ $M_\odot$ and the production runs above that threshold.

While assuming spherical symmetry and that the ICM follows the universal pressure profile is a reasonable approximation for the NOCOOL and REF simulations (top row) – in the sense that the MMF (empty black diamonds) recovers the intrinsic Y_{500}–M_{500} (black lines) well, with the exception of the lowest mass bin where it is biased high – the amplitude of the bias between the Y_{500}–M_{500} relation recovered by the MMF and the intrinsic one increases and the bias starts at increasingly high masses when AGN feedback is included (and its intensity increased; bottom row). It is worth pointing out that the fact that the MMF recovers the truth for both NOCOOL and REF is not really surprising as the simulations that were used to determine the universal pressure profile (from Borgani et al. 2004, Nagai, Kravtsov & Vikhlinin 2007 and Piffaretti & Valdarnini 2008) all included some prescription for radiative cooling, star formation and feedback from supernovae (i.e. they are similar to the REF model).

5.4 Investigation of the likely causes for the bias

Likely causes for the bias uncovered in the previous Section are: (i) source confusion at the low-mass end and (ii) deviation from the universal pressure profile at large radii. They are investigated in turn in the following two Subsections.

5.4.1 Source confusion

The issue of source confusion in cluster surveys, and more specifically in Sunyaev–Zel'dovich surveys (for which source confusion is expected to be more problematic since the strength of the Sunyaev–Zel'dovich effect is redshift independent), especially those using instruments with rather large beams (the *Planck* survey falls into that cat-

egory with angular resolutions ranging from $5'$ to $31'$ depending upon the channel frequency) has already been explored using simulations of various degrees of realism over the past fifteen years (e.g. Voit, Evrard & Bryan 2001; White, Hernquist & Springel 2002; Hallman et al. 2007; Holder, McCarthy & Babul 2007). In brief, they all concluded that confusion will be an issue for Sunyaev–Zel'dovich surveys of galaxies, groups and low-mass clusters ($M_{500} \lesssim 10^{14}\ \mathrm{M_\odot}$). For instance, Voit, Evrard & Bryan (2001) found using a back of the envelope calculation (using the Press–Schechter formalism) that the probability that any given line of sight will encounter a virialised structure with $k_B T \gtrsim 0.5\ \mathrm{keV}$ is of order unity and that the virialised regions of groups and clusters cover over a third of the sky. Their use of the Hubble volume simulations (e.g. Jenkins et al. 2001), which has the advantage over the analytic calculation of taking into account the clustering of virialised objects, corroborated their estimate of the group and cluster covering factor.

Figure 5.3 shows the mean angular separation θ normalised by the angular size θ_{500} of the central object as a function of the central object's M_{500}. The central objects are located at $z \leq 0.4$ in order to mimic the LBG sample. The solid, dashed and dot-dashed curves correspond to the distance to objects with $Y_{500} > Y_{500,\text{central object}}/3$, $Y_{500} > Y_{500,\text{central object}}/2$ and $Y_{500} > Y_{500,\text{central object}}$, respectively. The integrated Sunyaev–Zel'dovich signal Y_{500} was computed approximately using the self-similar prediction: $Y_{500} \propto M_{500}^{5/3}/d_A^2$ where d_A is the angular diameter distance. Both panels use the high resolution version of the AGN 8.0 simulation below $M_{500} = 2 \times 10^{13}\ \mathrm{M_\odot}$ and the production run above that threshold. Confusion is hence expected to be a source of large scatter (it could be more than a 100 per cent) at the low-mass end for estimates of the Sunyaev–Zel'dovich signal of individual haloes, as most of them have an object with a similar Sunyaev–Zel'dovich brightness (either in the foreground or the background) which overlaps with them in projection (i.e. $\theta/\theta_{500} < 2$). Note that this can lead to both flux overestimation and underestimation as haloes with an overlapping neighbour with a comparable Sunyaev–Zel'dovich signal will have their signal boosted (could be up to doubled), whereas haloes with no overlapping neighbour with a comparable Sunyaev–Zel'dovich signal could have their signal underestimated (or even become
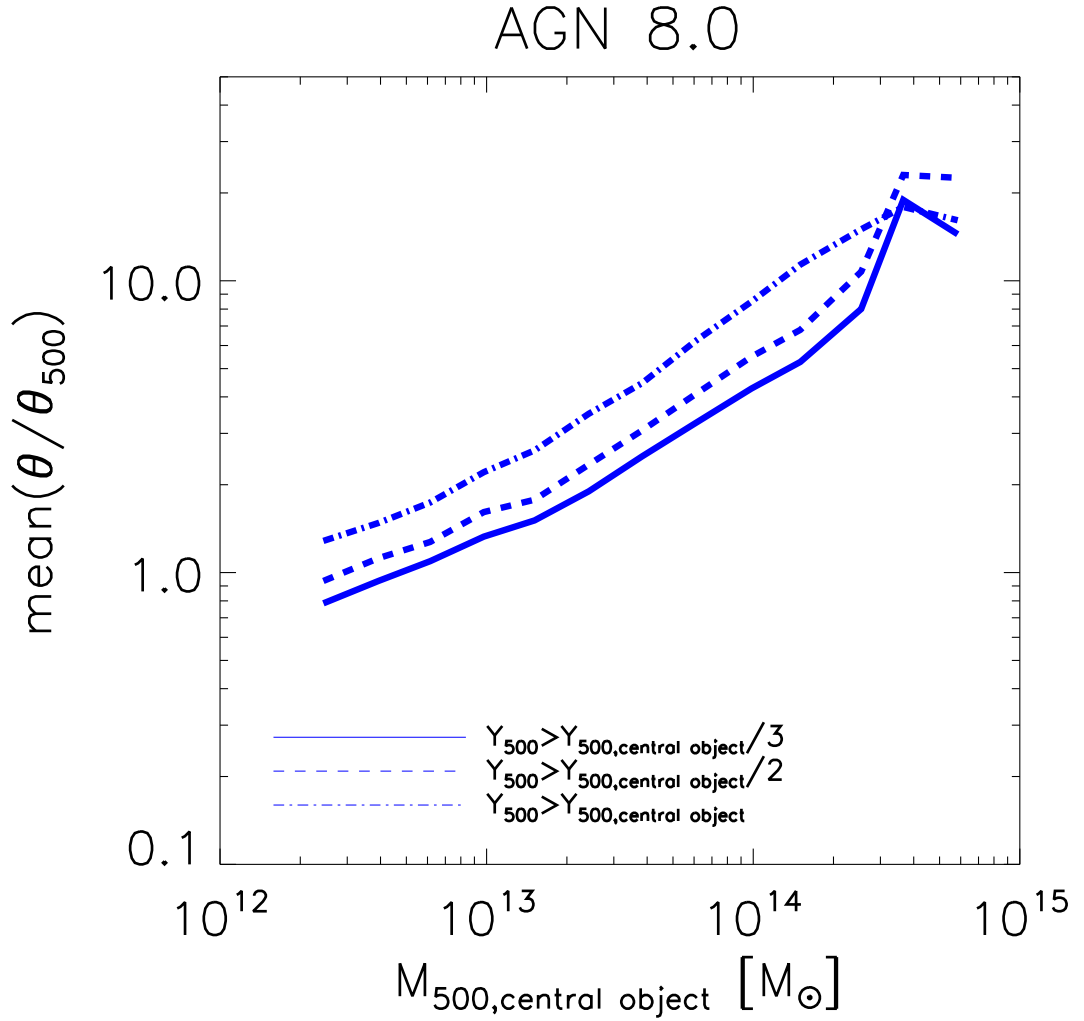
Figure 5.3: The mean separation as a function of the central object's M_{500}. The angular separation is normalised by the angular size θ_{500} of the central object. The central objects are located at $z \leq 0.4$. The solid, dashed and dot-dashed curves correspond to the distance to objects with $Y_{500} > Y_{500,\text{central object}}/3$, $Y_{500} > Y_{500,\text{central object}}/2$ and $Y_{500} > Y_{500,\text{central object}}$, respectively. The integrated Sunyaev–Zel'dovich signal Y_{500} was computed approximately using the self-similar prediction: $Y_{500} \propto M_{500}^{5/3}/d_A^2$ where d_A is the angular diameter distance. The high resolution version of the AGN 8.0 simulation is used below $M_{500} = 2 \times 10^{13}\ \mathrm{M}_\odot$ and the production run above that threshold. Confusion is thus expected to become problematic for individual objects.

undetectable) due to background overestimation.

While confusion is expected to result into sizeable errors in the recovered Sunyaev–Zel'dovich signals of individual low-mass haloes, the recovered mean Sunyaev–Zel'dovich signal (from stacking a large number of systems in mass bins) can still be unbi-
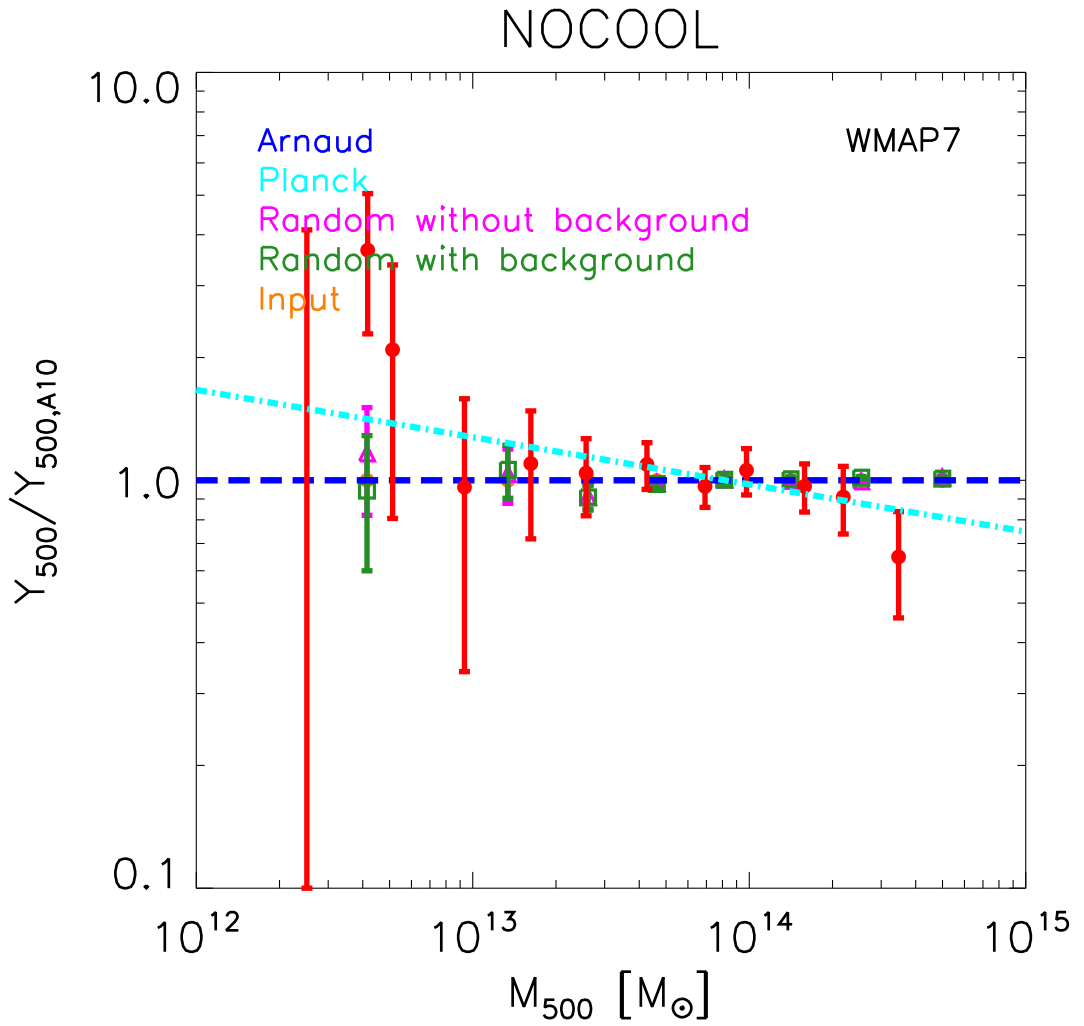
Figure 5.4: The Y_{500}–M_{500} relation at $z \leq 0.4$ for GNFW haloes. The blue dashed and cyan dot-dashed lines correspond to the empirical best-fitting scaling relations of A10 (see their equation 22) and PIntXI, respectively. The filled red circles with error bars represent the observational data of PIntXI. The filled orange circles correspond to the unweighted mean input Y_{500} (computed using the empirical best-fitting $Y_{500}-M_{500}$ of A10) in bins of M_{500}. The empty green squares and magenta triangles with error bars correspond to the weighted mean and errors for the maps generated by injecting the GNFW haloes corresponding to the input Y_{500} at random positions with and without using the original thermal Sunyaev–Zel'dovich maps from the NOCOOL simulation as background. The integrated Sunyaev–Zel'dovich signals have been normalised using the best-fitting empirical scaling relation of A10. The high resolution version of the NOCOOL simulation is used below $M_{500} = 2 \times 10^{13}$ M$_\odot$ and the production run above that threshold. The mean recovered signal is relatively insensitive to the presence of a Sunyaev–Zel'dovich background when a large number of haloes are stacked.

ased. To test this hypothesis, haloes that were generated using a template based on the universal pressure profile of A10 were injected into the original Compton y maps by

Jean-Baptiste Melin. The results of this test are presented in figure 5.4. For each of the haloes in the synthetic LBG catalogue of the NOCOOL simulation, the normalisation of the profile (or equivalently Y_{500}) was set using the empirical $Y_{500}-M_{500}$ relation of A10 (see their equation 22; dashed blue line). A new position was then drawn at random and the flux distributions from all the haloes in the catalogue were combined in order to generate a new Compton y map on which the MMF was run both with and without using the original Compton y maps of the NOCOOL simulations as background. The filled orange circles correspond to the unweighted mean input Y_{500} in bins of M_{500}. The empty green squares and magenta triangles with error bars correspond to the weighted mean and errors for the maps generated by injecting the generalised NFW (Nagai, Kravtsov & Vikhlinin 2007; see Section 5.4.2) haloes corresponding to the input Y_{500} at random positions with and without using the original thermal Sunyaev–Zel'dovich maps from the NOCOOL simulation as background. In order to limit the impact of the added noise (see Section 5.2.2), a hundred realisations of the small higher realisation simulation had to be used (instead of the usual 25) and 25 realisations were used for the large lower resolution simulation. The obtained results are consistent with there being no effects of uncorrelated confusion over the whole mass range (as the magenta and green symbols are consistent within their error bars with their input values) when a large number of haloes are stacked. The mean recovered signal is thus relatively insensitive to the presence of a Sunyaev–Zel'dovich background. This insensitivity to uncorrelated structures could be due to the fact that the MMF does not use the $k = 0$ mode (which corresponds to the constant mean y value of the map).

To summarise, the effects seen in both the observations and the simulations, especially at the low-mass end, must therefore be due to: (i) some mismatch between the intrinsic halo properties at large radii and the universal pressure profile and/or (ii) correlated confusion.

5.4.2 Deviations from the universal pressure profile

In order to convert the signals measured within $5\theta_{500}$ into Y_{500}, the *Planck* collaboration had to assume that the pressure profile is known and given by the universal pressure profile of A10. Their estimates of Y_{500} are therefore only reliable if the assumed pressure profile reasonably describes the pressure profiles of the observed systems over the whole mass and radial ranges probed by the *Planck* observations. In this Section, the extent to which the simulated pressure profiles deviate from the universal pressure profile and its potential consequences for the $Y_{500} - M_{500}$ relation are thus explored.

The generalised NFW (GNFW) model, first introduced by Nagai, Kravtsov & Vikhlinin (2007), was shown by simulations (e.g. Nagai, Kravtsov & Vikhlinin 2007; Kay et al. 2012) and observations (e.g. Mroczkowski et al. 2009; Arnaud et al. 2010; Plagge et al. 2010; Sun et al. 2011; Planck Intermediate Results V; Sayers et al. 2013; McDonald et al. 2014) alike to provide a reasonable description of the pressure profiles of groups and clusters (mostly local but the McDonald et al. 2014 sample of 80 clusters selected from the SPT 2500 deg^2 survey and followed up with *Chandra* covers the $0 \leq z \leq 1.2$ redshift range). This model has five free parameters (see Nagai, Kravtsov & Vikhlinin 2007):

$$\frac{P(r)}{P_{500}} = \frac{P_0}{(c_{500}r/r_{500})^\gamma [1 + (c_{500}r/r_{500})^\alpha]^{(\beta-\gamma)/\alpha}}, \tag{5.6}$$

where

$$P_{500} \equiv n_{e,500} k_B T_{500} \tag{5.7}$$

$$= \frac{500 f_b \rho_{crit}(z) \mu m_p G M_{500}}{\mu_e m_H 2 r_{500}}, \tag{5.8}$$

where $f_b \equiv \Omega_b/\Omega_m$ is the universal baryon fraction, μ and μ_e are the mean molecular weight and the mean molecular weight per free electron, respectively. Nagai, Kravtsov & Vikhlinin (2007) justified the choice of this particular functional form by the fact that the gas pressure distribution is primarily determined by the gravitational dominant dark matter, in which the gas is in hydrostatic equilibrium, and whose density has been shown to follow the NFW profile (e.g. Navarro, Frenk & White 1997).
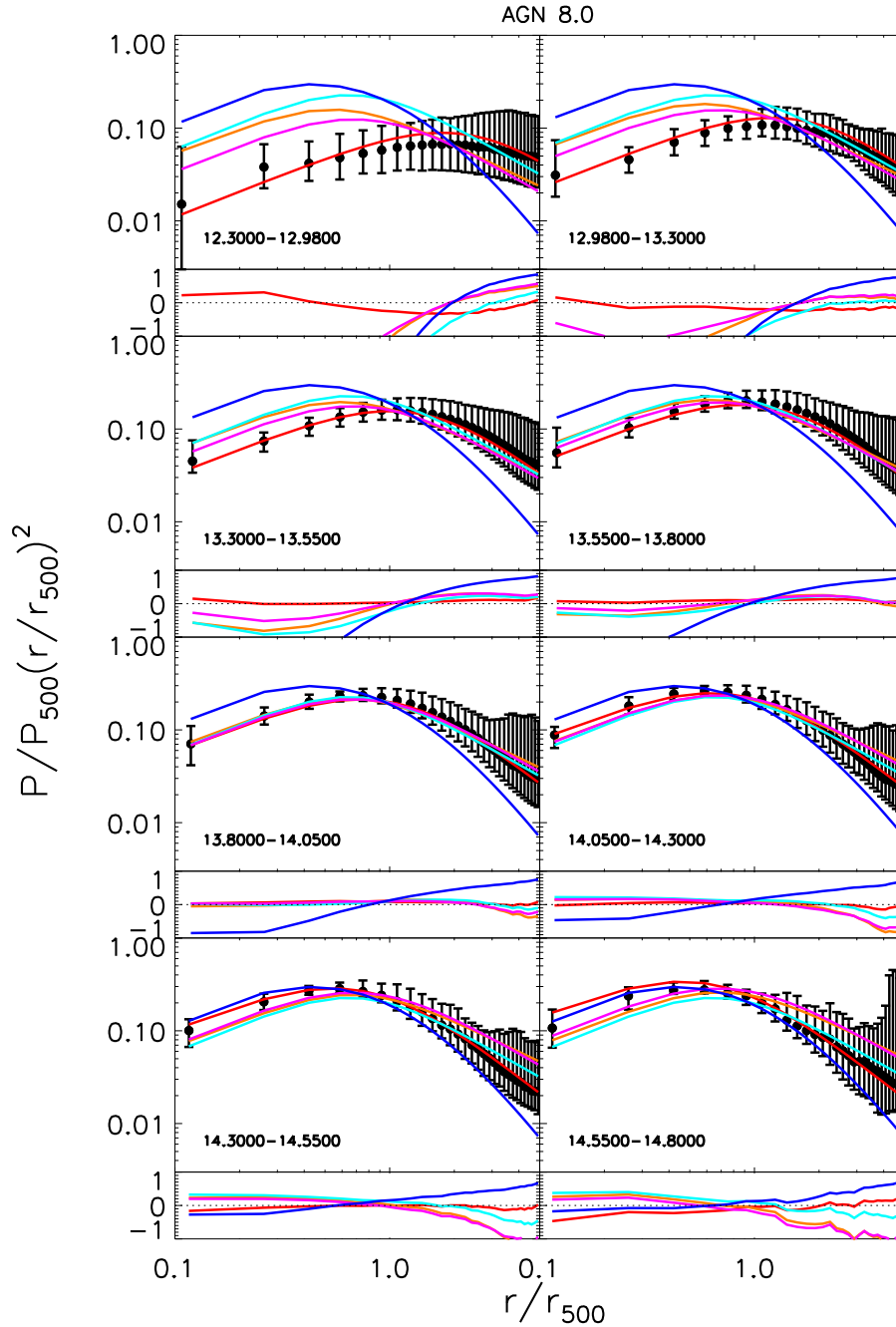
Figure 5.5: Mass-weighted pressure profiles for the AGN 8.0 model. The eight panels correspond to eight different mass bins (increasing from *top left* to *bottom right*). The bottom part of each panel shows the residuals of the best-fitting profiles. The top row uses the high resolution simulation whilst the bottom three use the standard resolution one. The black filled circles with error bars correspond to the median profile in the corresponding mass bin and the error bars encompass 68 per cent of the systems. The solid blue, cyan, orange, magenta and red lines correspond to the universal pressure profile of the appendix B of A10, the best-fitting GNFW functional form with all the parameters left free to vary, the best-fitting GNFW form but with the concentration now a power-law of mass, the best-fitting GNFW form but with the normalization now a power-law of mass, and the best-fitting GNFW form but with the concentration and normalisation now power-laws of mass, respectively. The shape of the pressure profiles is quite strongly mass-dependent and two of the GNFW coefficients thus have to be made mass-dependent in order to get a decent fit over the whole radial and mass ranges when AGN feedback is included.

Figure 5.5 shows the dimensionless mass-weighted pressure profiles for the AGN 8.0 model in eight different mass bins (increasing from top left to bottom right; the same bins were used for binning the Sunyaev–Zel'dovich signal in Figs. 5.2 and 5.4). The radii are normalised by r_{500} and the pressures by P_{500}. Note that in order to further reduce the dynamic range of the y-axis, $P/P_{500}(r/r_{500})^2$ is plotted. Note that the X-ray pressure profiles of the simulated groups and clusters from cosmo-OWLS have already been compared to the X-ray observations of Sun et al. (2011) (groups) and Arnaud et al. (2010) (clusters) by McCarthy et al. (2014), who found that the fiducial AGN model (AGN 8.0) under consideration here reproduces the pressure profiles of both groups and clusters well. The black filled circles with error bars correspond to the median profile in the corresponding mass bin and the error bars encompass 68 per cent of the systems. The solid blue, cyan, orange, magenta and red lines correspond to the universal pressure profile of the appendix B of A10, the best-fitting GNFW functional form with all the parameters left free to vary, the best-fitting GNFW form but with the concentration now a power-law of mass of the form $c_{500} = c_{500,0}(M_{500}/10^{14} \text{ M}_\odot)^\delta$, the best-fitting GNFW form but with the normalisation now a power-law of mass of the form $P_0 = P_{0,0}(M_{500}/10^{14} \text{ M}_\odot)^\epsilon$, and the best-fitting GNFW form but with the concentration and normalisation now power-laws of mass, respectively. The bottom part of each panel shows the residuals of the best-fitting profiles. The functional forms were fitted simultaneously to the eight median profiles with their error bars (i.e. to the filled black circles with error bars). The best-fitting parameters for the final model which has both the concentration and normalisation varying as power-laws of mass for the four cosmo-OWLS models used here and for both mass-weighted and median pressure profiles are listed in Table 5.2. From this figure, it is clear that the shape of the pressure profiles is quite strongly mass-dependent and that it is therefore necessary to make two of the GNFW coefficients (the normalisation and the concentration) mass-dependent in order to get a decent fit over the whole radial and mass ranges when AGN feedback is included. It is especially the case within r_{500} and for the low-mass systems.

In figure 5.6, the mean intrinsic spherically integrated Sunyaev–Zel'dovich signal–M_{500} relation in bins of M_{500} is shown, both unweighted (solid lines) and weighted

(dotted lines; as given by equation 5.3), as well as the observational data (filled red circles with error bars) and the results of the synthetic observations of the simulated maps for $z \leq 0.4$ (empty black diamonds) when using a MMF that assumes the best-fitting mass-dependent mass-weighted pressure profile for the AGN 8.0 simulation. The integrated Sunyaev–Zel'dovich signals have been normalised using the best-fitting scaling relation of A10 (see equation 5.5). The high resolution simulation was used below $M_{500} = 2 \times 10^{13}$ M$_\odot$ and the production run above that threshold. The only difference between figures 5.6 and 5.2 is the spatial template assumed by the MMF used for the synthetic observations (depicted by empty diamonds with error bars in both figures): for figure 5.2, the universal pressure profile of A10 was used, whereas in figure 5.6, the best-fitting mass-dependent mass-weighted pressure profile for the AGN 8.0 simulation was employed. When the mass-dependent best-fitting pressure profile obtained using the AGN 8.0 simulation is used as a spatial template by the matched filter and to compute the conversion factor from $Y_{5r_{500}}$ into Y_{500} (by numerically integrating the best-fitting pressure profile in each of the eight mass bins) for each of the eight mass bins used to stack the simulation results, the bias between the fluxes recovered by the MMF and the intrinsic ones which was striking for the AGN 8.0 model in figure 5.2 has now mostly disappeared (at least within the errors), even at the low-mass end. Similar results are obtained when the best-fitting median pressure profile (not shown here) is used instead. *Hence, the majority of the bias is due to a shape mismatch between the halo properties and the universal pressure profile, especially at large radii and low masses.*

Simulation	Median or mass-weighted	$P_{0,0}$	α	β	γ	$c_{500,0}$	δ	ϵ
NOCOOL	Mass-weighted	11515.667	0.677	4.113	-2.259	9.272	-0.049	-0.111
NOCOOL	Median	38879.965	0.518	5.545	-1.484	3.213	-0.013	-0.029
REF	Mass-weighted	0.528	2.208	3.632	1.486	1.192	0.051	0.210
REF	Median	0.694	1.489	4.512	1.174	0.986	0.072	0.245
AGN 8.0	Mass-weighted	0.581	2.017	3.835	1.076	1.035	0.273	0.819
AGN 8.0	Median	0.791	1.517	4.625	0.814	0.892	0.263	0.805
AGN 8.5	Mass-weighted	0.214	1.868	4.117	1.063	0.682	0.245	0.839
AGN 8.5	Median	0.235	1.572	4.850	0.920	0.597	0.246	0.864

Table 5.2: Results of the pressure profile fitting.
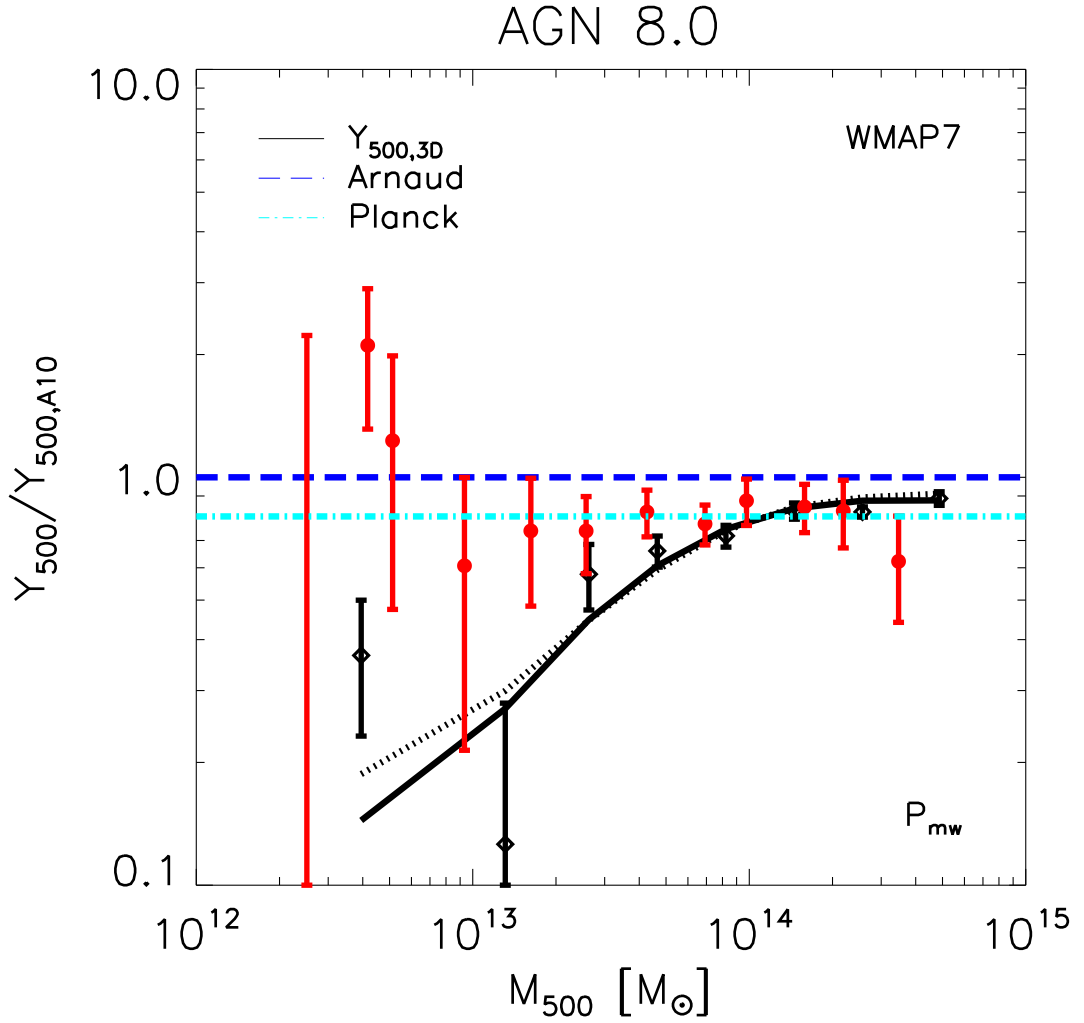
Figure 5.6: The $Y_{500} - M_{500}$ relation for $z \leq 0.4$. The blue dashed and cyan dot-dashed lines correspond to the best-fitting scaling relations of A10 and PIntXI, respectively. The solid and dotted black curves correspond to the unweighted and weighted mean spherically integrated Sunyaev–Zel'dovich signal–M_{500} relations in bins of M_{500} for the AGN 8.0 simulation, respectively. The filled red circles with error bars and empty black diamonds correspond to the observational data of PIntXI and the results of the synthetic observations of the simulated maps, respectively. The extraction was made using a MMF that assumes the mass-dependent best-fitting mass-weighted pressure profile obtained for the AGN 8.0 simulation. The $Y_{5r_{500}}$ to Y_{500} conversion factor for the fluxes extracted with the MMF was computed by integrating the best-fitting pressure profile in each of the eight mass bins as the conversion factor is now mass-dependent. The integrated Sunyaev–Zel'dovich signals have been normalised using the best-fitting scaling relation of A10. The high resolution version of AGN 8.0 was used below $M_{500} = 2 \times 10^{13}$ M$_\odot$ and the production run above that threshold. The majority of the bias is due to a shape mismatch between the halo properties and the universal pressure profile, especially at large radii and low masses.

5.5 Summary and Discussion

The cosmo-OWLS suite of cosmological hydrodynamical simulations described in detail in Chapter 2 was exploited to detect and attempt to explain the origin of the potential biases in the results obtained by the *Planck* collaboration when stacking SDSS galaxies to extend the integrated Sunyaev–Zel'dovich signal–total mass scaling relation down to galaxy masses. cosmo-OWLS constitutes an extension to the OWLS project (Schaye et al. 2010) whose aim is to aid the interpretation and analysis of large-scale structure surveys.

From the analysis presented here, the following conclusions are reached:

1. Taken at face value, the *Planck* result seems to favour a close to self-similar $Y_{500} - M_{500}$ relation (figure 5.1), implying that the haloes of galaxies, groups and clusters all have a gas fraction within r_{500} which is close to the universal baryon fraction and independent of mass. This is in contradiction with X-ray observations.

2. The multi-frequency matched filter (MMF) used by the *Planck* collaboration recovers fluxes which are biased increasingly high as feedback intensity increases (figure 5.2). Likely causes for the bias are: (i) source confusion at the low-mass end and (ii) deviations from the universal pressure profile at large radii, which were both examined.

3. Even though confusion has long been predicted to be an issue in the group and galaxy regimes for Sunyaev–Zel'dovich surveys with large beams and was expected to become problematic at the low-mass end (Figure 5.3), the MMF is able *on average* (over a large number of systems) to recover haloes generated using the universal pressure profile even in the presence of a Sunyaev–Zeld'dovich background, which rules out the uncorrelated component of confusion (figure 5.4).

4. When a mass-dependent best-fitting pressure profile obtained for one of the simulations (figure 5.5 and table 5.2) is used as a spatial template by the MMF, the

fluxes recovered for that simulation are mostly unbiased with respect to the intrinsic three-dimensional $Y_{500} - M_{500}$ relation of that simulation (figure 5.6). A shape mismatch is thus mostly responsible for the bias.

X-ray observations have consistently shown the existence of a strong trend of hot gas mass fraction with halo mass, such that galaxy groups are significantly hot gas depleted compared to the universal baryon fraction (e.g. Gastaldello et al. 2007; Pratt et al. 2009; Sun et al. 2009). The stellar fractions, measured using deep optical and near-infrared observations, are not sufficient to account for the missing baryons (e.g. Giodini et al. 2009; Leauthaud et al. 2012; Sanderson et al. 2013; Budzynski et al. 2014). Studies of local galaxies (such as the Milky Way and Andromeda) using absorption lines (e.g. Miller & Bregman 2013) suggest that this trend continues down to lower halo masses, signalling that low-mass haloes are lacking the vast majority of their universal share of baryons. Hydrodynamical simulations that include the effects of efficient AGN feedback *can* produce the steep trends in gas and baryon fractions with halo mass implied by the X-ray and optical observations (e.g. Chapter 2). The supermassive black holes that are thought to power the AGN have sufficient rest-mass energy for generating such a steepening, but there is no guarantee that they are in fact doing it (i.e. the coupling efficiency of the AGN radiation to the surrounding gas could be close to zero, and the resulting AGN feedback would then be extremely ineffective). Unfortunately, the feedback efficiency cannot yet be predicted from first principles. Nevertheless, numerous recent simulation studies (e.g. Bhattacharya, Di Matteo & Kosowsky 2008; Puchwein, Sijacki & Springel 2008; Fabjan et al. 2010; McCarthy et al. 2010; Stanek et al. 2010; McCarthy et al. 2011; Planelles et al. 2013; Short, Thomas & Young 2013; Planelles et al. 2014) have shown that efficient AGN feedback seems to be required to explain many observations. The gas mass fraction trend (and hence the Sunyaev–Zel'dovich signal–total mass scaling relation) is therefore a fundamental test of the whole AGN feedback paradigm.

The *Planck* stacked Sunyaev–Zel'dovich analysis thus came to the rather surprising conclusion that the $Y_{500} - M_{500}$ relation was approximately self-similar all the way from massive galaxy clusters down to the haloes of individual galaxies not much more

massive than the Milky Way. As $Y_{SZ} \propto M_{gas}T_{mw}$, and the temperature should always be close to the virial temperature, as to first order, it is set by the depth of the gravitational potential which is dominated by dark matter (see for instance McCarthy et al. 2010; see also Chapter 2), the simplest interpretation of the Planck results is that the gas fraction is constant and close to the universal baryon fraction. The *Planck* collaboration make that assumption when they integrate the halo mass function down to $M_{500} = 4 \times 10^{12}$ M$_\odot$ to reach the conclusion that they have detected about a quarter of all the cosmic baryons in the form of hot gas trapped in dark matter haloes.

Since the simulations used here require efficient and energetic AGN feedback to reproduce a variety of observed properties of groups and clusters (from X-ray to optical, through Sunyaev–Zel'dovich; see Chapter 2 and McCarthy et al. 2014), the veracity of the Planck results has been checked. In order to check for the impact of potentially important biases, the Planck analysis has been reproduced using the same methods applied to synthetic Sunyaev–Zel'dovich observations. This was conducted in a blind way as the 'true' answer (three-dimensional integrated signal from the original simulation) for a given halo was not known when the *Planck* matched filter was run by Jean-Baptiste Melin on the simulated maps. The shape of the matched filter turned out to be critically important, which, in hindsight, is not surprising as the *Planck* collaboration and other ongoing Sunyaev–Zel'dovich experiments with large beams are trying to determine the integrated Sunyaev–Zel'dovich signal within a region that is about 125 times smaller (in terms of volume) than the beam within which the measurement is in fact being conducted. The integrated Sunyaev–Zel'dovich signal within r_{500} (and thus the implied gas mass fraction) therefore cannot be reliably determined as it strongly depends upon the shape of the spatial template used for the matched filter. Hence, X-ray observations are in fact entirely consistent with the *Planck* results. To date, observational constraints on the shape of the gas pressure profiles beyond r_{500} (or even within r_{500} for haloes with $M_{500} \lesssim 10^{13}$ M$_\odot$) are basically non-existent.

Nevertheless, it is important to note that *Planck* has really detected an important fraction of the hot baryon content of the Universe as they have basically found hot gas fractions that are close to the universal baryon fraction, but within $5r_{500}$ (which cor-

responds to the aperture within which the Sunyaev–Zel'dovich measurements were made) and not r_{500}. This is then fully consistent with the predictions of the AGN feedback models (even for the most efficient ones).

A testable prediction is that future high-resolution Sunyaev–Zel'dovich experiments (such as SPT-3G and Advanced ACTpol), which will have sufficient angular resolution to measure the signal within r_{500} and will be sensitive enough to measure the Sunyaev–Zel'dovich signal of galaxy groups as well as galaxy clusters, should measure a bend in the $Y_{500} - M_{500}$ relation similar to the one observed in the $M_{gas} - M_{500}$ relation, as inferred from X-ray observations.

Chapter 6

XXL selection function

Ian McCarthy generated the X-ray images (in both broad and narrow bands). Lorenzo Faccioli transformed the provided X-ray maps into synthetic *XMM–Newton* images, ran the XXL detection pipeline on them and provided a list of detected galaxy clusters. Amandine Le Brun generated the truth halo and subhalo catalogues, matched them to the list of detected sources and computed the survey selection function.

6.1 The XXL project

The XXL project[1] is the largest survey approved so far on the ESA *XMM–Newton* X-ray telescope (6.78 Ms in total spread over 541 *XMM–Newton* observations). It is probing two contiguous 25 square degrees fields, mosaicked with 10 ks *XMM–Newton* exposures (in mosaic mode), to a sensitivity of $\sim 5 \times 10^{-15}$ erg s^{-1} cm^{-2} (Pierre et al. in preparation), which roughly corresponds to a depth of $z \sim 1.5 - 2$ for clusters and $z \sim 4$ for AGNs. Its multi-wavelength follow-up has been ongoing for the past few years (Optical, near-infrared, Sunyaev–Zel'dovich,...). Several hundred clusters and up to 30,000 AGNs are expected to be found (Pierre et al. 2011; Pierre et al. in preparation). The X-ray observations started mid-2011 and were finished mid-2013. The main goal of the survey is to use the evolution of a well-defined cluster sample

---
[1]http://irfu.cea.fr/xxl

to obtain competitive constraints on the nature of Dark Energy (see Pierre et al. 2011 for the forecasting of the survey ability to do so). In addition, it has the characteristics required to improve our knowledge of the physics of galaxies, galaxy clusters and AGNs.
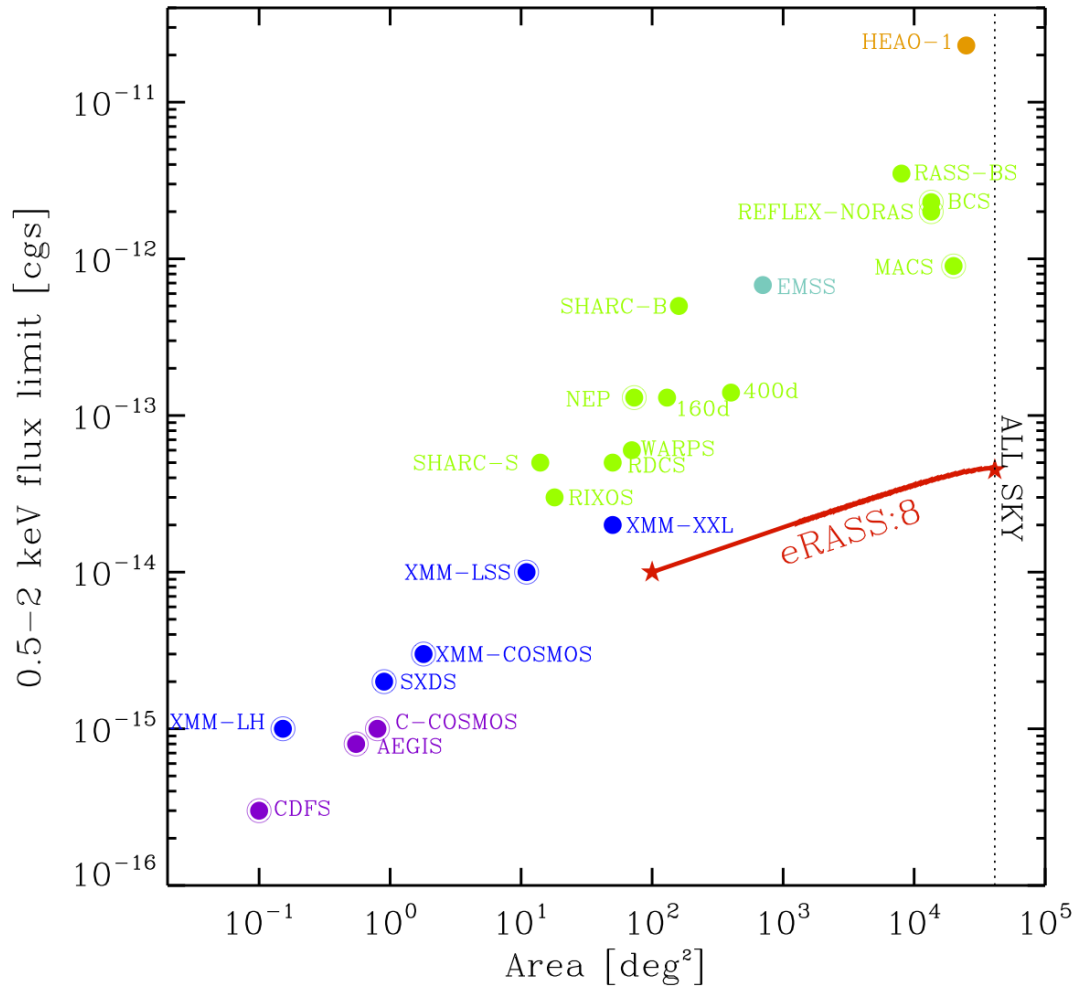
Figure 6.1: Sensitivity–covered area plane for past, ongoing and future X-ray cluster surveys. The *eRosita* surveys are represented as a solid red lines, whilst cyan, orange, green, blue and purple depict past and ongoing surveys conducted with *Einstein*, *HEAO-1*, *ROSAT*, *XMM–Newton* and *Chandra*, respectively. Figure taken from Merloni et al. (2012).

Figure 6.1 presents the loci in the sensitivity–covered area plane of a variety of past, ongoing (including XXL which is denoted as XMM-XXL) and future X-ray cluster surveys. The XXL project is therefore a compromise between (contiguous) covered

area and sensitivity.

6.2 On the importance of a well-known selection function for constraining cosmology with galaxy clusters

As already mentioned in Section 1.2, galaxy clusters can be used to constrain some of the cosmological parameters and in particular, the dark energy equation of state and its potential time evolution. The main quantities that can be used for that are the redshift evolution of the cluster number density (dn/dz), or of the cluster mass function ($dn/dM/dz$) (e.g. Allen et al. 2008; Vikhlinin et al. 2009a; Allen, Evrard & Mantz 2011; Pierre et al. 2011) as well as the baryon fractions. Such studies have to satisfy two fundamental requirements: (i) the cluster sample has to be well-characterised, i.e. it has to have a well-known selection function and (ii) cluster masses have to be reliably determined (e.g. from well-calibrated/understood mass-observable relations), as mass is the only independent variable in structure formation theory. The selection function describes the completeness and the purity of the observational sample as a function of the intensity of the observed signal and redshift of the object.

The utmost importance of these two requirements owes to the fact that they both directly enter the cluster modelling of, for instance, the cluster number counts and mass function (Pierre et al. 2011) as follows. The redshift evolution of the cluster number density can be expressed as:

$$\frac{dn}{dz} = \Delta\Omega \frac{d^2V}{d\Omega dz} \int_0^\infty P\left(M, z\right) \frac{dn\left(M, z\right)}{d\log M} d\log M \qquad (6.1)$$

where $\Delta\Omega$ is the survey beam angular size, $\frac{d^2V}{d\Omega dz} = \frac{c}{H_0} \frac{(1+z)^2 d_A^2(z)}{E(z)}$ is the cosmological volume factor for a FLRW metric, $P\left(M, z\right)$ is the *survey selection function* and the

comoving density of haloes of mass M, $dn/d \log M$, is given by:

$$\frac{dn(M,z)}{d \log M} = -\frac{\bar{\rho_m}}{M} \frac{d \log \sigma}{d \log M} f(\sigma, z) \tag{6.2}$$

where $\bar{\rho_m}$ is the present time value of the mean matter density, $\sigma(M, z)$ is the rms fluctuation of the density contrast and $f(\sigma, z)$ is the multiplicity function (e.g. from Tinker et al. 2008 which is calibrated using DM-only N-body simulations).

One of the ways to meet these two requirements is to use synthetic surveys from cosmological simulations. The remainder of this Chapter describes how synthetic XXL survey fields were generated (Section 6.3), processed in the same way as the 'real' XXL fields (Section 6.4), as well as how the detected clusters were matched to their counterparts in the input halo catalogue (Section 6.5) in order to obtain the survey selection function $P(M, z)$.

6.3 An example of a synthetic XXL survey field

A set of ten synthetic XXL fields with their associated X-ray images, such as the one presented on figure 6.2, have been generated, for each of the cosmo-OWLS physical models and for both the *WMAP*7 and *Planck* cosmologies, as follows:

1. The depth redshift z_{end} was chosen so as to avoid replications across the line of sight (see Section 4.2) for a 5×5 square degrees survey (which corresponds to the size and geometry of a single XXL field).

2. The simplest method for generating light cones was used to generate the gas light cones as it offers the best compromise between computing time and preservation of the clustering at large scales (see Section 4.4).

3. Cold ($T \leq 10^{5.2}$ K) and dense gas particles are prevented from emitting X-rays.

4. As X-ray emission comes from thermal bremsstrahlung and line emissions (from recombination of heavy elements), the X-ray count rate of particle k is given by
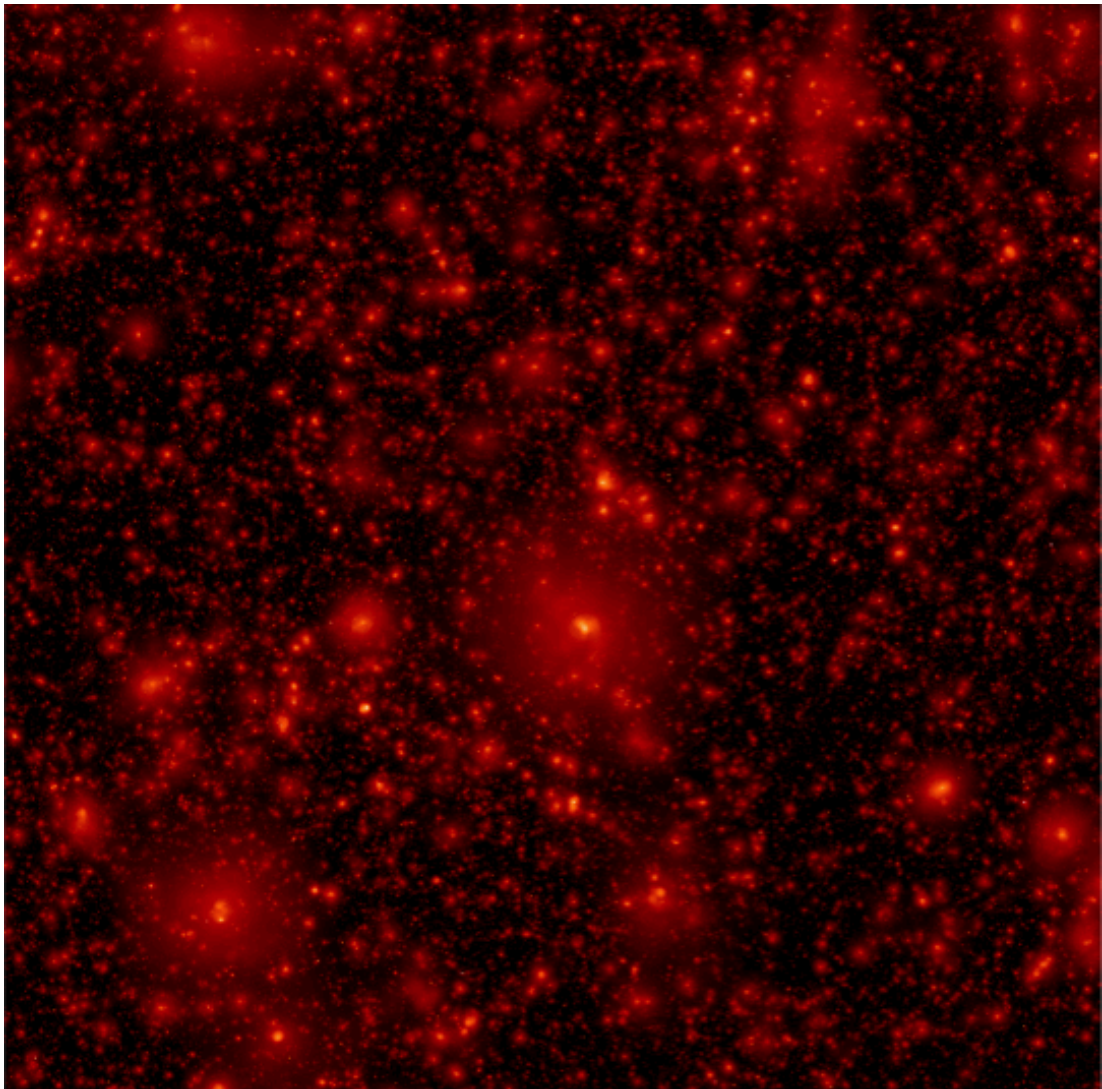
Figure 6.2: Synthetic X-ray image of the hot gas for a 5×5 square degrees survey with depth redshift $z_{end} = 3.0$ of the AGN 8.0 *WMAP*7 simulation.

(e.g. Sarazin 1986):

$$R_{X,k} = n_{e,k} n_{H,k} \Lambda_k V_k \qquad (6.3)$$

where $V_k = m_{gas}/\rho_{gas}$ is the volume occupied by particle k, n_e and n_H are the number densities of electrons and hydrogen atoms respectively, and Λ_k is the cooling function (in count units).

5. Following McCarthy et al. (2010) and Chapter 2, Λ is computed by interpolating pre-computed tables for the X-ray soft band[2] for each of the 11 elements, whose

---

[2]0.5–2.0 keV in the observer frame

abundances are self-consistently followed by the simulation code. The tables were generated with the Astrophysical Plasma Emission Code (APEC; Smith et al. 2001)[3].

6. The X-ray photon rates are turned into count rates per unit area by using the luminosity distance to particle k which are then SPH interpolated onto $2.5''$ on a side square pixels to become count rates per unit area per unit solid angle (in units of photon per s per cm^2 per square arcminute).

The generated X-ray images are still idealised realisations of the XXL fields, in the sense that they, among others, do not contain point sources (X-ray AGN), particle background, Galactic absorption, Milky Way foreground and instrumental effects. These effects were added by Lorenzo Faccioli using the *XMM–Newton* simulator (developed by Jean-Luc Sauvageot) as follows:

1. Count rates per unit area per square arcminute were converted into number of counts per unit area per square arcminute by assuming a 10 ks exposure.

2. Galactic absorption was corrected for following Morrison & McCammon (1983). It roughly corresponds to dividing the count rates by a constant factor of ~ 1.09.

3. The number of counts per unit area per unit solid angle in each pixel was scaled by the ratio of the number of counts from a bremsstrahlung spectrum with $T = 3$ keV, $Z = 0.3\,Z_\odot$ and $z = 0.5$ to the counts of a delta function spectrum at 1 keV. They were both determined using the online WebSpec[4] tool. This ratio is smaller than one (it is ~ 0.85) and the 'surviving photons' are assigned an energy equal to 1 keV[5].

4. It includes a spatially-uniform particle background with an energy distribution that follows a spectrum taken during a 200 ks *XMM–Newton* observation with

---

[3]http://cxc.harvard.edu/atomdb/

[4]http://heasarc.gsfc.nasa.gov/webspec/webspec.html

[5]This is no longer necessary as Lorenzo Faccioli has now been provided with a set of 15 images per 25 square degrees field in bands of width 0.1 keV for the energy range 0.5–2.0 keV.
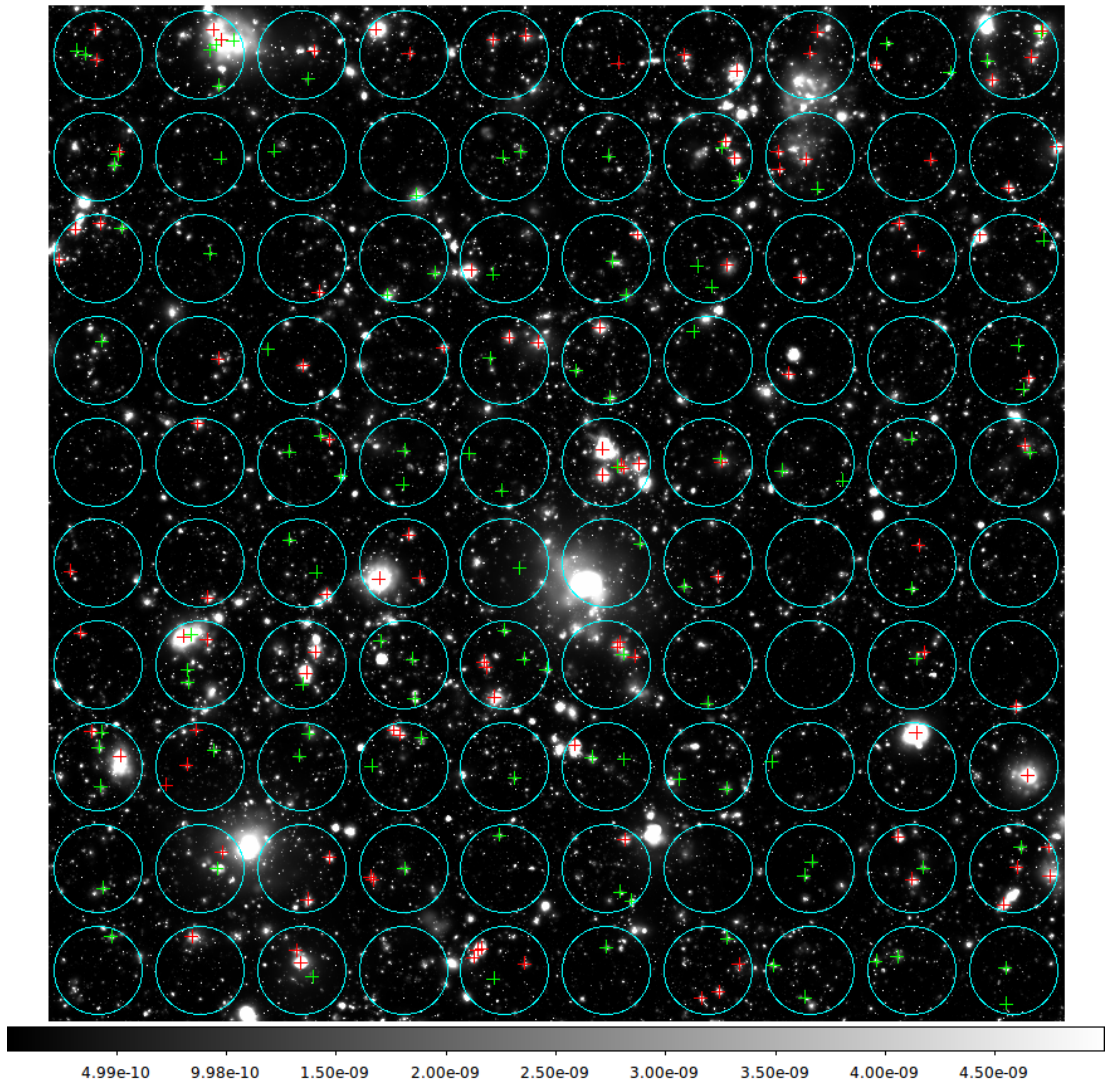
Figure 6.3: Synthetic X-ray image of the hot gas for the 5×5 square degrees survey with depth redshift $z_{end} = 3.0$ shown on figure 6.2 with the *XMM–Newton* pointings overlaid. The cyan circles correspond to the inner $13'$ of the $15'$ radius *XMM–Newton* pointings. The red and green crosses correspond respectively to the C1 (109 of them) and C2 (107 of them) clusters detected by the XXL pipeline, respectively. Figure courtesy of Lorenzo Faccioli.

the filter in position CLOSED (i.e. it is free from X-ray photons) and in the absence of flares.

5. The photon energy, spectral response, pixel size and effective area of the *XMM– Newton* instruments, the characteristics of the THIN filter, the vignetting, the energy-dependent point spread function, as well as the bad pixels and the gaps between CCDs for each of the three EPIC *XMM–Newton* detectors used for XXL (i.e. the two MOS detectors and the PN detector) were taken into account

and event lists which only contain the photons in the 0.5–2.0 keV band were created.

6. The AGN background was added following the observed $\log N - \log S$ from Moretti et al. (2003). 80 536 AGN are uniformly distributed down to a flux limit of 10^{-16} erg s^{-1} cm^{-2} with a spectral energy distribution which is assumed to be a power law (in energy) with the typical power-law index of -1.9 (e.g. Marconi et al. 2004).

7. The event lists were turned into 0.5–2.0 keV images for each of the three detectors and into exposure maps using the latest calibration files.

6.4   The XXL detection pipeline

The XXL detection pipeline, which was then run by Lorenzo Faccioli on the synthetic *XMM–Newton* X-ray images, is an improved version of the one that was developed for the *XMM* Large-Scale Structure (*XMM*-LSS; which served as a pilot to the XXL survey) survey by Pacaud et al. (2006) (see also Clerc et al. 2012). In brief, when run on simulated images, it works as follows:

1. The simulated images for the three detectors are combined into a single image.

2. It then uses the approach advocated and extensively tested by Valtchanov, Pierre & Gastaud (2001), which combines wavelet filtering using the task MR_FILTER of the multi-resolution package MR/1 (Starck, Murtagh & Bijaoui 1998) and source detection using SEXTRACTOR (Bertin & Arnouts 1996). The primary source catalogues (for both point and extended sources) are created by running SEXTRACTOR on the wavelet-filtered image. In order to avoid edge effects, SEXTRACTOR is only run on the inner 13' of the 15' radius *XMM–Newton* pointings (shown as cyan circles on figure 6.3).

3. The properties of the sources detected by SEXTRACTOR are determined using an improved version of the maximum likelihood profile fitting procedure XAMIN

which was designed for *XMM*-LSS by Pacaud et al. (2006). It determines 38 parameters, among which are the detection likelihood (DET_ML), extent (EXT) and extent likelihood (EXT_LIKE) of each detected source by fitting (i) a point-source model convolved with the analytic *XMM–Newton* point spread function, taken from the *XMM–Newton* calibration data base and then an extended source profile, and (ii) a spherically symmetric β-model (Cavaliere & Fusco-Femiano 1976) given by $S_X(r) \propto [1 + (r/r_c)^2]^{-3\beta+1/2}$ with β set to the canonical value of $2/3$ convolved with the *XMM–Newton* point spread function. The likelihood of the fits is computed using a modified version of the C-statistic (Cash 1979), which is then used to choose the best-fitting model. The extent likelihood is obtained by computing the difference between the C-statistics of the best-fitting point-like and extended source models.

4. Finally, based on the values of the extent, extent likelihood and detection likelihood parameters determined by XAMIN, the sources detected by SEXTRACTOR are classified in three main categories (see Pacaud et al. 2006; Clerc et al. 2012; Pierre et al. in preparation): (i) 'real' point sources with DET_ML > 15 as this threshold was shown to be the best compromise between purity and completeness by Pacaud et al. (2006), (ii) C1 extended sources which should have a negligible contamination by misclassified point sources are selected as fulfilling simultaneously the following three conditions: DET_ML > 32, EXT $> 5''$ and EXT_LIKE > 33, and (iii) C2 extended sources which could be contaminated by point sources at the 50 per cent level correspond to sources with EXT $> 5''$, EXT_LIKE > 15 and no constraint on DET_ML.

The outputs of the XXL detection pipeline for each of the ten synthetic surveys generated using the AGN 8.0 *WMAP*7 simulation which were provide by Lorenzo Faccioli contain for each of the sources classified as either C1 or C2: (i) the RA and Dec (in $2.5''$ pixel coordinates) of the centre of the detected source (as determined by SEXTRACTOR), (ii) the count rate, (iii) the core radius and (iv) whether the source was classified as a C1 or C2.

6.5 Halo matching and computation of the survey selection function

The outputs from the XXL detection pipeline described in the previous section were matched to halo and subhalo catalogues (hereafter truth catalogues) generated especially for this purpose. A constant matching radius R_{match} was discovered by experimentation not to be a pertinent choice, while a matching radius which depends on the angular size of the candidate (sub)haloes in the truth catalogues turned out to be much more appropriate. The matching was also attempted in terms of subhaloes instead of haloes since it became evident, by visual inspection of the haloes that overlap with the detected clusters, that the pipeline is also detecting substructures (e.g. groups in the process of merging to form a cluster). The selection function should thus be computed using the matching to the truth subhalo catalogues. Nevertheless, for the sake of completeness, the results of both the halo and the subhalo matching and the corresponding selection functions will be presented here.

The truth catalogues for both haloes and subhaloes were generated as follows:

1. The haloes and subhaloes with $M_{500} \geq 10^{12}$ $M_{\odot}$ were extracted from the halo and subhalo light cones that correspond to the ten X-ray maps (i.e. the same random transformations have been applied to the halo and subhalo catalogues as outputted by SUBFIND and to the gas particles taken directly from the snapshots). Note that the subhaloes do not have a value of M_{500} associated to them. To get around this, a power-law of the form $V_{max} = 10^A (M_{500}/10^{14}$ $M_{\odot})^{\alpha}$ where V_{max} is the subhalo's maximum circular velocity was fitted for each snapshot with $z \leq 3.0$ using the central subhaloes of the AGN 8.0 *WMAP7* simulation and used to assign a M_{500} to all the subhaloes (both central and satellites) contained in the light cones. V_{max} was chosen (the subhalo mass M_{sub} could also in principle have been used) as it is expected to be the quantity the least affected by e.g. tidal stripping and thus a more robust proxy of the subhalo's M_{500} at infall.

2. As SEXTRACTOR was only run on non-overlapping $13'$ radius 'pointings' (they

are separated by $30'$ and depicted by cyan circles on figure 6.3), only the (sub)haloes with their centre not more than R_{match} outside of the boundaries of a pointing were included in the truth catalogues (i.e. they have to at least overlap with a pointing). These (sub)haloes are the ones used to compute the number of possible of possible matches $N(M_{500}, z)$ as a function of mass and redshift as shown on figures 6.4 for haloes and 6.6 for subhaloes, respectively.

3. The bolometric luminosity of the (sub)haloes is computed assuming the median BCES (Akritas & Bershady 1996) orthogonal $L_{bol} - M_{500}$ relation corrected for Malmquist bias of Pratt et al. (2009) $L_{bol} = 1.38 \times 10^{44} E(z)^{7/3} (M_{500}/2 \times 10^{14} \, h_{70}^{-1} \, \mathrm{M}_\odot)^{2.08} \, h_{70}^2$ erg s^{-1} and then turned into their bolometric flux f_{bol} and surface brightness S_{bol} using the luminosity distance d_L to the (sub)halo in the light cones and its angular size $\theta_{500} = R_{500}/d_A$ where d_A is the angular diameter distance to the (sub)halo in the light cones. Only the (sub)haloes with $f_{bol} > 10^{-16}$ erg s^{-1} cm^{-2} (which roughly corresponds to the point-source sensitivity of the EPIC instruments of *XMM–Newton*[6]) are considered as potential matches.

For each detected cluster (either C1 or C2), the matching to the truth catalogues is then done as follows:

1. The distance between the position of the detected cluster (as measured by SEx-TRACTOR) and the centre of the (sub)haloes needs to be smaller than the matching radius R_{match}. By experimentation, $R_{match} = 0.25\theta_{500}$ was found to lead to a good compromise between completeness and purity.

2. The (sub)haloes also need to have $f_{bol} > 10^{-16}$ erg s^{-1} cm^{-2}.

3. They then need to have their centre not more than R_{match} outside of a pointing.

4. Finally, the matching (sub)halo is the one with the maximum bolometric flux amongst all the (sub)haloes (if any) that fulfil the previous three criteria.

---

[6]http://xmm.esa.int/external/xmm_user_support/documentation/uhb_2.5/node38.html
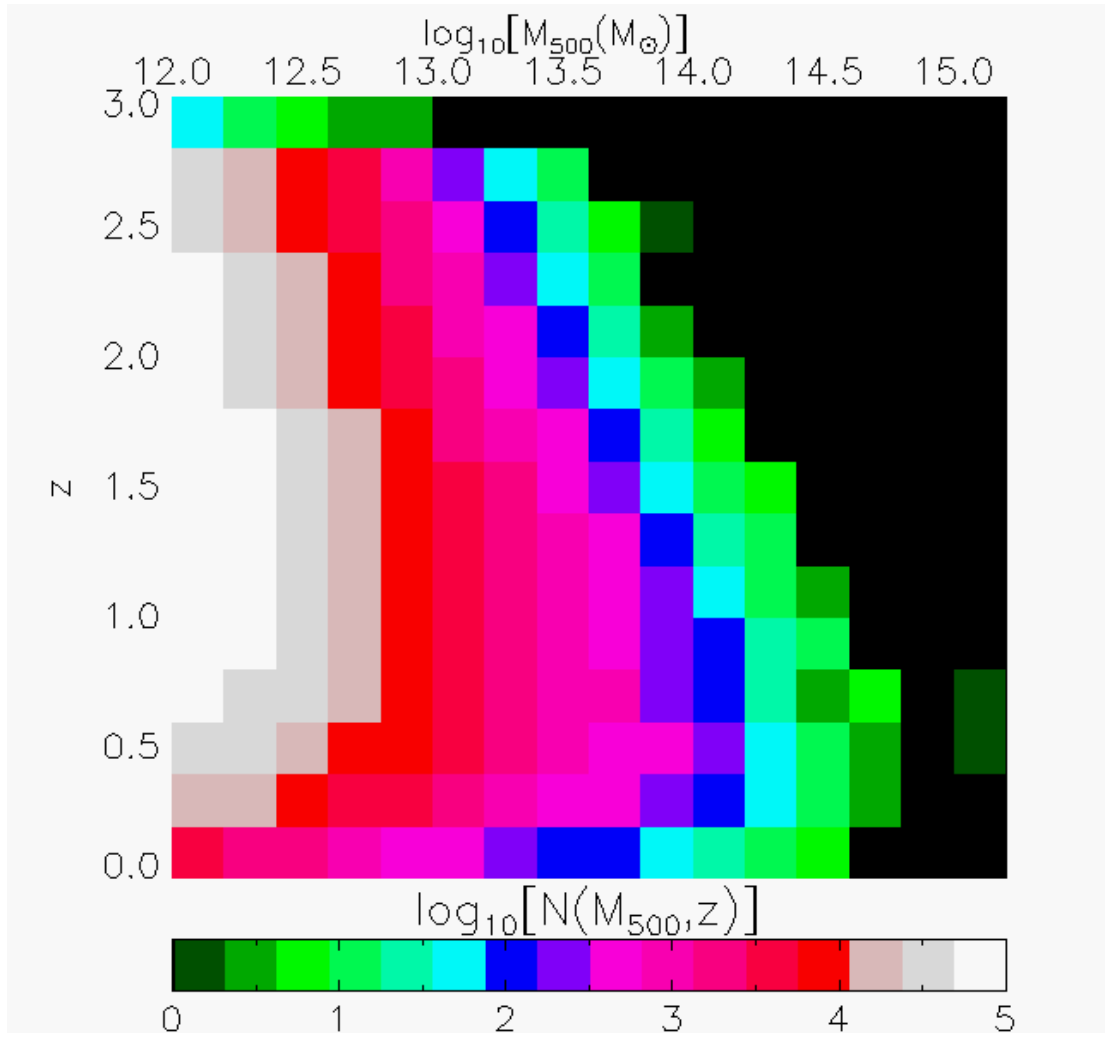
Figure 6.4: Number of possible matches for $R_{match} = 0.25\theta_{500}$ using the halo truth catalogues of the AGN 8.0 *WMAP*7 simulation.

Note that criteria 2 and 3 are enforced when constructing the truth catalogues. The maximum bolometric flux criterion was found by visual inspection of the matches to lead to reliable matches more frequently than an analogous maximum surface brightness criterion. It is worth noting that when using the maximum surface brightness criterion to determine the matching (sub)halo, the (sub)haloes matched C1 and C2 populations are found to extend to slightly higher redshift than in the maximum flux case.

The ten maps and their corresponding truth catalogues were combined for computing the selection function $P(M_{500}, z)$ and the number of systems that could have been de-
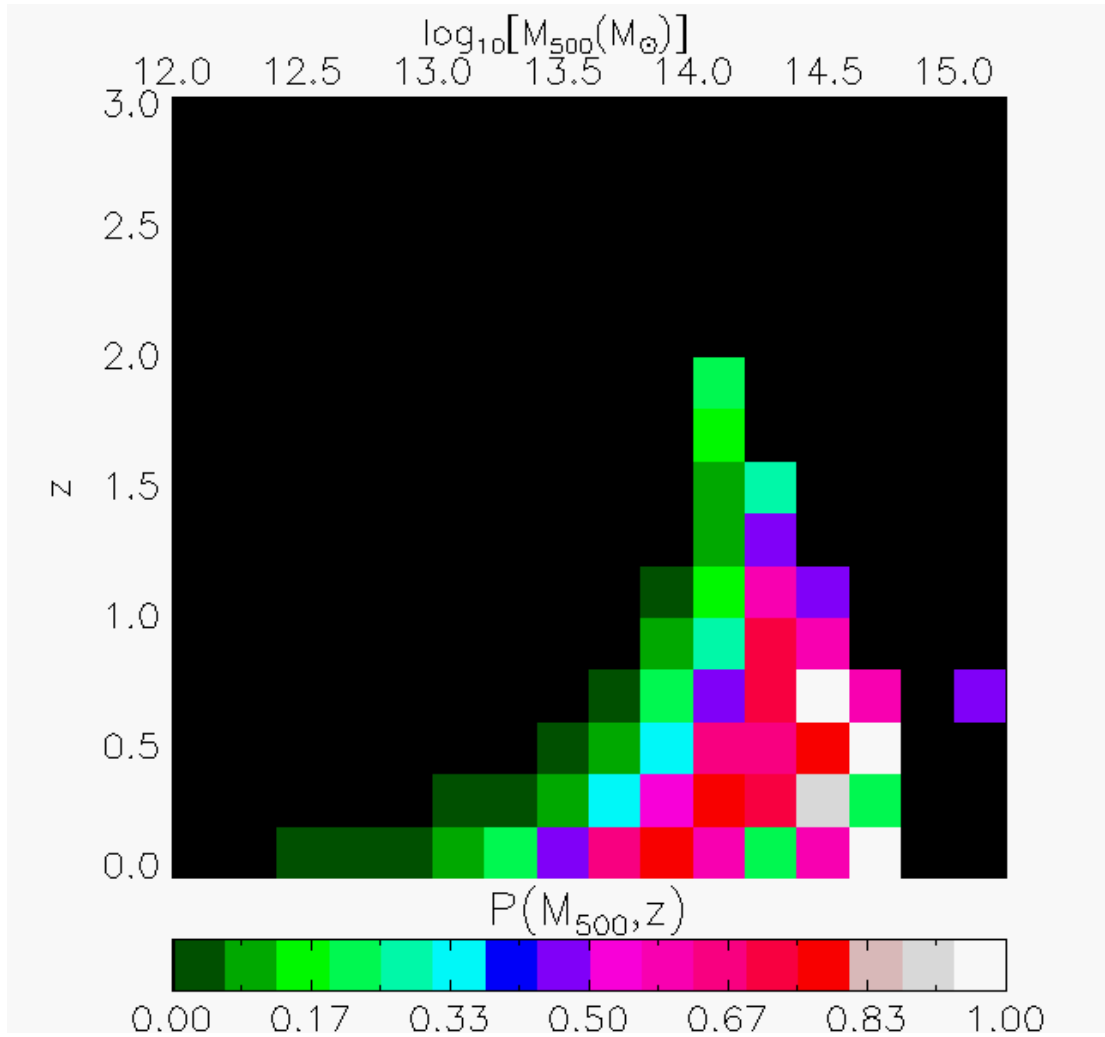
Figure 6.5: Selection function for $R_{match} = 0.25\theta_{500}$ using the halo truth catalogues of the AGN 8.0 *WMAP*7 simulation.

tected $N(M_{500}, z)$ in order to improve the statistics (especially at the high-mass end). $N(M_{500}, z)$ was computed by binning in total mass (using $\Delta \log_{10} M_{500} = 0.2$) and redshift (using $\Delta z = 0.2$) all the (sub)haloes with $M_{500} \geq 10^{12} \, M_{\odot}$ whose centre is not more than R_{match} outside the limits of a pointing in the ten (sub)halo catalogues. The results for the haloes and subhaloes using a matching radius $R_{match} = 0.25\theta_{500}$ are displayed in figures 6.4 and 6.6, respectively. The C1 and C2 populations were considered jointly for computing the selection function $P(M_{500}, z)$. In order to do so, the number of unique (sub)haloes[7] that match the detected combined C1 and C2 populations for the

---

[7]The same (sub)halo can be matched to several of the detected clusters (irrespective of their C1 or C2 classification) but should not be counted several times for the computation of the selection function since, especially in the case of subhaloes, it should not be 'detected' more than once.

ten maps considered simultaneously were binned in total mass (using $\Delta \log_{10} M_{500} = 0.2$) and redshift (using $\Delta z = 0.2$). The resulting $N_{unique\ match}(M_{500}, z)$ was then divided by $N(M_{500}, z)$ to obtain the selection function $P(M_{500}, z)$, which is shown in figures 6.5 and 6.7 when using a matching radius $R_{match} = 0.25\theta_{500}$ in the case of haloes and subhaloes, respectively.

The two pairs of figures (figures 6.4 and 6.5 and figures 6.6 and 6.7) suggest that: (i) XXL does not find groups less massive than $\log_{10}[M_{500}(\mathbf{M_\odot})] \sim 13.5$ for $z > 0.2$ and even at $z < 0.2$, it is finding only a very small fraction of this population, (ii) XXL is best at finding low-mass clusters with $14.0 \lesssim \log_{10}[M_{500}(\mathbf{M_\odot})] \lesssim 14.5$ at $z \lesssim 0.75$, where it is detecting about 60-70 per cent of these, and (iii) the pipeline is missing a few very massive, nearby systems (see green and purple/magenta pixels in bottom right of figures 6.5 and 6.7), as is already evident visually on figure 6.3.

Increasing the matching radius to $R_{match} = 0.5\theta_{500}$ does not affect the combined results much. The differences between the selection functions computed using haloes and subhaloes are also limited to: (i) detecting slightly more high-mass ($\log_{10}[M_{500}(\mathbf{M_\odot})] \sim 14.25$) systems at $z \sim 1$ and (ii) slightly fewer high-mass ($\log_{10}[M_{500}(\mathbf{M_\odot})] \sim 14.5$) systems at $z \sim 0$ when subhaloes are used for the matching.

In the near-future, some more work will need to be conducted in order to:

1. Verify that the detected population looks similar to the real population detected by XXL. This will give us more confidence in the $P(M_{500}, z)$ obtained using the simulations.

2. Fold the selection function obtained using the simulations into the cosmological analyses.

3. Assess the impact of selection on the determined scaling relations and their evolution.
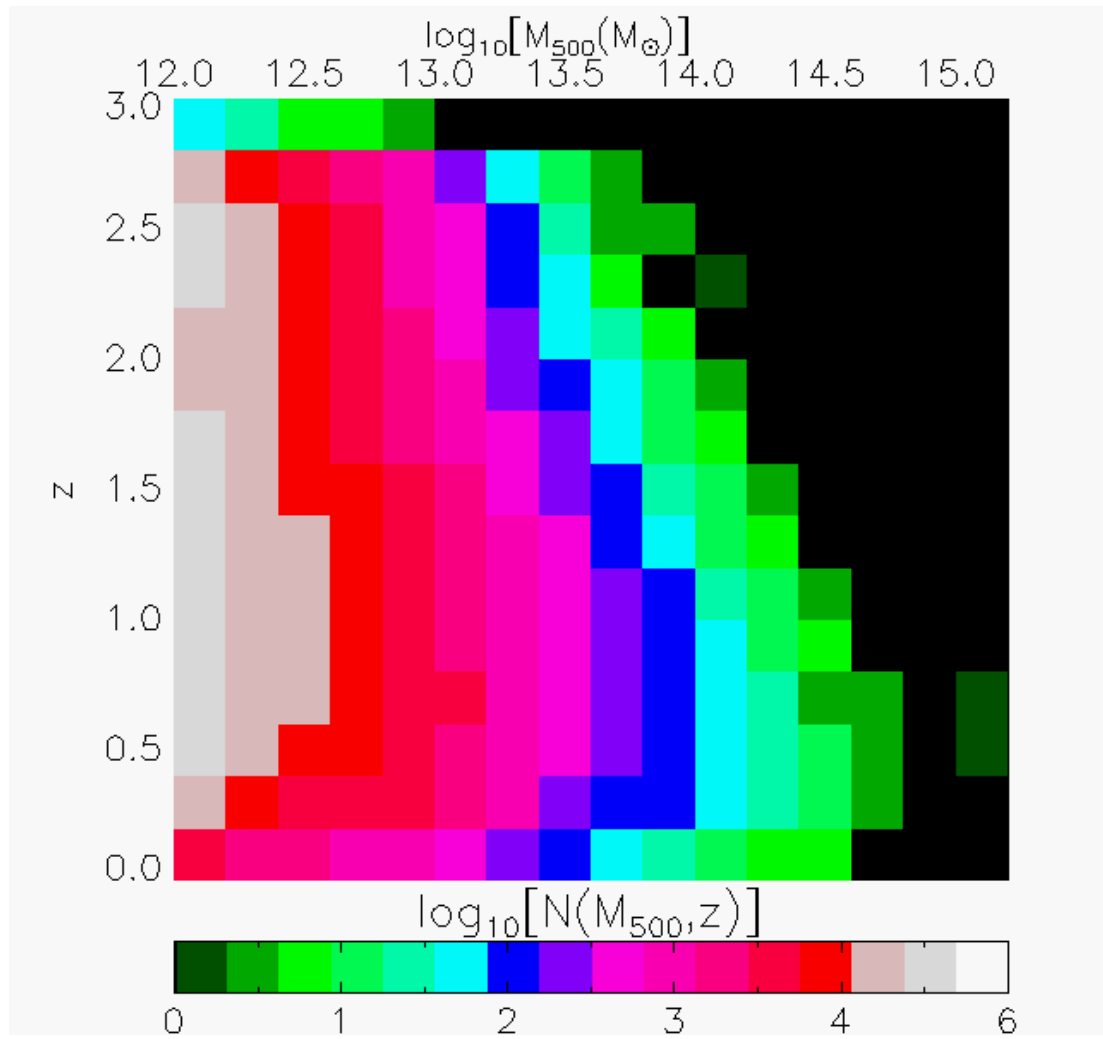
Figure 6.6: Number of possible matches for $R_{match} = 0.25\theta_{500}$ using the subhalo truth catalogues of the AGN 8.0 *WMAP*7 simulation.
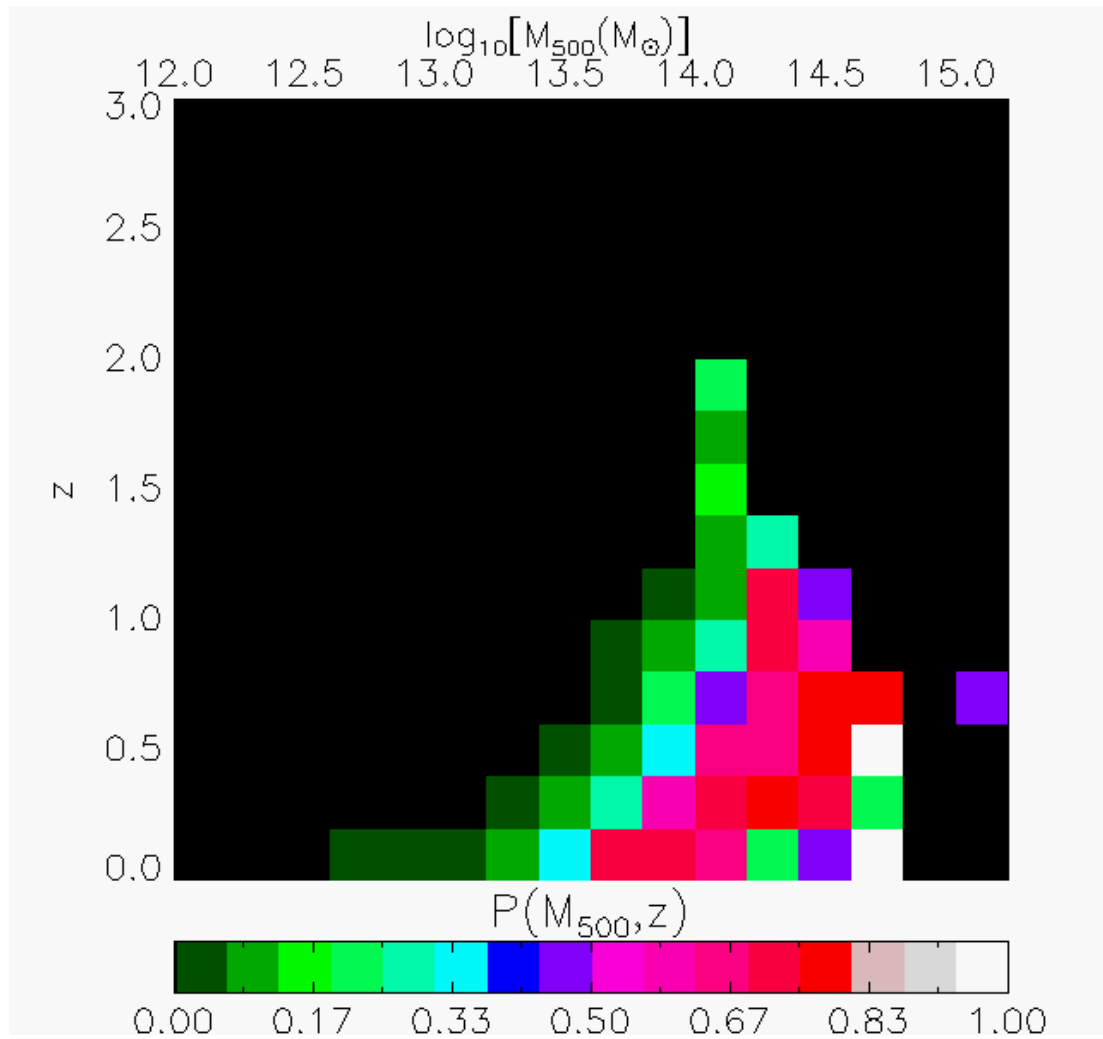
Figure 6.7: Selection function for $R_{match} = 0.25\theta_{500}$ using the subhalo truth catalogues of the AGN 8.0 *WMAP*7 simulation.

Chapter 7

Conclusions and Future Work

This thesis took advantage of a new suite of large-volume cosmological hydrodynamical simulations, which were designed with ongoing and upcoming cluster cosmology surveys in mind, to study the astrophysical and cosmological aspects of galaxy clusters.

In Chapter 2, the new suite of state-of-the-art simulations with varying 'sub-grid' physics, christened cosmo-OWLS, was introduced and compared to a wide range of observations, from X-ray luminosity and temperature to Sunyaev–Zel'dovich flux, through I-band mass-to-light ratio, dominance of the brightest cluster galaxy and central black hole masses, by producing synthetic observations and mimicking observational analysis techniques. These comparisons demonstrated that some of the AGN feedback models can produce a realistic *population* of galaxy groups and clusters. This opened the door to the creation of synthetic surveys for helping the interpretation of cluster surveys, together with assessing the impact of selection.

In Chapter 3, the same simulations were employed to investigate the scatter and evolution of the hot gas properties of the realistic populations of galaxy groups and clusters as a function of the fundamental non-gravitational physics of galaxy formation. The median relations and their log-normal scatter were found to be well-described by evolving broken power-laws. The self-similar model predictions (for both the evolution and the mass slope) were found to break down when efficient AGN feedback is included, and the log-normal scatter to vary mildly with mass, be relatively insensitive

to galaxy formation physics and decrease with increasing redshift.

Chapter 4 presented the development and testing of a multi-purpose light cone software package, which was used to create realistic synthetic surveys from various simulations. It showed that the simplest method for generating light cones results in the best compromise between conservation of the large-scale structures and computing speed.

Chapter 5 exploited synthetic Sunyaev–Zel'dovich observations, generated for the cosmo-OWLS suite of simulations using the developed light cone software package, to check the veracity of some of the results reported by the *Planck* collaboration in late 2012. Taken at face value, their results seem to favour a close to self-similar scaling relation between the Sunyaev–Zel'dovich flux and the total mass, which is in contradiction with X-ray and absorption line observations. The matched filter used by the *Planck* collaboration recovers fluxes that are biased high when feedback is included. The likely causes for the bias, confusion and deviations from the universal pressure profile, were both investigated. The impact of source confusion turned out to be negligible when the signal is averaged over a large number of systems, and the bias was found to be mostly due to a shape mismatch (in terms of pressure profiles).

Finally, Chapter 6 presented a first attempt at using synthetic X-ray observations, generated for the cosmo-OWLS suite using a combination of the developed light cone software and the *XMM–Newton* simulator and processed with the detection pipeline of the XXL survey to quantify the selection function of the survey. Preliminary results suggest that: (i) the XXL survey is not able to find the large majority of groups, (ii) it is best at finding low-mass clusters at low-redshift and (iii) the pipeline fails to detect a few very massive, extended, nearby systems.

This thesis presented some of the first applications of the cosmo-OWLS suite of simulations and its synthetic surveys. Some other potential applications are:

1. The origin of the hydrostatic and spectroscopic biases could be investigated.

2. The scatter and evolution of the optical properties of the simulated galaxy groups and clusters, such as optical richness, K-band luminosity, stellar mass and weak

lensing mass could be investigated as a function of galaxy formation physics.

3. The origin of the scatter and evolution of the hot gas and stellar properties of the simulated populations of galaxy groups and clusters could be investigated.

4. A careful comparison of the observed and simulated scatter and evolution of the hot gas properties could be conducted. This would require the self-consistent modelling of the selection function of the observational data sets the simulations will be compared to.

5. The dependence upon baryonic physics and cosmology of the selection function of X-ray surveys could be studied.

6. In addition to detecting hundreds of galaxy groups and clusters, the XXL survey has found more than 10 000 X-ray AGN. It would thus be interesting to be able to generate synthetic surveys that include the X-ray AGN in a self-consistent manner. They could be used for making predictions for e.g. the clustering of X-ray AGN and to study the impact of AGN contamination on the detection of X-ray galaxy clusters (for instance, close pairs of AGN at high redshift could be mistaken for a galaxy cluster by a detection pipeline).

7. The synthetic X-ray surveys that include the X-ray emission from AGN (when present) could be compared to existing observational constraints on the X-ray background. This would provide another test of the physics of galaxy formation.

8. Synthetic kinetic Sunyaev–Zel'dovich surveys could be used to prepare future Sunyaev–Zel'dovich experiments (e.g. to check whether they could potentially detect outflows from AGN feedback).

9. Synthetic weak lensing and cosmic shear surveys could be compared to early results from the Dark Energy Survey and to make predictions for the upcoming *Euclid*.

10. It could be interesting to compare the physical properties of the galaxy groups and clusters detected at different wavelengths and to cross-correlate, for instance, synthetic shear and Sunyaev–Zel'dovich maps.

11. Finally, one could compare the growth and physical properties of the brightest cluster galaxies of galaxy clusters which have been selected in the same way in the simulations and the observations.

Appendix A

Resolution study

The sensitivity of the results of Chapter 2 to numerical resolution is examined. As currently available hardware prevents the running of higher resolution simulations in $400\ h^{-1}$ Mpc on a side boxes, smaller simulations were used for testing numerical convergence. They are $100\ h^{-1}$ Mpc on a side and use 2×256^3 particles (which is the same resolution as our 2×1024^3 particles in $400\ h^{-1}$ Mpc box runs) and 2×512^3 particles (i.e. eight times higher mass resolution and two times higher spatial resolution). They assume the *WMAP*7 cosmology. Note that when comparing AGN models at different resolutions, the same *halo* mass limit for BH particle seeding and BH seed mass (see Section 2.2.1 for seeding details) are adopted and that the convergence tests are made using the true physical properties of the simulated systems (i.e. no synthetic observations were used).

In Fig. A.1, the median gas mass fraction–M_{500} (*left*) and I-band total mass-to-light ratio–M_{500} (*right*) relations at $z = 0$ are compared for systems with $12.9 \lesssim \log_{10}[M_{500}(\mathrm{M_\odot})]$ $\lesssim 14.75$ at the resolution of the production runs (dashed lines) and at eight times higher mass resolution (solid lines) for four of the models used (NOCOOL, REF, AGN 8.0 and AGN 8.5). Global properties are found to be adequately converged down to $\log_{10}[M_{500}(\mathrm{M_\odot})]$ ~ 13.3 (i.e. a few times 10^{13} $\mathrm{M_\odot}$) at the resolution of the cosmo-OWLS runs.

In Fig. A.2, the evolution of the global BH density and of the cumulative BH density present in seed-mass BHs (black and grey curves) are compared when box size, reso-
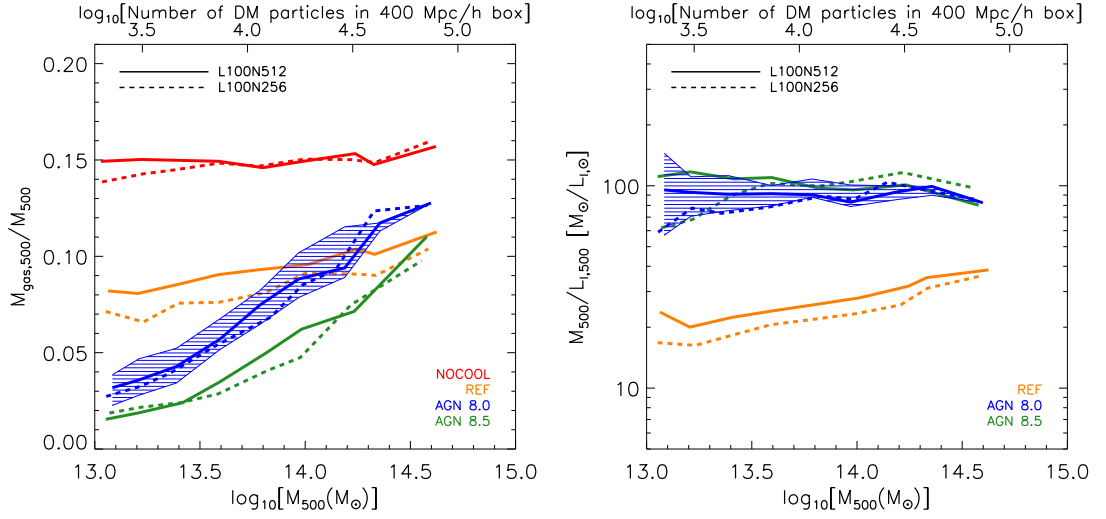
Figure A.1: Effect of numerical resolution on the median gas mass fraction–M_{500} and I-band total mass-to-light ratio–M_{500} relations at $z = 0$. The simulations used here assume the *WMAP*7 cosmology. Global properties are adequately converged down to $\log_{10}[M_{500}(\mathrm{M_\odot})] \sim 13.3$ (i.e. a few times 10^{13} $\mathrm{M_\odot}$). Both panels use the true physical properties (gas fraction, total mass and I-band total mass-to-light ratio) of the simulated systems (i.e. no synthetic observations were used).

lution and BH seeding are varied for both the AGN 8.0 and AGN 8.5 models. Varying box size at fixed resolution and seeding parameters from $100\ h^{-1}$ Mpc (dashed lines) to $400\ h^{-1}$ Mpc (long-dashed lines) on a side has no noticeable effect upon the evolution of the global BH density and cumulative density in seed BHs for $z \leq 3$ for both the AGN 8.0 and AGN 8.5 models (i.e. the dashed lines and long-dashed lines lie on top of each other). Varying resolution at fixed box size and seeding parameters from the resolution of the production runs (dashed lines) to eight times higher mass resolution (solid lines) affects the evolution of both densities up to the present time in both AGN models. Finally, varying the halo mass limit for BH particle seeding and the BH seed mass from the values used for the original OWLS AGN model (triple-dot-dashed lines) to eight times higher masses as used for the production runs (solid, dashed and long-dashed lines) at fixed box size and mass resolution (solid lines), leads to higher BH and seed BH densities at all redshifts.

Overall, however, the differences are not that large between the different models and all are approximately consistent with the observational constraints on the $z \approx 0$ mass

density of SMBHs of Shankar et al. (2004).
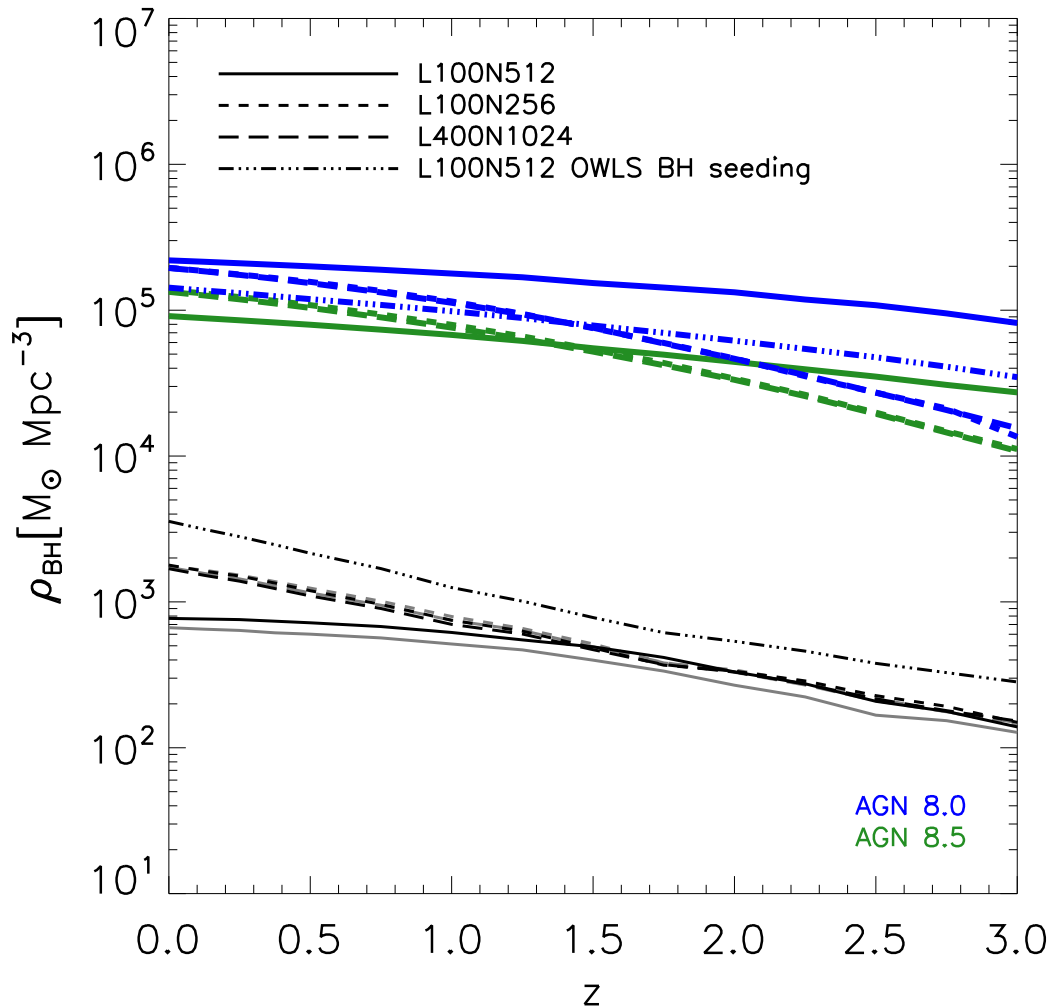
Figure A.2: Effect of box size, numerical resolution and BH seeding on the evolution of the cosmic BH density. The simulations used here assume the *WMAP*7 cosmology. The black and grey curves show the cumulative density in seed BHs for the AGN 8.0 and AGN 8.5 models, respectively. The solid lines correspond to the simulations run in a $100 \ h^{-1}$ Mpc on a side box at eight times higher mass resolution than the production runs. The dashed lines and long-dashed lines (which are virtually on top of each other) correspond to the simulations run in $100 \ h^{-1}$ Mpc and $400 \ h^{-1}$ Mpc on a side boxes at the resolution of the production runs, respectively. All these simulations use the same halo mass limit for BH particle and BH seed mass as the production runs. The triple-dot-dashed lines correspond to the high resolution runs but with the BHs injected in eight times less massive haloes and with a eight times lower seed mass as they were originally in the OWLS AGN model (see Booth & Schaye (2009) and Section 2.2.1).

Appendix B

Hydrostatic bias and spectroscopic temperatures

In Fig. B.1, the median hydrostatic bias–M_{500} relation is plotted for the various simulations, where the hydrostatic bias is defined as $\frac{M_{500,hse,spec}-M_{500}}{M_{500}}$. Consistent with previous simulation studies (e.g. Mathiesen, Evrard & Mohr 1999; Rasia et al. 2006; Nagai, Vikhlinin & Kravtsov 2007; Kay et al. 2012; Nelson et al. 2014), a mean bias of ~ -20 per cent is found for both groups and clusters. The scatter, which for clarity's sake is only shown for the AGN 8.0 model, increases with decreasing total mass.

In Fig. B.2, the median bias of 'uncorrected' temperatures due to spectral fitting as a function of M_{500} is plotted for the various simulations. Previous studies (e.g. Mathiesen & Evrard 2001; Mazzotta et al. 2004; Rasia et al. 2006; Khedekar et al. 2013) found that the spectral temperatures are generally biased low compared to the mass-weighted temperatures. The level (and even the sign) of the bias are found here to be dependent on the details of the sub-grid physics implementation.
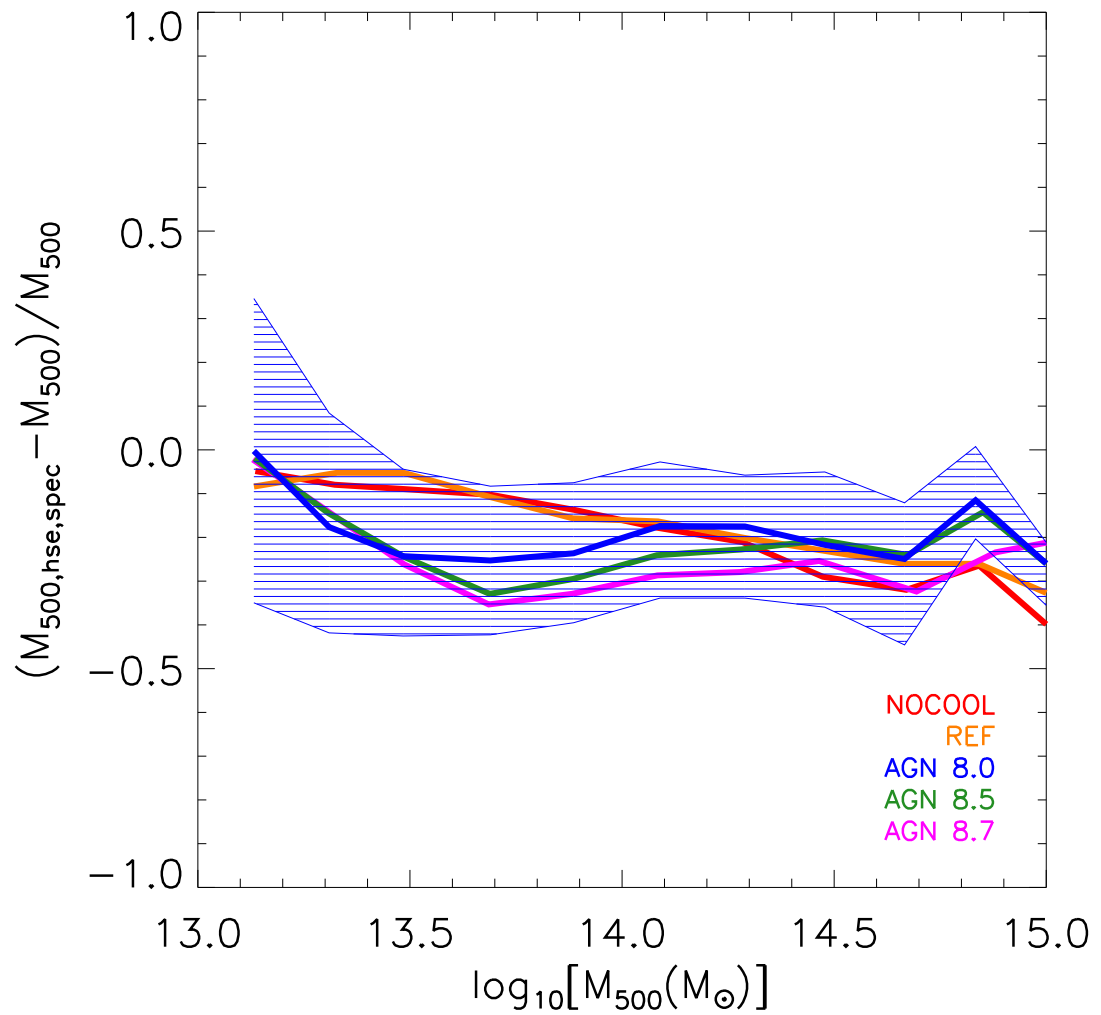
Figure B.1: Hydrostatic bias as a function of M_{500} at $z = 0$. Consistent with previous simulation studies, a mean bias of ~ -20 per cent is found for both groups and clusters. The scatter increases with decreasing total mass.
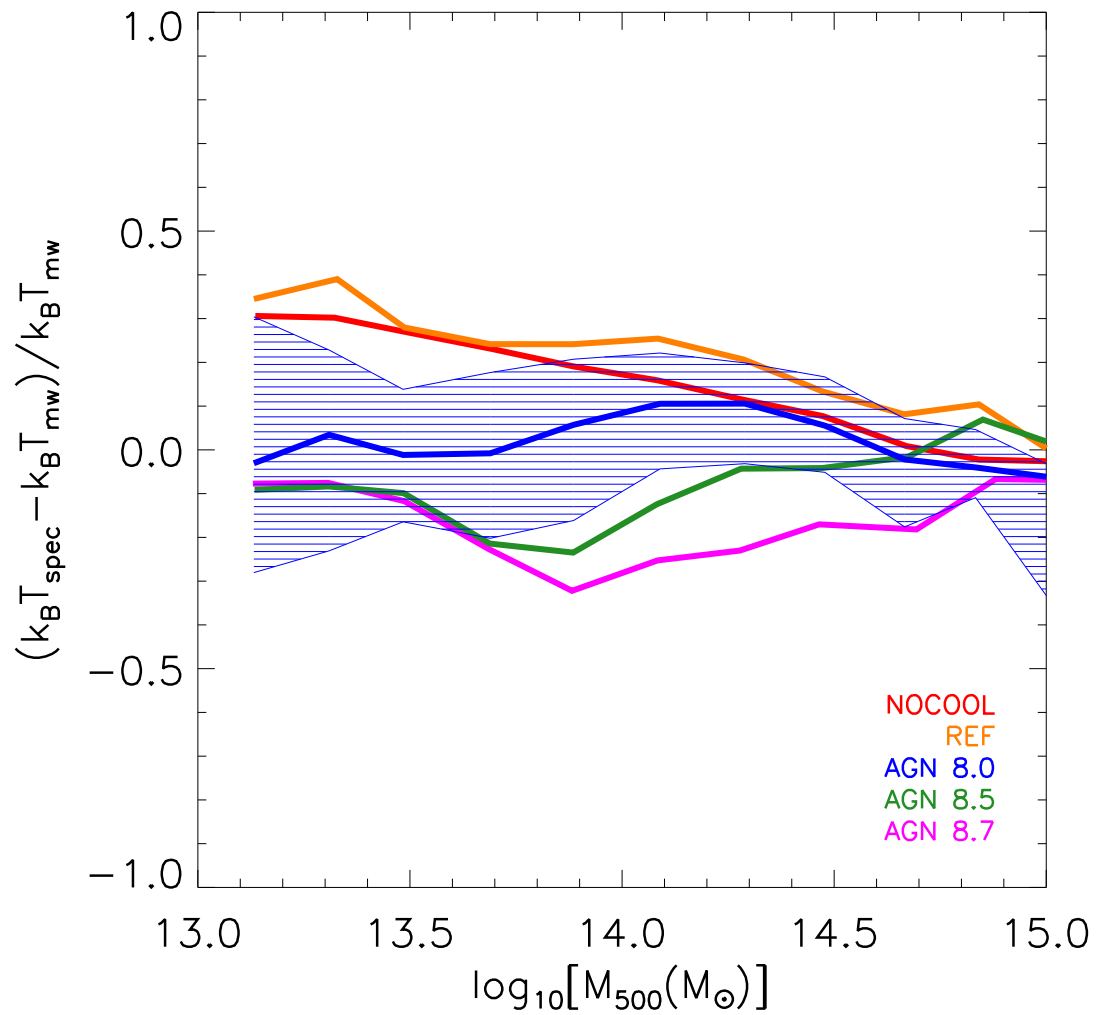
Figure B.2: Bias of 'uncorrected' temperatures due to spectral fitting as a function of M_{500} at $z = 0$. The level (and even the sign) of the bias depend on the details of the implemented sub-grid physics.

Appendix C

Results for the other physical models

We present the results of the fitting procedures described in Section 3.4 for the three of the other cosmo-OWLS physical models in *Planck* cosmology.

Scaling relation	Median or scatter	A	α	β	χ^2	Number of degrees of freedom
$T_{spec} - M_{500}$	Median	0.198	0.389	0.532	0.044	21
$T_{spec} - M_{500}$	Scatter	−0.947	0.428	0.280	0.142	21
$L_{0.5-2.0keV} - M_{500}$	Median	43.718	2.317	1.268	0.188	21
$L_{0.5-2.0keV} - M_{500}$	Scatter	−0.338	−0.503	−0.093	0.171	21
$M_{gas,500} - M_{500}$	Median	13.139	0.054	1.013	0.006	21
$M_{gas,500} - M_{500}$	Scatter	−1.395	−0.198	−0.0401	0.885	21
$Y_{X,500} - M_{500}$	Median	13.314	0.454	1.560	0.027	21
$Y_{X,500} - M_{500}$	Scatter	−0.897	0.242	0.252	0.164	21
$d_A^2 Y_{500} - M_{500}$	Median	−5.574	0.601	1.643	0.011	21
$d_A^2 Y_{500} - M_{500}$	Scatter	−0.949	0.129	0.106	0.467	21

Table C.1: Results of the evolving power-law fitting (given by equation 3.14) to both the median relation and the log-normal scatter about it for the NOCOOL simulation. The scatter is the log-normal scatter in the natural logarithm of the Y variable.

Scaling relation	Median or scatter	A''	α''	β''	γ''	δ''	χ^2	Number of degrees of freedom
$T_{spec} - M_{500}$	Median	0.224	0.335	0.709	0.484	−0.072	0.031	19
$T_{spec} - M_{500}$	Scatter	−0.983	0.566	−0.110	0.330	0.220	0.107	19
$L_{0.5-2.0keV} - M_{500}$	Median	43.789	2.271	1.524	1.109	−0.004	0.036	19
$L_{0.5-2.0keV} - M_{500}$	Scatter	−0.345	−0.439	−0.252	−0.094	0.113	0.161	19
$M_{gas,500} - M_{500}$	Median	13.142	0.046	1.037	1.010	−0.014	0.006	19
$M_{gas,500} - M_{500}$	Scatter	−1.409	−0.172	−0.132	−0.013	0.033	0.875	19
$Y_{X,500} - M_{500}$	Median	13.333	0.406	1.709	1.528	−0.069	0.020	19
$Y_{X,500} - M_{500}$	Scatter	−0.948	0.400	−0.217	0.333	0.241	0.109	19
$d_A^2 Y_{500} - M_{500}$	Median	−5.572	0.586	1.684	1.643	−0.028	0.011	19
$d_A^2 Y_{500} - M_{500}$	Scatter	−1.028	0.269	−0.382	0.261	0.173	0.339	19

Table C.2: Results of the evolving broken power-law fitting (given by equation 3.17) to both the median relation and the log-normal scatter about it for the NOCOOL simulation. The scatter is the log-normal scatter in the natural logarithm of the Y variable.

Scaling relation	Median or scatter	A	α	β	χ^2	Number of degrees of freedom
$T_{spec} - M_{500}$	Median	0.301	0.418	0.537	0.067	21
$T_{spec} - M_{500}$	Scatter	−0.804	−0.315	−0.075	0.152	21
$L_{0.5-2.0keV} - M_{500}$	Median	43.095	2.553	1.203	0.114	21
$L_{0.5-2.0keV} - M_{500}$	Scatter	−0.403	−0.941	−0.182	0.287	21
$M_{gas,500} - M_{500}$	Median	12.926	0.293	1.080	0.009	21
$M_{gas,500} - M_{500}$	Scatter	−1.056	−0.884	−0.123	0.148	21
$Y_{X,500} - M_{500}$	Median	13.247	0.545	1.589	0.046	21
$Y_{X,500} - M_{500}$	Scatter	−0.897	−0.450	−0.067	0.474	21
$d_A^2 Y_{500} - M_{500}$	Median	−5.713	0.632	1.706	0.047	21
$d_A^2 Y_{500} - M_{500}$	Scatter	−0.969	−0.042	−0.057	0.401	21

Table C.3: Results of the evolving power-law fitting (given by equation 3.14) to both the median relation and the log-normal scatter about it for the REF simulation. The scatter is the log-normal scatter in the natural logarithm of the Y variable.

Scaling relation	Median or scatter	A''	α''	β''	γ''	δ''	χ^2	Number of degrees of freedom
$T_{spec} - M_{500}$	Median	0.339	0.314	0.853	0.472	-0.152	0.039	19
$T_{spec} - M_{500}$	Scatter	-0.850	-0.159	-0.526	-0.006	0.241	0.104	19
$L_{0.5-2.0keV} - M_{500}$	Median	43.081	2.672	0.903	1.204	0.210	0.082	19
$L_{0.5-2.0keV} - M_{500}$	Scatter	-0.438	-0.811	-0.550	-0.131	0.204	0.255	19
$M_{gas,500} - M_{500}$	Median	12.931	0.266	1.151	1.076	-0.045	0.008	19
$M_{gas,500} - M_{500}$	Scatter	-1.054	-0.944	0.019	-0.111	-0.113	0.136	19
$Y_{X,500} - M_{500}$	Median	13.277	0.444	1.880	1.544	-0.156	0.026	19
$Y_{X,500} - M_{500}$	Scatter	-0.936	-0.336	-0.408	-0.004	0.171	0.444	19
$d_A^2 Y_{500} - M_{500}$	Median	-5.689	0.596	1.837	1.658	-0.040	0.035	19
$d_A^2 Y_{500} - M_{500}$	Scatter	-1.016	0.030	-0.318	0.038	0.080	0.353	19

Table C.4: Results of the evolving broken power-law fitting (given by equation 3.17) to both the median relation and the log-normal scatter about it for the REF simulation. The scatter is the log-normal scatter in the natural logarithm of the Y variable.

Scaling relation	Median or scatter	A	α	β	χ^2	Number of degrees of freedom
$T_{spec} - M_{500}$	Median	0.204	0.410	0.689	0.058	21
$T_{spec} - M_{500}$	Scatter	-0.780	-0.365	-0.145	0.680	21
$L_{0.5-2.0keV} - M_{500}$	Median	42.633	3.463	1.711	0.283	21
$L_{0.5-2.0keV} - M_{500}$	Scatter	-0.472	-0.570	0.180	0.658	21
$M_{gas,500} - M_{500}$	Median	12.696	0.604	1.387	0.102	21
$M_{gas,500} - M_{500}$	Scatter	-0.884	-0.483	-0.418	1.465	21
$Y_{X,500} - M_{500}$	Median	12.974	0.959	2.038	0.337	21
$Y_{X,500} - M_{500}$	Scatter	-0.695	-0.202	-0.210	0.681	21
$d_A^2 Y_{500} - M_{500}$	Median	-5.894	0.929	2.041	0.161	21
$d_A^2 Y_{500} - M_{500}$	Scatter	-0.790	0.144	-0.210	0.584	21

Table C.5: Results of the evolving power-law fitting (given by equation 3.14) to both the median relation and the log-normal scatter about it for the AGN 8.5 simulation. The scatter is the log-normal scatter in the natural logarithm of the Y variable.

Scaling relation	Median or scatter	A''	α''	β''	γ''	δ''	χ^2	Number of degrees of freedom
$T_{spec} - M_{500}$	Median	0.251	0.304	1.032	0.606	−0.151	0.018	19
$T_{spec} - M_{500}$	Scatter	−0.768	−0.434	0.039	−0.155	−0.119	0.671	19
$L_{0.5-2.0keV} - M_{500}$	Median	42.642	3.352	1.983	1.721	−0.202	0.249	19
$L_{0.5-2.0keV} - M_{500}$	Scatter	−0.568	−0.520	−0.507	0.041	−0.012	0.369	19
$M_{gas,500} - M_{500}$	Median	12.747	0.413	1.932	1.315	−0.305	0.032	19
$M_{gas,500} - M_{500}$	Scatter	−0.804	−0.641	0.116	−0.570	−0.210	1.341	19
$Y_{X,500} - M_{500}$	Median	13.089	0.599	3.108	1.860	−0.558	0.055	19
$Y_{X,500} - M_{500}$	Scatter	−0.783	0.099	−1.089	−0.079	0.476	0.497	19
$d_A^2 Y_{500} - M_{500}$	Median	−5.814	0.770	2.578	1.890	−0.213	0.038	19
$d_A^2 Y_{500} - M_{500}$	Scatter	−0.856	0.503	−1.167	−0.151	0.611	0.336	19

Table C.6: Results of the evolving broken power-law fitting (given by equation 3.17) to both the median relation and the log-normal scatter about it for the AGN 8.5 simulation. The scatter is the log-normal scatter in the natural logarithm of the Y variable.

Bibliography

Abazajian K. N., Adelman-McCarthy J. K., Agüeros M. A., Allam S. S., Allende Prieto C., An D., Anderson K. S. J., Anderson S. F., Annis J., Bahcall N. A., et al., 2009, ApJS, 182, 543

Abell G. O., 1958, ApJS, 3, 211

Agertz O., Moore B., Stadel J., Potter D., Miniati F., Read J., Mayer L., Gawryszczak A., Kravtsov A., Nordlund Å., Pearce F., Quilis V., Rudd D., Springel V., Stone J., Tasker E., Teyssier R., Wadsley J., Walder R., 2007, MNRAS, 380, 963

Akritas M. G., Bershady M. A., 1996, ApJ, 470, 706

Allen S. W., Evrard A. E., Mantz A. B., 2011, ARA&A, 49, 409

Allen S. W., Rapetti D. A., Schmidt R. W., Ebeling H., Morris R. G., Fabian A. C., 2008, MNRAS, 383, 879

Anders E., Grevesse N., 1989, Geochimica et Cosmochimica Acta, 53, 197

Andersson K., Benson B. A., Ade P. A. R., Aird K. A., Armstrong B., Bautz M., Bleem L. E., Brodwin M., Carlstrom J. E., Chang C. L., Crawford T. M., Crites A. T., de Haan T., Desai S., Dobbs M. A., Dudley J. P., Foley R. J., Forman W. R., Garmire G., George E. M., Gladders M. D., Halverson N. W., High F. W., Holder G. P., Holzapfel W. L., Hrubes J. D., Jones C., Joy M., Keisler R., Knox L., Lee A. T., Leitch E. M., Lueker M., Marrone D. P., McMahon J. J., Mehl J., Meyer S. S., Mohr J. J., Montroy T. E., Murray S. S., Padin S., Plagge T., Pryke C., Reichardt C. L., Rest A., Ruel J., Ruhl J. E., Schaffer K. K., Shaw L., Shirokoff E., Song J., Spieler

H. G., Stalder B., Staniszewski Z., Stark A. A., Stubbs C. W., Vanderlinde K., Vieira J. D., Vikhlinin A., Williamson R., Yang Y., Zahn O., Zenteno A., 2011, ApJ, 738, 48

Arnaud M., Evrard A. E., 1999, MNRAS, 305, 631

Arnaud M., Pointecouteau E., Pratt G. W., 2007, A&A, 474, L37

Arnaud M., Pratt G. W., Piffaretti R., Böhringer H., Croston J. H., Pointecouteau E., 2010, A&A, 517, A92

Bahé Y. M., McCarthy I. G., King L. J., 2012, MNRAS, 421, 1073

Balogh M. L., Mazzotta P., Bower R. G., Eke V., Bourdin H., Lu T., Theuns T., 2011, MNRAS, 412, 947

Balogh M. L., Pearce F. R., Bower R. G., Kay S. T., 2001, MNRAS, 326, 1228

Bandara K., Crampton D., Simard L., 2009, ApJ, 704, 1135

Bartelmann M., 2010, Reviews of Modern Physics, 82, 331

Battaglia N., Bond J. R., Pfrommer C., Sievers J. L., 2012, ApJ, 758, 74

Baugh C. M., 2006, Reports on Progress in Physics, 69, 3101

Becker M. R., Kravtsov A. V., 2011, ApJ, 740, 25

Benson A. J., Bower R. G., Frenk C. S., Lacey C. G., Baugh C. M., Cole S., 2003, ApJ, 599, 38

Benson A. J., Cole S., Frenk C. S., Baugh C. M., Lacey C. G., 2000, MNRAS, 311, 793

Bertin E., Arnouts S., 1996, A&AS, 117, 393

Bhattacharya S., Di Matteo T., Kosowsky A., 2008, MNRAS, 389, 34

Birkinshaw M., 1999, Physics Reports, 310, 97

Birkinshaw M., Hughes J. P., Arnaud K. A., 1991, ApJ, 379, 466

Blaizot J., Wadadekar Y., Guiderdoni B., Colombi S. T., Bertin E., Bouchet F. R., Devriendt J. E. G., Hatton S., 2005, MNRAS, 360, 159

Blanton M. R., Roweis S., 2007, AJ, 133, 734

Blanton M. R., Schlegel D. J., Strauss M. A., Brinkmann J., Finkbeiner D., Fukugita M., Gunn J. E., Hogg D. W., Ivezić Ž., Knapp G. R., Lupton R. H., Munn J. A., Schneider D. P., Tegmark M., Zehavi I., 2005, AJ, 129, 2562

Bode P., Ostriker J. P., Weller J., Shaw L., 2007, ApJ, 663, 139

Böhringer H., Schuecker P., Guzzo L., Collins C. A., Voges W., Schindler S., Neumann D. M., Cruddace R. G., De Grandi S., Chincarini G., Edge A. C., MacGillivray H. T., Shaver P., 2001, A&A, 369, 826

Böhringer H., Schuecker P., Pratt G. W., Arnaud M., Ponman T. J., Croston J. H., Borgani S., Bower R. G., Briel U. G., Collins C. A., Donahue M., Forman W. R., Finoguenov A., Geller M. J., Guzzo L., Henry J. P., Kneissl R., Mohr J. J., Matsushita K., Mullis C. R., Ohashi T., Pedersen K., Pierini D., Quintana H., Raychaudhury S., Reiprich T. H., Romer A. K., Rosati P., Sabirli K., Temple R. F., Viana P. T. P., Vikhlinin A., Voit G. M., Zhang Y.-Y., 2007, A&A, 469, 363

Booth C. M., Schaye J., 2009, MNRAS, 398, 53

Booth C. M., Schaye J., 2010, MNRAS, 405, L1

Borgani S., Dolag K., Murante G., Cheng L.-M., Springel V., Diaferio A., Moscardini L., Tormen G., Tornatore L., Tozzi P., 2006, MNRAS, 367, 1641

Borgani S., Finoguenov A., Kay S. T., Ponman T. J., Springel V., Tozzi P., Voit G. M., 2005, MNRAS, 361, 233

Borgani S., Kravtsov A., 2011, Advanced Science Letters, 4, 204

Borgani S., Murante G., Springel V., Diaferio A., Dolag K., Moscardini L., Tormen G., Tornatore L., Tozzi P., 2004, MNRAS, 348, 1078

Bower R. G., Benson A. J., Malbon R., Helly J. C., Frenk C. S., Baugh C. M., Cole S., Lacey C. G., 2006, MNRAS, 370, 645

Bruzual G., Charlot S., 2003, MNRAS, 344, 1000

Bryan G. L., 2000, ApJL, 544, L1

Budzynski J. M., Koposov S. E., McCarthy I. G., Belokurov V., 2014, MNRAS, 437, 1362

Carlstrom J. E., Holder G. P., Reese E. D., 2002, ARA&A, 40, 643

Cash W., 1979, ApJ, 228, 939

Cavagnolo K. W., Donahue M., Voit G. M., Sun M., 2009, ApJS, 182, 12

Cavaliere A., Fusco-Femiano R., 1976, A&A, 49, 137

Chabrier G., 2003, PASP, 115, 763

Chilingarian I. V., Melchior A.-L., Zolotukhin I. Y., 2010, MNRAS, 405, 1409

Chilingarian I. V., Zolotukhin I. Y., 2012, MNRAS, 419, 1727

Clerc N., Sadibekova T., Pierre M., Pacaud F., Le Fèvre J.-P., Adami C., Altieri B., Valtchanov I., 2012, MNRAS, 423, 3561

Coil A. L., Davis M., Szapudi I., 2001, PASP, 113, 1312

Cole S., Hatton S., Weinberg D. H., Frenk C. S., 1998, MNRAS, 300, 945

Colless M., Dalton G., Maddox S., Sutherland W., Norberg P., Cole S., Bland-Hawthorn J., Bridges T., Cannon R., Collins C., Couch W., Cross N., Deeley K., De Propris R., Driver S. P., Efstathiou G., Ellis R. S., Frenk C. S., Glazebrook K., Jackson C., Lahav O., Lewis I., Lumsden S., Madgwick D., Peacock J. A., Peterson B. A., Price I., Seaborne M., Taylor K., 2001, MNRAS, 328, 1039

Crain R. A., Eke V. R., Frenk C. S., Jenkins A., McCarthy I. G., Navarro J. F., Pearce F. R., 2007, MNRAS, 377, 41

Croft R. A. C., Di Matteo T., Davé R., Hernquist L., Katz N., Fardal M. A., Weinberg D. H., 2001, ApJ, 557, 67

Croston J. H., Pratt G. W., Böhringer H., Arnaud M., Pointecouteau E., Ponman T. J., Sanderson A. J. R., Temple R. F., Bower R. G., Donahue M., 2008, A&A, 487, 431

Croton D. J., Springel V., White S. D. M., De Lucia G., Frenk C. S., Gao L., Jenkins A., Kauffmann G., Navarro J. F., Yoshida N., 2006, MNRAS, 365, 11

Cunha C. E., Lima M., Oyaizu H., Frieman J., Lin H., 2009, MNRAS, 396, 2379

da Silva A. C., Barbosa D., Liddle A. R., Thomas P. A., 2000, MNRAS, 317, 37

Dalla Vecchia C., Schaye J., 2008, MNRAS, 387, 1431

Dalla Vecchia C., Schaye J., 2012, MNRAS, 426, 140

Davé R., Katz N., Weinberg D. H., 2002, ApJ, 579, 23

Davé R., Oppenheimer B. D., Sivanandam S., 2008, MNRAS, 391, 110

David L. P., Jones C., Forman W., Vargas I. M., Nulsen P., 2006, ApJ, 653, 207

De Lucia G., Blaizot J., 2007, MNRAS, 375, 2

Diaferio A., Kauffmann G., Colberg J. M., White S. D. M., 1999, MNRAS, 307, 537

Dicke R. H., Peebles P. J. E., Roll P. G., Wilkinson D. T., 1965, ApJ, 142, 414

Dolag K., Borgani S., Murante G., Springel V., 2009, MNRAS, 399, 497

Dubois Y., Devriendt J., Slyz A., Teyssier R., 2010, MNRAS, 409, 985

Duffy A. R., Schaye J., Kay S. T., Dalla Vecchia C., 2008, MNRAS, 390, L64

Ebeling H., Edge A. C., Bohringer H., Allen S. W., Crawford C. S., Fabian A. C., Voges W., Huchra J. P., 1998, MNRAS, 301, 881

Edge A. C., Stewart G. C., 1991, MNRAS, 252, 414

Edge A. C., Stewart G. C., Fabian A. C., Arnaud K. A., 1990, MNRAS, 245, 559

Edwards L. O. V., Hudson M. J., Balogh M. L., Smith R. J., 2007, MNRAS, 379, 100

Eisenstein D. J., Hu W., 1999, ApJ, 511, 5

Ettori S., Borgani S., Moscardini L., Murante G., Tozzi P., Diaferio A., Dolag K., Springel V., Tormen G., Tornatore L., 2004, MNRAS, 354, 111

Evrard A. E., Henry J. P., 1991, ApJ, 383, 95

Evrard A. E., MacFarland T. J., Couchman H. M. P., Colberg J. M., Yoshida N., White S. D. M., Jenkins A., Frenk C. S., Pearce F. R., Peacock J. A., Thomas P. A., 2002, ApJ, 573, 7

Fabian A. C., 1994, ARA&A, 32, 277

Fabian A. C., 2012, ARA&A, 50, 455

Fabjan D., Borgani S., Tornatore L., Saro A., Murante G., Dolag K., 2010, MNRAS, 401, 1670

Ferland G. J., Korista K. T., Verner D. A., Ferguson J. W., Kingdon J. B., Verner E. M., 1998, PASP, 110, 761

Foster A. R., Ji L., Smith R. K., Brickhouse N. S., 2012, ApJ, 756, 128

Friedmann A., 1922, Zeitschrift fur Physik, 10, 377

Gastaldello F., Buote D. A., Humphrey P. J., Zappacosta L., Bullock J. S., Brighenti F., Mathews W. G., 2007, ApJ, 669, 158

Giodini S., Pierini D., Finoguenov A., Pratt G. W., Boehringer H., Leauthaud A., Guzzo L., Aussel H., Bolzonella M., Capak P., Elvis M., Hasinger G., Ilbert O., Kartaltepe J. S., Koekemoer A. M., Lilly S. J., Massey R., McCracken H. J., Rhodes J., Salvato M., Sanders D. B., Scoville N. Z., Sasaki S., Smolcic V., Taniguchi Y., Thompson D., COSMOS Collaboration, 2009, ApJ, 703, 982

Gioia I. M., Maccacaro T., Schild R. E., Wolter A., Stocke J. T., Morris S. L., Henry J. P., 1990, ApJS, 72, 567

Gonzalez A. H., Sivanandam S., Zabludoff A. I., Zaritsky D., 2013, ApJ, 778, 14

Gonzalez A. H., Zaritsky D., Zabludoff A. I., 2007, ApJ, 666, 147

Guo Q., White S., Angulo R. E., Henriques B., Lemson G., Boylan-Kolchin M., Thomas P., Short C., 2013, MNRAS, 428, 1351

Guo Q., White S., Boylan-Kolchin M., De Lucia G., Kauffmann G., Lemson G., Li C., Springel V., Weinmann S., 2011, MNRAS, 413, 101

Haardt F., Madau P., 2001, in Clusters of Galaxies and the High Redshift Universe Observed in X-rays, Neumann D. M., Tran J. T. V., eds.

Hallman E. J., O'Shea B. W., Burns J. O., Norman M. L., Harkness R., Wagner R., 2007, ApJ, 671, 27

Hand N., Addison G. E., Aubourg E., Battaglia N., Battistelli E. S., Bizyaev D., Bond J. R., Brewington H., Brinkmann J., Brown B. R., Das S., Dawson K. S., Devlin M. J., Dunkley J., Dunner R., Eisenstein D. J., Fowler J. W., Gralla M. B., Hajian A., Halpern M., Hilton M., Hincks A. D., Hlozek R., Hughes J. P., Infante L., Irwin K. D., Kosowsky A., Lin Y.-T., Malanushenko E., Malanushenko V., Marriage T. A., Marsden D., Menanteau F., Moodley K., Niemack M. D., Nolta M. R., Oravetz D., Page L. A., Palanque-Delabrouille N., Pan K., Reese E. D., Schlegel D. J., Schneider D. P., Sehgal N., Shelden A., Sievers J., Sifón C., Simmons A., Snedden S., Spergel D. N., Staggs S. T., Swetz D. S., Switzer E. R., Trac H., Weaver B. A., Wollack E. J., Yeche C., Zunckel C., 2012, Physical Review Letters, 109, 041101

Herranz D., Sanz J. L., Hobson M. P., Barreiro R. B., Diego J. M., Martínez-González E., Lasenby A. N., 2002, MNRAS, 336, 1057

Herschel W., 1785, Royal Society of London Philosophical Transactions Series I, 75, 213

Hilton M., Romer A. K., Kay S. T., Mehrtens N., Lloyd-Davies E. J., Thomas P. A., Short C. J., Mayers J. A., Rooney P. J., Stott J. P., Collins C. A., Harrison C. D., Hoyle B., Liddle A. R., Mann R. G., Miller C. J., Sahlén M., Viana P. T. P., Davidson

M., Hosmer M., Nichol R. C., Sabirli K., Stanford S. A., West M. J., 2012, MNRAS, 424, 2086

Holder G. P., McCarthy I. G., Babul A., 2007, MNRAS, 382, 1697

Jenkins A., Frenk C. S., White S. D. M., Colberg J. M., Cole S., Evrard A. E., Couchman H. M. P., Yoshida N., 2001, MNRAS, 321, 372

Johnson R., Ponman T. J., Finoguenov A., 2009, MNRAS, 395, 1287

Jones M., Saunders R., Alexander P., Birkinshaw M., Dilon N., Grainge K., Hancock S., Lasenby A., Lefebvre D., Pooley G., 1993, Nature, 365, 320

Kaiser N., 1986, MNRAS, 222, 323

Kaiser N., 1991, ApJ, 383, 104

Kay S. T., da Silva A. C., Aghanim N., Blanchard A., Liddle A. R., Puget J.-L., Sadat R., Thomas P. A., 2007, MNRAS, 377, 317

Kay S. T., Peel M. W., Short C. J., Thomas P. A., Young O. E., Battye R. A., Liddle A. R., Pearce F. R., 2012, MNRAS, 422, 1999

Kay S. T., Thomas P. A., Jenkins A., Pearce F. R., 2004, MNRAS, 355, 1091

Khedekar S., Churazov E., Kravtsov A., Zhuravleva I., Lau E. T., Nagai D., Sunyaev R., 2013, MNRAS, 431, 954

Kitzbichler M. G., White S. D. M., 2007, MNRAS, 376, 2

Kolb E. W., Turner M. S., 1990, The early universe.

Komatsu E., Smith K. M., Dunkley J., Bennett C. L., Gold B., Hinshaw G., Jarosik N., Larson D., Nolta M. R., Page L., Spergel D. N., Halpern M., Hill R. S., Kogut A., Limon M., Meyer S. S., Odegard N., Tucker G. S., Weiland J. L., Wollack E., Wright E. L., 2011, ApJS, 192, 18

Kravtsov A. V., Borgani S., 2012, ARA&A, 50, 353

Kravtsov A. V., Vikhlinin A., Nagai D., 2006, ApJ, 650, 128

Lachièze-Rey M., 1995, Cosmology. Cambridge University Press

Lahav O., Fabian A. C., Edge A. C., Putney A., 1989, MNRAS, 238, 881

Larson R. B., 1974, MNRAS, 169, 229

Laureijs R., Amiaux J., Arduini S., Auguères J. ., Brinchmann J., Cole R., Cropper M.,
   Dabin C., Duvet L., Ealet A., et al., 2011, ESA report (arXiv:1110.3193)

Leauthaud A., Finoguenov A., Kneib J.-P., Taylor J. E., Massey R., Rhodes J., Ilbert
   O., Bundy K., Tinker J., George M. R., Capak P., et al., 2010, ApJ, 709, 97

Leauthaud A., George M. R., Behroozi P. S., Bundy K., Tinker J., Wechsler R. H.,
   Conroy C., Finoguenov A., Tanaka M., 2012, ApJ, 746, 95

Lin Y.-T., Mohr J. J., 2004, ApJ, 617, 879

Lin Y.-T., Mohr J. J., Stanford S. A., 2004, ApJ, 610, 745

Lin Y.-T., Stanford S. A., Eisenhardt P. R. M., Vikhlinin A., Maughan B. J., Kravtsov
   A., 2012, ApJL, 745, L3

Lumb D. H., Bartlett J. G., Romer A. K., Blanchard A., Burke D. J., Collins C. A.,
   Nichol R. C., Giard M., Marty P. B., Nevalainen J., Sadat R., Vauclair S. C., 2004,
   A&A, 420, 853

Mantz A., Allen S. W., Ebeling H., Rapetti D., Drlica-Wagner A., 2010a, MNRAS,
   406, 1773

Mantz A., Allen S. W., Rapetti D., Ebeling H., 2010b, MNRAS, 406, 1759

Mantz A. B., Allen S. W., Morris R. G., Rapetti D. A., Applegate D. E., Kelly P. L.,
   von der Linden A., Schmidt R. W., 2014, MNRAS, 440, 2077

Marconi A., Risaliti G., Gilli R., Hunt L. K., Maiolino R., Salvati M., 2004, MNRAS,
   351, 169

Markevitch M., 1998, ApJ, 504, 27

Markwardt C. B., 2009, in Astronomical Society of the Pacific Conference Series, Vol. 411, Astronomical Data Analysis Software and Systems XVIII, Bohlender D. A., Durand D., Dowler P., eds., p. 251

Marriage T. A., Acquaviva V., Ade P. A. R., Aguirre P., Amiri M., Appel J. W., Barrientos L. F., Battistelli E. S., Bond J. R., Brown B., Burger B., Chervenak J., Das S., Devlin M. J., Dicker S. R., Bertrand Doriese W., Dunkley J., Dünner R., Essinger-Hileman T., Fisher R. P., Fowler J. W., Hajian A., Halpern M., Hasselfield M., Hernández-Monteagudo C., Hilton G. C., Hilton M., Hincks A. D., Hlozek R., Huffenberger K. M., Handel Hughes D., Hughes J. P., Infante L., Irwin K. D., Baptiste Juin J., Kaul M., Klein J., Kosowsky A., Lau J. M., Limon M., Lin Y.-T., Lupton R. H., Marsden D., Martocci K., Mauskopf P., Menanteau F., Moodley K., Moseley H., Netterfield C. B., Niemack M. D., Nolta M. R., Page L. A., Parker L., Partridge B., Quintana H., Reese E. D., Reid B., Sehgal N., Sherwin B. D., Sievers J., Spergel D. N., Staggs S. T., Swetz D. S., Switzer E. R., Thornton R., Trac H., Tucker C., Warne R., Wilson G., Wollack E., Zhao Y., 2011, ApJ, 737, 61

Mathiesen B., Evrard A. E., Mohr J. J., 1999, ApJL, 520, L21

Mathiesen B. F., Evrard A. E., 2001, ApJ, 546, 100

Maughan B. J., Jones C., Forman W., Van Speybroeck L., 2008, ApJS, 174, 117

Maughan B. J., Jones L. R., Ebeling H., Scharf C., 2006, MNRAS, 365, 509

Mazzotta P., Rasia E., Moscardini L., Tormen G., 2004, MNRAS, 354, 10

McCarthy I. G., Babul A., Bower R. G., Balogh M. L., 2008, MNRAS, 386, 1309

McCarthy I. G., Balogh M. L., Babul A., Poole G. B., Horner D. J., 2004, ApJ, 613, 811

McCarthy I. G., Le Brun A. M. C., Schaye J., Holder G. P., 2014, MNRAS, 440, 3645

McCarthy I. G., Schaye J., Bower R. G., Ponman T. J., Booth C. M., Dalla Vecchia C., Springel V., 2011, MNRAS, 412, 1965

McCarthy I. G., Schaye J., Ponman T. J., Bower R. G., Booth C. M., Dalla Vecchia C., Crain R. A., Springel V., Theuns T., Wiersma R. P. C., 2010, MNRAS, 406, 822

McConnell N. J., Ma C.-P., 2013, ApJ, 764, 184

McDonald M., Benson B. A., Vikhlinin A., Aird K. A., Allen S. W., Bautz M., Bayliss M., Bleem L. E., Bocquet S., Brodwin M., Carlstrom J. E., Chang C. L., Cho H. M., Clocchiatti A., Crawford T. M., Crites A. T., de Haan T., Dobbs M. A., Foley R. J., Forman W. R., George E. M., Gladders M. D., Gonzalez A. H., Halverson N. W., Hlavacek-Larrondo J., Holder G. P., Holzapfel W. L., Hrubes J. D., Jones C., Keisler R., Knox L., Lee A. T., Leitch E. M., Liu J., Lueker M., Luong-Van D., Mantz A., Marrone D. P., McMahon J. J., Meyer S. S., Miller E. D., Mocanu L., Mohr J. J., Murray S. S., Padin S., Pryke C., Reichardt C. L., Rest A., Ruhl J. E., Saliwanchik B. R., Saro A., Sayre J. T., Schaffer K. K., Shirokoff E., Spieler H. G., Stalder B., Stanford S. A., Staniszewski Z., Stark A. A., Story K. T., Stubbs C. W., Vanderlinde K., Vieira J. D., Williamson R., Zahn O., Zenteno A., 2014, ApJ submitted (arXiv:1404.6250)

McNamara B. R., Nulsen P. E. J., 2007, ARA&A, 45, 117

Melin J.-B., Bartlett J. G., Delabrouille J., 2006, A&A, 459, 341

Menanteau F., González J., Juin J.-B., Marriage T. A., Reese E. D., Acquaviva V., Aguirre P., Appel J. W., Baker A. J., Barrientos L. F., Battistelli E. S., Bond J. R., Das S., Deshpande A. J., Devlin M. J., Dicker S., Dunkley J., Dünner R., Essinger-Hileman T., Fowler J. W., Hajian A., Halpern M., Hasselfield M., Hernández-Monteagudo C., Hilton M., Hincks A. D., Hlozek R., Huffenberger K. M., Hughes J. P., Infante L., Irwin K. D., Klein J., Kosowsky A., Lin Y.-T., Marsden D., Moodley K., Niemack M. D., Nolta M. R., Page L. A., Parker L., Partridge B., Sehgal N., Sievers J., Spergel D. N., Staggs S. T., Swetz D., Switzer E., Thornton R., Trac H., Warne R., Wollack E., 2010, ApJ, 723, 1523

Merloni A., Predehl P., Becker W., Böhringer H., Boller T., Brunner H., Brusa M., Dennerl K., Freyberg M., Friedrich P., Georgakakis A., Haberl F., Hasinger G., Meidinger N., Mohr J., Nandra K., Rau A., Reiprich T. H., Robrade J., Salvato M., Santangelo A., Sasaki M., Schwope A., Wilms J., German eROSITA Consortium t., 2012, MPE online document (arXiv:1209.3114)

Messier C., 1784, Catalogue des Nébuleuses et des amas d'Étoiles (Catalog of Nebulae and Star Clusters). Tech. rep.

Milgrom M., 1983, ApJ, 270, 365

Miller C. J., Nichol R. C., Reichart D., Wechsler R. H., Evrard A. E., Annis J., McKay T. A., Bahcall N. A., Bernardi M., Böhringer H., Connolly A. J., Goto T., Kniazev A., Lamb D., Postman M., Schneider D. P., Sheth R. K., Voges W., 2005, AJ, 130, 968

Miller M. J., Bregman J. N., 2013, ApJ, 770, 118

Mitchell N. L., McCarthy I. G., Bower R. G., Theuns T., Crain R. A., 2009, MNRAS, 395, 180

Moretti A., Campana S., Lazzati D., Tagliaferri G., 2003, ApJ, 588, 696

Morrison R., McCammon D., 1983, ApJ, 270, 119

Mroczkowski T., Bonamente M., Carlstrom J. E., Culverhouse T. L., Greer C., Hawkins D., Hennessy R., Joy M., Lamb J. W., Leitch E. M., Loh M., Maughan B., Marrone D. P., Miller A., Muchovej S., Nagai D., Pryke C., Sharp M., Woody D., 2009, ApJ, 694, 1034

Mulchaey J. S., Jeltema T. E., 2010, ApJL, 715, L1

Mushotzky R. F., 1984, Physica Scripta Volume T, 7, 157

Nagai D., Kravtsov A. V., Vikhlinin A., 2007, ApJ, 668, 1

Nagai D., Vikhlinin A., Kravtsov A. V., 2007, ApJ, 655, 98

Navarro J. F., Frenk C. S., White S. D. M., 1997, ApJ, 490, 493

Nelson K., Lau E. T., Nagai D., Rudd D. H., Yu L., 2014, ApJ, 782, 107

Neto A. F., Gao L., Bett P., Cole S., Navarro J. F., Frenk C. S., White S. D. M., Springel V., Jenkins A., 2007, MNRAS, 381, 1450

Nord B., Stanek R., Rasia E., Evrard A. E., 2008, MNRAS, 383, L10

Osmond J. P. F., Ponman T. J., 2004, MNRAS, 350, 1511

Pacaud F., Pierre M., Adami C., Altieri B., Andreon S., Chiappetti L., Detal A., Duc P.-A., Galaz G., Gueguen A., Le Fèvre J.-P., Hertling G., Libbrecht C., Melin J.-B., Ponman T. J., Quintana H., Refregier A., Sprimont P.-G., Surdej J., Valtchanov I., Willis J. P., Alloin D., Birkinshaw M., Bremer M. N., Garcet O., Jean C., Jones L. R., Le Fèvre O., Maccagni D., Mazure A., Proust D., Röttgering H. J. A., Trinchieri G., 2007, MNRAS, 382, 1289

Pacaud F., Pierre M., Refregier A., Gueguen A., Starck J.-L., Valtchanov I., Read A. M., Altieri B., Chiappetti L., Gandhi P., Garcet O., Gosset E., Ponman T. J., Surdej J., 2006, MNRAS, 372, 578

Panagoulia E. K., Fabian A. C., Sanders J. S., 2014, MNRAS, 438, 2341

Peacock J. A., 1999, Cosmological Physics. Cambridge University Press

Penzias A. A., Wilson R. W., 1965, ApJ, 142, 419

Perlmutter S., Aldering G., Goldhaber G., Knop R. A., Nugent P., Castro P. G., Deustua S., Fabbro S., Goobar A., Groom D. E., Hook I. M., Kim A. G., Kim M. Y., Lee J. C., Nunes N. J., Pain R., Pennypacker C. R., Quimby R., Lidman C., Ellis R. S., Irwin M., McMahon R. G., Ruiz-Lapuente P., Walton N., Schaefer B., Boyle B. J., Filippenko A. V., Matheson T., Fruchter A. S., Panagia N., Newberg H. J. M., Couch W. J., Project T. S. C., 1999, ApJ, 517, 565

Peterson J. R., Fabian A. C., 2006, Physics Reports, 427, 1

Peterson J. R., Kahn S. M., Paerels F. B. S., Kaastra J. S., Tamura T., Bleeker J. A. M., Ferrigno C., Jernigan J. G., 2003, ApJ, 590, 207

Peterson J. R., Paerels F. B. S., Kaastra J. S., Arnaud M., Reiprich T. H., Fabian A. C., Mushotzky R. F., Jernigan J. G., Sakelliou I., 2001, A&A, 365, L104

Pierre M., Pacaud F., Juin J. B., Melin J. B., Valageas P., Clerc N., Corasaniti P. S., 2011, MNRAS, 414, 1732

Piffaretti R., Valdarnini R., 2008, A&A, 491, 71

Plagge T., Benson B. A., Ade P. A. R., Aird K. A., Bleem L. E., Carlstrom J. E., Chang C. L., Cho H.-M., Crawford T. M., Crites A. T., de Haan T., Dobbs M. A., George E. M., Hall N. R., Halverson N. W., Holder G. P., Holzapfel W. L., Hrubes J. D., Joy M., Keisler R., Knox L., Lee A. T., Leitch E. M., Lueker M., Marrone D., McMahon J. J., Mehl J., Meyer S. S., Mohr J. J., Montroy T. E., Padin S., Pryke C., Reichardt C. L., Ruhl J. E., Schaffer K. K., Shaw L., Shirokoff E., Spieler H. G., Stalder B., Staniszewski Z., Stark A. A., Vanderlinde K., Vieira J. D., Williamson R., Zahn O., 2010, ApJ, 716, 1118

Planck 2013 Results XVI, 2013, A&A submitted (arXiv:1303.5076)

Planck 2013 Results XX, 2013, A&A submitted (arXiv:1303.5080)

Planck Early Results IX, 2011, A&A, 536, A9

Planck Early Results VIII, 2011, A&A, 536, A8

Planck Early Results XI, 2011, A&A, 536, A11

Planck Intermediate Results I, 2012, A&A, 543, A102

Planck Intermediate Results III, 2013, A&A, 550, A129

Planck Intermediate Results IV, 2013, A&A, 550, A130

Planck Intermediate Results V, 2013, A&A, 550, A131

Planck Intermediate Results XI, 2013, A&A, 557, A52

Planelles S., Borgani S., Dolag K., Ettori S., Fabjan D., Murante G., Tornatore L., 2013, MNRAS, 431, 1487

Planelles S., Borgani S., Fabjan D., Killedar M., Murante G., Granato G. L., Ragone-Figueroa C., Dolag K., 2014, MNRAS, 438, 195

Pointecouteau E., Giard M., Benoit A., Désert F. X., Aghanim N., Coron N., Lamarre J. M., Delabrouille J., 1999, ApJL, 519, L115

Ponman T. J., Cannon D. B., Navarro J. F., 1999, Nature, 397, 135

Ponman T. J., Sanderson A. J. R., Finoguenov A., 2003, MNRAS, 343, 331

Pratt G. W., Arnaud M., Piffaretti R., Böhringer H., Ponman T. J., Croston J. H., Voit G. M., Borgani S., Bower R. G., 2010, A&A, 511, A85

Pratt G. W., Croston J. H., Arnaud M., Böhringer H., 2009, A&A, 498, 361

Puchwein E., Sijacki D., Springel V., 2008, ApJL, 687, L53

Puchwein E., Springel V., Sijacki D., Dolag K., 2010, MNRAS, 406, 936

Rasia E., Ettori S., Moscardini L., Mazzotta P., Borgani S., Dolag K., Tormen G., Cheng L. M., Diaferio A., 2006, MNRAS, 369, 2013

Rasia E., Meneghetti M., Martino R., Borgani S., Bonafede A., Dolag K., Ettori S., Fabjan D., Giocoli C., Mazzotta P., Merten J., Radovich M., Tornatore L., 2012, New Journal of Physics, 14, 055018

Rasmussen J., Ponman T. J., 2009, MNRAS, 399, 239

Rasmussen J., Ponman T. J., Mulchaey J. S., Miles T. A., Raychaudhury S., 2006, MNRAS, 373, 653

Rasmussen J., Sommer-Larsen J., Pedersen K., Toft S., Benson A., Bower R. G., Grove L. F., 2009, ApJ, 697, 79

Riess A. G., Filippenko A. V., Challis P., Clocchiatti A., Diercks A., Garnavich P. M., Gilliland R. L., Hogan C. J., Jha S., Kirshner R. P., Leibundgut B., Phillips M. M., Reiss D., Schmidt B. P., Schommer R. A., Smith R. C., Spyromilio J., Stubbs C., Suntzeff N. B., Tonry J., 1998, AJ, 116, 1009

Romer A. K., Nichol R. C., Holden B. P., Ulmer M. P., Pildis R. A., Merrelli A. J., Adami C., Burke D. J., Collins C. A., Metevier A. J., Kron R. G., Commons K., 2000, ApJS, 126, 209

Romer A. K., Viana P. T. P., Liddle A. R., Mann R. G., 2001, ApJ, 547, 594

Roncarelli M., Moscardini L., Borgani S., Dolag K., 2007, MNRAS, 378, 1259

Roncarelli M., Moscardini L., Tozzi P., Borgani S., Cheng L. M., Diaferio A., Dolag K., Murante G., 2006, MNRAS, 368, 74

Rozo E., Rykoff E. S., Evrard A., Becker M., McKay T., Wechsler R. H., Koester B. P., Hao J., Hansen S., Sheldon E., Johnston D., Annis J., Frieman J., 2009, ApJ, 699, 768

Sanderson A. J. R., O'Sullivan E., Ponman T. J., Gonzalez A. H., Sivanandam S., Zabludoff A. I., Zaritsky D., 2013, MNRAS, 429, 3288

Sarazin C. L., 1986, Reviews of Modern Physics, 58, 1

Sayers J., Czakon N. G., Mantz A., Golwala S. R., Ameglio S., Downes T. P., Koch P. M., Lin K.-Y., Maughan B. J., Molnar S. M., Moustakas L., Mroczkowski T., Pierpaoli E., Shitanishi J. A., Siegel S., Umetsu K., Van der Pyl N., 2013, ApJ, 768, 177

Scaramella R., Cen R., Ostriker J. P., 1993, ApJ, 416, 399

Schaye J., Dalla Vecchia C., 2008, MNRAS, 383, 1210

Schaye J., Dalla Vecchia C., Booth C. M., Wiersma R. P. C., Theuns T., Haas M. R., Bertone S., Duffy A. R., McCarthy I. G., van de Voort F., 2010, MNRAS, 402, 1536

Sehgal N., Bode P., Das S., Hernandez-Monteagudo C., Huffenberger K., Lin Y.-T., Ostriker J. P., Trac H., 2010, ApJ, 709, 920

Sehgal N., Trac H., Acquaviva V., Ade P. A. R., Aguirre P., Amiri M., Appel J. W., Barrientos L. F., Battistelli E. S., Bond J. R., Brown B., Burger B., Chervenak J., Das S., Devlin M. J., Dicker S. R., Bertrand Doriese W., Dunkley J., Dünner R., Essinger-Hileman T., Fisher R. P., Fowler J. W., Hajian A., Halpern M., Hasselfield M., Hernández-Monteagudo C., Hilton G. C., Hilton M., Hincks A. D., Hlozek R., Holtz D., Huffenberger K. M., Hughes D. H., Hughes J. P., Infante L., Irwin K. D., Jones A., Baptiste Juin J., Klein J., Kosowsky A., Lau J. M., Limon M., Lin Y.-T., Lupton R. H., Marriage T. A., Marsden D., Martocci K., Mauskopf P., Menanteau F., Moodley K., Moseley H., Netterfield C. B., Niemack M. D., Nolta M. R., Page L. A., Parker L., Partridge B., Reid B., Sherwin B. D., Sievers J., Spergel D. N., Staggs S. T., Swetz D. S., Switzer E. R., Thornton R., Tucker C., Warne R., Wollack E., Zhao Y., 2011, ApJ, 732, 44

Sehgal N., Trac H., Huffenberger K., Bode P., 2007, ApJ, 664, 149

Shankar F., Salucci P., Granato G. L., De Zotti G., Danese L., 2004, MNRAS, 354, 1020

Short C. J., Thomas P. A., 2009, ApJ, 704, 915

Short C. J., Thomas P. A., Young O. E., 2013, MNRAS, 428, 1225

Short C. J., Thomas P. A., Young O. E., Pearce F. R., Jenkins A., Muanwong O., 2010, MNRAS, 408, 2213

Sijacki D., Springel V., Di Matteo T., Hernquist L., 2007, MNRAS, 380, 877

Skibba R. A., van den Bosch F. C., Yang X., More S., Mo H., Fontanot F., 2011, MNRAS, 410, 417

Slipher V. M., 1914, Popular Astronomy, 22, 19

Smith R. J., Hudson M. J., Nelan J. E., Moore S. A. W., Quinney S. J., Wegner G. A., Lucey J. R., Davies R. L., Malecki J. J., Schade D., Suntzeff N. B., 2004, AJ, 128, 1558

Smith R. K., Brickhouse N. S., Liedahl D. A., Raymond J. C., 2001, ApJL, 556, L91

Spergel D. N., Bean R., Doré O., Nolta M. R., Bennett C. L., Dunkley J., Hinshaw G., Jarosik N., Komatsu E., Page L., Peiris H. V., Verde L., Halpern M., Hill R. S., Kogut A., Limon M., Meyer S. S., Odegard N., Tucker G. S., Weiland J. L., Wollack E., Wright E. L., 2007, ApJS, 170, 377

Springel V., 2005, MNRAS, 364, 1105

Springel V., Di Matteo T., Hernquist L., 2005, MNRAS, 361, 776

Springel V., White S. D. M., Jenkins A., Frenk C. S., Yoshida N., Gao L., Navarro J., Thacker R., Croton D., Helly J., Peacock J. A., Cole S., Thomas P., Couchman H., Evrard A., Colberg J., Pearce F., 2005, Nature, 435, 629

Springel V., White S. D. M., Tormen G., Kauffmann G., 2001, MNRAS, 328, 726

Springel V., Yoshida N., White S. D. M., 2001, New Astronomy, 6, 79

Stanek R., Evrard A. E., Böhringer H., Schuecker P., Nord B., 2006, ApJ, 648, 956

Stanek R., Rasia E., Evrard A. E., Pearce F., Gazzola L., 2010, ApJ, 715, 1508

Staniszewski Z., Ade P. A. R., Aird K. A., Benson B. A., Bleem L. E., Carlstrom J. E., Chang C. L., Cho H.-M., Crawford T. M., Crites A. T., de Haan T., Dobbs M. A., Halverson N. W., Holder G. P., Holzapfel W. L., Hrubes J. D., Joy M., Keisler R., Lanting T. M., Lee A. T., Leitch E. M., Loehr A., Lueker M., McMahon J. J., Mehl J., Meyer S. S., Mohr J. J., Montroy T. E., Ngeow C.-C., Padin S., Plagge T., Pryke C., Reichardt C. L., Ruhl J. E., Schaffer K. K., Shaw L., Shirokoff E., Spieler H. G., Stalder B., Stark A. A., Vanderlinde K., Vieira J. D., Zahn O., Zenteno A., 2009, ApJ, 701, 32

Starck J.-L., Murtagh F. D., Bijaoui A., 1998, Image Processing and Data Analysis

Stott J. P., Collins C. A., Burke C., Hamilton-Morris V., Smith G. P., 2011, MNRAS, 414, 445

Stott J. P., Edge A. C., Smith G. P., Swinbank A. M., Ebeling H., 2008, MNRAS, 384, 1502

Stott J. P., Hickox R. C., Edge A. C., Collins C. A., Hilton M., Harrison C. D., Romer A. K., Rooney P. J., Kay S. T., Miller C. J., Sahlén M., Lloyd-Davies E. J., Mehrtens N., Hoyle B., Liddle A. R., Viana P. T. P., McCarthy I. G., Schaye J., Booth C. M., 2012, MNRAS, 422, 2213

Sun M., Sehgal N., Voit G. M., Donahue M., Jones C., Forman W., Vikhlinin A., Sarazin C., 2011, ApJL, 727, L49

Sun M., Voit G. M., Donahue M., Jones C., Forman W., Vikhlinin A., 2009, ApJ, 693, 1142

Sunyaev R. A., Zeldovich Y. B., 1970, Comments on Astrophysics and Space Physics, 2, 66

Sunyaev R. A., Zeldovich Y. B., 1972, A&A, 20, 189

Szalay A. S., Ellis R. S., Koo D. C., Broadhurst T. J., 1991, in American Institute of Physics Conference Series, Vol. 222, After the first three minutes, Holt S. S., Bennett C. L., Trimble V., eds., pp. 261–275

The Dark Energy Survey Collaboration, 2005, White paper submitted to the Dark Energy Task Force (astro-ph/0510346)

Thomas P., Carlberg R. G., 1989, MNRAS, 240, 1009

Tinker J., Kravtsov A. V., Klypin A., Abazajian K., Warren M., Yepes G., Gottlöber S., Holz D. E., 2008, ApJ, 688, 709

Valtchanov I., Pierre M., Gastaud R., 2001, A&A, 370, 689

van Daalen M. P., Schaye J., Booth C. M., Dalla Vecchia C., 2011, MNRAS, 415, 3649

van Daalen M. P., Schaye J., McCarthy I. G., Booth C. M., Dalla Vecchia C., 2014, MNRAS, 440, 2997

van Haarlem M. P., Frenk C. S., White S. D. M., 1997, MNRAS, 287, 817

Vanderlinde K., Crawford T. M., de Haan T., Dudley J. P., Shaw L., Ade P. A. R., Aird K. A., Benson B. A., Bleem L. E., Brodwin M., Carlstrom J. E., Chang C. L., Crites A. T., Desai S., Dobbs M. A., Foley R. J., George E. M., Gladders M. D., Hall N. R., Halverson N. W., High F. W., Holder G. P., Holzapfel W. L., Hrubes J. D., Joy M., Keisler R., Knox L., Lee A. T., Leitch E. M., Loehr A., Lueker M., Marrone D. P., McMahon J. J., Mehl J., Meyer S. S., Mohr J. J., Montroy T. E., Ngeow C.-C., Padin S., Plagge T., Pryke C., Reichardt C. L., Rest A., Ruel J., Ruhl J. E., Schaffer K. K., Shirokoff E., Song J., Spieler H. G., Stalder B., Staniszewski Z., Stark A. A., Stubbs C. W., van Engelen A., Vieira J. D., Williamson R., Yang Y., Zahn O., Zenteno A., 2010, ApJ, 722, 1180

Velliscig M., van Daalen M. P., Schaye J., McCarthy I. G., Cacciato M., Le Brun A. M. C., Dalla Vecchia C., 2014, MNRAS, 442, 2641

Vikhlinin A., Burenin R. A., Ebeling H., Forman W. R., Hornstrup A., Jones C., Kravtsov A. V., Murray S. S., Nagai D., Quintana H., Voevodkin A., 2009a, ApJ, 692, 1033

Vikhlinin A., Kravtsov A., Forman W., Jones C., Markevitch M., Murray S. S., Van Speybroeck L., 2006, ApJ, 640, 691

Vikhlinin A., Kravtsov A. V., Burenin R. A., Ebeling H., Forman W. R., Hornstrup A., Jones C., Murray S. S., Nagai D., Quintana H., Voevodkin A., 2009b, ApJ, 692, 1060

Voges W., Aschenbach B., Boller T., Bräuninger H., Briel U., Burkert W., Dennerl K., Englhauser J., Gruber R., Haberl F., Hartner G., Hasinger G., Kürster M., Pfeffermann E., Pietsch W., Predehl P., Rosso C., Schmitt J. H. M. M., Trümper J., Zimmermann H. U., 1999, A&A, 349, 389

Voit G. M., 2005, Reviews of Modern Physics, 77, 207

Voit G. M., Evrard A. E., Bryan G. L., 2001, ApJL, 548, L123

Voit G. M., Kay S. T., Bryan G. L., 2005, MNRAS, 364, 909

Voit G. M., Ponman T. J., 2003, ApJL, 594, L75

Weinberg D. H., Mortonson M. J., Eisenstein D. J., Hirata C., Riess A. G., Rozo E., 2013, Physics Reports, 530, 87

White M., Hernquist L., Springel V., 2002, ApJ, 579, 16

White S. D. M., Frenk C. S., 1991, ApJ, 379, 52

White S. D. M., Navarro J. F., Evrard A. E., Frenk C. S., 1993, Nature, 366, 429

White S. D. M., Rees M. J., 1978, MNRAS, 183, 341

Wiersma R. P. C., Schaye J., Smith B. D., 2009, MNRAS, 393, 99

Wiersma R. P. C., Schaye J., Theuns T., Dalla Vecchia C., Tornatore L., 2009, MNRAS, 399, 574

Yang X., Mo H. J., Jing Y. P., van den Bosch F. C., Chu Y., 2004, MNRAS, 350, 1153

York D. G., Adelman J., Anderson, Jr. J. E., Anderson S. F., Annis J., Bahcall N. A., Bakken J. A., Barkhouser R., Bastian S., Berman E., Boroski W. N., Bracker S., Briegel C., Briggs J. W., Brinkmann J., Brunner R., Burles S., Carey L., Carr M. A., Castander F. J., Chen B., Colestock P. L., Connolly A. J., Crocker J. H., Csabai I., Czarapata P. C., Davis J. E., Doi M., Dombeck T., Eisenstein D., Ellman N., Elms B. R., Evans M. L., Fan X., Federwitz G. R., Fiscelli L., Friedman S., Frieman J. A., Fukugita M., Gillespie B., Gunn J. E., Gurbani V. K., de Haas E., Haldeman M., Harris F. H., Hayes J., Heckman T. M., Hennessy G. S., Hindsley R. B., Holm S., Holmgren D. J., Huang C.-h., Hull C., Husby D., Ichikawa S.-I., Ichikawa T., Ivezić Ž., Kent S., Kim R. S. J., Kinney E., Klaene M., Kleinman A. N., Kleinman S., Knapp G. R., Korienek J., Kron R. G., Kunszt P. Z., Lamb D. Q., Lee B., Leger R. F.,

Limmongkol S., Lindenmeyer C., Long D. C., Loomis C., Loveday J., Lucinio R., Lupton R. H., MacKinnon B., Mannery E. J., Mantsch P. M., Margon B., McGehee P., McKay T. A., Meiksin A., Merelli A., Monet D. G., Munn J. A., Narayanan V. K., Nash T., Neilsen E., Neswold R., Newberg H. J., Nichol R. C., Nicinski T., Nonino M., Okada N., Okamura S., Ostriker J. P., Owen R., Pauls A. G., Peoples J., Peterson R. L., Petravick D., Pier J. R., Pope A., Pordes R., Prosapio A., Rechenmacher R., Quinn T. R., Richards G. T., Richmond M. W., Rivetta C. H., Rockosi C. M., Ruthmansdorfer K., Sandford D., Schlegel D. J., Schneider D. P., Sekiguchi M., Sergey G., Shimasaku K., Siegmund W. A., Smee S., Smith J. A., Snedden S., Stone R., Stoughton C., Strauss M. A., Stubbs C., SubbaRao M., Szalay A. S., Szapudi I., Szokoly G. P., Thakar A. R., Tremonti C., Tucker D. L., Uomoto A., Vanden Berk D., Vogeley M. S., Waddell P., Wang S.-i., Watanabe M., Weinberg D. H., Yanny B., Yasuda N., SDSS Collaboration, 2000, AJ, 120, 1579

Yoshida N., Colberg J., White S. D. M., Evrard A. E., MacFarland T. J., Couchman H. M. P., Jenkins A., Frenk C. S., Pearce F. R., Efstathiou G., Peacock J. A., Thomas P. A., 2001, MNRAS, 325, 803

Zwicky F., 1933, Helvetica Physica Acta, 6, 110

Zwicky F., Herzog E., Wild P., Karpowicz M., Kowal C. T., 1961, Catalogue of galaxies and of clusters of galaxies, Vol. I